ESEA

Institute of Energy Systems
and Electrical Drives

Sensorless Control of a Salient Pole Synchronous Reluctance Machine for High Rotational Speeds

DIPLOMA THESIS

Conducted in partial fulfillment of the requirements for the degree of a

Diplom-Ingenieur (Dipl.-Ing.)

supervised by

O.Univ.Prof. Dipl.-Ing. Dr.techn. Manfred Schrödl
Univ.Ass. Dipl.-Ing. Dr.techn. Matthias Hofer

submitted at the

Technische Universität Wien

Faculty of Electrical Engineering and Information Technology
Institute of Energy Systems and Electrical Drives

by
Bernhard Reiter, BSc.
Matriculation number 0627559
Penzingerstraße 36-38 / 1 / 5
1140 Wien
Österreich

Wien, 18 Jan 2018

Department of Electrical Drives and Machines
A-1040 Wien, Gusshausstr. 25-29/370-2, Internet: https://www.ieam.tuwien.ac.at

Danksagung

Ich danke Prof. Manfred Schrödl für das ermöglichen dieser Diplomarbeit und die Einladung zur Teilnahme an diversen Antriebstechnik Konferenzen. Meinem Betreuer Dr. Matthias Hofer danke ich dafür, dass er stets und prompt Zeit hatte mich bei Fragestellungen der Arbeit an sich, und beim Verfassen dieses Dokuments zu Unterstützen.

Größte Dankbarkeit und Wertschätzung möchte ich meinen Eltern Gabriele und Alfred zum Ausdruck bringen. Ohne ihre langjährige Unterstützung, ihre Geduld, ihr Verständnis und ihre Liebe wäre es mir unmöglich gewesen an der TU Wien erfolgreich zu studieren. Dies gilt insbesondere auch für meine Großmutter Paula und meine Partnerin Beril. Deren unerschütterlicher Glaube und vorbehaltloses Vertrauen halfen mir alle Situationen zu meistern.
Alles geht.

Außerdem möchte ich mich bei Kollegen, Freunden und Weggefährten für ihre Zeit und motivierenden Worte bedanken: Philipp, Thomas, Richard, Florian, Ivo, Bettina und Georg.

Wien, 18. Jänner 2018

Abstract

This thesis describes the design, implementation and optimization of field-oriented control for a salient pole synchronous reluctance machine including flux weakening operation to reach high rotational speeds. At first a rotary encoder is used for shaft position measurement. This serves as foundation for the adoption of sensorless field-oriented control where the rotary encoder is substituted by mathematical models. The system's target application is a variable speed drive capable of four quadrant operation.

Standstill operation and slow shaft rotation in sensorless mode are enabled by application of the INFORM method. A dedicated PWM pattern resembling three distinct voltage space vectors is used at low speeds to apply the method directly. If required, a transition to a classical symmetric PWM pattern and a back-electromotive force based estimation method allow for sensorless operation at medium and high shaft speeds. Upon reaching the limit of available DC-link voltage, flux weakening is realized by restricting the reference current space vector alongside the positive or negative MTPA line. In case of sensorless operation, additional constraints result into an allowed region for the reference current space vector that lies between the positive and negative MTPA lines. Mechanical shaft speeds of up to $26\,000\,\mathrm{rpm}$ and $24\,000\,\mathrm{rpm}$ were achieved in sensor-based and sensorless modes respectively.

Chapter 1 motivates this thesis and defines its scope by three topics. Connections to prior and ongoing academical work is established. A patent search report on the subject matter issued by the Austrian Patent Office (ÖPA) is presented.

Chapter 2 describes all three major system parts. These are: The machine, the voltage source inverter and the rotary encoder. Important aspects to properly construct the experimental setup are also covered.

Chapter 3 describes the targeted digital signal controller TMS320F28335 and applied numerical methods. Advice on how to increase computational performance for that specific device is given.

Chapter 4 covers every subsystem that is incorporated into the field-oriented control scheme in detail. Aspects to maintain high voltage reserves and achieve high rotational speeds are highlighted. A flux weakening strategy that distinguishes transient and quasi-stationary operational states is presented.

Chapter 5 completes the system description. The implemented INFORM variant is classified and subsequently assessed with respect to prior set quality targets. Further, the used back electromotive force based method is presented. A transition strategy to link both methods and necessary modifications of the sensor-based system are discussed. Sensorless flux weakening is described by systematically considering voltage, torque and angular error constraints. All discussed subsystems are verified by executing representative speed trajectories.

Chapter 6 concludes the thesis, and relates its outcomes to the three topics that were defined in the first chapter.

Kurzzusammenfassung

Diese Arbeit beschreibt Entwurf, Implementierung und Realisierung einer feldorientierten Regelung für eine Synchron-Reluktanzmaschine mit ausgeprägten Polen inklusive Feldschwächung zum Erreichen hoher Drehzahlen. Zunächst wird ein Drehgeber zur Positionsbestimmung verwendet. Dies dient als Grundlage für die sensorlose Regelung, wo der Drehgeber durch mathematische Modelle ersetzt wird. Die Anwendung des Systems ist als drehzahlgeregelter vierquadranten Antrieb vorgesehen.

Stillstand und Betrieb mit geringen Drehzahlen im sensorlosen Fall werden mittels IN-FORM Verfahrens erreicht. Ein PWM Pulsmuster bestehend aus drei unterschiedlichen Spannungsraumzeigern ermöglicht die eingebettete Anwendung des besagten Verfahrens. Gegebenenfalls erfolgt eine Umschaltung auf das klassische symmetrische PWM Pulsmuster und ein EMK-basiertes sensorloses Verfahren um mittlere und hohe Drehzahlen zu erzielen. Bei Erreichen der Spannungsgrenze des Umrichters erfolgt eine Feldschwächung durch Beschränkung des Soll-Stromraumzeigers entlang der positiven bzw. der negativen MTPA Linie. Im sensorlosen Fall führen zusätzliche Nebenbedingungen zu einem neuen zulässigen Bereich für mögliche Soll-Stromraumzeiger, welcher zwischen besagten Linien liegt. Mechanische Drehzahlen von bis zu $26\,000\,\mathrm{U/min}$ und $24\,000\,\mathrm{U/min}$ im sensorgestützten bzw. im sensorlosen Betrieb wurden erreicht.

Kapitel 1 erläutert die Motivation dieser Arbeit und definiert ihren Umfang anhand dreier Themenblöcke. Vorangegangene und aktuelle Forschungsarbeiten werden zusammengefasst. Ein Recherchebericht des Österreichischen Patentamts zum Gegenstand der Arbeit wird ebenfalls vorgestellt.

Kapitel 2 beschreibt alle wesentlichen Teile des Systems: Die Maschine, den Spannungszwischenkreisumrichter und den Inkrementalgeber. Wichtige Aspekte bezüglich Erstellung und Inbetriebnahme des Versuchaufbaus werden ebenfalls behandelt.

Kapitel 3 beschreibt den verwendeten Prozessor TMS320F28335 und verwendete numerische Methoden. Hinweise zur bestmöglichen Ausnutzung der zur Verfügung stehenden Rechenleistung werden ebenso gegeben.

Kapitel 4 beschreibt jede Komponente der feldorientierten Regelung detailliert. Aspekte hinsichtlich hoher Spannungsreserven und Drehzahlen werden hervorgehoben. Eine Feldschwächstrategie, welche zwischen transientem und quasi-stationärem Betriebszustand unterscheidet, wird präsentiert.

Kapitel 5 schließt die Systembeschreibung ab. Die implementierte INFORM Variante wird klassifiziert und anhand zuvor definierter Qualitätskriterien bewertet. Danach erfolgt eine Beschreibung des EMK-basierten Verfahrens. Eine Strategie um zwischen beiden Methoden zu wechseln, sowie notwendige Modifikationen des sensorgestützten Systems werden ebenfalls behandelt. Sensorlose Feldschwächung wird systematisch anhand bestehender Beschränkungen bezüglich Spannung, Moment und Winkelfehler beschrieben. Alle Subsysteme werden durch charakteristische Drehzahltrajektorien verifiziert.

Kapitel 6 fasst die Arbeit zusammen und behandelt mittels erlangter Erkenntnisse die drei eingangs definierten Themenblöcke.

Contents

1 Scope and Outline of this Thesis

1.1 Motivation

Two important fields of research covered by the "Department of Electrical Drives and Machines" are: (sensorless[1]) active magnetic bearings (AMBs) and (sensorless) control of electrical machines. A long-term goal is to build a prototype drive system featuring AMBs that requires no position sensor at all and can run from standstill up to several ten thousand revolutions per minute.

Such a prototype therefore comprises a set of AMBs, an electric drive and one or several inverters with software to control them. A design decision to merge motor and bearing actuation & control into a single device[2] was taken to reduce communication overhead that can become a critical issue at high speeds. A salient pole synchronous reluctance machine (SynRM) was chosen as machine type. It combines advantages regarding safety and compatibility to AMBs (due to non-usage of permanent magnets) as well as sensorless capability (due to salience).

A sensorless variable speed drive aimed at high speeds using a "standard" three phase inverter had to be built and developed independently from the other two components. The development process and the presentation of its results, trade-offs and conclusions are the content of this thesis. The research outcomes and developed motor control software shall be used as a starting basis to realize the targeted high-speed sensorless AMB prototype in the future. For now, the strategy is to build and optimize one system (Motor, AMB, Inverter) at a time.

More specifically, this thesis describes the development of a sensor-based and sensorless variable speed drive[3] for a salient pole synchronous reluctance machine that is capable of flux weakening to reach mechanical shaft speeds of $26\,000$ rpm(sensored) & $24\,000$ rpm (sensorless). To achieve sensorless operation the so-called "silent" INFORM is adopted and subsequently switched to a back-electromotive force based method, designated as SynRM-BEMF, for higher speeds. Therefore, actuating PWM[4] patterns and observer models are switched. According to the next Section 1.2 this specific combination of above specified properties and features is considered to be an advancement in the field of electric drives.

The specific SynRM covered here was designed in [1]. The assembly of this motor marked the start of this work. Formally, three thesis topics are formulated to define the scope and author's scientific contribution to the field. They will be discussed in depth in the last Chapter 6.

---

[1] The term "sensorless" commonly denotes absence of a shaft encoder in the field of electrical machines. Current sensors and other sensor devices are adopted.

[2] a so-called "multi-phase inverter"

[3] capable of four quadrant operation; sine commute type.

[4] <u>P</u>ulse <u>W</u>idth <u>M</u>odulation

<div align="center">THESIS TOPIC 1:</div>

The salient pole synchronous reluctance machine, simulated in [1] shall be assembled. A proper test bench that incorporates this machine should be built. Together with a provided voltage source inverter, basic field-oriented control should be implemented. The simulated machine's characteristics & parameters should be verified. That is: Magnetic linearity, stator resistor, direct- and quadrature axis inductances.

<div align="center">THESIS TOPIC 2:</div>

To reach high mechanical shaft speeds, flux weakening methods shall be adopted. Suitable methods should be chosen for both sensor-based and sensorless operation. If possible the chosen strategy should be split into a "transient" and "quasi-stationary" part and a method to switch between the two should be established. Operational speeds as high as possible should be reached safely. Challenges encountered to reach these speeds as well as ultimate limits should be investigated, quantified, solved and documented.

<div align="center">THESIS TOPIC 3:</div>

Sensorless operation at standstill and low speeds shall be achieved by using an INFORM variant with embedded voltage test shots (3 active space vector modulation). Thereto currents should be measured at low-side bridge shunts of the used inverter. At medium to high speeds a method based on the integration of the stator voltage space vector (SynRM-BEMF) shall be implemented. Both methods should be assessed independently, with prior defined quality criteria. Challenges encountered to reach these criteria as well as ultimate limits should be investigated, quantified, solved and documented. A proper way to switch observer models as well as PWM patterns should be established.

1.2 Prior Art, State of the Art

1.2.1 TU Wien internal

As discussed above, the SynRM of the drive train was designed in [1]. The master thesis [2] investigated a legacy variant of INFORM for SynRMs. Then [3] delivered the proof of concept for the above listed topics two and three without flux weakening (a "proof of concept" simulation was conducted there). This work greatly benefited from the descriptions and findings of [3] and the author hopes to serve his successor in a similar way.

Regarding multiphase inverters, [4] generated an initial design. Its ideas and the discovered challenges contributed to the successor's [5] very positive outcome.

Concerning AMBs, the dissertation [6] establishes a foundation to apply a variant of the INFORM method at AMBs. The newest contribution is given by the master thesis [7].

1.2.2 External

A good resource on reluctance machines is [8] and the listed literature therein. Several other sources will be cited within the respective context and the reader is referred to the bibliography at the end of this thesis.

Additionally, the Austrian Patent Office (ÖPA) offered the possibility to conduct a patent literature search free of charge for Austrian students upon application. The service was granted for this thesis and the results can be inspected in Appendix A.1. Two aspects are interesting at this stage:

- The search task was specified for *"Sensorless control of synchronous reluctance machines for the whole speed range using two different methods"*. The actual description was more exhaustive (see thesis abstract) to gain better results and is quoted in a simplified way here.

- Eight patents were cited and the "subject matter" of this thesis was classified using the IPC[5] and CPC[6] system. This marks a very good starting point for future patent literature search. The main two subclasses stated were H02P and H02K. The patents are referenced in Appendix A.1 together with a patent classification.

1.3 Notation & Nomenclature

As a general notation convention in this document unscaled quantities are represented with upper case letters whereas scaled quantities are denoted with lower case letters. Regarding *time*, scaling will be applied only in Section 2.2 for didactic reasons. After this section indexed lower case and upper case letters t_i, T_i and τ will denote time related constants and quantities. A variable's time dependency will be indicated by e.g. $v = v(t)$ or as sampled time discrete signal e.g. $l_k = l[k] = l(kT_s)$, $k \in \mathbb{Z}$ with T_s being the corresponding[7] sample time.

In the frequency domain s denotes the Laplace variable, e.g. $G = G(s)$ for a plant. After their definition the dependence of t and s respectively is often omitted for reasons of simplicity and readability, but will be indicated where necessary. Vectors and matrices are written in bold letters e.g. $\mathbf{r}, \mathbf{H}$. As it is common in electrical engineering complex numbers and quantities $\underline{z} \in \mathbb{C}$ are underlined and for the imaginary unit the letter 'j' is utilized instead of 'I' to avoid ambiguity with electrical currents, e.g. $\underline{z} = a + \mathrm{j}b$.

Since the specific type of electrical machine covered in this thesis is a synchronous reluctance machine there is no need to distinguish between rotor- and stator-related space vector quantities. All current, flux and voltage space vectors are stator-related by default and the subscript $(\cdot)_s$ is omitted. The superscript $(\cdot)^{\alpha\beta}$ or $(\cdot)^{dq}$ indicates the used coordinate systems for space vectors. If no superscript is used the equation is independent of the used coordinate system.

Presented numerical values are rounded using the tie-breaking rule of *round half away from zero*, e.g. $1.5 \approx 2$ and $-1.5 \approx -2$. If an equation contains a numeral and this is the exact value the "$=$" sign is used, for rounded values "$\approx$" is used. Tables may contain rounded and exact values. Presented real time data from the operating motor is displayed in I4Q12 (16-bit) format due to the measurement device's resolution, see Section 2.1, Section 3.4. However the actual processing data format for almost all presented quantities within the DSC[8] is I8Q24 (32-bit). The terms DSC and DSP[9] are used synonym as the manufacturer of the deployed TI-28335 uses both terms for this device.

---

[5] International <u>P</u>atent <u>C</u>lassification
[6] <u>C</u>ooperative <u>P</u>atent <u>C</u>lassification
[7] Throughout this thesis three sample times will occur: $T_{ADC} < T_{fast} < T_{slow}$. From the context of the accompanying text it will always be clear which discrete time scale is applying.
[8] <u>D</u>igital <u>S</u>ignal <u>C</u>ontroller
[9] <u>D</u>igital <u>S</u>ignal <u>P</u>rocessor

2 System Description

In this chapter the realized SynRM drive system will be introduced and described comprehensively. Figure 2.1 illustrates the electric drive development configuration of this thesis.
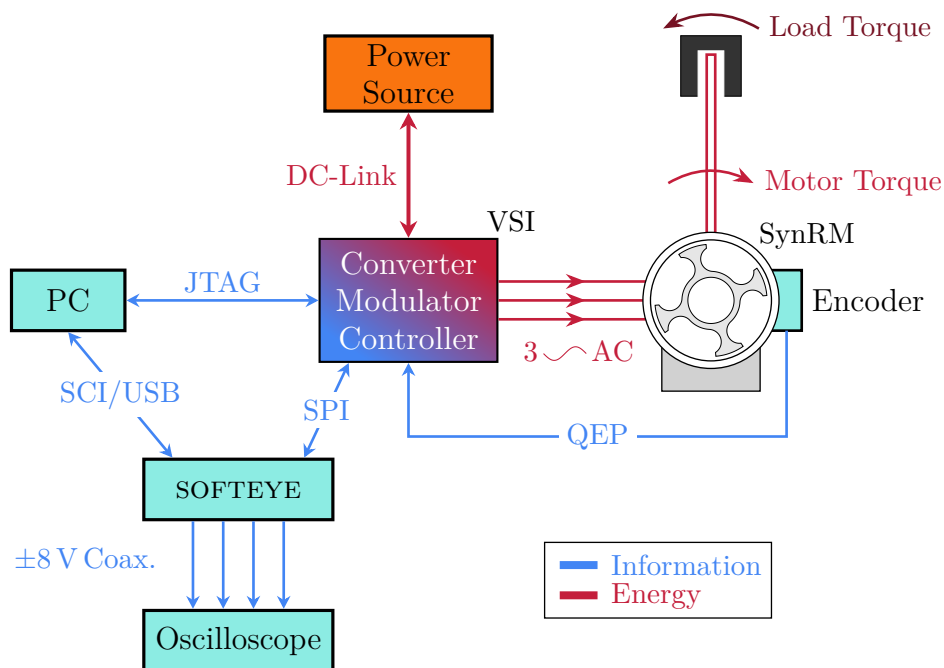
Figure 2.1: SynRM drive key components and their connections

Both information and energy flows are apparent at the $\underline{V}$oltage $\underline{S}$ource $\underline{I}$nverter (VSI). A $\underline{D}$irect $\underline{C}$urrent (DC) - Link is established at the VSI by connecting an unipolar power source. The power stage of the VSI is designated as converter and comprises of three half bridge silicon n-channel MOSFET[1] elements. Switching signals are calculated by a software modulator. They are applied to each gate terminal to convert DC voltages and currents to $\underline{A}$lternating $\underline{C}$urrent (AC) quantities. A description of the power stage, measurements and important features of the VSI is given in Section 2.5.

Power conversion, modulation, measurements and communications are coordinated by a $\underline{D}$igital $\underline{S}$ignal $\underline{C}$ontroller (DSC). The target hardware is a Texas Instruments TMS320F28335. It is described in Chapter 3. The DSC hosts sensor-based and sensorless $\underline{F}$ield-$\underline{O}$riented $\underline{C}$ontrol (FOC) software. Both methods present the core matter of this thesis and are described in Chapter 4

---

[1]$\underline{M}$etal $\underline{O}$xide $\underline{S}$emiconductor $\underline{F}$ield-$\underline{E}$ffect $\underline{T}$ransistor

and Chapter 5. Scaling as important paradigm for analysis and implementation is discussed in Section 2.2.

Space vector methods will be used to derive a mathematical model as basis for FOC in Section 2.3. A detailed overview and description of SynRMs is given in Section 2.4. There the previously derived model will be adapted for the salient pole SynRM deployed. The specific rotor design from [1] is also depicted in Figure 2.1. The shaft's mechanical position information is of fundamental importance for sensored FOC and the assessment of sensorless FOC. It is measured by an incremental encoder and transmitted to the VSI in Quadrature Encoder Pulse format. Encoder and decoding process at the VSI's firmware are described in Section 2.6.

When adopting FOC, a sinusoidal three phase AC current system is applied to the SynRM's stator terminals. The electric machine transforms electric energy into mechanical energy in the form of shaft torque and shaft speed. In this thesis the motor's shaft is loaded by friction to test each system feature exhaustively.

Debug, program and monitoring tools are indicated at the left side of Figure 2.1. A presentation of the actual assembly and these tools commences this chapter in Section 2.1.

The famous quote *"The whole is greater than the sum of its parts"* is especially true for high performance electrical drives. It also constitutes the paradigm of this thesis. Each of the above mentioned hardware & software components has to be inspected, configured and used in an integrative way rather than in an isolated approach. Only then a sensorless high performance system can be realized.

2.1 Experimental Setup

In Figure 2.2, photographs of the SynRM drive system's essential components are depicted. In the course of this thesis a base plate and sensor fixture were designed and assembled. Mechanical drawings of these parts can be inspected in Appendix B.2. The inverter's schematics are supplied in Appendix B.1 and will be referenced on numerous occasions. The SynRM rotor that was designed in [1] is also photographed. Its actual 2D shape is depicted in various figures, e. g. Figure 2.1. Exact dimensions and drawings of shaft, motor housing and accompanying parts is available at TU Wien, [9].

Important devices used throughout this thesis are listed in Table 2.1. The SOFTEYE that is mentioned in both figures is a debugging tool that is built and maintained by TU Wien. Dedicated firmware for both, host device and target device is necessary. It establishes a synchronous connection to the inverter using the SPI[2] protocol at a polling rate of T_{fast} (which is the system's main task). An asynchronous connection to the host system (PC) is maintained by usage of an SCI[3] protocol. It also converts up to four user defined variables to voltages that can be displayed using an oscilloscope. It is capable of processing three common data types in embedded systems: `int`, `long` and `float`. Such a device is of great importance for a smooth development process. The GPIO[4] bank indicated on the top left of Figure 2.2 also served for debug purposes such as Task-time measurements.

---

[2]Serial Peripheral Interface
[3]Serial Communications Interface
[4]General Purpose Input Output

Phase UVW

QEP

U_{DC}

GPIO (Dbg.)

reluctant rotor

Softeye   JTAG
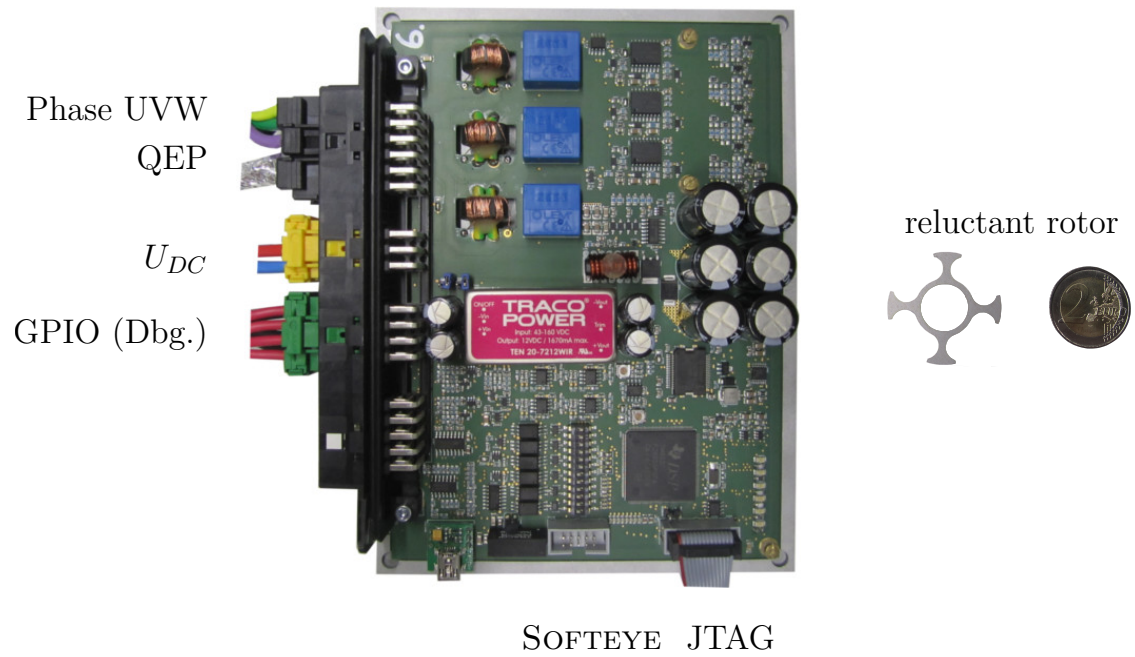
sensor, mounting & interface

Phase UVW & QEP

damper pad   star point
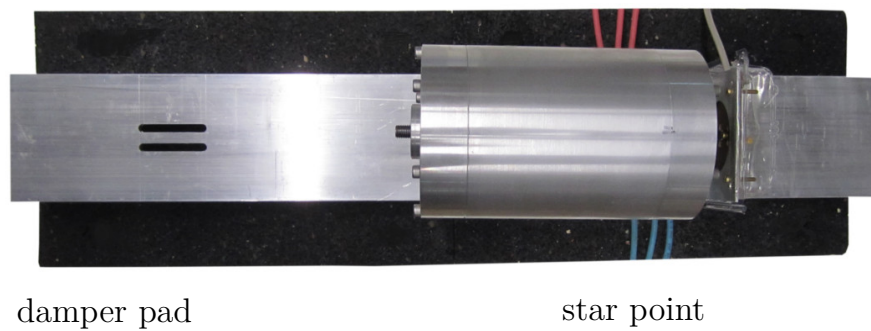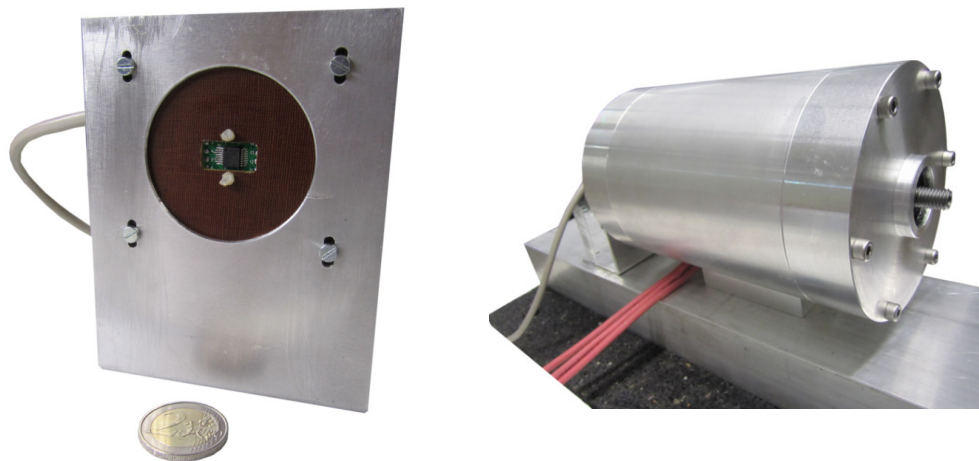
Figure 2.2: SynRM drive impressions; 2€ coins depicted; different scaling between photographs

Equipment Overview	
Device	Type
Power Supply	Delta Elektronika SM660-AR-11
Power Supply	Heiden EA-PS 9750-25
Oscilloscope	Agilent InfiniiVision DSO-X 3014A
Current Probe Amplifier	Tektronix TCPA300
Current Probe	Tektronix TCP303
Multimeter	Fluke 73 III
SOFTEYE Debug Probe	HW: 2014
JTAG Debug Probe	Texas Instruments XDS100v2
USB Isolator	Delock 62588

Table 2.1: Measurement devices, power sources and debug devices used to carry out this thesis

A black damping pad is also visible in Figure 2.2. When the system was operated without such a damper plate, vibrations would cause the magnetic pill mounted on the shaft to displace. This eventually destabilized the system. Such effects became apparent at a range of over 20 krpm.

During early concept and assembly stages of the thesis a goal was to use two motors with to inverters at a later process step. This way a complete motor test set-up would be available for testing and parameter identification. A claw coupling (KTR Rotex GS14 1.1) was ordered and a mechanical adapter to connect both shaft ends to this coupling was designed and built. Due to the mechanical dimensions of motor shaft and housing shield only a claw coupling variant with screw fixation could be considered. According to [10] the maximum possible speed for this coupling is 15.9 krpm. As the thesis progressed substantially higher speeds were reached and a restriction back to this value was deemed unnecessary. The strategy then was to investigate all topics of Section 1.1 using only a "caliper-like" brake (not depicted) to load the motor. This delivered good results. Nevertheless a combination of load machine and telemetry machine should be considered for further investigations.

In Table 2.2 an overview of used software tools is given.

2.2 Scaling

Scaling or normalization is the process of transforming physical system quantities comprised of numbers and SI-units to a dimensionless per-unit[5] based representation with a narrowed numerical range. It is an essential process offering numerous advantages at the design and implementation stage of practical control systems.

To normalize a variable (for instance an electric current) it is divided by a so called base value

---

[5]The term *per-unit* (p.u.) refers to a quantity that is expressed as a fraction of a chosen base value.

Software Overview	
Program/Tool	Version
Code Composer Studio	6.1.2.00015
Compiler	TI v16.9.0.LTS
SOFTEYE Debug Probe	v20F8
Matlab	R2015b
Maple	18
Ansys Maxwell	14
TeXstudio	2.12.4
Operating System	Windows 7 Professional SP1

Table 2.2: Utilized software overview

of the same physical dimension, e. g.

$$i_{\mathrm{U}}\left(t\right) = \frac{I_{\mathrm{U}}\left(t\right)}{I_B} \tag{2.1}$$

with $I_{\mathrm{U}}\left(t\right)$ as the instantaneous Phase-U current as a function of time t of a three-phase load, I_B as the chosen base value and $i_{\mathrm{U}}\left(t\right)$ as the scaled dimensionless version of $I_{\mathrm{U}}\left(t\right)$. The subscript B indicates a chosen base value.

For fixed point target MCU's[6] and data formats scaling is mandatory since the numerical range of representable numerals is bound to a minimum and a maximum value depending on the available integer-bits. But also floating point[7] MCU's take advantage of proper scaling to small intervals around zero since the numerical precision of a floating point represented number is best around this numerical range [11],[12],[13].

Additional advantages of scaling are

- intuitive insight into the system status;

- increased portability of the source code from different target systems;

- maximum utilization of available precision for fixed- and floating-point data representations;

- thus improved numerical performance in terms of roundoff- and truncation-errors in mathematical algorithms.

In [14] general scaling guidelines for practical control systems are given. For the field of electrical drives however a best-practise scaling approach exists[8] that will be applied here.

---

[6]Micro-Controller-Units
[7]Throughout this thesis the term *floating point* refers to the IEEE 754 Single-Precision Floating-Point format.
[8]see also [15]

$$\gamma_B := 1\,\text{rad} \tag{2.2}$$

is defined. Throughout this document, unless otherwise noted, $\gamma(t)$ is the (scaled) *electrical* angle, viz.

$$\gamma(t) := \frac{\gamma_e(t)}{\gamma_B} \ . \tag{2.3}$$

Its numeric value is the same as γ_e in Radians and may be converted to Degrees[°] or an implementation friendly 4IQ28 format[9] where applicable. To arrive at consistent sets of scaled equations without additional multiplicative factors the base values for current- voltage- and time-quantities can be chosen without constraints. All the other base values are derived from those former three. For currents the peak value of the *rated* phase current is selected. Voltages are scaled with the peak value of the *rated* phase voltage which in case of the three half-bridge VSI from Section 2.5 is related to the DC-Link voltage by a factor of two-thirds [16, 17] . This yields

$$I_B := \hat{I}_{Ph-Rated} = 18\,\text{A} \ , \tag{2.4}$$

$$U_B := \hat{U}_{Ph-Rated} = U_{DC} \cdot \frac{2}{3} = 40\,\text{V} \ . \tag{2.5}$$

Both of these quantities therefore stem from the machine design outlined in Section 2.4. Peak values are adopted due to the nature of space vector theory dealing with instantaneous quantities. The base values for the quantities of time and angular velocity should not be chosen independently as this would cause extra multiplicative factors in the machine equations. This is demonstrated with the help of (2.36). Said equation is normalized using the scheme from (2.1),

$$\Omega_e(t) = \frac{\mathrm{d}\gamma_e(t)}{\mathrm{d}t} \quad \Leftrightarrow \quad \omega(\tau) = \frac{\mathrm{d}\gamma(\tau)}{\mathrm{d}\tau} \cdot \frac{\gamma_B}{T_B \Omega_B} \ . \tag{2.6}$$

In (2.6) time, electrical-angle and -angular velocity were scaled using (2.3) and $t = \tau T_B, \Omega_e = \omega \Omega_B$. Furthermore τ and ω indicate scaled time and scaled *electrical* angular velocity with T_B and Ω_B as their base values respectively.

To conserve consistence between the scaled and unscaled equations of (2.6) the relation

$$\frac{\gamma_B}{T_B \Omega_B} \overset{!}{=} 1 \tag{2.7}$$

has to be satisfied. With (2.2) this leads to

$$\Omega_B = \frac{\gamma_B}{T_B} \ . \tag{2.8}$$

So either T_B or Ω_B can be chosen independently. Considering the time-discrete digital nature of the implemented control system it is prudent to choose T_B in relation to the occurring sample time(s). This will then lead to "convenient" numerical coefficients for time-discrete observer and controller structures as will be shown in Chapter 4. Chapter 3 introduces the SLOW and FAST

---

[9]see Chapter 3

tasks/routines with designated sample times $T_s = T_{fast} = 67\,\mu\text{s}$ and $T_{slow} = 6 \cdot T_{fast} = 402\,\mu\text{s}$. Therefore the base time value was chosen to be

$$T_B := 200\,\mu\text{s} \tag{2.9}$$

Substituting (2.9) into (2.8) gives

$$\Omega_B = \frac{1\,\text{rad}}{200\,\mu\text{s}} = 5000\,\text{rad/s} \tag{2.10}$$

$$f_B = \frac{\Omega_B}{2\pi} \approx 796\,\text{Hz} \ , \tag{2.11}$$

with f_B as the electrical base frequency. Due to (2.36) the base value for the *mechanical* angular velocity Ω_{B_m} is also defined when the pole pair number $p = 2$ is substituted

$$\Omega_{B_m} = \frac{\Omega_B}{p} = 2500\,\text{rad/s} \tag{2.12}$$

$$f_{B_m} = \frac{\Omega_{B_m}}{2\pi} \approx 398\,\text{Hz} \ . \tag{2.13}$$

The mechanical shaft base speed expressed in revolutions per minute is therefore about $23\,880\,\text{rpm}$.

The scaled angular velocity ω can originate from or be referenced to either the mechanical or electrical angular velocity as long as the proper base value is chosen. The current context of ω will always be clearly explained. At this point it is important to emphasize the difference between the terms *base values* and *rated values*. Former are oriented towards the specific *implementation* of a control system whereas latter are related to the *application* of said system. Considering mechanical shaft speeds $\Omega_m(t)$ the rated value Ω_{Rated_m} may be different[10] from the chosen base value Ω_{B_m}. Transformation, e.g. for a user interface is easily achieved with proper rescaling.

Once I_B, U_B and T_B are chosen the base values for flux-linkage, impedance, inductance, capacitance, torque, power and inertia can be derived. For flux-linkage Ψ Faraday's law[11] $U(\partial \mathscr{A}) = -\frac{\mathrm{d}\Psi(\mathscr{A})}{\mathrm{d}t}$ combined with the considerations of (2.6) yields the flux-linkage base value

$$\Psi_B = U_B \cdot T_B \ . \tag{2.14}$$

As mentioned above the base value of the flux linkage may differ from the rated value that usually originates from the machine design, see Section 2.4. In the same manner Ohm's law $U = R \cdot I$, the elementary equations[12] of an ideal lossless inductance $u_L(t) = L \cdot \frac{\mathrm{d}i_L(t)}{\mathrm{d}t}$ and capacitor $i_C(t) = C \cdot \frac{\mathrm{d}u_C(t)}{\mathrm{d}t}$ can be utilized to specify consistent base values for impedances $\underline{Z}$, inductances L and capacitors C

$$Z_B = \frac{U_B}{I_B} \tag{2.15}$$

$$L_B = \frac{U_B}{I_B} \cdot T_B \tag{2.16}$$

$$C_B = \frac{I_B}{U_B} \cdot T_B \tag{2.17}$$

---

[10] As *rated* value, the shaft speed that is indicating the start of the field weakening region could be chosen.
[11] see also [18],[19]
[12] see also [20]

The provided shaft torque $T_e(t)$ and a load torque $T_L(t)$ of an electrical drive is normalized with a base value of T_{eB} that is calculated using the basic relation for mechanical shaft power $P_m(t)$ in rotational dynamic systems $P_m(t) = \Omega_m(t) \cdot T_e(t)$, viz.

$$T_{eB} = \frac{P_B}{\Omega_{B_m}} = 3 \cdot p \cdot \frac{U_B}{\sqrt{2}} \frac{I_B}{\sqrt{2}} \cdot \frac{1}{\Omega_B} \ . \tag{2.18}$$

Again the base value of provided torque will probably differ $T_{eB} \neq T_{rated}$ from a rated value specified for a certain application, since the apparent power of a three phase load was used for the scaling of P_m,

$$P_B = 3 \cdot U_{Ph-Rated} \cdot I_{Ph-Rated} = 3 \cdot \frac{U_B}{\sqrt{2}} \frac{I_B}{\sqrt{2}} \ . \tag{2.19}$$

The remaining quantity that frequently occurs in the system equations of electrical drives is the inertia Θ. It is commonly expressed with an auxiliary variable called *mechanical time constant* T_M indicating the time needed for the motor to reach Ω_{B_m} from standstill when accelerated with T_{eB} under no-load condition. Newton's second law (conservation of momentum) yields

$$\Theta \cdot \frac{\mathrm{d}\Omega_m(t)}{\mathrm{d}t} = \sum T(t) \tag{2.20}$$

$$\Theta \cdot \frac{\Omega_{B_m} - 0}{T_M - 0} = T_{eB} \tag{2.21}$$

$$\Theta = \frac{T_{eB} \cdot T_M}{\Omega_{B_m}} \ . \tag{2.22}$$

Either T_M or Θ can be easily identified when shaft torque and speed is measured or estimated as will be shown in Section 4.6.

When working with scaled variables it is important to memorize the base values they were referenced to. Table 2.3 summarizes the chosen and derived base values used for the control system of the synchronous reluctance drive.

2.3 Space Vector Theory

Space vectors are the fundamental mathematical tool in this thesis to describe the transient- and steady-state-behavior of the proposed synchronous reluctance machine. Based on resources from TU Wien [21] and the famous works of Pál Károly Kovács and István Rácz [22, 23] the so called *space vector method* will be outlined here.

Space vectors (or spatial phasors) describe the effective spatial orientation and magnitude of airgap quantities present in electric machines such as flux, magneto motive-force (MMF) and electrical field strength. Using them greatly simplifies calculation and description of said quantities. As will become apparent, the general Maxwell-Equations, a system of PDEs[13] dependent in space $\mathbf{r} \in \mathbb{R}^3$ and time t, are reduced to an algebraic system of ODEs[14] only dependent in time t and two-dimensional coordinates.

---

[13]<u>P</u>artial <u>D</u>ifferential <u>E</u>quations
[14]<u>O</u>rdinary <u>D</u>ifferential <u>E</u>quations

Quantity	Symbol	Base Value
chosen		
Voltage	U_B	40 V
Current	I_B	18 A
Time	T_B	200 µs
Electrical Shaft Angle	γ_B	1 rad
derived		
Electrical angular Shaft velocity	Ω_B	5000 rad/s
Mechanical angular Shaft velocity	Ω_{B_m}	2500 rad/s
Electrical Shaft frequency	f_B	796 Hz
Mechanical Shaft frequency	f_{B_m}	398 Hz
Impedance	Z_B	2.22 Ω
Inductance	L_B	444 µH
Capacitance	C_B	90 µF
Shaft Torque	T_{eB}	0.432 N m
Power	P_B	1.08 k W

Table 2.3: Summary of used base values

Before space vectors can be defined and used several idealized assumptions are necessary. Not all of these can be met by a full degree when dealing with actual built electric machines. However the differences between abstract models and real apparatus will be specified and shown to be negligible for the SynRM in this work.

Concerning the spatial aspects of quantities a circular-cylindrical coordinate system $\{r, \varepsilon, z\}$ with corresponding orthonormal base vectors $\{\mathbf{e}_r, \mathbf{e}_\varepsilon, \mathbf{e}_z\}$ is introduced in Figure 2.3. Referring to Figure 2.3 further assumptions are:

  I Field quantities are invariant of the translational coordinate z. A two dimensional plane cross sectioning the rotor & stator into two translational equally long parts with $z = 0$ is considered.

  II Concerning mechanical quantities δ denotes the airgap width, r_S is the stator bore radius and r_R, l_R characterize the maximum rotor radius and length of the rotor respectively. Those quantities are related via $r_R + \delta = r_S$ and $\delta \ll \{r_S, r_R, l_R\}$

  III The permeability within air gap is approximately $\mu_{airgap} \approx \mu_0$. The stator and rotor are comprised of magnetic material ("iron") with a permeability of $\mu_{iron} = \mu_0 \cdot \mu_{r_{iron}}$ with $\mu_{r_{iron}} \gg 1$. Thus, the relation $\mu_{airgap} \ll \mu_{iron}$ holds at the interfaces stator/airgap and airgap/rotor. According to the theory of electromagnetic fields [18, 20] the field lines inside the airgap will therefore be perpendicular to the stator and rotor surfaces if said interfaces are free of surface currents. For the magnetic field strength within the airgap $\mathfrak{g}$ this yields $\mathbf{H}\left(\mathbf{r}, t\right) = \left(H_r, H_\varepsilon, H_z\right)^{\mathrm{T}} \approx \left(H_r\left(\mathbf{r}, t\right), 0, 0\right)^{\mathrm{T}}$ with $\mathbf{r} \in \mathfrak{g} := \{\mathbf{r} \mid r \in \left(r_R, r_R + \delta\right), \ z = 0, \ \varepsilon \in [0 \ldots 2\pi)\}$.
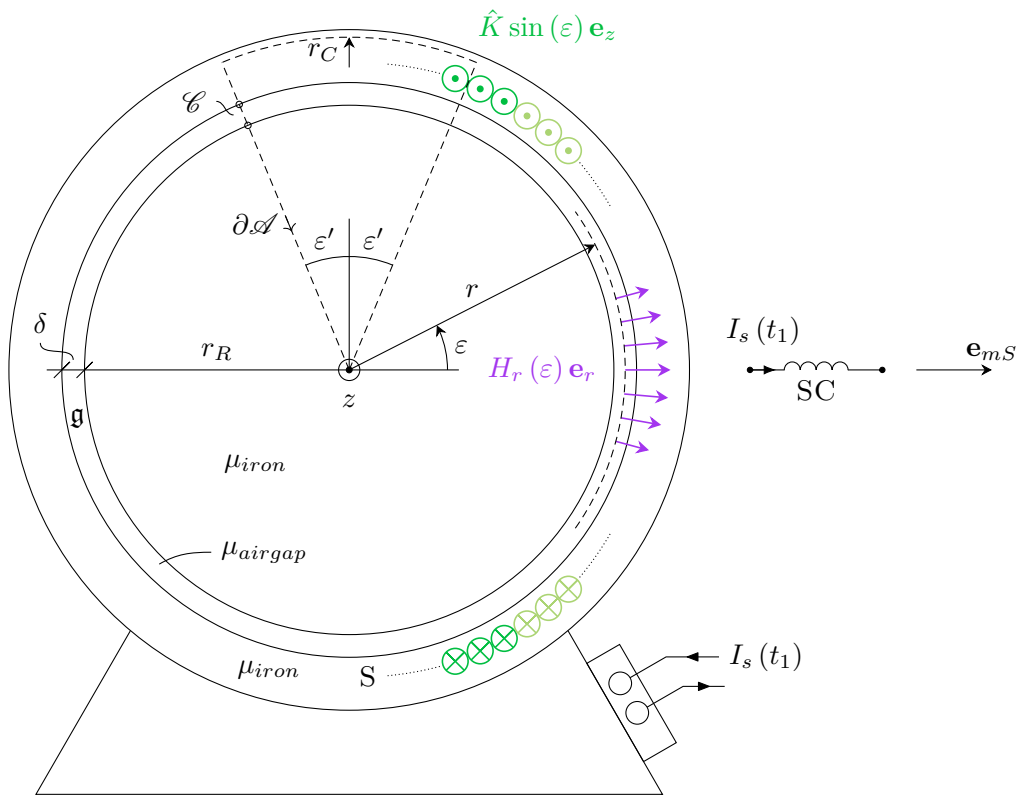
Figure 2.3: Regarding space vectors

IV The incorporated (magnetic) materials are linear. This implies that the values of permeabilities are constant.

V Due to I,II,III it is valid to assume that the vast majority of the magnetic potential[15] $V(\mathscr{C})$ linked to an oriented curve $\mathscr{C}$ is present within the airgap. Other potentials occurring alongside various curves completely inside stator/rotor material are negligible. This is often referred to as *"absence of magnetic losses"*. The magnetic field strength being the local representative of the potential can be sufficiently analysed when considering only $H_r(\mathbf{r}, t)$ $\mathbf{r} \in \mathfrak{g}$ and $r = const.$ instead of $\mathbf{H}(\mathbf{r}, t)$. Without the loss of generality a specific instant in time t_1 will be specified and $H_r(\mathbf{r}, t_1)$ will be written as $H_r(\varepsilon)$. Its global counterpart $V(\varepsilon)$ is given by

$$V(\varepsilon) = \int_{\mathscr{C}_\varepsilon} \mathbf{H} \cdot \mathrm{d}\mathbf{s} \ . \tag{2.23}$$

with $\mathrm{d}\mathbf{s}$ being an infinitesimal element of the oriented curve $\mathscr{C}_\varepsilon$ that penetrates the airgap at an angle of ε.

VI With assumptions I-V the *fundamental requirement of space vector theory* can be specified. The resultant field strength component of the air gap shall have a spatially sinusoidal characteristic, viz.

$$H_r(\varepsilon) \stackrel{!}{=} \hat{H}_r \cos(\varepsilon) = \Re\{\hat{H}_r\, \mathrm{e}^{\mathrm{j}\varepsilon}\} \ , \tag{2.24}$$

VII Combining IV and VI from above the flux density of the airgap $B_r(\varepsilon) = \mu_{airgap} \cdot H_r(\varepsilon)$ will then also be sinusoidal. Figure 2.3 shows the necessary means to fulfill Equation (2.24) namely a spatially sinusoidal surface current density inside the stator

$$\mathbf{K}(\varepsilon) \stackrel{!}{=} \hat{K} \sin(\varepsilon)\, \mathbf{e}_z \ . \tag{2.25}$$

This property of the surface current is also called *sinusoidal distribution of windings* which poses another condition for the duly use of space vectors.

The distributed-winding solenoid S of Figure 2.3 is fed by an instantaneous current of $I_s(t_1)$ and its armature yield a pole number of $2p_s = 2$. The realization of solenoids through different winding techniques that fulfill Equation (2.25) and Equation (2.24) respectively is outside the scope of this thesis and a mayor topic in the field of designing electric machines. A valued contribution to this topic was authored by the Austrian scientist Heinrich Sequenz, [24]. A more recent resource is [25]. The specific design of the distributed stator coil for the SynRM of this thesis was conducted in [1].

VIII Evaluating Ampères law

$$V(\partial \mathscr{A}) = I(\mathscr{A}) \tag{2.26}$$

on the left- and right handed side using suggested "piece-of-cake" shaped integral path of Figure 2.3 the resulting magnetic potential can be derived as

$$V_s(\varepsilon) = \hat{K} r_c \cos(\varepsilon) \ , \tag{2.27}$$

---

[15]Throughout this thesis a dominant magnetic field configuration is assumed, [18]. Oriented curves $\mathscr{C}$ can be assigned with values of a magnetic potential $V(\mathscr{C})$, oriented closed curves $\partial \mathscr{A}$ as boundaries of consistent oriented surfaces $\mathscr{A}$ can also be assigned with values of magnetic potential that is equal to the enclosed magneto-motive force using Ampères law $V(\partial \mathscr{A}) = I(\mathscr{A})$. Displacement currents are neglected.

fulfilling Equation (2.24), with r_c as the core radius depicted in Figure 2.3. This function is commonly known as field excitation curve of the airgap. Its maximum is located $\varepsilon = 0$ and designated with a distinct direction $\mathbf{e}_{mS}$ called the magnetic axis of the distributed solenoid S, plotted on the right border of Figure 2.3. The spatial period λ_V of the field excitation curve is introduced as

$$V_s\left(\varepsilon + \lambda_{V_s}\right) = V_s\left(\varepsilon\right) \tag{2.28}$$

with a value of

$$\lambda_{V_s} = \frac{360\,^\circ{}_{\text{mech}}}{p_s} = 360\,^\circ{}_{\text{mech}} \tag{2.29}$$

in the case of one pole pair p_s. Attention should be paid to the fact that the spatial phase difference between the maxima of excitation current Equation (2.25) and field excitation curve Equation (2.27) is $90\,^\circ{}_{\text{mech}}$.

Besides a symbolic concentrated solenoid SC is printed in space whose well defined MMF $\boldsymbol{\Theta} = N_{sc}I_s\left(t_1\right)\mathbf{e}_\Theta$ is collinear with $\mathbf{e}_{mS}$ if it is fed with the same current $I_s\left(t_1\right)$ as the distributed coil S.

Taking I-VIII into account the current space vector for a single phase distributed coil such as S of Figure 2.3 can be readily defined as

$$\mathbf{I}_s\left(t_1\right) = I_s\left(t_1\right)\mathbf{e}_{mS} \ . \tag{2.30}$$

Current space vectors are therefore linked with the physical quantity of magnetic potential $V\left(\varepsilon\right)$ and its local representative $H_r\left(\varepsilon\right)$. They are assigned with the spatial direction of the magnetic axis for a given winding configuration when its armature is excited with an electric current at time instant t_1. Regarding terminology space vectors are no classical physical vector quantities like forces $\mathbf{F}$ or impulses $\mathbf{p}$ but obey the laws of vector-algebra and are hence called vectors for simplicity.

    The above considerations are now generalized to derive a model for the deployed SynRM being a poly phase, multi pole AC machine in contrast to the previous single phase two-pole example. Figure 2.4 shows a scheme of the machine design [1] in context with the previous considerations. A new symbol for the mechanical azimuthal angle in a reference frame perpendicular to the shaft axis, γ_m is introduced. The stator comprises of a single layer i̲ntegral s̲lot d̲istributed w̲inding (ISDW) system filled into $Q = 24$ slots, constituting $m = 3$ phases and $2p = 4$ poles yielding an integral value of slots-per-phase-per-pole $q_M = \frac{Q}{2pm} = 2$. Each pair of slots is assigned conductors of a specific armature having reference directions pointing outwards $\odot$ or inwards $\otimes$ from the depicted cross section. Each of the terminals UVW consists of two parallel connected armature coils, e. g. U1U1' $\parallel$ U2U2'. Those pairs of coils are connected in a star configuration[16]. The field excitation curve of the given winding system can be found, when specifying two terminal currents at the time instant t and applying Kirchhoff's current law

$$I_\text{U}\left(t\right) + I_\text{V}\left(t\right) + I_\text{W}\left(t\right) = 0 \ , \tag{2.31}$$

for the remaining terminal current in combination with Ampères law Equation (2.26) and assumptions I-V for an integral path $\partial\mathscr{A}$ circulating the winding system. It is prudent to

---

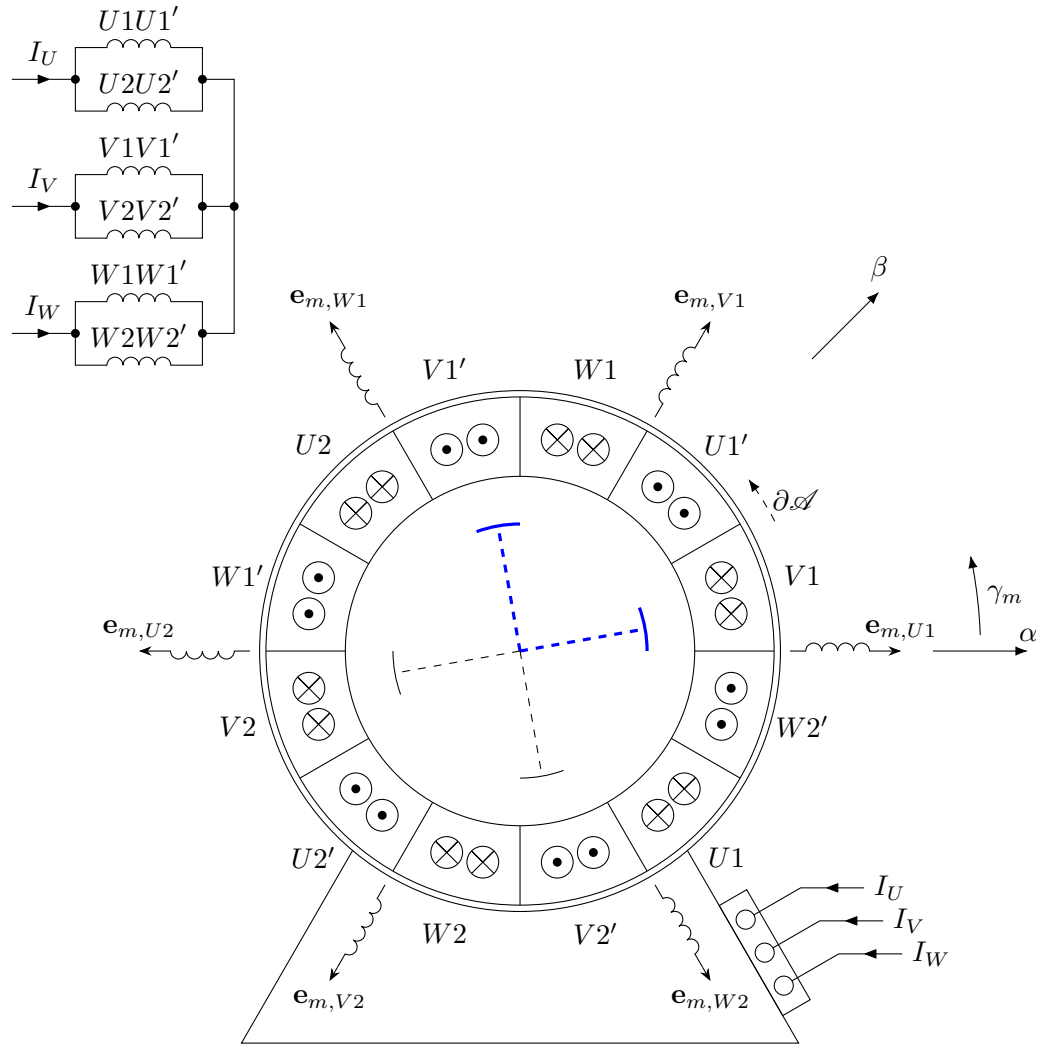[16]Therefore, the terminal current is equal to the phase current.

Figure 2.4: Magnetizing scheme and wiring of the deployed SynRM comprising of three phases and four poles; Introduction of a stator-fixed $(\alpha\beta)$ reference frame; One revolution corresponds to $360\,°_{\text{mech}}$.

undertake said calculation for each phase at a time and take advantage of the superposition principle since this is always valid when dealing with magneto-motive forces, [18, 19, 21, 26].

Due to the discrete number of stator slots VII is not realizable and thus the field excitation curve of each phase in turn will be shaped trapezoidal violating VI & VIII. However, when each of the curves are superimposed the resulting field excitation curve can be stated by means of a Fourier series representation

$$V\left(\gamma_m, t\right) = V_0 + \sum_{k=1}^{\infty} \hat{V}_k \cos\left(2\gamma_{k\,m} - \gamma_{k\,m_0}\left(t\right)\right) \ , \tag{2.32}$$

at a specific instant in time t. By Equation (2.32) a wave of the magnetic potential propagating around the motor airgap's circumference is formulated. For the zero sequence component $V_0 = 0$ is assumed. The SynRM featured here was designed to have a largely dominant fundamental component ($k = 1$) and negligible harmonic components ($k > 1$). Relating to Equation (2.32) this allows for the simplification

$$V\left(\gamma_m, t\right) \approx \hat{V}_1 \cos\left(2\gamma_m - \gamma_{m_{1,0}}\left(t\right)\right) \ . \tag{2.33}$$

The exact trend of Equation (2.32) can be calculated by means of a finite element analysis tool such as MAXWELL from the company ANSYS. Effects of the non-sinusoidal distribution of electromagnetic field quantities[17] for the specific SynRM of this thesis were reported in [1].

For the following definition of space vectors only the fundamental wave component Equation (2.33) will be used. When inspecting Equation (2.32) and Equation (2.33) it becomes apparent that the spatial period of the fundamental field excitation curve is defined by the stator winding distribution of Figure 2.4 and has a value of

$$\lambda_V = \frac{360\,°_{\mathrm{mech}}}{p} = 180\,°_{\mathrm{mech}} \ , \tag{2.34}$$

and that no new information can be gained when observing field quantities after this period for a given current excitation[18]. It is common to define the electrical angle γ_e as a quantity which covers stated spatial period on a new scale measured in $[°_{\mathrm{elec}}]$ and treat the motor in terms of this new quantity. The electrical angle and angular velocity $\Omega_e\left(t\right)$ as the time derivative are related to the mechanical angle γ_m and angular velocity Ω_m through

$$\gamma_e\left(t\right) = p \cdot \gamma_m\left(t\right) \ , \tag{2.35}$$

$$\Omega_e\left(t\right) = \frac{\mathrm{d}\gamma_e\left(t\right)}{\mathrm{d}t} = p \cdot \frac{\mathrm{d}\gamma_m\left(t\right)}{\mathrm{d}t} = p \cdot \Omega_m\left(t\right) \tag{2.36}$$

Every single armature coil in Figure 2.4 has a designated magnetic axis with a well defined direction in space, e. g. W1W1' $\rightarrow \mathbf{e}_{mW1}$. Referring to VIII these directions are now spatially displaced by $45\,°_{\mathrm{mech}} \stackrel{\wedge}{=} 90\,°_{\mathrm{elec}}$ from their respective excitation armatures. A symbolic concentrated coil is depicted in each direction referring to the previous example. Based on the above explanations it is valid to confine the portrayed scheme of Figure 2.4 to an "equivalent electric machine" covering

---

[17]such as harmonics in induced voltages under sinusoidal current excitation and cogging torque
[18]if the actual realization of the stator winding system is symmetrical after this period

Figure 2.5: Equivalent abstracted SynRM comprising two poles; Three-phase current space vector definition; Introduction of a rotor-fixed (*dq*) reference frame; One revolution corresponds to $360\,^\circ_{\text{elec}} \mathrel{\widehat{=}} 180\,^\circ_{\text{mech}}$.

$360\,^\circ_{\text{elec}}$. This is achieved by the introduction of a reference frame $\alpha\beta$ which is defined to be fixed to the stator, whose axes are $90\,^\circ_{\text{elec}}$ apart and whose α axis coincides with $\mathbf{e}_{mU1}$. Afterwards the machine is reprinted in terms of a full electric period and shown in Figure 2.5. The magnetic axes of corresponding armature coils from Figure 2.4 now possess the same direction on the electrical scale: e.g., $\mathbf{e}_{mV1}, \mathbf{e}_{mV2} \rightarrow \mathbf{e}_{mV1,2}$. A distinction between electrical vs. mechanical scales as well as the terms vectors vs. space vectors is achieved by adopting the method of complex numbers for the $\alpha\beta$ reference frame, designating real axis to α the imaginary axis to β. The three spatial directions of the armature's magnetic axes can then be described with the help of complex numbers yielding

$$\mathbf{e}_{mU1,2} \quad \mapsto \quad \mathrm{e}^{\mathrm{j}0} \tag{2.37}$$

$$\mathbf{e}_{mV1,2} \quad \mapsto \quad \mathrm{e}^{\mathrm{j}\frac{2\pi}{3}} \tag{2.38}$$

$$\mathbf{e}_{mW1,2} \quad \mapsto \quad \mathrm{e}^{\mathrm{j}\frac{4\pi}{3}} \tag{2.39}$$

A space vector for each of the three phases can now be defined being collinear with the respective magnetic axis as it was done in Equation (2.30) for a single phase system. As clarified before the operation of superimposing those three vectors is valid as they represent magnetic potentials viz. MMFs. This finally leads to the definition of the stator current space vector used to describe the

three phase machine in this thesis

$$\underline{I}^{\alpha\beta}(t) = \frac{2}{3}\left(I_{\mathrm{U}}(t) + I_{\mathrm{V}}(t)\,\mathrm{e}^{\mathrm{j}\frac{2\pi}{3}} + I_{\mathrm{W}}(t)\,\mathrm{e}^{\mathrm{j}\frac{4\pi}{3}}\right) \tag{2.40}$$

Equation (2.40) is also known as amplitude invariant, simplified[19] *Clarke transformation*, [27]. Thereby balanced quantities viz. absence of zero sequence components is assumed and in the case of the SynRM's currents fulfilled by Equation (2.31). The leading factor $\frac{2}{3}$ ensures that amplitude values of three-phase quantities are preserved in their $(\alpha\beta)$ representation. This is not true for the reactive power values[20]. As mentioned above the stator current space vector is physically related to the airgap's radial field strength component.
The chosen implementation of Equation (2.40) in scaled variables is given by

$$i_{\alpha}(t) = \Re\{\underline{i}^{\alpha\beta}(t)\} = \frac{2}{3}\left(i_{\mathrm{U}}(t) - \frac{1}{2}\left(i_{\mathrm{V}}(t) + i_{\mathrm{W}}(t)\right)\right)\ , \tag{2.41}$$

$$i_{\beta}(t) = \Im\{\underline{i}^{\alpha\beta}(t)\} = \frac{1}{\sqrt{3}}\left(i_{\mathrm{V}}(t) - i_{\mathrm{W}}(t)\right)\ . \tag{2.42}$$

For the specific measurement and scaling of the motor's phase currents see Section 2.5 and Section 2.2.
Below Equation (2.40) is rewritten for a general three phase space vector variable $\underline{\zeta}$ that constitutes from its phase quantities $\zeta_k \quad k \in \{1,2,3\}$ denoting U,V,W:

$$\underline{\zeta}^{\alpha\beta}(t) = \frac{2}{3}\sum_{k=1}^{3}\zeta_k(t)\ \mathrm{e}^{\mathrm{j}\frac{2\pi}{3}(k-1)}\ . \tag{2.43}$$

The given space vector definition of Equation (2.43) can be formally utilized to define a stator voltage space vector

$$\underline{U}^{\alpha\beta}(t) = \frac{2}{3}\left(U_{\mathrm{U}}(t) + U_{\mathrm{V}}(t)\,\mathrm{e}^{\mathrm{j}\frac{2\pi}{3}} + U_{\mathrm{W}}(t)\,\mathrm{e}^{\mathrm{j}\frac{4\pi}{3}}\right)\ , \tag{2.44}$$

with $U_{\mathrm{U}}(t), U_{\mathrm{V}}(t)$ and $U_{\mathrm{W}}(t)$ as the instantaneous phase-to-neutral voltages of the stator coils of the terminals UVW.
A stator flux linkage space vector can also be defined as

$$\underline{\Psi}^{\alpha\beta}(t) = \frac{2}{3}\left(\Psi_{\mathrm{U}}(t) + \Psi_{\mathrm{V}}(t)\,\mathrm{e}^{\mathrm{j}\frac{2\pi}{3}} + \Psi_{\mathrm{W}}(t)\,\mathrm{e}^{\mathrm{j}\frac{4\pi}{3}}\right)\ , \tag{2.45}$$

where $\Psi_{\mathrm{U}}(t), \Psi_{\mathrm{V}}(t)$ and $\Psi_{\mathrm{W}}(t)$ denote the instantaneous flux linkages allocated to the aforementioned stator coils. According to [21] the stator voltage space vector Equation (2.44) is physically linked to the translational component (z) of the electrical field strength while the stator flux linkage space vector Equation (2.45) relates to the radial magnetic flux density. All three space vectors can be seen as snapshots of their respective sinusoidal airgap quantities. As complex numbers they can either be represented by Cartesian coordinates e.g. Equation (2.41) or by polar coordinates consisting a magnitude and electrical polar angle. Their angles and absolute values

---

[19]The generalization to unbalanced quantities is called $(\alpha\beta\gamma)$ Clarke Transformation.

[20]Another definition of Equation (2.40) uses $\sqrt{\frac{2}{3}}$ as leading factor preserving reactive powers rather than amplitudes and is therefore called power invariant Clarke transformation, [16].

define the maxima's location and magnitude of said airgap quantities around the circumference at a specific time instant t.

The *inverse Clarke transformation* as counterpart to Equation (2.43) is given by

$$\zeta_1(t) = \Re\{\underline{\zeta}^{\alpha\beta}(t)\} \tag{2.46}$$

$$\zeta_2(t) = \Re\{\underline{\zeta}^{\alpha\beta}(t)\,\mathrm{e}^{-\mathrm{j}\frac{2\pi}{3}}\}\ , \tag{2.47}$$

$$\zeta_3(t) = \Re\{\underline{\zeta}^{\alpha\beta}(t)\,\mathrm{e}^{-\mathrm{j}\frac{4\pi}{3}}\}\ , \tag{2.48}$$

$$\tag{2.49}$$

and formulates the projection of a given space vector $\underline{\zeta}$ to its three constituting phase defined in Equation (2.43).

The distributed stator coil of each phase can be modeled as Resistor-Inductor series connection expressed by

$$U_{\mathrm{U}}(t) = R_s\,I_{\mathrm{U}}(t) + \frac{\mathrm{d}\Psi_{\mathrm{U}}(t)}{\mathrm{d}t}\ , \tag{2.50}$$

$$U_{\mathrm{V}}(t) = R_s\,I_{\mathrm{V}}(t) + \frac{\mathrm{d}\Psi_{\mathrm{V}}(t)}{\mathrm{d}t}\ , \tag{2.51}$$

$$U_{\mathrm{W}}(t) = R_s\,I_{\mathrm{W}}(t) + \frac{\mathrm{d}\Psi_{\mathrm{W}}(t)}{\mathrm{d}t} \tag{2.52}$$

where an equal stator resistance R_s for each phase is assumed. When multiplying Equation (2.50) by $\frac{2}{3}$, Equation (2.51) by $\frac{2}{3}\mathrm{e}^{\mathrm{j}\frac{2\pi}{3}}$, Equation (2.52) by $\frac{2}{3}\mathrm{e}^{\mathrm{j}\frac{4\pi}{3}}$ and adding both left- and right-hand sides under consideration of the above stated space vector definitions the important stator voltage space vector equation can be derived as

$$\underline{U}^{\alpha\beta}(t) = R_s\underline{I}^{\alpha\beta}(t) + \frac{\mathrm{d}\underline{\Psi}^{\alpha\beta}(t)}{\mathrm{d}t}\ . \tag{2.53}$$

This equation relates terminal quantities to space vectors which in term are characterising field quantities within the airgap.

In modern *Field-Oriented Control* (FOC) of electrical drives the above defined space vector quantities are translated to a rotating reference frame in contrast to the previous introduced stator fixed ($\alpha\beta$) reference frame. In case of synchronous machines a reference frame fixed to the rotor (designated as *dq*) is utilized and depicted in Figure 2.5. During regular operation this frame rotates with the same electrical frequency as the applied three phase system at the terminals hence the name synchronous machines. The d̲irect axis is commonly assigned to the salient pole which is also the flux path the least reluctance viz. highest inductance. The q̲uadrature axis is $90\,°_{\mathrm{elec}}$ apart and characterized by highest reluctance for the flux viz. least inductance. The name "field-oriented" control relates towards the idea of transforming necessary control quantities to the (*dq*) frame since field variables in terms of space vectors appear as constants[21] in that frame for a motor spinning with constant shaft speed[22]. It is expedient to use (*dq*) coordinates of space vectors for control. Even if the shaft speed is variable the signals of (*dq*) space vector quantities

---

[21]under ideal circumstances, cf. I-VIII

[22]This is commonly named the "quasi-stationary operation" case.

are still much more efficient to tackle for the control system compared to signals related to the $(\alpha\beta)$ frame being sinusoidal functions of time in the quasi-stationary case.

Transformation rules between the two reference frames $(\alpha\beta) \leftrightarrow (dq)$ are derived with the help of Figure 2.5. The depicted stator current space vector $\underline{I}$ is interpreted as an arbitrary space vector quantity $\underline{\zeta}$ and expressed in both reference frames yielding

$$\underline{\zeta}^{dq}(t) = \left|\underline{\zeta}\right| e^{j\gamma_{dq}(t)} = \left|\underline{\zeta}\right| e^{j(\gamma_{\alpha\beta}(t) - \gamma_d(t))} = \underbrace{\left|\underline{\zeta}\right| e^{j\gamma_{\alpha\beta}(t)}}_{\underline{\zeta}^{\alpha\beta}(t)} e^{-j\gamma_d(t)} \ , \tag{2.54}$$

$$\underline{\zeta}^{dq}(t) = \underline{\zeta}^{\alpha\beta}(t) e^{-j\gamma_d(t)} \tag{2.55}$$

what is commonly known as amplitude invariant *Park Transformation*, [28]. The reverse operation

$$\underline{\zeta}^{\alpha\beta}(t) = \underline{\zeta}^{dq}(t) e^{j\gamma_d(t)} \ . \tag{2.56}$$

translates (dq) quantities back to the stator fixed $(\alpha\beta)$ reference frame. The Park Transformation is sometimes combined with the Clarke Transformation Equation (2.43). Generalizations and variations to unbalanced[23] three phase systems and power invariance are available, the same remarks as above apply.

When inspecting Equation (2.54) and Equation (2.56) it becomes clear that the position information of the rotor's direct axis $\gamma_d(t)$ measured in the $\alpha\beta$ reference frame is of fundamental importance to realize FOC systems. One way to obtain this information is through a separate sensor device such as described in Section 2.6. The resulting sensor-based FOC system is the topic of Chapter 4 and forms the basis for a sensorless FOC system which allows the omission of a dedicated sensor device and derives an estimation of $\gamma_d(t) \to \hat{\gamma}_d(t)$ based on stator voltages, currents and mathematical models. Methods and system structure of the sensorless FOC system are covered in Chapter 5.

As the FOC system operates within a (dq) reference frame it is necessary to transform the stator voltage equation Equation (2.53) to (dq) coordinates. In a first step Equation (2.56) is used and the product rule is applied:

$$\underline{U}^{dq}(t) e^{j\gamma_d(t)} = R_s \underline{I}^{dq}(t) e^{j\gamma_d(t)} + \frac{d}{dt}\left(\underline{\Psi}^{dq}(t) e^{j\gamma_d(t)}\right) \ , \tag{2.57}$$

$$\underline{U}^{dq}(t) e^{j\gamma_d(t)} = R_s \underline{I}^{dq}(t) e^{j\gamma_d(t)} + e^{j\gamma_d(t)}\frac{d}{dt}\underline{\Psi}^{dq}(t) + \underline{\Psi}^{dq}(t)\frac{d}{dt} e^{j\gamma_d(t)} \ . \tag{2.58}$$

$$\tag{2.59}$$

Subsequently the chain rule is applied for the last term and the common factor $e^{j\gamma_d(t)}$ is crossed out yielding

$$\underline{U}^{dq}(t) = R_s \underline{I}^{dq}(t) + \frac{d\underline{\Psi}^{dq}(t)}{dt} + j\Omega_d(t) \underline{\Psi}^{dq}(t) \ , \tag{2.60}$$

with $\Omega_d(t) = \frac{d\gamma_d(t)}{dt}$ as the electrical rotor velocity.

Space vectors allow for an elegant lightweight description of the instantaneous torque $T_e(t)$ present at the shaft provided by the electrical drive depending on its terminal quantities. A

---

[23]The common designation is then "dq0 Transformation".

derivation based on electromechanical energy conversion can be found in [29] & [23] and results in the coordinate invariant equation

$$T_e\left(t\right) = -\frac{3}{2}p\,\Im\{\underline{I}^*\left(t\right)\underline{\Psi}\left(t\right)\}\ .\tag{2.61}$$

It is important to note that in actual electric drives a phenomenon known as cogging torque[24] will always appear due to a discrete stator geometry with a finite number of slots in combination with a specific stator & rotor design and certain non-ideal magnetic materials [30]. Using space vectors as defined above this effect cannot be modeled. It is an important task for the machine designer to minimize cogging torque because it appears as disturbance signal when the motor is operated with the use of space vectors. Integration of the so called Maxwell Stress Vector [18] covers these effects and yields the resulting torque acting on a body within the hull $\partial\mathscr{V}_1$ and respect to the origin $\mathscr{O}$

$$\mathbf{T}^e_{R\mathscr{O}} = \int_{\partial\mathscr{V}_1}\frac{1}{\mu_0}\mathbf{r}_{\mathscr{O}} \times \left(\mathbf{n}\cdot\mathbf{B}\mathbf{B} - \frac{1}{2}B^2\mathbf{n}\right)\mathrm{d}A\ .\tag{2.62}$$

In Equation (2.62) $\mathbf{r}_{\mathscr{O}}$ denotes the position vector with respect to the origin $\mathscr{O}$. Furthermore $\mathbf{B}$ is the magnetic flux density with an absolute value of B. Finite-element software tools allow the evaluation of Equation (2.62) and help to obtain a proper machine geometry design with negligent cogging torque. In Section 2.4 it will be shown that skewing the rotor also reduces the cogging torque significantly. The above remarks on torque show that space vectors in general are a convenient tool to describe dominant effects and to efficiently control electrical drives that fulfill the criteria presented in I-VIII sufficiently[25]. Instead of dealing with field quantities the knowledge of terminal currents and voltages gives information to control the motor at a high performance level. The price one has to pay is the need of an adequate machine design or, lacking thereof, deal with a decreased performance. It is not uncommon that the condition III will be violated during operation due to saturation of the magnetic material. In such a case the usage of local approximations of the inductances is valid.

To conclude the discussion alternative ways to derive a mathematical model are mentioned: Reluctance Networks [31],[32] allow for a detailed description of the occurring physical effects but require great effort in terms of modeling, calibration of the model and computation power when building control systems using such models. It is also possible to incorporate spatial harmonics into the definition of space vectors, [33].

However very vast majority of poly phase AC electrical drives, such as the deployed SynRM, are built for (fundamental wave) space vector control.

2.4 Synchronous Reluctance Machines

The following section classifies Synchronous Reluctance Machines (SynRM) and derives a model of the deployed machine that is later used for control.

---

[24]also called "torque ripple"
[25]More stringent but less intuitive conditions are II:$\delta \to 0$ and III:$\mu_{r_{iron}} \to \infty$

used design

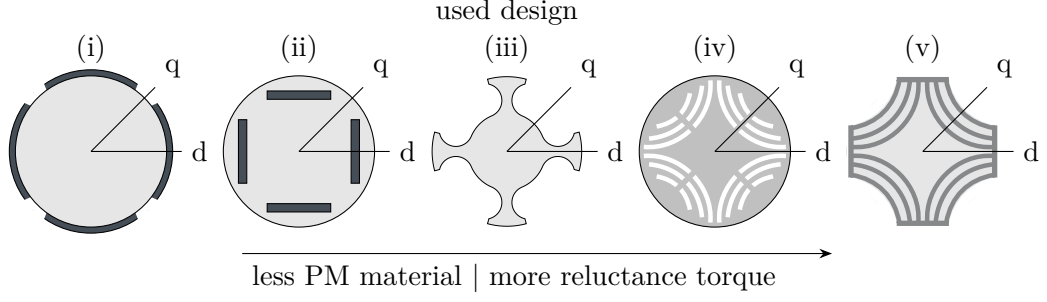less PM material | more reluctance torque

Figure 2.6: Classification and schematic cross sections of four-pole Surface Mounted Permanent Magnet- (SMPM) (i), Interior Permanent Magnet- (IPM) (ii) and SynRM- rotor types. (iii) salient pole design from [1]: topic of this thesis; (iv) transversally laminated rotor with flux barriers, cf. [8]; (v) axially laminated rotor, cf. [34]. Magnetic soft material.

2.4.1 Principle of Operation

Synchronous Reluctance Machines (SynRM) are characterized by the fact that their torque output can be reasoned by reluctance forces rather than Lorentz forces. To illustrate their principle of operation the fundamental equation regarding torque of an *electromechanical energy converter* first formulated by Joseph-Louis Lagrange shall be considered [29],[32],[16]:

$$T_e^{EM}(i, \gamma_e) = \left[\frac{\partial \mathscr{W}_m^*(i, \gamma_e)}{\partial \gamma_e} \right]_{i=const.} . \tag{2.63}$$

That is to say, the torque exhibited on a general electromechanical system with the degree of freedom γ_e (as defined above) constitutes from the magnetic co-energy's rate of change regarding said degree of freedom at constant armature current i with

$$\mathscr{W}_m^*(i, \gamma_e) = \left[\int_0^i \psi(i, \gamma_e) \, \mathrm{d}i \right]_{\gamma_e=const.} , \tag{2.64}$$

for the magnetic co-energy content due to this magnetizing current i and flux linkage ψ. Stated equations Equation (2.63), Equation (2.64) are valid for any type of electrical machine. For SynRM in particular the "change of magnetic co-energy regarding the electrical angle γ_e" is based upon magnetic saliency over the rotor's circumference. Thereto, the machine's rotor is made of magnetic material and (in the simplest case) poses two prominent flux paths such as the used salient pole configuration (iii) of Figure 2.6. Other prominent representations of SynRM and PM motor designs with their (dq) axes definitions are shown in Figure 2.6 that will be covered later. Magnetizing the machine's stator armature then corresponds to Equation (2.64) while a variation of reluctance due to the rotors geometrical design relates to Equation (2.63) and eventually exerts torque. A detailed coverage of the above material can be found in [29] and [16].

2.4.2 Mathematical Model and Classification

Theoretical groundwork concerning modeling of SynRM was laid early by a paper of Doherty and Nickle [35] based upon the two reaction theory formulated by Blondel [36] and Park [28].

The consideration of a (dq) rotor fixed coordinate frame and unification into space vector theory of Section 2.3 is therefore valid.

In a generalized model of magnetically salient machines the flux linkage as space vector relating to the (dq) frame is formulated as

$$\underline{\Psi}^{dq} = \Psi_d \left(I_d, I_q \right) + \mathrm{j}\Psi_q \left(I_d, I_q \right) \ , \tag{2.65}$$

whose components are given each by a non-linear function of the current space vector (so called flux linkage maps / surface plots). Together with Equation (2.57) this information would be sufficient to formulate a flux-based model of the machine. Such a model then needs to be calibrated to the deployed SynRM. Electric currents are easier to measure and control than magnetic fluxes, which can only be indirectly controlled using currents. Furthermore they can be directly measured at the inverter. For this reason a general current-based model will be proposed and will subsequently be simplified on grounds of the finite element simulation results in Section 2.4.5. Based upon this proposed, simplified model the control system will be designed and optimized in Chapter 4 and Chapter 5. To accommodate this approach direct- and quadrature-axis apparent inductances[26] are introduced as

$$L_d \left(I_d, I_q \right) = \frac{\Psi_d \left(I_d, I_q \right)}{I_d} \tag{2.66}$$

$$L_q \left(I_d, I_q \right) = \frac{\Psi_q \left(I_d, I_q \right)}{I_q} \tag{2.67}$$

where cross coupling can be formally integrated into one inductance parameter. Reciprocity is assumed. In the general formulation apparent inductances need to be distinguished from the incremental inductances given by

$$L_d^\Delta \left(I_d', I_q' \right) = \left[\frac{\partial \Psi_d \left(I_d, I_q \right)}{\partial I_d} \right]_{I_d', I_q'} \ , \quad L_{dq}^\Delta \left(I_d', I_q' \right) = \left[\frac{\partial \Psi_d \left(I_d, I_q \right)}{\partial I_q} \right]_{I_d', I_q'} \tag{2.68}$$

$$L_q^\Delta \left(I_d', I_q' \right) = \left[\frac{\partial \Psi_q \left(I_d, I_q \right)}{\partial I_q} \right]_{I_d', I_q'} \ , \quad L_{qd}^\Delta \left(I_d', I_q' \right) = \left[\frac{\partial \Psi_q \left(I_d, I_q \right)}{\partial I_d} \right]_{I_d', I_q'} \ . \tag{2.69}$$

Using Equation (2.65)-Equation (2.67) the torque equation Equation (2.61) for SynRM resembles as (dependencies omitted):

$$T_e = \frac{3}{2} p \left(L_d - L_q \right) I_d I_q \ . \tag{2.70}$$

When rewriting the stator current space vector in polar coordinates using $I = \left| \underline{I}^{dq} \right|$ and θ as the polar angle measured from the positive d-axis, also called MMF-angle,

$$\underline{I}^{dq} = I \mathrm{e}^{\mathrm{j}\theta} = I_d + \mathrm{j}I_q \ , \tag{2.71}$$

Equation (2.70) results in

$$T_e = \frac{3}{4} p \left(L_d - L_q \right) I^2 \sin \left(2\theta \right) \ . \tag{2.72}$$

---

[26]sometimes referred to as "secant inductances"

Evidently this machine type exerts torque due to its inductance variation between d and q axes. The most important figure of merit for SynRM is therefore the magnetic saliency ratio which is defined as

$$\xi := \frac{L_d}{L_q} \, , \tag{2.73}$$

and due to Equation (2.66),Equation (2.67) appears generally dependent on the stator current space vector components I_d and I_q. Machine designers of SynRM often try to maximize saliency allocating high amounts of reluctance torque from the geometrical design. In Chapter 5 it will be shown that a significant saliency value is beneficial for zero/low-speed sensorless methods such as the implemented INFORM method. Figure 2.6 shows three different rotor topologies which are preferred in industrial applications when SynRM are deployed. To compare different machine topologies the saliency ratio at rated value conditions is taken into account. This allows for a relation of the above rotor types in terms of saliency:

$$\xi^{IPM} < 1 \leq \xi^{SMPM} < \xi^{salient} < \xi^{FxB} < \xi^{ax-lam} \tag{2.74}$$

Mentioning conventional SMPM (i) and IPM (ii) machines illustrates the fact that SynRM are completely free of permanent magnet material. This makes them attractive in terms of simpler design effort and project complexity, as well from a cost oriented side. Fault tolerance and safety on the machine side is also greatly increased when avoiding permanent magnet material inside the rotor which leads to zero induced stator fault currents in case of a line-to-line short. All three presented SynRM types in Figure 2.6 (iii), (iv) & (v) share these advantages but pose several differences in terms of mechanical robustness, manufacturing complexity, saliency and design effort:

- Flux barrier (FxB) type (iv): The idea of guiding flux paths within a transversally laminated rotor was first proposed by Kostko [37] and subsequently optimized to achieve saliency values of roughly $\xi^{FxB} \in [2 \ldots 10]$. This high reluctance torque potential makes the FxB type a prominent candidate for sensored servo applications ranging from low to medium speed ranges. In [8] the concept of a permanent magnet assisted SynRM is investigated where ferrite magnets are placed inside the flux barrier cavities, with a beneficial effect for several performance characteristics. However the design of a proper rotor geometry for this machine type is a challenging task when aiming for high saliency and robustness to sustain high mechanical speeds. Furthermore these types are typically designed to operate deep inside the non linear region of the flux maps of Equation (2.65) making them very demanding in terms of model, identification and computational power requirements especially when sensorless operation is the ultimate goal.

- Axially laminated type (v): Even higher saliency ratios can be achieved when deploying corn-oriented bended sheets of metal to form an axially laminated rotor. To achieve mechanical robustness additional bolts need to be driven through said sheet packages. A prominent design was published in [34] and reported saliency ratios of $\xi^{ax-lam} > 12$. A high saliency ratio typically boosts power factor and improves the motor's flux weakening properties[27]. But these advantages come at the cost of very high manufacturing complexity and costs as well as model complexities such as the previous FxB type (iv). Altogether this type does not fulfill the targeted requirements.

---

[27]cf. Section 4.7

- Salient pole type (iii): The highest mechanical robustness is achieved when using a geometrical layout without cavities or additional mechanical fixtures. Achievable saliency ratios are $\xi^{salient} \in [1.3\ldots3]$, cf. [38]. Design and manufacturing of a rotor topology in salient pole configuration such as the proposed design [1] is generally less complex and less expansive than the other two introduced SynRM types. The flux path in *q*-direction will typically not (or only in an insignificant manner) saturate because the material corresponding to those field lines is mainly comprised of air, which is magnetically linear. Therefore the parameter L_q can assumed to be constant (linear inductance), simplifying the machine model and easing computational requirements.

Based on these grounds the salient pole SynRM is the best candidate for the targeted embedded sensorless servo application for high speeds.

2.4.3 Model Reduction

Under consideration of the simulation results in Section 2.4.5 and [8],[39] the following simplifications for the flux model of the designed machine are justified:

1. Cross coupling effects are neglected. In [39] a finite element calculation of a salient pole SynRM shows that self inductances differ from the mutual inductances by one order of magnitude or higher.

2. The machine is assumed to operate within the linear range without considerable iron saturation effects. Together with the statements above this means that the inductance in *d*-direction L_d can also be assumed as constant. To enable magnetic bearing in future work as outlined in Chapter 1 the machine was designed to have a large airgap $\delta = 1$mm which can be seen as the main physical reason for this simplification.

When applying 1 & 2 apparent and incremental inductances coincide, $L_d^\Delta = L_d$, $L_q^\Delta = L_q$ and mutual inductances become zero $L_{dq}^\Delta = L_{qd}^\Delta = 0$. The flux equation of the machine Equation (2.65) resembles to

$$\underline{\Psi}^{dq} = L_d I_d + \mathrm{j}L_q I_q \ . \tag{2.75}$$

Substituting Equation (2.75) into the stator voltage equation Equation (2.60) and combining the torque expression Equation (2.70) with Newton's second law leads to a state space model for the Synchronous Reluctance Machine of this thesis:

$$\frac{\mathrm{d}I_d}{\mathrm{d}t} = \frac{1}{L_d}\left(U_d - R_s I_d + p\Omega_m L_q I_q\right) \tag{2.76}$$

$$\frac{\mathrm{d}I_q}{\mathrm{d}t} = \frac{1}{L_q}\left(U_q - R_s I_q - p\Omega_m L_d I_d\right) \tag{2.77}$$

$$\frac{\mathrm{d}\gamma_m}{\mathrm{d}t} = \Omega_m \tag{2.78}$$

$$\frac{\mathrm{d}\Omega_m}{\mathrm{d}t} = \frac{1}{\Theta}\left(\frac{3}{2}p\left(L_d - L_q\right)I_d I_q - T_L\right) \tag{2.79}$$

The rotor's inertia is denoted by Θ, a mechanical load torque is represented by T_L and $\gamma_d = p\gamma_m$. Time dependencies are omitted. For the target implementation these equations are scaled

as described in Section 2.2 leading to the set of equations forming the basis of design and implementation of the sensored & sensorless control system:

$$\frac{\mathrm{d}i_d}{\mathrm{d}t} = \frac{1}{l_d T_B} \left(u_d - r_s i_d + \omega l_q i_q \right) \tag{2.80}$$

$$\frac{\mathrm{d}i_q}{\mathrm{d}t} = \frac{1}{l_q T_B} \left(u_q - r_s i_q - \omega l_d i_d \right) \tag{2.81}$$

$$\frac{\mathrm{d}\gamma_m}{\mathrm{d}t} = \omega \frac{1}{p T_B} \tag{2.82}$$

$$\frac{\mathrm{d}\omega}{\mathrm{d}t} = \frac{1}{T_M} \left(l_d - l_q \right) i_d i_q - \frac{t_L}{T_M} \tag{2.83}$$

Instead of six non-linear parameters in the general case above the flux model of the machine can be properly described using only two constant inductance parameters. Note that due to scaling with the respective base values electrical and mechanical shaft speed coincide as ω in the scaled equations. This said quantity is usually considered constant in terms the currents rate-of-change time horizon in the first two above equations. With this final simplification the non-linear MIMO[28] system Equation (2.60), Equation (2.65) Equation (2.70) can be validly streamlined to an electrical Equation (2.80)-Equation (2.81) and a mechanical subsystem Equation (2.82)-Equation (2.83). Henceforth, ω is treated as a "slowly changing" parameter within the LTI[29]-MIMO electrical subsystem. In control theory the above strategy of different time horizons is often designated as *singular perturbation method*, [40],[41]. From an implementation perspective this is also the reason to adopt cascaded control with Equation (2.80)-Equation (2.81) as the inner cascade executed within a FAST task and Equation (2.82)-Equation (2.83) as the outer cascade controlled[30] within a SLOW task, see Chapter 3.

2.4.4 Control Strategies

The machine parameter of saliency ratio ξ and the control choice of MMF angle θ have a substantial influence on the SynRM's Equation (2.80)-Equation (2.83) performance during operation. To obtain the highest torque value for a given current space vector magnitude Equation (2.72) is normalized and formulated as an optimization problem:

$$\begin{aligned} \underset{\theta \in \mathbb{R}}{\text{maximize}} \quad & t_e = \frac{1}{2} \left(l_d - l_q \right) i^2 \sin\left(2\theta \right) \\ \text{subject to} \quad & \{l_d, l_q, i\} = const. \end{aligned} \tag{2.84}$$

The solution of Equation (5.45) is called "Maximum Torque Per Ampere" control and in this case given by

$$\theta_{MTPA} = 45°_{\text{elec}} \tag{2.85}$$

$$t_{e_{MTPA}} = \frac{1}{2} \left(l_d - l_q \right) i^2 \tag{2.86}$$

---

[28]Multiple Input/Multiple Output

[29]Linear Time Invariant

[30]The term "controlled" is important here referring to the controller. Other than the controller, the observer for the mechanical subsystem is implemented within the FAST task.

Figure 2.7: Steady state vector diagram of the deployed SynRM under MTPA control: $\omega = 0.6$, $i = 1$, $\theta = 45°_{\text{elec}}$; Parameters from Section 2.4.5; Scale of $7 : 1$

hence $i_d = i_q$. In the magnetically non-linear case the inductances are functions of the current space vector Equation (2.66), Equation (2.67) and MTPA is achieved by a set of MMF angles for each operation point called "MTPA-Control-Trajectory". These values are typically $> 45°_{\text{elec}}$ due to the fact that l_d is more likely to decrease because of saturation than l_q [31]. Intuitively, $(l_d - l_q)$ is greater, when a higher proportion of the current space vector is allocated to i_q.

Figure 2.7 shows a typical steady state vector diagram in the case of adopting MTPA control. When neglecting stator resistances the stationary power factor of the SynRM can be found as

$$\cos(\varphi) = \frac{\xi - 1}{\sqrt{\xi^2 \frac{1}{\sin^2 \theta} + \frac{1}{\cos^2 \theta}}} \tag{2.87}$$

and maximized with respect to the MMF angle:

$$\begin{aligned} \underset{\theta \in \mathbb{R}}{\text{maximize}} \quad & [\cos(\varphi)](\theta) \\ \text{subject to} \quad & \xi = const. \end{aligned} \tag{2.88}$$

to yield

$$\theta_{MPF} = \operatorname{atan}\left(\sqrt{\xi}\right) \tag{2.89}$$

$$\cos(\varphi)_{MPF} = \frac{\xi - 1}{\xi + 1} \ . \tag{2.90}$$

---

[31] the airgap is shorter that direction

Property	Value/Description
Rated Peak Current (Phase)	18 A
Rated Peak Voltage (Phase)	40 V
Slot Turn Number N_{slot}	20
Realized Rotor Skewing	$12\,°_{\text{mech}}$
Torque Ripple[a]	20%
Airgap Length δ	1 mm
Metal Sheet Material[b]	M 400-50A (EN10106)
Ball Bearing[c] Limiting Speed	33000 rpm

[a] @ rated current and 8000 rpm, $\hat{M}/\overline{M}$
[b] applicable for Stator & Rotor
[c] Type: SKF E2.6001-2Z/C3

Table 2.4: Additional machine parameters

As for the MTPA strategy above the MPF (Maximum Power Factor) values are constants in the magnetically linear case and trajectories in the (i_d, i_q) plane in the non-linear case.
These two use cases are only two examples of controlling SynRM in compliance to a specific goal. In Section 4.7 and Chapter 5 control strategies of $t_e(\omega)$ and $\theta(\omega)$ will be presented in detail to achieve high speed sensorless operation deep inside the flux weakening region. This emphasizes the versatility of SynRM making them attractive candidates for research and optimization.

2.4.5 Simulation and Realization

The main limiting component in the preceding work [3] was the machine. Therefore a new rotor and stator were designed in [1] as a solid base for this thesis. Initially the design aimed for a DC-link voltage that was approximately six times larger as the used $U_{DC} = 60\,\text{V}$ (see Section 2.5).

However the time the motor was built such an inverter was not available and the machine needed to be adapted. A common way to do this in the field of electric machines is to change the coil group's interconnections. By reducing the resulting turns (and therefore also induced voltage) by a factor of six, the rated current can also be increased by a factor of six to get the same magnetic behavior as the MMF is "current · turns". This altered machine was realized with a rotor skewing of $12\,°_{\text{mech}}$ to reduce torque ripple. Additional information is given in Table 2.4.

Ideally the altered machine should result in the same simulation results in terms of graph *trends* (and therefore qualitative behavior) as reported in [1]. This was confirmed by a point wise simulation carried out using the new machine parameters. Results used for the first development iteration in Chapter 4 are reported in Table 2.5. The saliency ratio is the same as for the original design.

2.5 Voltage Source Inverter

By inspection of Figure 2.1 it becomes clear that the voltage source inverter is of central importance in a modern electrical drive system. Through its components and circuitry the device realizes the

Parameter	Symbol	Value	
		absolute	scaled
Stator Resistance	R_s^{calc}	$34.9\,\mathrm{m\Omega}$	0.0153
d-Axis Inductance	L_d^{sim}	$423\,\mathrm{\mu H}$	0.95
q-Axis Inductance	L_q^{sim}	$211\,\mathrm{\mu H}$	0.47
Saliency Ratio	ξ^{sim}	2.01	2.01

Table 2.5: Machine parameters from design prior to empirical parameter identification

functions of power conversion (DC → AC in this application), safety measures, analogue to digital conversion, communication, debugging and motor control. Prior to this thesis a suitable inverter was designed and built. It was already shown in Section 2.1. A set of schematic details is provided in Appendix B.1 and will be referred to where applicable. The design and layout of such a device could easily fill another thesis[32]. The current section aims to present the reader its specifications and parameters that are important in the context of this thesis. It is also instructive to discuss the analogue to digital signal chain that converts physical currents into software variables.

Description, Specifications

The voltage source inverter can be classified as integrated two-level inverter comprising three half bridge n-channel power MOSFETs. The control unit is a Texas Instruments 28335 DSC, described in Chapter 3. Figure 2.8 depicts a semantic correct representation of the inverter's power stage and measurement interface. The corresponding realized circuit is depicted in Figure B.2 [33]. Another common designation for this power electronic topology is "B6C". The attribute *integrated* relates to the fact that all stages (power conversion, measurement and control) are located at the same PCB[34], absent of galvanic isolations between each other. Analogue and digital ground are separated and connected only once. At the given voltage range this "integrated" approach is common and has advantages such as reduced complexity, size, cost and design effort. On the other hand the presence or absence of noise at measurement signals has to be checked and taken care of properly, see the second half of this section.

Two different voltage potentials (+) or (−) can be applied to a three phase load, resulting in $2^3 = 8$ valid combinations of top and bottom switches $\mathrm{SW_T^{UVW}}\,\&\,\mathrm{SW_B^{UVW}}$. Said switches are always operated complimentary, that is $\mathrm{SW_B^U} = \neg\,\mathrm{SW_T^U}$ and so on. Otherwise the DC-link would be short circuited. The term *shoot through* is used for this fault state. Table 2.6 summarizes the resulting possible scaled voltage space vectors for each valid switching combination. The motor's star point is not connected to the inverter. A simple analysis then reveals: phase voltage levels are either $\pm\frac{1}{3}U_{DC}$ or $\pm\frac{2}{3}U_{DC}$. A distinction between half bridge voltages and phase voltages is necessary, see also [16], [17]. Figure 4.2 illustrates said quantities. Strategies to realize arbitrary

---

[32]such as [5]

[33]R_U of Figure 2.8 corresponds to R_{215} in Figure B.2 and so on. The printed top and bottom switching signals relate to PWM outputs, e. g. $\mathrm{SW_T^U} \Leftrightarrow$ `HI_U_CU_DO` in Figure B.4.
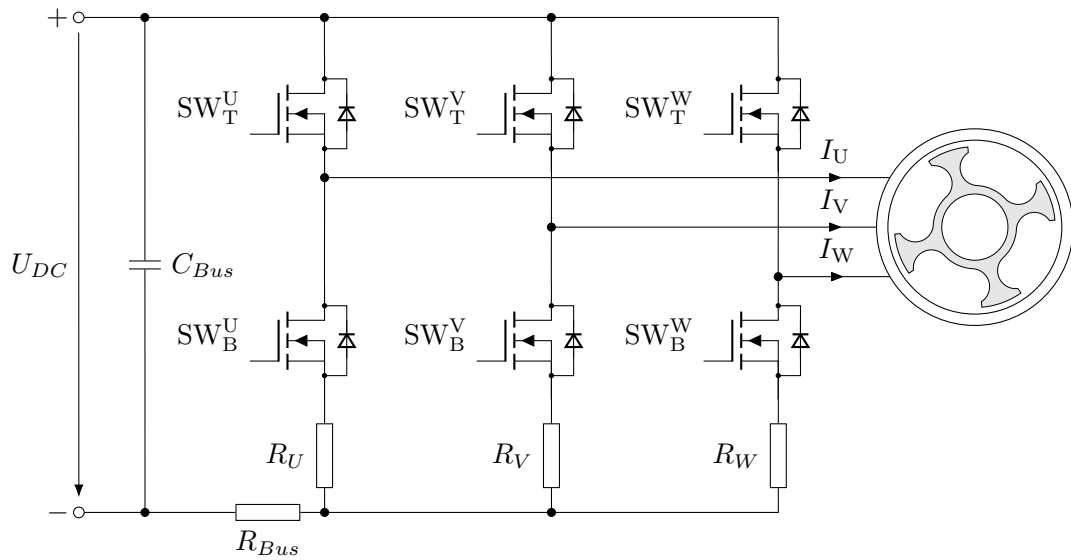
[34]Printed Circuit Board

Figure 2.8: Simplified illustration of the inverter's power stage and low-side shunt measurement interface connected to the SynRM, cf. Figure B.2

voltage space vectors (so called sinusoidal commutation) via a software modulator are covered in Section 4.2 and Section 5.2.3.

With the inverters current equipped parts DC link voltages of $U_{DC} \in [40\,\text{V} \ldots 90\,\text{V}]$ and load phase currents of up to $\pm 30\,\text{A}$ are achievable. The device is operated at $U_{DC} = 60\,\text{V}$ and PWM switching frequencies of $15\,\text{kHz}$. Hardware trip circuits currently allow for currents of up to $\pm 25\,\text{A}$, a roughly 40% overload range of the nominal $\pm 18\,\text{A}$ phase peak current. Furthermore DC-link voltages $U_{DC} \in [50\,\text{V} \ldots 70\,\text{V}]$ and temperatures up to $70\,^{\circ}\text{C}$ are allowed. The thesis [7] proved an operational capability of up to $20\,\text{kHz}$ continuous and $40\,\text{kHz}$ for single identification burst[35] measurements.

Current Measurement

Motor current measurement is needed to realize FOC. In this thesis the motor's phase currents are measured via low-side bridge shunts R_U, R_V, R_W of Figure 2.8. These symbolic resistors correspond to R_{215}, R_{216},, R_{217} in Figure B.2. In depth knowledge of the analogue to digital conversion process in conjunction with the DSC's actuation (ePWM) and conversion (ADC[36]) peripherals is required to achieve high performance operation. Thereto, the process to obtain *one scaled phase current value* (Phase U) in software is described here. This is specified as *measurement point*. Multiple measurement points form a *measurement task*[37] and multiple tasks in turn are designated as a *measurement agenda* within one sample period. In Section 4.2 and Section 5.2.3 such an agenda will be related to the actuating PWM switching patterns. For now,

---

[35]Adjustments to the ADC interface as described in [7] have to be applied to achieve this value.

[36]<u>A</u>nalog to <u>D</u>igital <u>C</u>onverter

[37]Roman numerals I,II,III. . . used as designation, see Figure 4.4 and Figure 5.4 in later sections.

Top Switch States			Resulting Scaled Voltage Space Vector	
SW_T^U	SW_T^V	SW_T^W		
1	0	0	$\underline{u}_{U+}$	$= 1\mathrm{e}^{\mathrm{j}0\,°\mathrm{elec}}$
1	1	0	$\underline{u}_{W-}$	$= 1\mathrm{e}^{\mathrm{j}60\,°\mathrm{elec}}$
0	1	0	$\underline{u}_{V+}$	$= 1\mathrm{e}^{\mathrm{j}120\,°\mathrm{elec}}$
0	1	1	$\underline{u}_{U-}$	$= 1\mathrm{e}^{\mathrm{j}180\,°\mathrm{elec}}$
0	0	1	$\underline{u}_{W+}$	$= 1\mathrm{e}^{\mathrm{j}240\,°\mathrm{elec}}$
1	0	1	$\underline{u}_{V-}$	$= 1\mathrm{e}^{\mathrm{j}300\,°\mathrm{elec}}$
1	1	1	$\underline{u}_{sh+}$	$= 0$
0	0	0	$\underline{u}_{sh-}$	$= 0$

Table 2.6: Three phase, two level inverter available voltage space vectors; $1 = $ on/high , $0 = $ off/low; Bottom switch states are complimentary; Scaling according to Section 2.2; see also Figure 4.2

a single measurement point for I_U is described.

The usage of low-side bridge shunts restricts the possible measurement time frame to durations where the respective phase is connected to the lower potential $(-)$. That is the case when $\mathrm{SW}_T^U = 0 \Leftrightarrow \mathrm{SW}_B^U = 1$ and so on. Under ideal[38] circumstances the voltage at R_U (R_{215}) is a function of the motor phase current I_U during that period. The potential nodes `PH_U_P` and `PH_U_N` in Figure B.2 are routed to a differential amplifier depicted in Figure B.3. Under the assumption of ideal OPAs[39] and with the abbreviations

$$r_A = \frac{R_{301}}{R_{302} + R_{303}} \approx 100.671 \tag{2.91}$$

$$r_B = 2 + r_A \tag{2.92}$$

$$r_C = \frac{R_{311}\|R_{313}}{R_{307} + R_{308}} = \frac{r_A}{2} \tag{2.93}$$

$$r_D = 1 + r_C \tag{2.94}$$

the 28335 ADC input voltage `ISHU_AI_CU` at Figure B.3 can be derived as:

$$\texttt{ISHU\_AI\_CU} = 3\,\mathrm{V}\,\frac{r_D}{r_B} + \frac{r_A r_D}{r_B} \cdot \texttt{PH\_U\_P} - r_C \cdot \texttt{PH\_U\_N} \tag{2.95}$$

Substituting nominal resistor values into Equation (2.95) yields

$$\texttt{ISHU\_AI\_CU} = 1.5\,\mathrm{V} + k_{sh} I_U \tag{2.96}$$

$$k_{sh} = \frac{75}{1.49} \cdot 10^{-3} \mathrm{V/A} \tag{2.97}$$

---

[38]A clarification is given at the end of this section.

[39] <u>O</u>perational <u>A</u>mplifiers

Thereby a bipolar current range was mapped to an unipolar voltage range, suitable for ADC conversion as required by the TI-28335, [42]:

$$[-30 \ldots 30]_{\text{A}} \quad \Leftrightarrow \quad [0 \ldots 3]_{\text{V}} \tag{2.98}$$

This ADC input voltage is converted to a 12 bit raw value of the format I4Q12 that is stored within a 16 bit register. The settings are described Section 3.3. In terms of signals this means:

$$[0 \ldots 3]_{\text{V}} \quad \Leftrightarrow \quad [0 \ldots 0.999 \cdots]_{\text{I4Q12}} \tag{2.99}$$

for analog to digital conversion.

An important remark here: During development substantial noise levels became apparent when ADC current measurements were compared against measurements of a current clamp. A convenient way to counter these effects is to oversample a quantity and take the median of the array of samples as "true" value. The median is more robust to noise if compared to the mean value of a data set. The final configuration is as follows: When two active (symmetric) PWM patterns are applied[40] three samples per phase are taken and their median is calculated using Equation (3.4). When three active PWM patterns are applied[41] four samples per phase are taken and Equation (3.5) is used to calculated their median.

After this step a cast to the "working" `IQmath` format I8Q24 is necessary. According to [43] this should be executed as

$$\texttt{iu\_vadc} = \_\texttt{IQmpy}\left(\_\texttt{IQ}\left(3.0\right),\, \_\texttt{IQ12toIQ}\left(\left(\_\texttt{iq}\right)\texttt{iu\_raw\_median}\right)\right) - \_\texttt{IQ}\left(1.5\right) \tag{2.100}$$

The software variable `iu_vadc` then represents a (virtual) voltage level of $[-1.5 \ldots 1.4999 \cdots]_{\text{I8Q24}}$ that corresponds to $[-30 \ldots 30]_{\text{A}}$. In a last step Equation (2.96) is used together with the currents base value and an offset correction to obtain the scaled phase current:

$$\texttt{iu\_pu} = \texttt{iu\_vadc} \cdot \frac{-1}{k_{sh}} \cdot \frac{1}{I_B} - \texttt{iu\_offs\_cal} \tag{2.101}$$

The quantity `iu_pu` corresponds to i_U introduced in Section 2.2 and used throughout this thesis. A multiplication by -1 is necessary due to different reference directions between ADC voltage and motor phase current (which is always towards the star point).

Calibration

Due to non-ideal part values for resistors and voltage sources on the inverter gain and offset errors will influence the above described process. Both are compensated in software. The offset correction `iu_offs_cal` is determined online each time when the system executes its start-up routine. All PWM switches are open and therefore a value of zero should be obtained for i_U. This state is applied for 1000 FAST Tasks. A low pass filtering is applied to the measured current value in this state only. The value obtained after this duration will be used as `iu_offs_cal` for subsequent operation. Gain errors are not compensated directly. Instead a series of measurements was conducted using a current clamp as reference (offset correction was already applied). The

---

[40]cf. Section 4.2
[41]cf. Section 5.2.3

purpose was to rank all three current phases according to their "goodness" in terms of linear measurement characteristics. Then the best two phases were picked: Phase U and Phase V for this particular inverter. For all other future measurements only two currents were measured and Kirchhoff's rule was used to obtain the Phase W current as $i_W = -i_U - i_V$.

A very important quantity in the context of shunt-based current measurement is the analogue interface time constant τ_{an}. When inspecting the differential amplifier's output in Figure B.3 together with the standard ADC input circuitry of the 28335, a low pass filter becomes apparent. The RC time constant calculated from nominal values is $1.22\,\mu s$. Measurements conducted directly at the ADC Phase U current input pin `ADCINA2` roughly confirm this value, as the result of these measurements was $\tau_{an} \approx 1\,\mu s$. After the Phase U is connected to the $(-)$ terminal the controller has to wait at least 2-3 τ_{an} before[42] conversion results become valid. This reasoning will become very important in Section 4.2.

Voltage and Temperature Measurement

Motor phase voltages are not measured despite an existing opportunity. Instead the controller output (reference voltages) will be used as "measured" voltages. Reasons for this is a reduced measurement time frame. In the previously referenced modulation sections (Section 4.2 and Section 5.2.3) it will be shown that a reduced measurement window corresponds to a higher possible voltage output.

An exception to this is the DC-link voltage which is measured once per FAST Task. Temperatures from top and bottom sides of the PCB are also measured using linear active thermistors (MCP9700).

---

[42]The well known formula $1 - \mathrm{e}^{-t/\tau_{an}}$ applies in this context

2.6 Angular Position Measurement and Calibration

To successfully deploy Field Oriented Control (FOC) knowledge of the rotor's *d*-axis position $\gamma_d(t)$ is of fundamental importance. This was reasoned at the end of Section 2.3 when the *Park Transformation* for space vectors was introduced in Equation (2.55). In the following section the sensor device that was used to measure angular positions will be described. Additionally, crucial aspects regarding both Hard- and Software will be highlighted to properly use the sensor up to its speed limits.

This section will be concluded by the definition of a tuned measured angular value γ_{enc} that forms the basis of Chapter 4 and is used to assess sensorless model quality in Chapter 5.

Magnetic Rotary Encoder AS5040

The SynRM drive system comprises the AS5040 Magnetic Rotary Encoder device manufactured by ams AG, [44]. This sensor is a contact-less rotary position measurement system-on-chip. It provides the position information in various output modes and formats at its pins. The measurement principle is based on a two-pole magnetic pill placed on the rotating shaft as illustrated in Figure 2.9. The pill's rotating magnetic field is measured by a hall array located inside the resting chip facing said pill at short distance. An in-depth instruction on selecting and placing the magnetic pill is given by [45].

The AS5040 sensor's maximum resolution is 10-bit which yields a discretization in terms of "angular steps" of $360\,[°_{\text{mech}}]/(2^{10}) \approx 0.35\,[°_{\text{mech}}]$. For the SynRM featured here this corresponds to $\approx 0.7\,[°_{\text{elec}}]$. The device's maximum recommended operational speed is 30 000 rpm. It is configured as an incremental encoder to be read out in "*Default Mode 0.0 (Quad A/B Mode)*". A dedicated hardware peripheral support for this mode by means of decoders, gates, counters and registers located on the 28335 target hardware is utilized. This hardware bank is called *Enhanced Quadrature Encoder Pulse (eQEP) Module* and a detailed description is given in [46]. If correctly set-up and configured the position information of the sensor can be obtained by a simple register readout within the firmware. No further communication protocols between sensor and target hardware are necessary using this approach. Therefore computational requirements and software complexity are eased. No *additional* dead-time is introduced by propagation delay of transmitting and processing sensor data.
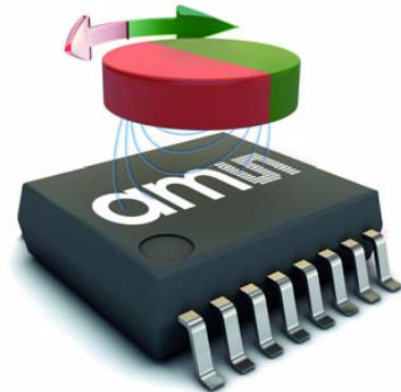

Figure 2.9: Illustration of AS5040 facing a magnetic pill, courtesy of ams AG [44]

Angular Data Representation

As recently outlined a full mechanical revolution of $360\,[°_{\text{mech}}]$ corresponds to 1024 states/values of the eQEP counter. Due to a pole pair number of $p = 2$, two electrical revolutions will occur.

Therefore the following semantic mapping between counter values and electric angles is evident[43]:

$$\left[\, 0(512) \,\ldots\, 511(1023) \,\right]_{\mathbb{N}} \quad \Leftrightarrow \quad \left[\, 0 \ldots 360 \,\right)_{[°_{\mathrm{elec}}]} \tag{2.102}$$

When measuring angular values as positive numbers in counterclockwise direction the interval mapping given by Equation (2.102) and

$$\left[\, 0 \ldots 360 \,\right)_{[°_{\mathrm{elec}}]} \quad \Leftrightarrow \quad \left[\, 0 \ldots 180 \,\right)_{[°_{\mathrm{elec}}]} \to \left[\, -180 \ldots 0 \,\right)_{[°_{\mathrm{elec}}]} \tag{2.103}$$

are semantically equivalent. This last basic relationship builds the bridge to the actual implementation and representation of angular values within the firmware. There, the interval $\left[\, -180 \ldots 180 \,\right)_{[°_{\mathrm{elec}}]}$ will be mapped to $\left[\, -8, \ldots 7.999 \cdots \right]_{\mathrm{IQ28}}$. That is, a full electric revolution will be represented by the whole dynamic range of the I4Q28 data format[44]. This fixed point data format is of `signed long` data type that is coded as two's complement binary number on the 28335 DSP. The matter of data formats and types is covered more in detail at Section 3.2.

When 1 LSB is added to the highest possible representable numeral of a two's complement coded variable it will overflow to its smallest negative numeral. This behavior correctly resembles the angular overflow that is happening at $180\,[°_{\mathrm{elec}}]$, viz. Equation (2.103). Figures that plot angle signals such as Figure 5.12 demonstrate mentioned overflow (labels are rescaled). Software simplicity and performance is enormously enhanced as wrapping of angular values "is done" via hardware (two's complement overflow) rather than using if/else statements in software. Such a strategy is therefore considered compulsory to efficiently implement FOC. This is particularly true for sensorless FOC.

The sine and cosine function values of an electric angle are needed to carry out the Park and inverse Park transformation given by equations (2.55), (2.56). To obtain these values the IQMATH library's functions `IQsinPU(.)` and `IQcosPU(.)` are used. They require a scaled angular argument with 1_{IQ24} corresponding to $360\,[°_{\mathrm{elec}}]$ in the chosen `GLOBAL_Q` format of 24. A division by 16 and subsequent bitwise right shift $\gg$ of 4 applied to I4Q28 angular values achieves the required conversion.

The following equivalence true for angular values and their data representations summarizes the statements from above:

$$\left[\, -180 \ldots 180 \,\right)_{[°_{\mathrm{elec}}]} \quad \Leftrightarrow \quad \left[\, -8, \ldots 7.999 \cdots \right]_{\mathrm{IQ28}} \quad \Leftrightarrow \quad \left[\, -0.5, \ldots 0.4999 \cdots \right]_{\mathrm{IQ24}} \tag{2.104}$$

Finally the transformation from raw integer eQEP counter values to electrical angles in I4Q28 format can be specified:

$$\gamma_{enc}^{raw} = (\texttt{eQEPcounter}) \ll (28 - 10 + 1 + 4) \,, \tag{2.105}$$

where a left shift of 28 transforms the raw mechanical count value from I32Q0 to I4Q28 and -10 normalizes it to the [p.u.] intervall of $[0 \ldots 1]$. The electrical angle is calculated by a left shift of 1. To eventually implement the mapping stated in Equation (2.104) an additional left shift of 4 (multiplication by 16) is applied.

---

[43]For readability reasons the subtraction of $\approx 0.7\,[°_{\mathrm{elec}}]$ at the end of each interval is neglected.

[44]Another data format resembling the same behavior but with decreased resolution is the 16bit I4Q12 . This is the data format that is used for online debugging and plotting signal trends.

Position Offset Calibration
The magnetic pill's index position and rotor's d-axis location do not coincide for most cases when the pill is placed onto the shaft. This constant position offset value needs to be determined and subtracted from the eQEP counter's raw value. It is identified automatically by rotating the shaft with a feedforward voltage space vector of low magnitude and 1 Hz (mechanical) each time the motor is started. In Equation (2.105) the quantity `eQEPcounter` represents the already calibrated counter.

Mechanical and Electrical Interface
The AS5040 chip was circuited onto an adapter PCB for 5V operation as recommended in [44]. The Chip-Select (CS) pin has to be pulled down at all times. A sensor front-plate hosts the PCB mechanically. A sensor mounting-plate places the sensor fixture facing the magnetic pill on the SynRM's shaft. Slotted holes are present in both parts to fine-adjust the position of the chip surface alongside all three spatial directions. Drawings of the designs can be inspected in Appendix B.2. As far as possible non-ferromagnetic material was used[45] for all described components.

The incremental position information is given by two electrical square wave signals (line designations A,B) and a pulse shaped index signal (line designation I) indicating a full mechanical revolution. In the given configuration the manufacturer specifies *2 x 256 pulses per revolution, no missing pulse up to 30 000rpm*, see [44]. At maximum shaft speed the square wave frequency can then be concluded as $f_{QEP} = 500\text{Hz} \cdot 256 = 128\text{kHz}$. The LSB pulse width present on the index signal line is given by $T_{LSB} = 1/\left(4 f_{QEP}\right) = 1.95\text{µs}$. All three signals pass through a signal conditioning interface on the VSI before they apply at the DSPs eQEP Pins. Said circuit can be inspected on the schematic, see Figure B.5. The interface consists of a voltage divider plus low pass filter (LPF) and a pair of protection diodes.

An analysis of the referenced circuit for line A (the other two lines follow accordingly) yields a cutoff frequency of

$$f_c^{QEP} = \frac{1}{2\pi} \cdot \frac{R_{907} + R_{912}}{R_{907}\,R_{912}} \cdot \frac{1}{C_{910}} \ , \tag{2.106}$$

where the component designations of Figure B.5 were used. To support the above stated operational mode the nominal capacitors C_{910}, C_{911} and C_{912} were replaced by 330pF/100V components. The cutoff frequency given by Equation (2.106) of the signal conditioning LPF is then

$$f_c^{QEP} = 401.9\text{kHz} \ . \tag{2.107}$$

A quick simulation in MATLAB/SIMULINK was carried out to ensure that the filtered square waves of all three signal lines are not distorted too severly. These signals need to comply to electrical specifications of the 28335 DSP stated in [47, p. 116ff].

Signal Integrity Issues and Robustness Enhancement
During implementation and test of the current controllers described in Section 4.4 numerous over-current trips at the VSI occurred. Eventually the error source was located at the signal

---

[45]aluminum platings, brass screws / nuts and fiber composite material designated "Pertinax"
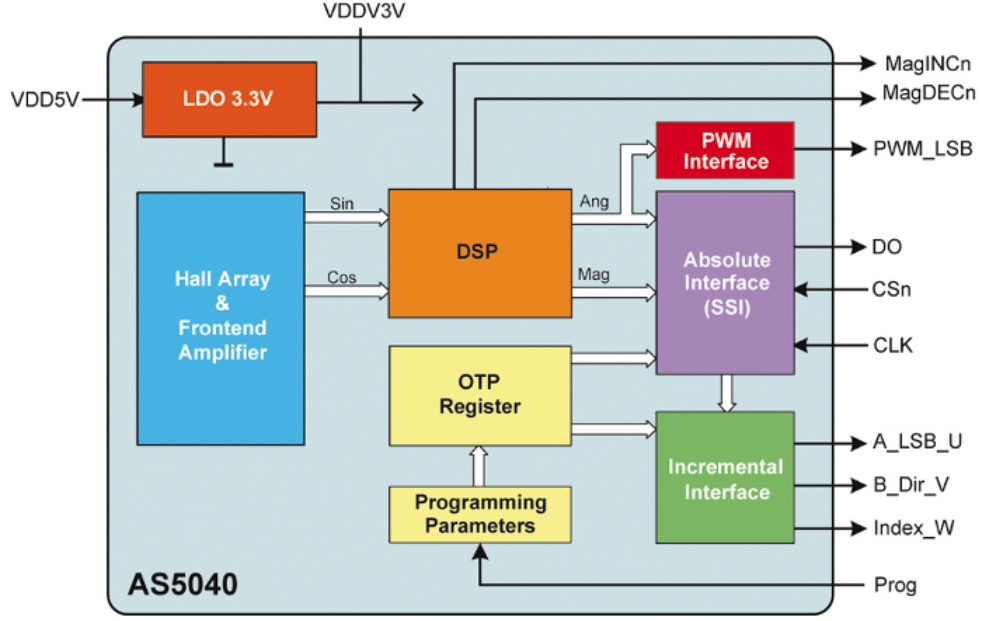
Figure 2.10: Block diagram of AS5040 system-on-chip and output pin designation, courtesy of ams AG [44]. Note that the position information has to pass the SSI interface before it is provided at A/B/I incremental outputs.

lines of the rotary encoder. Voltage signals (A,B,I) got corrupted at certain operational states, see Figure B.1. Therefore, the position information γ_d was lost. The correct rotor reference frame could not be maintained anymore. Ultimately the current feedback loop destabilized and triggered hardware over-current protection failsafe systems.

To counter this phenomenon a feature called *GPIO Input Qualification* of the 28335 DSP was utilized. Signals present at the eQEP GPIO-input pins were "oversampled" and a robust HIGH/LOW state was accepted by a certain amount of consecutive HIGH/LOW samples. A detailed description can be found in [47, p. 132]. The specific deployed settings were: Sampling Period of $2 \cdot T_{sysclk}$, sampling window of six consecutive samples of $12 \cdot T_{sysclk}$, reliable detection after one additional system clock period due to asynchronous nature of external signals, viz. $13 \cdot T_{sysclk}$. At $f_{sysclk} = 150\text{MHz} = 1/T_{sysclk}$ an input delay of 86.6ns is introduced that can correspond to a worst case angular error of $0.7\,[^\circ_{\text{elec}}]$. However this is a small price one has to pay for the reliable fix of these critical faults. After adoption of the described settings no more errors of this kind occurred.

Dead Time Effects and Compensation
The shaft's position information of the *d*-axis, γ_d cannot be provided instantaneously to the sensor's host device. After sampling and internal processing the information is converted into quadrature pulse format and made available at the output pins. Figure 2.10 clarifies this process.

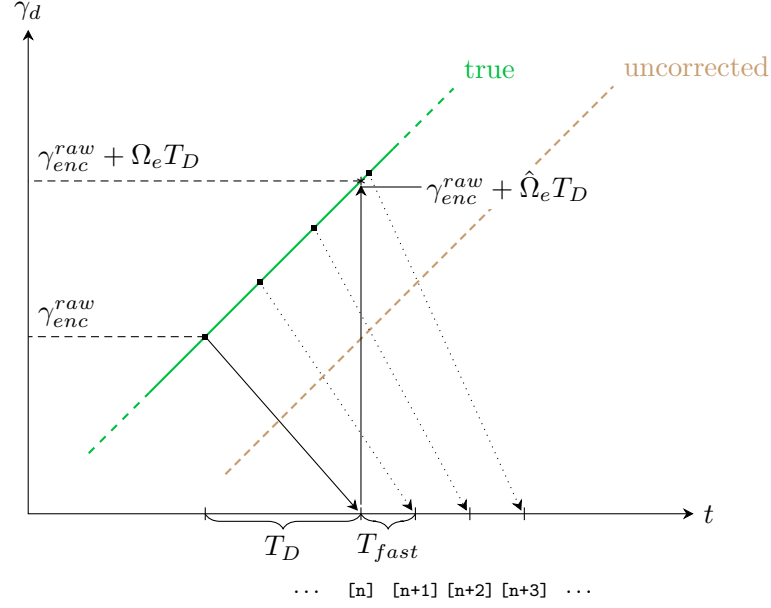At the time instant the DSP reads out this data the motor shaft has already changed its

Figure 2.11: Dead-time delay effects when measuring *d*-axis angular position γ_d with rotary encoders. Constant electrical shaft speed Ω_e during the dead time period of T_D is assumed. Consecutive FAST tasks are indicated below the time-abscissa.

position by a certain angle that is dependent on its speed. These very important dead-time aspects are illustrated in Figure 2.11.

A specific encoder value of γ_{enc}^{raw} will be read in FAST task [n] after a dead time delay of T_D due to the above described effects. Assuming constant shaft speed Ω_e during T_D the measurement error e is given by the difference to the "true" shaft position, viz.

$$e = \gamma_{enc}^{raw} - (\gamma_{enc}^{raw} + \Omega_e T_D) \tag{2.108}$$
$$e = -\Omega_e T_D \tag{2.109}$$

The dead time period T_D can be referenced as *System propagation delay incremental output* in [44] to be $T_D = 192\,\mu s$. The last recent expression for the angular error is rewritten as numerical value equation:

$$e_{[°_{elec}]} = -6\,p\,\Omega_{m_{[rpm]}}T_{D_{[s]}} \tag{2.110}$$

where $\Omega_e = p\,\Omega_m$ was used, see Equation (2.36). Therefore the angular error caused by dead time effects increases linearly with the shaft speed. At $30\,000$rpm Equation (2.110) yields an (enormous) error value of $69.12\,[°_{elec}]$. Even at a rated speed of $\omega = 0.183$ a measurement error of around $10\,[°_{elec}]$ will occur, emphasizing the need of counter-acting these dead time effects. To systematically compensate the error e it can be subtracted from the raw measured encoder angle to yield the "true" angle γ_d^{act},

$$\gamma_d^{act} = \gamma_{enc}^{raw} - e = \gamma_{enc}^{raw} + \Omega_e T_D \; . \tag{2.111}$$

Because the actual shaft speed Ω_e is observed[46] as rated value of $\hat{\omega}$ rather than measured the following approach is taken to implement Equation (2.111):

An auxiliary quantity for e in Equation (2.109) is introduced in the I8Q24 data format used for [p.u.] value representation

$$e_{aux}^{\text{IQ24}} = \hat{\omega} \cdot f_B T_{fast} \ . \tag{2.112}$$

The last two terms in Equation (2.112) are constants that were defined in Section 2.2. In Section 4.3 $\hat{\omega}$ will be introduced as scaled angular velocity resulting from the deployed Luenberger observer. The value of e_{aux}^{IQ24} represents an electrical angular error in a per-unit format as if the dead time would have been T_{fast}.

This auxiliary quantity is converted into I4Q28 data format commonly adopted for angular values as described previously in this section,

$$e_{aux}^{\text{IQ28}} = \left(e_{aux}^{\text{IQ24}} \cdot 16 \right) \ll 4 \ . \tag{2.113}$$

Finally, it is multiplied by a tuning factor $k_{\gamma D}$ and added to the raw value as derived in Equation (2.111):

$$\boxed{\gamma_{enc} = \gamma_{enc}^{raw} + e_{aux}^{\text{IQ28}} \cdot k_{\gamma D}} \tag{2.114}$$

In the final implementation the dead-time correction factor was calibrated to $k_{\gamma D} = 2.325$, see Table 4.7. Taking into account that the dead-time error is compensated "in portions of T_{fast}" the nominal correction factor would yield as $192/67 \approx 2.87$. This value however destabilized the control system at speeds beyond $\hat{\omega} > 0.8$. The proposed setting corresponds to an apparent dead time of $156\,\mu s$. Settings below this value introduce angular errors that manifest into significant erroneous values of $i_d, i_q > 0$ during no load operation. Values reflecting correct physical behavior should average around zero at speeds $\omega < 0.5$ and increase due to viscous friction and aerodynamic drag. The proposed calibration setting of $k_{\gamma D} = 2.325$ therefore represents a trade-off between stability and physically correct representation. Three sources for the dead-time discrepancy between $192\,\mu s$ and $156\,\mu s$ can be identified:

- The true shaft speed is estimated as $\hat{\omega}$ rather than measured as discussed in Section 4.3.

- Angle and current values are not measured *exactly* at the same time instant. For high speed FOC applications it is desireable to measure both as close as possible on the time scale. The measurement agenda presented in Section 4.2 shows that current values used in FAST task `[n]` are measured at the end of `[n-1]` and that the sensor data is read out at the beginning of `[n]` after configuration and launch of the ADC. So there is a delay present between both measurement instants that can be quantified to be several microseconds but in total $< 10\,\mu s$.

- The mechanical alignment between chip's surface and magnetic pill probably has an indirect effect on Equation (2.114) as this is the only software-compensation of measured angular errors applied. An improved alignment would probably have an impact on the choice of $k_{\gamma D}$. This is especially true for high shaft speeds. Instructions can be found in [45].

---

[46]cf. Section 4.3

Conclusion about the Use of Rotary Encoders
As presented in Section 4.7.6 the maximum sensor speed of 30 000rpm was reached, validating the above considerations and the taken approach of Equation (2.114). Nevertheless the paragraphs in this section stress the need to consider and optimise every aspect (electrical, mechanical, software) carefully when the sensor device should be pushed to its limits.

It also becomes clear that a sensorless control system is absent of all accompanying detrimental side effects presented here. A considerable amount of time and money can be saved and robustness can be gained by replacing the rotary encoder by a mathematical model. But the proper inclusion of a rotary encoder is a mandatory step for the development and assessment of a high-performance sensorless control system.

2.7 Concluding Remarks

In the preceding work of [3] a (four pole) salient pole SynRM with $\xi^{pre} = 1.3512$ was proposed and, under several limitations, proved to be capable of full sensorless operation up to a speed of 12 krpm. Shaft speeds beyond that value and deep flux weakening could not be established. Several reasons such as cogging torque, low saliency, limited computation power and ambiguity in the choice of flux weakening parameters were proposed as reasons. The stator of [3] comprised a <u>f</u>ractional <u>s</u>lot <u>c</u>oncentrated <u>w</u>inding (FSCW), the rotor was not skewed.

The research result of [3] showed a proof of concept for operating a SynRM with the proposed sensorless methods. But a machine comprising of a simple stator design with FSCW significantly violating VI/VII and absence of rotor skewing in combination with a simple mathematical model such as Equation (2.80)-Equation (2.83) was not fully capable to reach all requirements.

In retrospect a *trade-off can be formulated between model complexity and machine simplicity*. To push the system limitations further either a motor that is accurately described with Equation (2.80)-Equation (2.83) can be designed or the mathematical model itself can be adapted/expanded to incorporate additional effects. The strategy of TU Wien in this research topic was to follow the former path to design and build a motor accurately fulfilling the proposed space vector theory requirements of Section 2.3 I-VIII and control it by means of the above derived system equations. The main reason for this is given by the aim of building a low cost sensorless control system using an established embedded DSP available on the market[47]. As presented in Chapter 1 the goal of this work is to push the system limits of [3] further and investigate the deep flux weakening region achieving sensorless control from standstill to high speeds in all four quadrants of operation. From re-evaluation of the finite element simulation [1] in Section 2.4.5 it can be predicted that Equation (2.80)-Equation (2.83) describe the real SynRM accurately which is a promising starting point for the aforementioned goal.

---

[47]by the time of writing the unit cost of a 28335 DSP Chip was about $\approx 13€$

3 Processor and Numerical Aspects

This chapter briefly describes the target hardware DSC and the basic program structure. Adopted data formats are discussed and advice is given on how to reduce execution time. In the last section of this chapter common mathematical methods that proved useful for this work are explained.
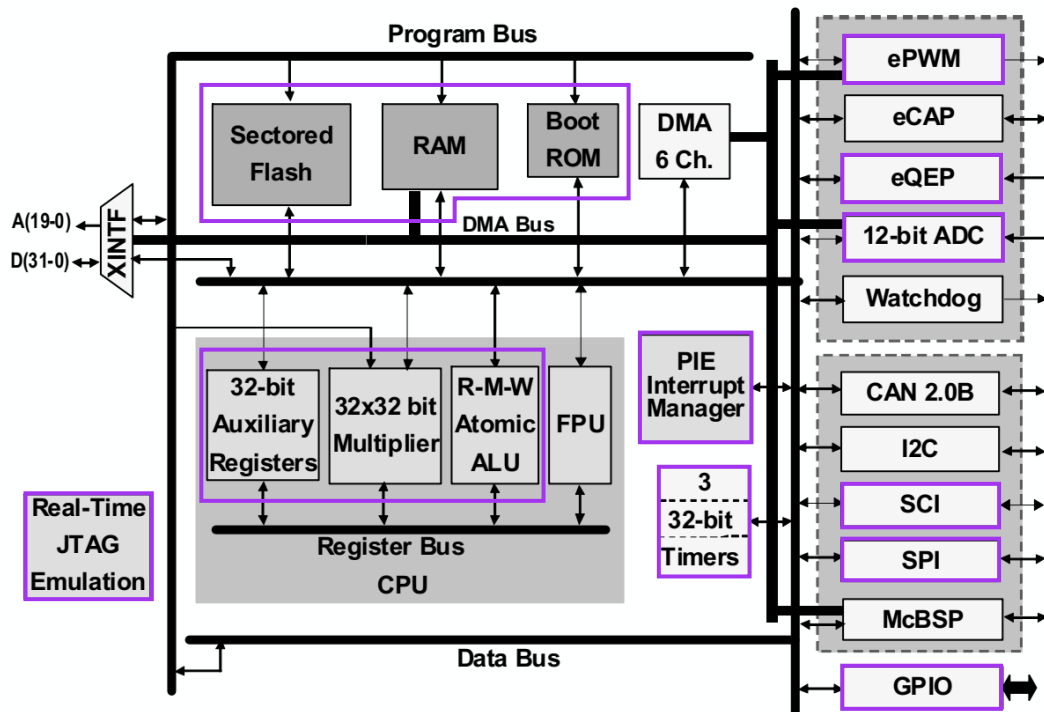
3.1 Texas Instruments TMS320F28335

Figure 3.1: 28335 Block Diagram w/ highlighted used resources & peripherals;
Modified from [43]

Figure 3.1 shows the Harvard architecture overview of the TI-28335 with used units/peripherals highlighted. At the time of writing the device has been active since ten years but is still supported by the manufacturer TEXAS INSTRUMENTS due to its performance and popularity. It comprises a 32bit C28x core, clocked here at 150 MHz. A RAM of 68Kbyte is available as well as 512Kbyte FLASH. The ADC has a resolution of 12bit. This core is supported by dedicated hardware units,

that is: counters, logical gates, registers and so on, so-called peripherals. They target specific tasks such as PWM generation or QEP interfacing. It also has a dedicated floating point unit (FPU), but it was not used in this thesis for reasons given in Section 3.2.

A profound understanding of the 28335 and the usage of its peripherals can greatly enhance a motor control application's performance using this hardware. Thus, a considerable amount of time was invested to gather knowledge in this field. The result on this time investment was a FAST Task[1] execution time of 50.59 μs which corresponds to ≈ 75% CPU usage. This can be considered as a good value given the amount of code that is executed in that routine.

This chapter shall only point out the most important aspects and direct the reader to proper resources. A very good resource is [43]. Other recommended documents are the ADC user guide [42], the ePWM user guide [48], the eQEP user guide [46], the device's data manual [47] as well as the device's system control/interrupt guide [49].

3.2 Data Types and Formats

The motor control application software was deployed in the so-called `IQmath`-format and used the `IQmath`-library, provided by TEXAS INSTRUMENTS, [50]. It provides highly optimized arithmetic, trigonometric and other common mathematical functions for fixed point an floating point targets.

`IQmath`	
Format	Purpose
I4Q28	angular related calculations
I8Q24	control and general calculations
I15Q17	auxiliary (increased range)
I11Q21	auxiliary (increased range)
I4Q12	modulator, ADC & debug
I1Q15	identification

Table 3.1: Overview of adopted `IQmath` formats

`IQmath`-format *interprets* a `long`-type variable as if it would be a fixed point fractional variable. An example notation is I4Q28. Then 28bits are used for the fractional portion and the numerical resolution is 2^{-28}. Three bits in this case are used for the integer part to yield a dynamic range of $\pm 2^3$. The first bit is always used as sign bit. Consequently, the format's resolution and dynamic range is always fix. The mathematical methods behind manipulating such numbers to yield correct results precisely is the content of the `IQmath`-library.

Table 3.1 reports the deployed `IQmath` formats together with their main purposes. According to [43] a resolution value of higher than I13Q19 is recommended for sensorless operation. The highlighted format of I8Q24 has reasonable high resolution while it allows to represent values in the order of 100.

---

[1]That is the interrupt service routine that comprises most of the executable code.

The 28335 would allow for `float` but the question arises if the usage of this data format is beneficial. In [43], page 181 this is answered by a 3% decrease (improvement) of execution time for a sensorless AC induction application. The cost is linking a new library and adopting linker and some source code files. A seamless switch to fixed-point only devices is also hampered as intense testing would be necessary. Based on these reasons only the `IQmath` library was used.

3.3 Program Structure and Performance

The SynRM drive system was implemented as standalone Flash application.

As it is common for cascaded control (see Figure 4.1) two interrupt service routines, Fast and Slow task were configured at intervals of $T_{fast} = 67\,\mu s$ and $T_{slow} = 6 \cdot T_{fast}$. The Fast task was linked to the `EPWM1` module and corresponding interrupt which is the master for all other `EPWMx` modules on the 28335. The Slow task was linked to `EPWM5` module and corresponding interrupt. It was enabled at the end of the 6th Fast Task's execution time. Thus, synchronization between both tasks was ensured. If this scheme was not adopted, speeds higher than 21 krpm could not be achieved. ADC measurement instant(s) were calculated every Fast Task according to the operational state, see Figure 4.4 and Figure 5.4. To trigger the ADC, `EPWM4` was, but not its interrupt as the ADC's own `SEQ1INT` has the highest priority of all available interrupts at the 28335. The device's interrupts have a "hard-wired" priority. A re-prioritization is in principle possible but quite complicated. Having explained the basic structure the following ranking can be provided from [49]:

$$\texttt{SEQ1INT} > \texttt{TZxINT} > \texttt{EPWM1INT} > \texttt{EPWM5INT} \tag{3.1}$$

where `TZxINT` is a tripzone interrupt that stops all software due to a trip state detected on the inverter.

With [42] and the setting of an acquisition window of $2\,T_{ADC}$ the following important relationship for the measurement time of N_s samples can be stated:

$$T_{ADC} = \frac{1}{12.5\,\text{MHz}} = 80\,\text{ns} \tag{3.2}$$

$$T_{meas}^{ADC}(N_s) = (1 + 1 + 1)N_s \cdot T_{ADC} + 3\,T_{ADC} + 0.4\,\mu\text{s}\,(EOC) \tag{3.3}$$

EOC stands for end-of-conversion, is implementation dependent and usually $0.4\,\mu\text{s}$ for this application. The ADC could be accelerated by clocking up T_{ADC}. On the other hand any value higher than $12.5\,\text{MHz}$ introduces non linearities according to [42].

Advice on increasing performance

The adoption of the following check-list additionally to the methods mentioned above increases the software's performance considerably:

- **inlining** every possible function. This only comes at the cost of increased code size, a fact that can be often neglected.

- **porting** every possible function **to RAM** as long as there is enough memory available. This must also be done for `IQmath` functions.

- **porting** every variable, constant and array to RAM as long as there is enough memory available.

- **usage of hardware peripherals**, e. g. avoid software timers, when hardware timers are available.

- usage of the **compiler's optimization option** at its highest level.

3.4 Applied Numerical Methods

General mathematical methods used at different stages of this thesis are described here.

3.4.1 Median Filtering

In Section 2.5 it was reasoned to oversample motor phase currents and subsequently calculate the data set's median to improve robustness against noise. The median value of three unsorted values $\{x_1, x_2, x_3\}$ can be efficiently found using

$$x_{m3} = \max\left(\ \min\left(x_1, x_2\right)\ ,\ \min\left(\max\left(x_1, x_2\right), x_3\right)\right) \tag{3.4}$$

where only four comparisons are necessary. This formula was used for current measurement when the motor was operated with a two-active (symmetric) PWM pattern, see Section 4.2.

When calculating current slope values out of two measured current values such as shown in Figure 5.4, the inverter's noise levels were still to high if Equation (3.4) was used. The reason for this is given by the differentiating character of the operation. The expansion to a median value calculation out of four conversions showed satisfying results. Execution time is very critical for these calculations as they directly influence the measurement time frame. A nifty way to find the median *value* (not index!) of an unsorted array of four elements $\{x_1, x_2, x_3, x_4\}$ is to iterate the array once. Thereby the total sum is calculated $\Sigma_{xi} = x_1 + x_2 + x_3 + x_4$ and the minimum and maximum values are determined as x_{min} and x_{max}. After the sweep the array is still unsorted. But when minimum and maximum values are subtracted from the total sum, the sum of the two middle elements is obtained because $\Sigma_{xi} = x_{min} + x_{m-} + x_{m+} + x_{max}$. This term is then twice the array's median, since this is precisely the definition of an even numbered array's median value:

$$x_{m4} = \frac{x_{m-} + x_{m+}}{2} = \frac{\Sigma_{xi} - x_{min} - x_{max}}{2} \tag{3.5}$$

Using this approach saves computation time to sort the array. Only the median value is of interest, not the element's order. Six comparisons are needed to find the arrays min./max values.

3.4.2 Solving Initial Value Problems

Initial value problems (IVP) of the form

$$\frac{\mathrm{d}x}{\mathrm{d}t} = f\left(x, u, t\right) \quad x\left(t_0\right) = 0, \quad u\left(t_0\right) = 0 \tag{3.6}$$

can be conveniently solved using numerical methods such as the (explicit) Forward Euler algorithm given by:

$$x_{k+1} = x_k + h\,f\left(x_k, u_k, k\,h\right)\ .\tag{3.7}$$

The quantity h is called step-size and corresponds to a sample time $T_s = T_{fast}$ in the scope of this thesis. Local truncation, order and numerical stability increase with smaller step-sizes, viz. higher sampling frequencies. This is especially true for this presented algorithm.

3.4.3 Low-Pass Filtering

A first-order low-pass filter depicted in Figure 3.2 comprised of a resistor R and a capacitor C, input voltage u_x and output voltage u_y is considered. Its differential equation is given by

$$u_x = RC\frac{\mathrm{d}u_y}{\mathrm{d}t} + u_y\ .\tag{3.8}$$

Application of Equation (3.7) and rearranging yields

Figure 3.2: A simple RC low-pass filter

$$u_{y_k} = \left(\frac{\tau}{\tau + T_s}\right)u_{y_{k-1}} + \left(\frac{T_s}{\tau + T_s}\right)u_{x_k}\ ,\tag{3.9}$$

With $\tau = RC$. By Equation (3.9) the Exponential Moving Average (EMA) algorithm with (input, output) $\mapsto (y_k, x_k)$

$$y_k = \alpha y_{k-1} + (1 - \alpha)\,x_k\tag{3.10}$$

is resembled and proven to be a very good computational approximation of first-order low-pass filtering. The time constant τ translates to the filter coefficient α as

$$\alpha = \frac{\tau}{\tau + T_s}\tag{3.11}$$

and is dependent of the specific sample time of the routine executing the EMA algorithm.

4 Field-Oriented Control

This chapter describes the field oriented control (FOC) of Synchronous Reluctance Machines utilizing rotary encoders as source for position information. The subject matter covered here serves as foundation for the implementation of sensorless FOC, covered in the next Chapter 5.

The system's final configuration is discussed in Section 4.1. There, Figure 4.1 gives a comprehensive overview of all subsystems that will be described in subsequent sections of this chapter as well as in Chapter 5.

A voltage source inverter is used to actuate the SynRM, see Section 2.5. The process to realize a calculated reference voltage space vector $\underline{u}_{\alpha\beta}^r$ with this device is covered in Section 4.2. A crucial relationship between inverter & DSC parameters, measurement agenda and maximum possible reference voltage space vector are also derived there.

A clarification of the system development steps' chronological order is necessary at this point. As a general rule, all plots in this chapter are captured using the final system configuration as described in the corresponding sections with parameters summarized in Section 4.8. In a first development step machine parameters from simulation[1] were used to design feedback/feedforward[2] current controllers and the Luenberger observer described in Section 4.3. Then, a feedback PI speed controller was obtained by careful manual tuning. Subsequently the identification process described in Section 4.6 was carried out.

The results, reported in Table 4.3, were then used in a second development iteration to obtain improved two-degree-of-freedom current controllers (Section 4.4), a more accurate Luenberger observer (Section 4.3) and a design-based speed controller (Section 4.5). Eventually flux weakening methods were investigated and implemented as described in Section 4.7. The system "as-is" was pushed to its limits (electrical/mechanical/computational). These limits are documented in Section 4.7.6.

4.1 Control Structure Overview

In Figure 4.1 a complete system overview is provided to the reader that refines the initial system overview given in Figure 2.1. The adoption of cascaded control[3] is common for variable speed drive (VSD) applications such as the system of this thesis. Visible in the top left of the figure: An inner loop executes a torque command given in the form of $\underline{i}_{dq}^r$ by the outer loop, which is in turn calculated based up the machine's torque equation (see Equation (2.70) and Section 4.5.3). Current control is established by calculating a desired voltage space vector $\underline{u}_{dq}^r$ that consists of a

---

[1] cf. Table 2.5

[2] In control theory this combination of feedforward & feedback branch is also called two-degree-of-freedom control.

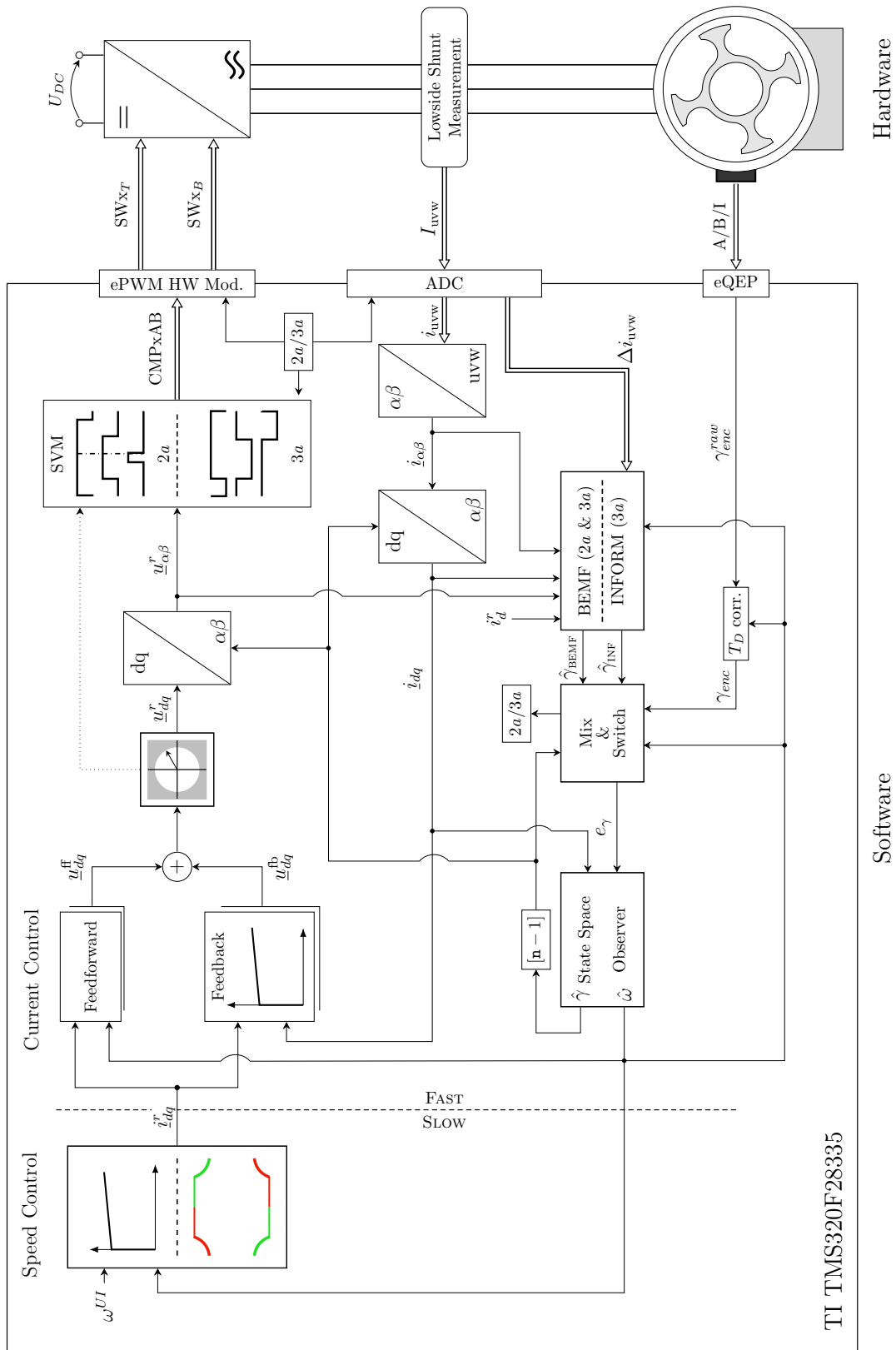[3] Therefore for the sample times $\frac{T_{slow}}{T_{fast}} \geq 6$ is mandatory.

Figure 4.1: Complete system overview

feedforward and a feedback portion, see Section 4.4. The dq-reference frame is used for current control using the Clarke/Park transformation with the electrical d-axis angle $\hat{\gamma}$, calculated from the dead-time corrected[4] γ_{enc}.

The interface between Software and Hardware is given by the register banks of the ePWM, ADC and eQEP peripheral modules of the TI-28335. These registers and relevant firmware need to be configured according to the needs of the target (inverter & DSC) *and* application (sensor-based and sensorless SynRM VSD). Therefore, they are reasoned as *application and target dependent* blocks, whereas each block on the right side of those three blocks is only *application dependent*. TU Wien has invested great effort to separate these blocks using a modular software paradigm. The author's contribution in this scope was the debugging, testing and improvement of the *application/target dependent* blocks as well as the creation of the complete "left side" of Figure 4.1.

In the scope of this chapter the Mix & Switch block has to be considered as a through-connection. Also, only two active ($2a$) space vector modulation is used. The three active method ($3a$) is used for the INFORM method and both topics are covered in Chapter 5[5], together with the BEMF method for high rotational speeds.

The right side of this detailed overview (Hardware) was already described in Chapter 2. Switching signals calculated by a software modulator are used to configure the DSC's ePWM registers to subsequently provide switching (voltage) commands for the half bridges MOSFET gate drivers. At the VSI an unipolar DC-Link voltage U_{DC} is converted into a three phase AC voltage through the execution of these switching commands, the SynRM is actuated with the desired $\underline{u}^r_{\alpha\beta}$. This process is covered in detail in the next section.

4.2 Space Vector Modulation

The usage of a two level voltage source inverter as discussed in Section 2.5 allows to apply six non-zero and two zero voltage space vectors to the SynRM. Depending on the top switch states the applied scaled voltage space vector results in

$$\underline{u}_{\{\text{SW}^U_T,\text{SW}^V_T,\text{SW}^W_T\}} = \{\text{SW}^U_T\} + \{\text{SW}^V_T\}\text{e}^{\text{j}\frac{2\pi}{3}} + \{\text{SW}^W_T\}\text{e}^{\text{j}\frac{4\pi}{3}} \ . \tag{4.1}$$

Table 2.6 lists all valid combinations. Figure 4.2 gives an overview of possible combinations in the $(\alpha\beta)$-plane.

In principle a synchronous machine can be operated using these vectors only. This is referred to as block commutation (of a brushless DC motor) [21], [17], [51]. In this thesis however arbitrary reference voltage space vectors calculated by current controllers $\underline{u}^r_{dq}$ shall be realized in the machine's airgap, see Section 2.3. Then, advantages for sensorless operation and a reduced torque ripple can be expected. This operation mode is designated as *sinusoidal commutation* or *continuous field operation*. It requires a dedicated subsystem (the modulator) that superimposes the eight available voltage space vectors to realize the control command $\underline{u}^r_{dq}$ as an average

---

[4]cf. Section 2.6

[5]The reader is also referred to Figure 5.1. Generally speaking such a system can be classified as *switched system* in a control theoretical context.
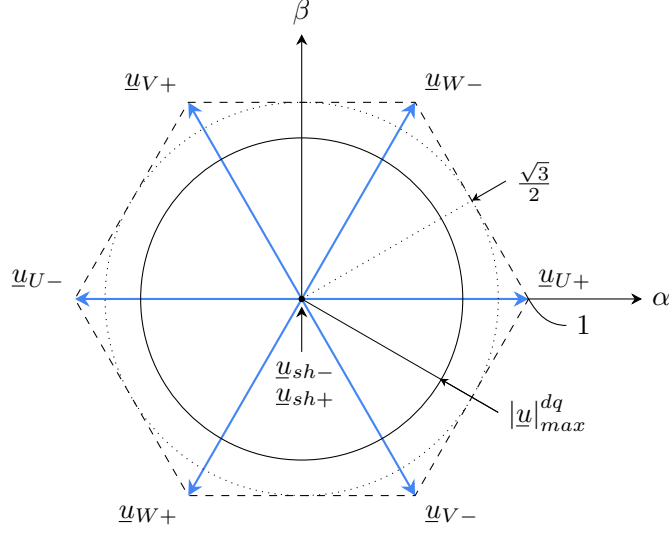
Figure 4.2: Available inverter voltage space vectors for 2-active SVM;
            Maximum orbits theoretical and practical

value. As depicted in Figure 4.1 the modulator's input is $\underline{u}^r_{\alpha\beta}$ calculated by the inverse park transformation of $\underline{u}^r_{dq}$.

This section summarizes the modulation process known as *space vector modulation* (SVM) or *symmetric PWM* from literature such as [16] in Section 4.2.1. Then controller output restriction, modulator and ADC agenda are coordinated to harness the system's full voltage potential in its given configuration. More voltage reserves are always beneficial for current controllers (Section 4.4) and flux weakening operation (Section 4.7).

4.2.1 Principle of Operation

First the sector in the $(\alpha\beta)$-plane of $\underline{u}^r_{\alpha\beta}$ is determined. It is defined by a clockwise and a counter-clockwise neighbor of realizable voltage space vectors. Inspection of Figure 4.2 shows that there are six possible sectors as a hexagon is established by all six active voltage space vectors.

Once the two neighbours are determined an auxiliary coordinate system $(\xi\eta)$ is introduced having the ξ axis coincided with the *clockwise* neighbour. A transformation of the reference voltage space vector to this coordinate system is carried out using

$$\underline{u}^r_{\xi\eta} = \underline{u}^r_{\alpha\beta}\,\mathrm{e}^{-\mathrm{j}\varphi_\xi}\;, \tag{4.2}$$

with φ_ξ being the ξ axis angle in $(\alpha\beta)$ coordinates. The idea of SVM is to superimpose found neighbors and lower/upper short vectors $\underline{u}_{sh+}, \underline{u}_{sh-}$ for T_{PWM} to obtain $\underline{u}^r_{\alpha\beta}$ *on average*. Therefore *two active* space vectors are used in every case and this term together with the abbreviation (2*a*) will be used frequently throughout this thesis. An expedient variant of SVM that minimizes needed switching actions is the so called symmetric PWM. First the calculation is carried out for $T_{PWM}/2$ before the resulting patterns are mirrored around this point[6] for the next PWM

---

[6]In [16] this is called *pulse centering*

actuation period. Starting point is the complex superposition equation:

$$\frac{T_{PWM}}{2} \underline{u}^r_{\xi\eta} \overset{!}{=} T_\xi \underline{u}_\xi + T_\eta \underline{u}_\eta + T_{sh} \cdot 0 \ , \tag{4.3}$$

with T_ξ, T_η and T_{sh} being the respective "on" times of the incorporated space vectors. These variable quantities carry the modulation information and need to be determined. Equation (4.3) is rewritten in Cartesian coordinates together with the above definitions:

$$\frac{T_{PWM}}{2} \left(u^r_\xi + \mathrm{j}u^r_\eta \right) = T_\xi \cdot 1 + T_\eta \left(\frac{1}{2} + \mathrm{j}\frac{\sqrt{3}}{2} \right) \ , \tag{4.4}$$

$$\frac{T_{PWM}}{2} = T_\xi + T_\eta + T_{sh} \ . \tag{4.5}$$

Above relations form a linear system of three equations and three unknowns. The solution is:

$$t_\eta = \frac{T_\eta}{T_{PWM}/2} = \frac{2}{\sqrt{3}} u^r_\eta \tag{4.6}$$

$$t_\xi = \frac{T_\xi}{T_{PWM}/2} = u^r_\xi - \frac{1}{\sqrt{3}} u^r_\eta \tag{4.7}$$

$$1 = t_\eta + t_\xi + t_{sh} \tag{4.8}$$

with $t_{sh} = \frac{T_{sh}}{T_{PWM}/2}$. These normalized space vector "on" times are related to normalized phase "on" times using the prior determined sector information. They are doubled by applying them around the center of a PWM period. This is depicted in the top half of Figure 4.3 (single phase top & bottom switching commands) and the top half of Figure 4.4 (three phase top switching commands). To realize calculated "on" times a translation into compare values is necessary. These values are written to the so called compare registers of the ePWM module and eventually appear as voltage pattern at the DSC's output pins[7]. A thorough consultation of the DSC's ePWM documentation [48] is recommended. The so called "Up-Count" mode for the ePWM counting unit should be adopted as it ensures compatibility with the second space vector modulation method covered in Section 5.2.3.

4.2.2 Constraints and Optimization

In this section control software, modulator output and ADC subsystem are coordinated to achieve the highest possible performance in the given system configuration. The following design targets are specified:

$\mathcal{A}$: minimize control related dead time effects and measurement time

$\mathcal{B}$: maximize voltage space vector in sinusoidal commutation operation

$\mathcal{C}$: find a relationship/trade-off between $\mathcal{A}$ and $\mathcal{B}$; choose the best suited values

---

[7]cf. Figure B.4, `EPWM1A, EPWM1B` for top and bottom switches of Phase U. These signals are routed to the gate drivers of the inverter. Said gate drivers electrically control the power MOSFETs to realize calculated switching commands.

Design Target $\mathcal{A}$

To minimize time-discrete control related[8] dead time effects, the time instants of current measurement and encoder based angular measurement should be placed as close as possible to each other. As depicted in Figure 4.3 motor phase currents are therefore measured at the end of a FAST Task #[n] and the encoder is read out at the beginning of FAST Task #[n+1]. Otherwise a control dead time of $T_{fast} = 67\,\mu\text{s}$ would degrade the system's performance and introduce instabilities at high velocities.

Figure 4.3 also defines the quantity of a compulsory pulse width in two active operation T_{PW}^{2a}. It relates to a time frame where the ideal bottom switching signal SW_B is on/high *at the end of the PWM period*. Due to the usage of low-side shunt current measurement and the need to minimize control dead time this is the only relevant time frame to for current measurement. In its final configuration the ADC is set up to measure the following quantities at measurement task I: $\{U_{DC}, U_{top}^{temp}, U_{bottom}^{temp}, I_U, I_V, I_U, I_V, I_U, I_V\}$. According to Equation (3.3) the needed measurement time frame is then $T_{meas}^{ADC}(9) = 2.8\,\mu\text{s}$. The green line in Figure 4.3 refers to this time frame. The time portion of $T_{meas}^{ADC}(9)$ needed to measure currents only and process the result (end of conversion) is $2.08\,\mu\text{s}$[9]. As discussed in Section 2.5 three current instants per phase are measured and median-filtered to counter inverter noise effects. The "best" two phases in terms of gain error where picked. The third current is obtained as $I_W = -I_U - I_V$ (Kirchhoff's rule).

An important property of semiconductor power switching devices is their different switch-on time (shorter) vs. switch-off time (longer). In the power MOSFET's data sheet [52] the difference for an example case is reported to be roughly $100\,\text{ns}$. This may seem negligible first, but this fault state would occur fifteen thousand times each second for each half bridge and would eventually damage the device irreversible. Consequently counter measures need to be adopted such as a shift of the ideal PWM patterns as depicted in Figure 4.3. This is done by configuring the ePWM module of the 28335 DSC. A parameter value of $T_{DB} = 1.25\,\mu\text{s}$ was chosen for both defined delays RED and FED.

The described modulation and measurement process is commonly known as *single reference PWM update with single measurement*, as the PWM pattern is adjusted once per T_{PWM}. To recap: It was calculated by mirroring the space vector modulation pattern for $T_{PWM}/2$ by Equation (4.6)-Equation (4.8).

Design Target $\mathcal{B}$

The above section and Figure 4.3 related ADC and inverter parameters to T_{PW}^{2a}. This quantity "results" from the calculation of space vector modulation pulse patterns. Generally speaking, voltage space vectors of higher magnitude will result in reduced T_{PW}^{2a} while lower magnitude voltage space vectors allow for an increased T_{PW}^{2a}. At $|\underline{u}_{\alpha\beta}^r| = \frac{\sqrt{3}}{2}$, viz. maximum possible amplitude for sinusoidal commutation $T_{PW}^{2a} = 0$. By comparing Equation (4.6)-Equation (4.8)

---

[8]These are effects of the same type as encoder related dead time effects, discussed in Section 2.6 but from the source of current measurement.

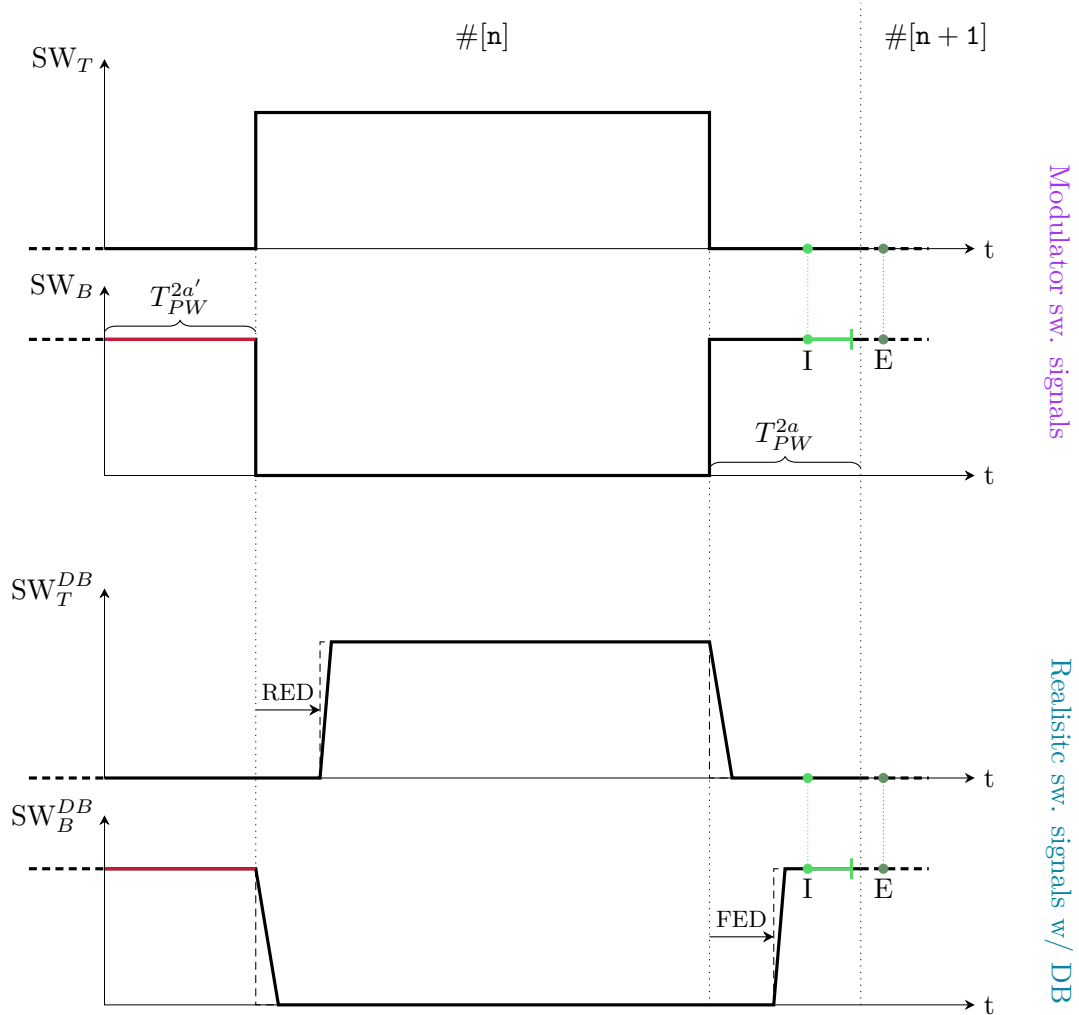[9]$3 \cdot 6\,T_{ADC} + 3\,T_{ADC} + 0.4\mu\text{s}\,(EOC)$

Figure 4.3: Single phase top and bottom switching signals: idealized (upper half) and realistic (lower half) trends; Strategy to place current measurement task I as close to encoder readout E as possible; Definition of compulsory pulse width in two active operation T_{PW}^{2a}; Definition of Rising Edge Delay (RED) and Falling Edge Delay (FED) to realize a Dead Band (DB) for shoot through prevention; Finite switch-on (shorter) and switch-off (longer) times for semiconductor power switching devices; Exaggerated illustration for didactic reasons; Analogue interface time constant not depicted; The quantity $T_{PW}^{2a'}$ (red time frame) here is equal to T_{PW}^{2a}, see section: "Design Target $\mathcal{C}$".

with Figure 4.3 it can be deducted that

$$T_{PW}^{2a} = \frac{t_{sh}}{2}\frac{T_{PWM}}{2} \ . \tag{4.9}$$

The final goal in this scope is to restrict the modulators output value[10] $|\underline{u}^r|$ just as much as needed to ensure a user specified T_{PW}^{2a}, while aiming for a value as high as possible.

This section quantifies the relationship between t_{sh} and $|\underline{u}^r|$. Thereto, a constrained optimization problem is formulated and solved. As objective function the squared absolute value of the reference voltage space vector $\underline{u}^r$ will be used. Manipulation of Equation (4.6) and Equation (4.7) leads to

$$u_\eta^r = \frac{\sqrt{3}}{2}t_\eta \ , \tag{4.10}$$

$$u_\xi^r = t_\xi + \frac{1}{2}t_\eta \ . \tag{4.11}$$

Calculating the scaled magnitude yields

$$(|\underline{u}^r|)^2 = |\left(u_\xi^r\right)^2 + (u_\eta^r)^2|^2 \tag{4.12}$$

$$= t_\xi^2 + t_\xi t_\eta + t_\eta^2 \tag{4.13}$$

$$= f_u^{2a}\left(t_\xi, t_\eta\right) \ . \tag{4.14}$$

A constrained optimization problem can be formulated using the substitution $\mathbf{t} = [t_\xi, t_\eta]^T$,

$$\begin{aligned} \underset{\{t_\xi, t_\eta\}}{\text{maximize}} \quad & f_u^{2a}\left(t_\xi, t_\eta\right) \\ \text{subject to} \quad & g\left(\mathbf{t}\right) = t_\xi + t_\eta + t_{sh} - 1 = 0 \\ & t_\xi \geq 0 \\ & t_\eta \geq 0 \end{aligned} \tag{4.15}$$

A common strategy to solve problems of this type is to set the inequality constraints inactive, solve the problem and check if the solution fulfills all constraints. For Equation (4.15) this means that only $g\left(\mathbf{t}\right) = 0$ is set active. To solve this reformulated problem an approach with an expanded objective function of the form

$$L\left(\mathbf{t}, \lambda\right) = f_u^{2a}\left(\mathbf{t}\right) + \lambda g\left(\mathbf{t}\right) \tag{4.16}$$

is used. The quantities $L\left(\mathbf{t}, \lambda\right)$ and λ are called Lagrangian- function and multiplier. According to [53] necessary conditions for optimality of Equation (4.16) are given by

$$\left(\frac{\partial}{\partial \mathbf{t}}L\right)^T\left(\mathbf{t}^*, \lambda^*\right) = \left(\nabla f_u^{2a}\right)\left(\mathbf{t}^*\right) + \left(\nabla g\right)\left(\mathbf{t}^*\right)\lambda^* \overset{!}{=} \mathbf{0} \tag{4.17}$$

$$\left(\frac{\partial}{\partial \lambda}L\right)^T\left(\mathbf{t}^*, \lambda^*\right) = g\left(\mathbf{t}^*\right) \overset{!}{=} 0 \tag{4.18}$$

---

[10] $|\underline{u}^r|$ corresponds to the current controllers output $|\underline{u}|_{max}^{\alpha\beta} = |\underline{u}|_{max}^{dq}$.

where the operator ∇ in this context is read as $\left(\frac{\partial}{\partial t_\xi}, \frac{\partial}{\partial t_\eta} \right)^T$. A symbolic solution of equations (4.17) and (4.18) is found as

$$\mathbf{t}^* = \begin{bmatrix} 0.5 - 0.5\,t_{sh} \\ 0.5 - 0.5\,t_{sh} \end{bmatrix} \tag{4.19}$$

$$\lambda^* = \frac{3}{2}\,(1 - t_{sh}) \tag{4.20}$$

Relating the solution given by Equation (4.19) to the original problem given by Equation (4.15) results in the trivial condition $t_{sh} < 1$. Above solution is substituted into the objective function of Equation (4.16):

$$f_u^{2a}\left(\mathbf{t}^*, t_{sh}\right) = \left(|\underline{u}|_{max}^{dq}\right)^2 = 3\left(\frac{1}{2} - \frac{1}{2}t_{sh}\right)^2 \tag{4.21}$$

Taking the square root results in the targeted relationship between short time and maximum space vector magnitude

$$|\underline{u}|_{max}^{dq} = \frac{\sqrt{3}}{2}\,(1 - t_{sh}) \tag{4.22}$$

It is emphasized that this relationship together with Equation (4.9) is true for *a half PWM period*. As calculated patterns are mirrored around $T_{PWM}/2$, see above. It is independent of the current space vectors modulation's sector.

Design Target $\mathcal{C}$

In principle Equation (4.22) gives a valid restriction strategy to ensure T_{PW}^{2a} at the end of the PWM cycle. However there is a way to exploit the paradigm of *single reference update* to boost the output voltage considerably that will be shown here. Eventually a "time-budget" of T_{PW}^{2a} will be formulated that integrates and refines above modeled effects of ADC measurement agenda T_{meas}^{ADC} and mandatory dead band T_{DB}.

When Equation (4.22) is used together with Equation (4.9) not only the desired time frame for ADC measurement T_{PW}^{2a} is ensured, but also a time frame of $T_{PW}^{2a'}$ as depicted by the red line in Figure 4.3. This time frame is of no use for measurement purposes due to dead time effects, explained earlier.

The quantity t_{sh} represents both, upper short state and lower short state, where only the latter state is of interest for the application. By a shift of the mirrored symmetric PWM pattern half of this quantity can be (semantically) "transferred" to the end of PWM. Then the upper short state (all top switches on) will occur only in the first half of[11] T_{PWM}. Conveniently the lower short state time frame is then occurring only[12] at the end of T_{PWM} where measurement occurs. The reference voltage space vector's value is maintained as the whole pattern is shifted within bounds of T_{PWM} (viz. the mean value is not affected by this process). The process is clarified in

---

[11]When current controllers demand the maximum allowed possible voltage space vector using this configuration.
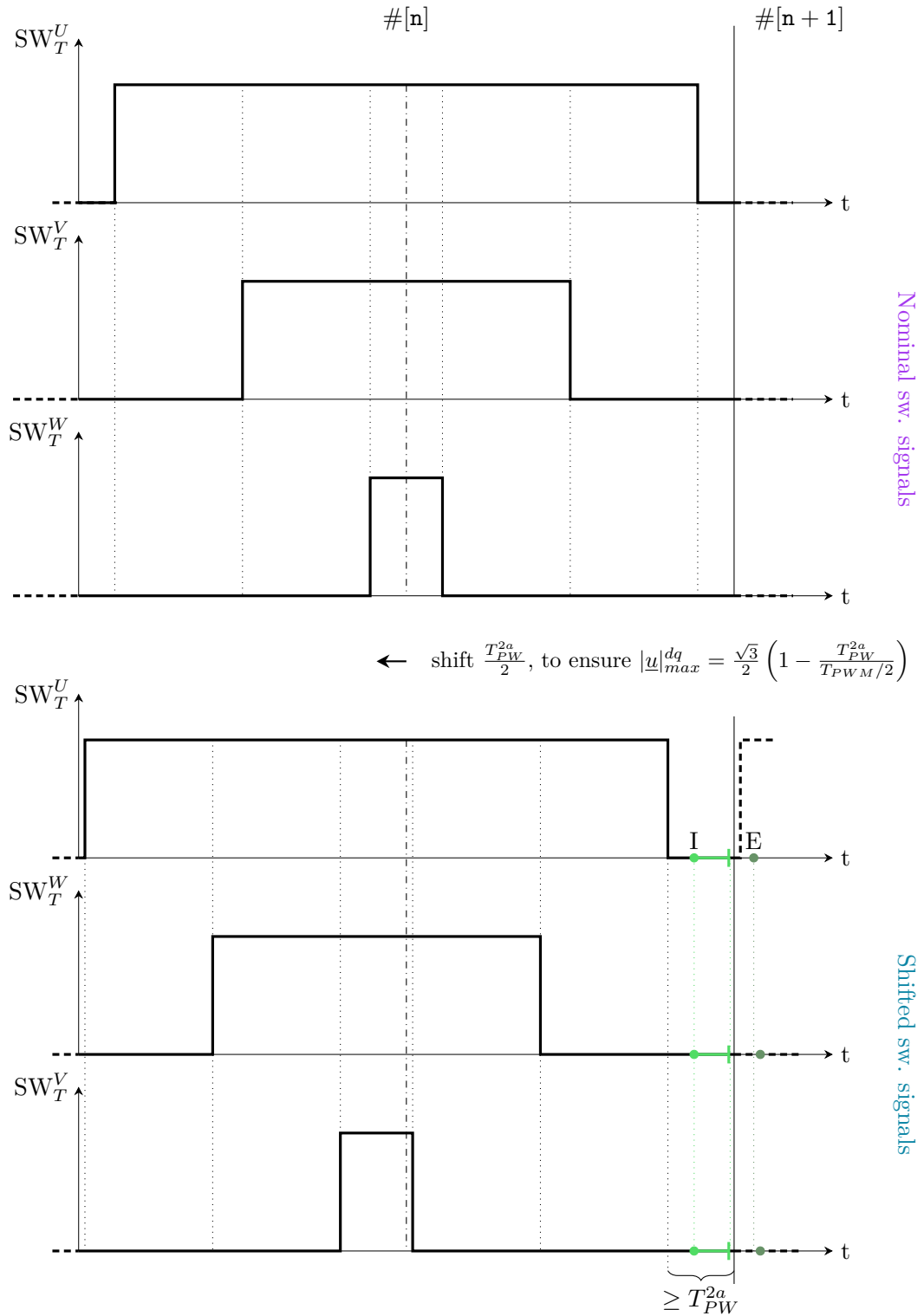[12]see above footnote

Figure 4.4: Two active space vector modulation switching commands: nominal & shifted for $\underline{u}^r_{\alpha\beta} = 0.675\mathrm{e}^{\mathrm{j}30^\circ_{el}}$; Measurement agenda (I) and encoder readout (E); By a shift as indicated the lower-short time frame at the beginning of `#[n]` so traded with the upper-short time frame at the beginning of the second half of `#[n]` and results into the desired amount of T^{2a}_{PW} at the end of `#[n]`; The reference space vector is not affected by this operation as all signal trends are shifted.

Figure 4.4. The shift parameter is ideally $\frac{T_{PW}^{2a}}{2}$ but was chosen slightly smaller for safety reasons. Given this shift operation applied, the following relationship is true:

$$|\underline{u}|_{max}^{dq} = \frac{\sqrt{3}}{2}\left(1 - \frac{T_{PW}^{2a}}{T_{PWM}/2}\right) \tag{4.23}$$

Without shifting $|\underline{u}|_{max}^{dq}$ would decrease considerable as $2 \cdot T_{PW}^{2a}$ would need to be used in Equation (4.23). The formula is not restricted to this specific application.

It can be used for any implementation of field-oriented control where 2-active modulation with single reference updating is implemented.

Application specific aspects become apparent when a time budget for T_{PW}^{2a} is formulated. For the SynRM operated in two-active mode, it is modeled as follows:

- A dead band time of $T_{DB} = 1.25\,\mu s$ has to be maintained as mentioned above.

- Following the signal path of the PWM outputs at the DSC's pins on Figure B.4 the signals are routed through a line driver for safety reasons before the are applied to the gate drivers. The switching commands are then translated into gate currents that let the power MOSFETs switch the motor phases to their respective potentials $(+)$ or $(-)$ in Figure 2.8. Consulting the respective device's data sheets for transition and turn-on times led to a parameter choice of $T_{1/0}^{\Sigma} = 0.15\,\mu s$ for this process.

- From the ADCs analogue measurement interface's perspective the output *starts* to adopt a final value that is proportional to the motor phase's current. The process is described in Section 2.5 and modeled by a first order time constant $\tau_{an} = 1\,\mu s$. The choice of a mandatory "wait duration" here is critical for the maximum possible output voltage as it consumes most of the time. A duration of five time constants would be an ideal choice, but this would yield in a rather low maximum possible output voltage. Considering the current measurement strategy with median filtering and the presence of inverter noise a value of 2.5 time constants[13], viz. $T_{2.5\tau_{an}} = 2.5\,\mu s$, was deemed to be sufficient. Intensive testing confirmed this choice.

- The ADC start of conversion point I in Figure 4.4 is placed such that current measurement values are converted after $T_{DB} + T_{1/0}^{\Sigma} + T_{2.5\tau_{an}}$. This means that DC-link voltages and temperature proportional voltages are already measured during $T_{2.5\tau_{an}}$. For the time budget of the compulsory pulse window time T_{PW}^{2a} this means that an additional time frame of $T_{ADC}^{meas}(6) = 2.08\,\mu s$ needs to be ensured, see Equation (3.2).

Consequently the two active compulsory time width budget and shift value are chosen as

$$T_{PW}^{2a} = T_{DB} + T_{1/0}^{\Sigma} + T_{2.5\tau_{an}} + T_{ADC}^{meas}(6) \tag{4.24}$$

$$= 1.25\,\mu s + 0.15\,\mu s + 2.5\,\mu s + 2.08\,\mu s = 5.98\,\mu s \tag{4.25}$$

$$T_{shift}^{2a} \leq \frac{T_{PW}^{2a}}{2} = 2.99\,\mu s \tag{4.26}$$

---

[13]$1 - e^{-2.5} \approx 92\%$

Using the value of 5.98 µs in Equation (4.23) leads to a maximum possible output voltage of (rounded down)

$$|\underline{u}|^{dq}_{max} = 0.71 \qquad (4.27)$$

such that this specified pulse window time is ensured. Without application of a shift the value of $2\,T^{2a}_{PW}$ must be used in Equation (4.23). This would result in a maximum possible reference voltage of ≈ 0.557, a significant decrease.

Equation (4.23) also applies when using transducers to measure motor phase currents at arbitrary time instants within T_{PWM}. The parameter T^{2a}_{PW} then represents a mandatory bootstrap time to operate the gate drivers properly. The above process can be further optimized in future work when the phases used for low-side shunt measurements are adapted to the active sector from space vector modulation's algorithm. That would mean using Phase V and Phase W (rather than Phase U and Phase V) in the case depicted in Figure 4.4.

In principle T^{2a}_{PW} can be further decreased by taking less phase current samples or increasing the ADC sampling frequency to a value higher than the configured 12.5 MHz. According to [42] the latter would introduce non-linearities in the measurement chain that would need a separate compensation. The former strategy to sample less values is not feasible for this particular inverter due to relative high noise levels, see Section 2.5. Another possibility would be to increase T_{PWM} as it occurs in the denominator of Equation (4.23). Such a reduction of the control system's sampling frequency is on the other hand not beneficial for high shaft speeds (corresponding to electric frequencies of the voltage space vector). See also the discussion in Section 4.7.6.

Another idea to increase the maximum possible voltage reference space vector is to decrease all upper short states and increase the lower short states accordingly. The relation of Equation (4.8) does not restrict the realization of t_{sh} to an upper short state or to a lower short state. Nevertheless, a minimum time duration for the upper short state is mandatory to ensure constant f_{PWM}.

All in all a considerable amount of time was spent in deriving and modeling Equation (4.23) as well as testing it with above given parameters. *This detailed description also emphasizes the ultimate trade-off between measurement time and control output magnitude for this system.* The resulting value of $|\underline{u}|^{dq}_{max} = 0.71$ proved to be a keystone in order to reach high rotational speeds through the use of flux weakening strategies (sensored and sensorless).

4.3 Angular Position Processing - Observer

A dedicated observer subsystem is needed due to two reasons: First, a shaft *position* rather than a shaft speed is measured, so the estimation of shaft speed $\omega \to \hat{\omega}$ is necessary to establish speed control, cf. Section 4.5. Second, estimated shaft positions from sensorless models covered in Chapter 5 need to be smoothed. If a raw estimated shaft angle is taken for FOC, the system may become unstable.

In this thesis a full order Luenberger observer is used. From the mechanical subsystem equations, an equivalent LTI discrete time system is calculated offline. The observer is then designed using the method of *pole placement* within the discrete time domain.

Electrical angle and electrical shaft speed will be processed. Therefore, the mechanical equations (2.82) and (2.83) are rewritten[14] to represent these quantities. As measured quantity the calibrated encoder angle in I4Q28 format γ_{enc} is taken, see Section 2.6. Therefore, the complete observer subsystem was implemented in I4Q28 data format. The load torque t_L is rewritten as $t_l := \frac{t_L}{T_M}$ and considered to be unknown but constant. This leads to the following set of equations:

$$\frac{\mathrm{d}}{\mathrm{d}t}\gamma_{enc} = \frac{8}{\pi}\frac{1}{T_B}\omega \tag{4.28}$$

$$\frac{\mathrm{d}}{\mathrm{d}t}\omega = \frac{l_d - l_q}{p \cdot T_M}i_d i_q - t_l \tag{4.29}$$

$$\frac{\mathrm{d}}{\mathrm{d}t}t_l = 0 \tag{4.30}$$

As inductances, results from simulations in Section 2.4.5 were taken for the initial design. After identification (covered in Section 4.6) the observer was redesigned using new values. The above equations resemble a LTI-SISO[15] system in state space representation [54]:

$$\dot{\mathbf{x}} = \mathbf{A}\mathbf{x} + \mathbf{b}u \qquad \mathbf{x}(t_0) = \mathbf{0} \tag{4.31}$$

$$y = \mathbf{c}^T\mathbf{x} \tag{4.32}$$

with the state $\mathbf{x} := [\gamma_{enc}, \omega, t_l]^T$ and the measured plant output $y := \gamma_{enc}$. The plant input here is defined as $u := i_d i_q$. Two important remarks: First, lower case letter symbols u and u_k are widely used as input quantity symbols in control theory. To stay consistent with common literature the same letter is also adopted here. The reader is advised not to confuse it with a voltage quantity (for which variants of the letter "u" are used in all other sections except this one and Section 4.4.4). Second, from the observer's perspective $i_d i_q$ is an external (non-controllable) input. The currents are not states in this scope. Thus, linear theory holds. A zero-order-hold (ZOH) equivalent discrete time system of Equation (4.31) is obtained by using the matrix exponential:

$$\mathbf{\Phi} \;=\; \exp\left(\mathbf{A}T_s\right) \tag{4.33}$$

$$\mathbf{\Gamma} \;=\; \int_0^{T_s} \exp\left(\mathbf{A}\tau\right)\mathbf{b}\,\mathrm{d}\tau \tag{4.34}$$

to yield

$$\mathbf{x}_{k+1} = \mathbf{\Phi}\mathbf{x}_k + \mathbf{\Gamma}u_k, \qquad \mathbf{x}(0) = \mathbf{0} \tag{4.35}$$

$$y_k = \mathbf{c}^T\mathbf{x}_k \tag{4.36}$$

Convenient numerical values for the matrix $\mathbf{\Phi}$ and input vector $\mathbf{\Gamma}$ are obtained by choosing the time's base value T_B in relation to the sample time $T_s = T_{fast}$, see Section 2.2. The full order Luenbeger observer structure is given by

$$\hat{\mathbf{x}}_{k+1} = \mathbf{\Phi}\hat{\mathbf{x}}_k + \mathbf{\Gamma}u_k + \hat{\mathbf{k}}_{\mathbf{L}}\left(\hat{y}_k - y_k\right), \qquad \hat{\mathbf{x}}(0) = 0 \tag{4.37}$$

$$\hat{y}_k = \mathbf{c}^T\hat{\mathbf{x}}_k \tag{4.38}$$

---

[14] $\gamma_m = p \cdot \gamma_e \mathbin{\widehat{=}} p \cdot \gamma_{enc}$; $\omega \to p \cdot \omega$ (use of a different base value)
[15] <u>S</u>ingle <u>I</u>nput <u>S</u>ingle <u>O</u>utput

where a feedback of estimated output $\hat{y}_k$ and measured output $y_k := \gamma_{enc}$ by means of an error weight vector $\hat{\mathbf{k}}_\mathbf{L} = [k_{L\gamma}, k_{L\omega}, k_{Lt}]^T$ is used to correct the state estimation. This allows to influence the closed loop dynamics (eigenvalues) of the estimation's error system $\mathbf{e}_k := \hat{\mathbf{x}}_k - \mathbf{x}_k$, given by

$$\mathbf{e}_{k+1} = \underbrace{\left(\mathbf{\Phi} + \hat{\mathbf{k}}_\mathbf{L}\mathbf{c}^T\right)}_{\mathbf{\Phi}_e}\mathbf{e}_k, \qquad \mathbf{e}(0) = \mathbf{e}_0 = \hat{\mathbf{x}}_0 - \mathbf{x}_0 \tag{4.39}$$

Additionally an initial estimation error $\mathbf{e}_0$ can be compensated. The error weight vector $\hat{\mathbf{k}}_\mathbf{L}$ is calculated using Ackermann's formula[16] for state space observers. Prerequisite to this is $\text{rank}\{\mathcal{O}\left(\mathbf{c}^T, \mathbf{\Phi}\right)\} \overset{!}{=} 3$. That means, the systems observability matrix has to be invertible. This is true for the above derived system. Then the process is to calculate an auxiliary quantity $\hat{\mathbf{v}}_1$ using

$$\underbrace{\begin{pmatrix} 0 \\ 0 \\ \vdots \\ 1 \end{pmatrix}}_{\mathbf{e}_n} = \underbrace{\begin{pmatrix} \mathbf{c}^T \\ \mathbf{c}^T\mathbf{\Phi} \\ \vdots \\ \mathbf{c}^T\mathbf{\Phi}^{n-1} \end{pmatrix}}_{\mathcal{O}(\mathbf{c}^T, \mathbf{\Phi})} \hat{\mathbf{v}}_1, \tag{4.40}$$

and subsequently evaluate

$$\hat{\mathbf{k}}_\mathbf{L} = -\hat{p}_{c,des}\left(\mathbf{\Phi}\right)\hat{\mathbf{v}}_1. \tag{4.41}$$

to yield $\hat{\mathbf{k}}_\mathbf{L}$. Thereby, the desired characteristic polynomial of the closed loop system $\hat{p}_{c,des}$ allows (in principle) to arbitrarily choose the eigenvalues of $\mathbf{\Phi}_e$. Roots have to be placed within the unity circle for stability. Values located too close to zero will yield in relatively large coefficients of $\hat{\mathbf{k}}_\mathbf{L}$. This would amplify measurement noise and therefore is undesirable.

For the sensor-based SynRM control system the following settings were taken:

$$\underline{\lambda}_M = \text{eig}\left(\mathbf{\Phi}\right) \tag{4.42}$$

$$\underline{\mathbf{z}}_{PL} = 0.975 \cdot \underline{\lambda}_M \tag{4.43}$$

$$\hat{p}_{c,des}\left(z\right) = \left(z - \underline{\mathbf{z}}_{PL,1}\right)\left(z - \underline{\mathbf{z}}_{PL,2}\right)\left(z - \underline{\mathbf{z}}_{PL,3}\right) \tag{4.44}$$

Results for $\hat{\mathbf{k}}_\mathbf{L}$ are reported in Table 4.7. Instead of the factor 0.975 in Equation (4.43), several other parameter values were investigated. Values as low as 0.86 still yielded reasonable good results. Factors lower than that resulted in unacceptable noise levels of $\hat{\gamma}$ and $\hat{\omega}$. For sensorless operation this factor needed to be adjusted even closer to 1 to conveniently smooth estimated angle values, see Section 5.5.2.

Validity of the above design has to be ensured. This is done by calculating the closed loop error system eigenvalues:

$$\underline{\lambda}_e = \text{eig}\left(\mathbf{\Phi} + \hat{\mathbf{k}}_\mathbf{L}\mathbf{c}^T\right) \tag{4.45}$$

$$\tag{4.46}$$

---

[16]cf. [54]

The values are given as:

$$\underline{\lambda}_{e,1} = 0.9749983\cdots + \text{j}0.000002871\cdots \tag{4.47}$$

$$\underline{\lambda}_{e,2} = 0.9749983\cdots - \text{j}0.000002871\cdots \tag{4.48}$$

$$\underline{\lambda}_{e,3} = 0.9750033\cdots \tag{4.49}$$

This confirms stability of the proposed design.

Two important aspects shall be emphasized at the end of this section. First, the observer should be located within the FAST Task. This improves transient performance considerably and eases the adoption of sensorless methods. Implementation variants with SLOW Task observers performed poorly at higher speeds. Second, an off-line design using MATLAB is recommended *within the time-discrete domain* using the proposed structure of Equation (4.37). The above results suggest an increased sensitivity to a narrow numerical band for proper settings. This is confirmed in Section 5.5.2 for sensorless operation.

4.4 Inner Loop: Current Control

As depicted in Figure 4.1 current control is established by using a feedforward and a feedback branch. In control theory this is called *two degree of freedom control.* Torque commands calculated by the speed controller are translated into a reference current space vector $\underline{i}_{dq}^{r}$ using certain realization strategies, see Section 4.5. Current control then calculates a reference voltage space vector $\underline{u}_{dq}^{r}$ that is realized by the modulator, described in Section 4.2. The voltage space vector command quantities are of the form

$$u_d^r = u_d^{\text{ff}} + u_d^{\text{fb}} \tag{4.50}$$

$$u_q^r = u_q^{\text{ff}} + u_q^{\text{fb}} \tag{4.51}$$

Both subsystems (feedforward and feedback) are described in the following sections.

4.4.1 Feedback Path, Design of Decoupled Current Controllers

The feedback current controllers are designed within continuous time *s*-domain. The idea is to use well established design rules for parallel PI controllers and subsequently discretize them in Section 4.4.2. For the plant model, a *decoupled* form of the stator voltage equations[17] is adopted. These equations are given by

$$u_d\left(t\right) = r_s i_d\left(t\right) + l_d T_B \frac{\text{d}i_d\left(t\right)}{\text{d}t} \tag{4.52}$$

$$u_q\left(t\right) = r_s i_q\left(t\right) + l_q T_B \frac{\text{d}i_q\left(t\right)}{\text{d}t} \tag{4.53}$$

The missing coupling terms $-\omega l_q i_q$ and $\omega l_d i_d$ are considered as disturbances for the feedback branch. They will be taken into account within the feedforward branch that is designed in Section 4.4.4. A parallel PI controller of the form

$$C\left(s\right) = k_P^{i_d}\left(1 + \frac{1}{sT_I^{i_d}}\right) = k_P^{i_d} + \frac{k_{I_c}^{i_d}}{s} \tag{4.54}$$

---

[17]cf. Equation (2.80) and Equation (2.81)

is calculated based upon the so-called SIMC[18] rules by Sigurd Skogestad, [14]. The process is described for i_d control here. An i_q controller can be derived by repeating the outlined process with different model parameters.

First Equation (4.52) is transformed into the s-domain, assuming $i_d\left(t_0^+ = 0\right)$. A control dead time of θ is added to the frequency domain model:

$$i_d\left(s\right) = \frac{k}{1 + \tau_{id}}\,\mathrm{e}^{-\theta s}\,u_d\left(s\right) \tag{4.55}$$

with $\tau_{id} = \frac{l_d T_B}{r}$, $k = \frac{1}{r}$. The Skogestad SIMC rules aim for a closed loop response of

$$T_{id} = \frac{i_d\left(s\right)}{i_d^r\left(s\right)} = \frac{1}{1 + \tau_c s}\,\mathrm{e}^{-\theta s} \tag{4.56}$$

with τ_c as user desired closed loop time constant. The design rules are given by (see Equation (4.54)):

$$T_I^{i_d} = \min\{\tau_{id}, c\left(\tau_c + \theta\right)\} \tag{4.57}$$

$$k_P^{i_d} = \frac{1}{k}\frac{\tau_{id}}{\tau_c + \theta} \tag{4.58}$$

The standard setting of $c = 4$ as described in [14] is used and yields good reference tracking performance. Decreasing this value improves disturbance rejection but also introduces significant overshoot. For the control dead time $\theta = T_{fast}$ is modeled. The user desired closed loop response time constant is chosen as $\tau_c = 0.3\,\mathrm{ms}$. A settling time of $5\tau_c = 1.5\,\mathrm{ms}$ is a reasonable value for closed loop current controllers. According to [14] this choice of $\tau_c = 0.3\,\mathrm{ms} \approx 4.5 \cdot \theta$ prefers stability, robustness and small input usage. At this point a time continuous parallel PI controller with parameters k_P and $k_{I_c} = \frac{k_P}{T_I}$ is obtained that needs to be discretized. This is described in the following section. The resulting discrete-time software parameters are presented in Section 4.4.3 and summarized in Table 4.7.

4.4.2 Implementation and Quasi-Continuous Control Strategy

As controller transfer functions and parameters are acquired, they are *directly* discretized[19] using the (explicit) Forward-Euler algorithm Equation (3.7) for target hardware implementation. By this approach all frequency-domain based design methods can be adopted and a realizable controller can be readily derived as follows. The process is described for i_d control here. It is equivalent for quantities i_q and ω. Considering the continuous time parallel PI controller from the previous section with $e_d = i_d^r - i_d$,

$$C\left(s\right) = \frac{u_d^{\mathrm{fb}}\left(s\right)}{e_d\left(s\right)} = k_P^{i_d} + \frac{k_{I_c}^{i_d}}{s} \tag{4.59}$$

$$u_d^{\mathrm{fb}}\left(s\right) = \left(k_P^{i_d} + \frac{k_{I_c}^{i_d}}{s}\right)e_d\left(s\right) \tag{4.60}$$

---

[18]<u>S</u>imple <u>I</u>nternal <u>M</u>odel <u>C</u>ontrol

[19]This is different from the derivation of an *equivalent linear discrete-time system* described in Section 4.3 and possible for both linear and non-linear systems. The quality of this approximation is increased by smaller sample times. In the specific case of current controllers for Equation (4.52),Equation (4.53) the relations $T_{fast} \ll \frac{l_d T_B}{r}, T_{fast} \ll \frac{l_q T_B}{r}$ justify the proposed approach

each path is inspected separately and discretized using Equation (3.7). The proportional path translates directly into the discrete time domain, viz.

$$u_{P,d[k+1]} = k_P^{i_d} e_{d[k]} \tag{4.61}$$

The integral path control law in the discrete time domain is derived by taking the inverse Laplace transform[20] and using Equation (3.7),

$$u_{I,d}(s) = \frac{k_{I_c}^{i_d}}{s} e_d(s) \tag{4.62}$$

$$\frac{\mathrm{d}u_{I,d}(t)}{\mathrm{d}t} = k_{I_c}^{i_d} e_d(t) \tag{4.63}$$

$$u_{I,d[k+1]} = u_{I,d[k]} + T_s k_{I_c}^{i_d} e_{d[k]} \tag{4.64}$$

$$u_{I,d[k+1]} = u_{I,d[k]} + k_I^{i_d} e_{d[k]} \tag{4.65}$$

so the discrete time integral path coefficient is dependent on the corresponding sample time , $k_I^{i_d} = T_s k_{I_c}^{i_d}$. The *unsaturated* controller (actuator) output is given by

$$v_{d[k+1]} = u_{P,d[k+1]} + u_{I,d[k+1]} \ . \tag{4.66}$$

All realizable controllers possess output limitations that can be described with

$$u_{d[k+1]}^{\mathrm{fb}} = \begin{cases} |u_d^r|_{min}, & v_{d[k+1]} < |u_d^r|_{min} \\ v_{d[k+1]}, & |u_d^r|_{min} < v_{d[k+1]} < |u_d^r|^{max} \\ |u_d^r|^{max}, & v_{d[k+1]} > |u_d^r|^{max} \end{cases} \tag{4.67}$$

where u_d^{fb} is the resulting saturated output of the feedback controller, and usually $|u_d^r|_{min} = -|u_d^r|^{max}$. In the scope of this section u_d^{fb} corresponds to the space-vector-modulator's reference values u_d^r and u_q^r where as in Section 4.5.1 it is linked to the reference torque t_e^r.

Parameters $|u_d^r|_{min}$ and $|u_d^r|^{min}$ are set by software with the aim of *virtually restricting* the controller output 'just' below its *real* limitations. A considerable performance boost of the overall drive control system can be achieved by a prudent choice of these values. Section 4.2.2 gives a detailed discussion of choosing output voltage limits incorporating system knowledge "outside the scope" of current feedback controllers under investigation (in this case: knowledge of the VSI). Choosing the output limit of t_e^r properly to achieve (sensorless) stable high speed operation is the main content of Section 4.7 & Section 5.6.

Anti-Windup

Closed loop systems comprised of controllers with subsystems that integrate error signals such as Equation (4.65) combined with actuator saturations Equation (4.67) are prone to windup [55]. If no countermeasures are adopted these effects can deteriorate the overall performance significantly. The proposed anti-windup enhancement for the implemented feedback controllers is to freeze the

---

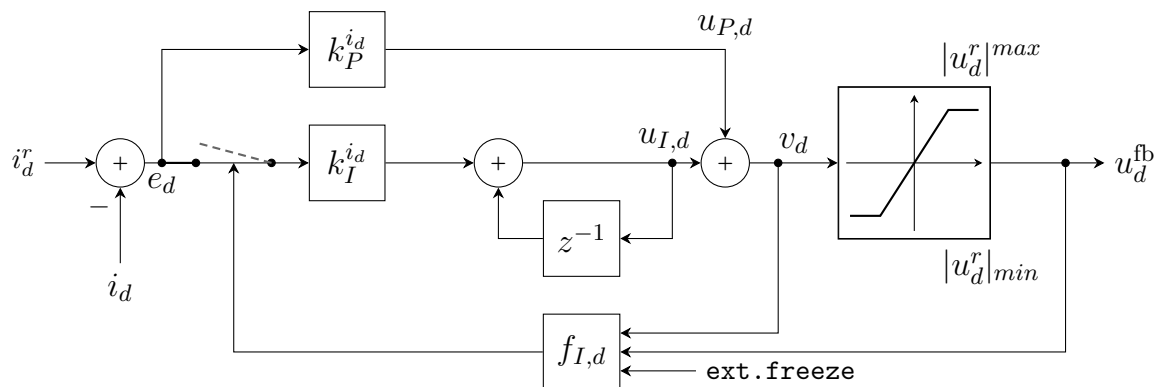[20]assuming $u_I^{i_d}(t_0^+) = 0$

Figure 4.5: Block-diagram of implemented time-discrete parallel PI controller with anti-windup enhancement; Implementation for i_d depicted, feedback controllers for i_q and ω follow accordingly.

Current Controllers	Setting	
Parameter	initial	tuned
$k_P^{i_d}$	0.52	0.45
$k_I^{i_d}$	0.024	0.016
$k_P^{i_q}$	0.326	0.35
$k_I^{i_q}$	0.0149	0.015

Table 4.1: Parallel PI current controller parameters

integrators content via a time dependent multiplicative factor, that is:

$$u_{I,d[k+1]} = u_{I,d[k]} + f_{I,d[k]} k_I^{i_d} e_{d[k]} \tag{4.68}$$

$$f_{I,d[k]} = \begin{cases} 1, & v_{d[k+1]} = u_{d[k+1]}^{\text{fb}} \ \wedge \ \texttt{ext.freeze} = 0 \\ 0, & \text{otherwise} \end{cases} \tag{4.69}$$

The integral portion of the PI controller is only updated if the output is unsaturated and the `ext.freeze` flag is set to zero, otherwise $u_{I,d[k+1]}$ stays frozen at its last unsaturated value. The condition to activate `ext.freeze` is given by a combined overflow of all desired controller outputs (feedback and feedforward), see Section 4.4.5.

The resulting feedback-controller that was described above is depicted in Figure 4.5. It can also serve as a schematic for the deployed feedback controllers of the quantities i_q and ω respectively.

4.4.3 Feedback Path, Controller Parameters

Table 4.1 reports the current controller paramters obtained by the design process and subsequent discretization as described in the above two sections. Generally speaking, the SIMC design

rules [14] of Equation (4.57) and Equation (4.58) delivered reasonable good values that can be readily used. The prior demanded time constant $\tau_c = 0.3\,\mu\text{s}$ and settling time of $5\tau_c$ can be achieved using the values reported in Table 4.1 and feedback control only. The i_d branch however showed overshoot and considering the fact that a feedforward branch is also active in the final configuration, the respective controller parameters were detuned as indicated in Table 4.1.

4.4.4 Feedforward Path, Exact Linearization

This section describes a way to derive a feedforward control law based on differential flatness theory and relates it to common known theory of electrical drives. Exact feedforward linearization will be adopted for both stator voltage equations based on [40]. Thereto, a non-linear affine input SISO system of order one shall be considered in state space representation:

$$\frac{\mathrm{d}x}{\mathrm{d}t} = f(x) + g(x)u \tag{4.70}$$

$$y = h(x) \tag{4.71}$$

In Equation (4.70) x denotes the state, u denotes the plant input and y represents the plant output to be controlled. All quantities are functions of time. Calculating the total derivative of y yields

$$\dot{y} = \frac{\mathrm{d}y}{\mathrm{d}t} = \frac{\partial h}{\partial x}\frac{\mathrm{d}x}{\mathrm{d}t} = \frac{\partial h}{\partial x}(f(x) + g(x)u) \tag{4.72}$$

$$= L_f h(x) + L_g h(x)u \tag{4.73}$$

The term $L_f h(x)$ is called Lie-derivative of h with respect to f. In higher order systems this term has the qualitative character of a directional derivative. For this example the term is set to $L_g h(x) \neq 0$, the system is said to have a relative degree of 1. From Equation (4.73) a feedforward control law for u can be derived as

$$u \stackrel{!}{=} u^{\text{ff}} = \frac{1}{L_g h(x^r)}(-L_f h(x^r) + \dot{y}^r) \tag{4.74}$$

with y^r as reference output trajectory and x^r as reference state trajectory. Substituting Equation (4.74) into Equation (4.73) *exactly linearizes* the system as the following relationship results:

$$\dot{y} = \dot{y}^r \tag{4.75}$$

Above theory is now related to the SynRM drive system. Comparing the direct axis stator voltage equation in state space representation,

$$\frac{\mathrm{d}i_d}{\mathrm{d}t} = \frac{1}{l_d T_B}(u_d - r_s i_d + \omega l_q i_q) \tag{4.76}$$

$$\tag{4.77}$$

with Equation (4.70) results in the following correspondences

$$x = i_d \tag{4.78}$$

$$f(x) = \frac{1}{T_B l_d}\left(-r i_d + \omega i_q l_q\right) \tag{4.79}$$

$$g(x) = \frac{1}{T_B l_d} \tag{4.80}$$

$$y = i_d \tag{4.81}$$

$$h(x) = 1 \tag{4.82}$$

$$\tag{4.83}$$

Applying the above scheme to Equation (4.76) gives

$$\frac{\partial h(x)}{\partial x} = 1 \tag{4.84}$$

$$L_f h(x) = f(x) \tag{4.85}$$

$$L_g h(x) = g(x) \tag{4.86}$$

$$\tag{4.87}$$

The relative degree of this system is 1, the output i_d is said to be differentially flat (each state can be expressed using this output and its derivatives, which is trivially fulfilled). The control law Equation (4.74) then resembles as

$$u_d^{\text{ff}} = T_B l_d \frac{\mathrm{d}i_d^r}{\mathrm{d}t} + r i_d^r - \hat{\omega} l_q i_q^r \tag{4.88}$$

where $\hat{\omega}$ has to be used in this system, because speed is not measured but estimated as described in Section 4.3.

Starting from the quadrature axis stator voltage equation

$$\frac{\mathrm{d}i_q}{\mathrm{d}t} = \frac{1}{l_q T_B}\left(u_q - r_s i_q - \omega l_d i_d\right) \tag{4.89}$$

and applying the same process, a control law for the quadrature axis voltage can be obtained as:

$$u_q^{\text{ff}} = T_B l_q \frac{\mathrm{d}i_q^r}{\mathrm{d}t} + r i_q^r + \hat{\omega} l_d i_d^r \tag{4.90}$$

The feedforward block in Figure 4.1 represents Equation (4.88) and Equation (4.90). The usage of current reference values $\left(i_d^r, i_q^r\right)$, calculated by the speed controller is crucial to reach high speed operation. Testing showed: if measured values are used the system becomes unstable. The terms $\hat{\omega} l_q i_q^r$ and $\hat{\omega} l_d i_d^r$ are also referred to as *decoupling network* in the theory of electric drives, [15].

For implementation both above control laws are *directly discretized*, see Section 4.4.2. To differentiate the reference currents they first need to be pre-filtered to restrict their bandwidth[21]. This is done by using Equation (3.10) with a choice of $\tau_{2DOF} = T_{fast}$. A time discrete causal FIR[22] differentiator from literature [56] with an input-output ($v_k \mapsto w_k$) relationship of

$$w_{[k]} = -\frac{1}{12}v_{[k]} + \frac{2}{3}v_{[k-1]} - \frac{2}{3}v_{[k-3]} + \frac{1}{12}v_{[k-4]} \tag{4.91}$$

is adopted. The usage of a differentiating part improves the current controllers performance by decreasing its rise time and settling time by $\approx 0.5\,\mu s$. This benefit comes at the cost of more aggressive signal trends of u_d^r and u_q^r. The differentiator is turned off in sensorless mode, see Section 5.5. In this chapter it is turned on for all following descriptions.

4.4.5 Combined Output, Saturation and Performance

As initially indicated by Equation (4.50) and Equation (4.51), feedback and feedforward control laws are added to obtain a reference voltage space vector $\underline{u}_{dq}^r$. To ensure the compulsory pulse width T_{PW}^{2a}, $|\underline{u}_{dq}^r|$ is restricted to $|\underline{u}|_{max}^{dq} = 0.71$ as resulted in Equation (4.27).

Should $|\underline{u}_{dq}^r| = \sqrt{u_d^{r\,2} + u_d^{r\,2}}$ exceed this value it is restricted back to it. The current voltage space vector's argument is preserved by

$$\varphi_u = \text{atan}\left(\frac{u_q^r}{u_d^r}\right) \tag{4.92}$$

$$u_{d,sat}^r = |\underline{u}|_{max}^{dq} \cdot \cos\left(\varphi_u\right) \tag{4.93}$$

$$u_{q,sat}^r = |\underline{u}|_{max}^{dq} \cdot \sin\left(\varphi_u\right) \tag{4.94}$$

The inner cascade is said to be *in saturation*, the `ext.freeze` variable is activated to freeze the controller's integrator parts, see Section 4.4.2. A flag `vcap` and a corresponding counter indicating /counting this state is activated. Both quantities are used for debugging and flux weakening identification, cf. Section 4.7 & Section 5.6.

Performance

The two degree of freedom current controller's performance can be assessed by inspection of Figure 4.10, Figure 4.14 and Figure 4.15. The usage of reference values within the feedforward branch is compulsory, otherwise the system destabilizes at higher speeds, starting with $\omega > 0.5$. The differentiator part of the feedforward branch reduces the initial rise time considerable, but it also introduces overshoot. Therefore it is prudent to design the feedback branches to contain no overshoot in their step-responses.

---

[21]Otherwise, signal noise would be differentiated also.
[22]Finite Impulse Response

4.5 Outer Loop: Speed Control

Once current control and observer structures are established at the FAST task, speed control can be achieved by cascading the inner loop inside an outer loop. This outer cascade is executed within the SLOW task. This situation is depicted in Figure 4.6. The quantity ω^{obs} , interfaced from the FAST→SLOW container is utilized as the measured feedback signal for speed control. In Section 4.1 the ratio between SLOW and FAST Task was specified as 6. Therefore $T_{slow} = 402\mu s$ and ω^{obs} represents each 6$^{\text{th}}$ output value from the FAST Task observer.

4.5.1 Feedback Path

Design and implementation of the speed controller in this thesis is based upon similar *quasi-continuous-control* paradigms and assumptions presented in Section 4.4 : A continuous-time parallel PI controller will be obtained in the continuous time (s) domain in a first step. Then it is discretized for target implementation by the (explicit) Forward-Euler-Method. This is justified because the incorporated time scale of the mechanical subsystem Equation (2.82)-Equation (2.83) is much higher than its associated sample time, viz. $T_{slow} \ll T_M$.

Controller Design

The strategy is to translate the system equation of the mechanical subsystem Equation (2.83) to a form susceptible to apply symmetrical optimum design. The electromagnetic motor torque was derived as

$$t_e\left(t\right) = i_d\left(t\right) i_q\left(t\right)\left(l_d - l_q\right) = \frac{1}{2}\,i^2\left(t\right)\sin\left(2\theta\right)\left(l_d - l_q\right)\;.\tag{4.95}$$

A speed controller calculates a reference torque t_e^r at its output. It is then translated to reference currents (i_d^r, i_q^r), see Section 4.5.3. For controller design, disturbances are set to zero, $t_L = 0$. Equation (2.83) then resembles as

$$\frac{\mathrm{d}\omega\left(t\right)}{\mathrm{d}t} = \frac{t_e\left(t\right)}{T_M}\;.\tag{4.96}$$

A Laplace transformation of the above equation and $\omega\left(t_0^+\right) = 0$ yields

$$\omega\left(s\right) = \frac{t_e\left(s\right)}{T_M}\frac{1}{s}\;.\tag{4.97}$$

A distinction between actual- and accessible-quantities for the controller is necessary. The shaft speed ω is observed instead of measured as described in Section 4.3 to provide ω^{obs}. The inner loop dynamics realizes a control command t_e^r at its input to actual torque t_e. Both processes are modeled using first order systems:

$$\omega^{obs}\left(s\right) = \frac{1}{1 + sT_{obs}}\,\omega\left(s\right)\tag{4.98}$$

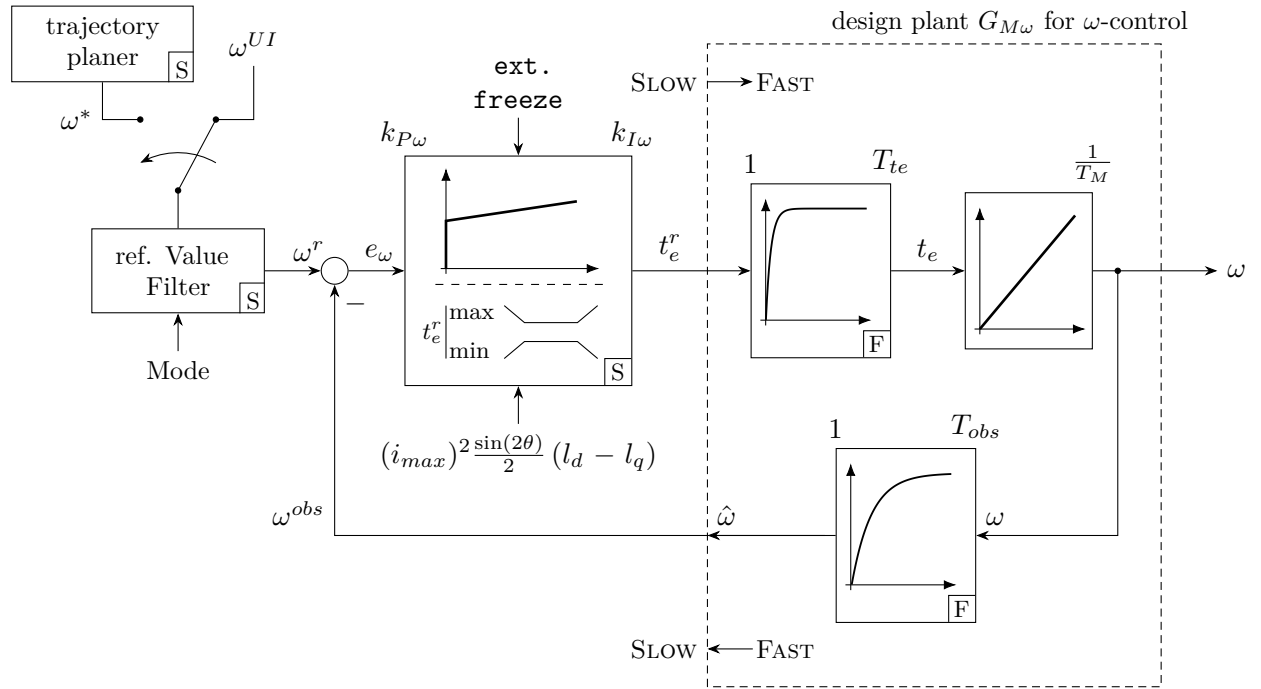$$t_e\left(s\right) = \frac{1}{1 + sT_{t_e}}\,t_e^r\left(s\right)\tag{4.99}$$

Figure 4.6: Speed controller overview: reference value path, feedback path, design model

Substituting Equation (4.98) and Equation (4.99) into Equation (4.97) results in the open loop design model for the speed controller depicted in the right half of Figure 4.6 given by the relations

$$\omega^{obs}(s) = G_{M\omega}(s)\, t_e^r(s) \tag{4.100}$$

$$\omega^{obs}(s) = \frac{1}{T_M} \cdot \frac{1}{s} \underbrace{\frac{1}{(1+sT_{obs})(1+sT_{t_e})}}_{1+s(T_{obs}+T_{t_e})+s^2 T_{obs}T_{t_e}} t_e^r(s) \tag{4.101}$$

$$\omega^{obs}(s) \approx \frac{1}{T_M} \cdot \frac{1}{s} \frac{1}{1+sT_{\Sigma\omega}} t_e^r(s) \tag{4.102}$$

Considerations/Measurements from Section 4.4, best practice from hands-on experience as well as a MATLAB simulation of the observer justify the choice of $T_{obs} = 6\,\text{ms}$ and $T_{te} = 0.5\,\text{ms}$. These typical values verify the neglection higher order terms of $G_{M\omega}$ in Equation (4.101) and emphasize the observer's importance in the design process. By Equation (4.102) a plant susceptible to symmetrical optimum (SO) tuning rules is obtained. With the motor parameters of Section 4.6, $T_{\Sigma\omega} = T_{obs} + T_{te}$ and [57],[58] the SO parallel PI discrete controller parameters are given by

$$k_{I\omega} = \frac{1}{4T_{\Sigma\omega}} \cdot T_{slow} \ , \tag{4.103}$$

$$k_{P_\omega} = \frac{1}{2}\frac{T_M}{T_{\Sigma\omega}} \ . \tag{4.104}$$

Speed Controller	Setting	
Parameter	initial	tuned
k_{P_ω}	22.91	7.16
$k_{I\omega}$	0.015	0.015

Table 4.2: Parallel PI speed controller parameters

Attention is drawn to the end of Section 2.4.3 that discussed different time horizons. When adopting cascaded control and taking perspective of the outer loop e. g. t_e^r, the inner loop will realize said reference value and will ideally appear as through-connection. That 'quasi-decouples' t_e^r from the actual values of i_d and i_q within the FAST task and justifies the above approach.

Controller Implementation

The speed controller as presented in this section comprises a feedback path and a signal conditioning reference path. The feedback subsystem is implemented as a time-discrete parallel PI controller. SO parameters of Table 4.2 and internal/external anti-windup inputs are used. Structurally this subsystem is of the same type as the current controller's feedback path presented in Section 4.4 and depicted in Figure 4.5.

Wind-up is avoided internally by freezing the integrator's value if the desired controller output[23] exceeds its associated limits $t_e^r\big|_{min}^{max}$. Equally to the current controllers the external freeze input of the speed controller is fed by the `vcap` flag, defined in Section 4.4.

The initial setting of the proportional path k_{P_ω} proved to be too aggressive as it aggravated wind-up issues of the lower cascade even if reference value filtering and flux weakening were active. The tuned settings for the sensored-mode in Table 4.2 deliver good dynamic tracking performance. The value of k_{P_ω} is critical for sensorless performance. A detailed discussion is given in Section 5.5. Adopting SO tuning rule Equation (4.103) yields reasonable values of k_{I_ω} and excellent stationary disturbance rejection performance. Only a slight detuning for sensorless operation is necessary.

4.5.2 Speed Reference Value Conditioning

Figure 4.6 indicates: Sources for speed reference values are given by a user controlled input ω^{UI} and a programmed test trajectory ω^*. The chosen source quantity is processed by a filter block to yield the speed loop's reference value ω^r with modes as described below:

- **through-connection**: This mode is used for debugging purposes only.

- **first-order low-pass filter**: This is the standard mode for sensored operation. Input values will be smoothed by means of Equation (3.10) with a time constant of $\tau_\omega = 20\,\text{ms}$. The signal input/output relationship can be inspected in the top plot of Figure 4.15. In mechatornic systems force/torque steps should never be applied directly to the plant. In

---

[23]designation v in Figure 4.5

case of an electric machine supported by ball bearings those bearings won't roll smoothly and therefore degrade fast when the shaft is accelerated abruptly.

- **slew-rate filter**: Default setting for sensorless operation. A detailed description is given in Section 5.5.

Closed loop tests support the conclusion that pre-filtering speed reference values is beneficial for overall system performance in sensored mode. It proved also to be paramount for stable, favorable system behavior in sensorless mode, see Section 5.5. This can be reasoned intuitively back in the continuous time domain considering $G_{M\omega}(s)$ of Equation (4.100) together with the designed PI controller of the form Equation (4.60) $C_\omega(s)$ with parameters from above.

First the closed loop noise sensitivity function is considered:

$$T_{te}(s) = \frac{C_\omega(s)}{1 + G_{M\omega}(s) C_\omega(s)} = \frac{t_e^r(s)}{\omega^r(s)} \ . \tag{4.105}$$

When directly applying a step for ω^r to this transfer function a significant overshoot in t_e will occur. As a consequence both upper- and lower-cascade will unnecessarily saturate[24]. Despite anti-windup measures system performance is significantly deteriorated. This qualitative statement is also true for the real system and was proven by extensive testing.

A remedy of this undesirable behavior is proposed in [54] by pre-filtering the reference value. Therefore *a trade-off is discovered between restricting the systems bandwidth and favorable, stable system performance given by the pre-filter's parameters*. This trade-off is of striking importance when adopting sensorless operation and will be further discussed in Section 5.5.

4.5.3 Torque Realization Strategies

Basic Relationships

With Equation (4.95) the speed controller's output signal t_e^r can be readily translated into current space vector reference values (i_d^r, i_q^r) that are interfaced to the inner loop via a SLOW→FAST container. These values are obtained by:

$$i^r = \sqrt{\frac{2}{(l_d - l_q)} \cdot \left| \frac{t_e^r}{\sin(2\theta^r)} \right|} \tag{4.106}$$

$$s_{te} = \text{sign}(t_e^r) \tag{4.107}$$

$$i_d^r = i^r \ \cos(\theta^r) \tag{4.108}$$

$$i_q^r = s_{te} \, i^r \ \sin(\theta^r) \ . \tag{4.109}$$

The torque sign is usually controlled via i_q's polarity. The system is capable to operate within all four quadrants of the ω/t_e^r plane[25]. The maximum stator current space vector magnitude[26] is

---

[24]which is in direct contrast to the proposed flux-weakening strategies of Section 4.7 and Section 5.6

[25]where $i_d > 0$ in all four quadrants; $i_q > 0$ in Q1,Q2 and $i_q < 0$ in Q3,Q4; $\omega > 0$ in Q1,Q4 and $\omega < 0$ in Q2,Q3

[26]determined by maximum motor temperature restrictions

given by i_{max}. Then, inherent output limits for the speed controller are derived as a function of the reference MMF angle θ^r. Manipulation of Equation (4.106) leads to

$$\sqrt{\frac{2}{(l_d - l_q)} \cdot \left| \frac{t_e^r}{\sin{(2\theta^r)}} \right|} \leq i_{max} \tag{4.110}$$

$$t_e^r|_{min}^{max} = \pm \left(i_{max} \right)^2 \frac{|\sin{(2\theta^r)}|}{2} \cdot (l_d - l_q) \ . \tag{4.111}$$

Equation (4.111) is also indicated in Figure 4.6. The motor is usually operated at rated conditions viz. $i_{max} = 1$. Using the MTPA condition Equation (2.85) yields

$$t_e^r|_{min}^{max} = \pm \frac{1}{2} \cdot (l_d - l_q) \ , \tag{4.112}$$

$$i_d^r|^{max} = \left| i_q^r \right|^{max} = \frac{1}{\sqrt{2}} \ . \tag{4.113}$$

As discussed in Section 2.4.4 there are more possibilities to choose θ^r hence this strategy is designated as `polar` mode in the speed controller's implementation. The next Section 4.6 will identify l_d and l_q. Substituting these results into Equation (4.112) yields a maximum/minimum value of

$$\boxed{t_e^r|_{min}^{max} = 0.179} \tag{4.114}$$

This value will be indicated on numerous occasions in the remaining document. In Section 4.7 a function for the output limit $t_e^r|_{min}^{max}(\omega)$ in `MTPA` mode (defined below) will be derived to achieve high speed operation.

Implemented Operational Modes

- The `polar` mode for arbitrary user specified MMF angles θ^r is given by the above equations (4.106)-(4.109).

- The `MTPA` mode is uses $\theta^r = 45\,°_{\text{elec}}$ in the above defined `polar` mode. Reference currents are calculated as:

$$i^r = \sqrt{\frac{2}{(l_d - l_q)} \cdot |t_e^r|} \tag{4.115}$$

$$s_{te} = \text{sign}\left(t_e^r \right) \tag{4.116}$$

$$i_d^r = i^r \frac{1}{\sqrt{2}} \tag{4.117}$$

$$i_q^r = s_{te}\, i^r \frac{1}{\sqrt{2}} \tag{4.118}$$

This mode is used as standard mode for sensored operation, discussed in this chapter. It is also utilized in conjunction with the next presented mode for sensorless operation.

- The `vpsm(id)` mode is characterized by a user choice of a constant value for $i_d^r > 0$. The output reference torque of the speed controller is then translated using Equation (4.95):

$$i_q^r = \frac{t_e^r}{(l_d - l_q)\, i_d^r} \tag{4.119}$$

  That is, speed is actively controlled using only the current space vector's quadrature component. Designated as *virtual-psm* mode a link to permanent magnet synchronous machine's behavior is intended. This mode is used for both identification in Section 4.6.2 and sensorless operation in Chapter 5. In the context of sensorless operation i_d^r in `vpsm(id)` will be designated as $i_d|_{min}(\omega)$.

- The current component's roles (independent vs. derived) in Equation (4.119) can be interchanged to define the `vpsm(iq)`[27] mode:

$$i_d^r = \frac{t_e^r}{(l_d - l_q)\, i_q^r} \tag{4.120}$$

  This mode is used for the purpose of parameter identification in Section 4.6.2.

Other Operational Modes

In [8] & [59] and referenced literature there several other possible operational modes are presented. Maximum Power Factor (`MPF`) was given by Equation (2.88) in Section 2.4.4.

The `MTPV` mode initially reduces direct axis flux ψ_d in order to optimally exploit available inverter voltage when voltage limitations become active. A way to calculate pairs of (i_d^r, i_q^r) to realize this mode is outlined in [1]. Usually this is done offline and requires the exact knowledge of inductances over a broad operational range. This implies the need for an extensive finite element simulation covering both 2D and 3D cases. Even more beneficial would be a thorough identification of the flux(inductance) maps by means of a load machine. A (nearly) magnetic linear motor is beneficial for both processes and tuning. As discussed in Section 2.4.5 only 2D data was available and a notable discrepancy became apparent between simulated and identified inductances in the next Section 4.6. Due to reasons given in Section 2.1 the motor was operated as single motor loaded by friction. This made identification over a broad high speed range at arbitrary current space vectors unfeasible.

Supported by these arguments the author chose to implement operational modes as described in the preceding paragraph and used these modes to achieve flux weakening operation for both sensored and sensorless control.

It is important to note that these proposed torque realization strategies are valid for magnetically linear SynRM with constant inductances. The machine deployed in this project possesses these characteristics, proved by the following identification in Section 4.6. In case of substantial saturations[28] a non-linear mapping incorporating flux maps

$$t_e^r \mapsto \left(i_d^r, i_q^r\right) \tag{4.121}$$

is necessary to meet requirements posed by the application in turn.

---

[27]During operation this mode proved to be marginally stable. Safety precautions (Hardware shutdown, Software limitations) are advised when operating the motor in the `vpsm(iq)` mode.

[28]commonly occurring at the FxB and axially-laminated SynRM type presented in Section 2.4

4.6 Identification of Machine Parameters

The subject matter discussed in the preceding Sections 4.1-4.5 was implemented and manually tuned using machine parameters obtained by simulation, see Section 2.4.5. Advanced features such as flux weakening and sensorless methods however require a sufficient well knowledge of stator resistance and (dq)-inductance values. Obsevers and two-degree of freedom current controllers also profit from properly identified machine parameters. All deviations from the "true" values result in constant disturbances acting on the closed loop system, see [54].

All following measurements of this section were conducted online and were configured to output data blocks of 200 samples per quantity in I1Q15 format to RAM. The sampling frequency for the data points was set to $1.5\,\text{kHz}$. The ambient temperature was within $19°\text{C} \dots 23°\text{C}$. After each measurement cycle the data blocks were read out via JTAG debug probe and post processed in MATLAB. The block's median was taken as representative value of the measured quantity. A description of the utilized `DATALOG` software structure is given in [60] and [43].

4.6.1 Stator Resistance

As discussed in Section 2.4.5 the realized SynRM has a slot-turn number of $N_{slot} = 20$. Regarding mechanical and geometrical parameters this is the only difference if compared to the initial machine design[29] of [1]. Using this new parameter within the proposed approach in [1] to calculate the stator phase resistance, a value of

$$R_s^{calc} = 34.9\,\text{m}\Omega \tag{4.122}$$

can be obtained. To verify this value a series of offline measurements has been carried out between terminals UV, UW and VW. Four-terminal sensing was adopted since the expected resistance value was of low magnitude. Measured resistance values are to be divided by two since the nature of this line-to-line sensing setup and the stator coil's star configuration. A power supply was configured to output currents between $[2\text{A} \dots 24\text{A}]$. The minimum and maximum values obtained this way are $35.25\,\text{m}\Omega$ and $36.25\,\text{m}\Omega$ respectively. The median of all measurement values was

$$R_s^M = 35.84\,\text{m}\Omega \;, \tag{4.123}$$

confirming the symmetry of the stator coil solenoids and the above calculation.

A second series of resistance measurements was conducted online comprising the VSI. At standstill current space vectors of varying[30] phase and magnitude were established by means of current control. Phase voltages were measured at the inverter. The stator resistance was calculated as quotient of measured voltage and current in α direction. A representative value of

$$R_s = 55\,\text{m}\Omega \tag{4.124}$$

was implemented in the firmware as this is the resistance value visible from the controller's perspective. The difference compared to Equation (4.123) can be explained by an increased series

---

[29]The slot-turn number of the original design was six times higher. Groups of six wires are soldered together. Background information is given in Section 2.4.5

[30] $\left|\underline{i}^{\alpha\beta}\right| \in [0.75 \dots 1.33],\ \arg\!\left(\underline{i}^{\alpha\beta}\right) \in [0 \dots 360\,[°_{\text{elec}}]]$

resistance introduced by cables and connectors. It is important to take the *measured* voltages u_α, u_β rather than the reference voltages from the modulator u_α^r, u_β^r for resistance identification. Voltage drops at freewheeling-diodes caused differences up to 4% between those scaled voltages[31]. This yielded unrealistic high resistance values. An accurate resistance value is also required for inductance identification presented in the following section.

4.6.2 Inductances

The breadboard setup of this thesis comprised a single motor that was loaded by friction. Reasons and descriptions for this configuration were given in Section 2.1. A self-commissioning method running at free-shaft will be proposed. For identification this implies that torque t_e and speed ω cannot be chosen independently any more. The versatility of the SynRM however allows to choose ω and either i_d^r or i_q^r independently.

Thus, the operational modes `vpsm(id)` and `vpsm(iq)`, specified in Section 4.5.3 are used for this identification method. Prior to identification simulation parameters are substituted in the above defined modes. Differences to actual values are compensated by the integrating part of the speed controller.

Two experiments were conducted at constant shaft speed $\omega = 0.5$ to identify l_d and l_q respectively. Cross coupling effects are not explicitly modeled due to considerations made in Section 2.4.3. An a priori unknown flux-current relationship is to be identified. Underlying equations for inductance identification are then given by the quasi-stationary stator voltage equation in the (dq)-reference frame:

$$u_d = ri_d - \omega\psi_q\left(i_q\right) \tag{4.125}$$

$$u_q = ri_q + \omega\psi_d\left(i_d\right) \tag{4.126}$$

Direct Axis Inductance

Operating at $\omega = 0.5$ in `vpsm(id)` mode, free shaft, a sweep over i_d^r was conducted. Together with this user value, the controller output voltage u_q^r and the prior identified stator resistance r were substituted into Equation (4.126):

$$u_q^r = ri_q + \omega\psi_d\left(i_d^r\right) \tag{4.127}$$

The direct axis flux ψ_d and the apparent direct axis inductance l_d were obtained as:

$$\psi_d\left(i_d^r\right) = \frac{u_q^r - ri_q}{\omega} \ , \tag{4.128}$$

$$l_d\left(i_d^r\right) = \frac{\psi_d\left(i_d^r\right)}{i_d^r} \ . \tag{4.129}$$

As described in Section 4.6.1 controller output voltages tend to be higher than measured voltages. At these speed and current levels however the relative error is relatively small compared to the previous section. To correctly *measure* voltages at frequencies in the magnitude of 1 kHz and higher a hardware refit would be required at the VSI. Furthermore, additional measurement

---

[31] a factor of three at this low magnitude

points in the agenda would cause a decrease of $\left|\underline{u}_{max}^{dq}\right|$ as was reasoned in Section 4.2.2. All these arguments lead to the design decision to exclusively use controller output voltages (u_d^r, u_q^r) for identification and sensorless models.

Quadrature Axis Inductance

Analog to the previous section a sweep over i_q^r in `vpsm(iq)` operational mode at $\omega = 0.5$ was conducted. The identification Equation (4.125) used was:

$$u_d^r = r i_d - \omega \psi_q \left(i_q^r \right) \tag{4.130}$$

The quadrature axis flux ψ_q and the apparent quadrature axis inductance l_q were obtained as:

$$\psi_q \left(i_q^r \right) = \frac{-\left(u_d^r - r i_d \right)}{\omega} \tag{4.131}$$

$$l_q \left(i_q^r \right) = \frac{\psi_q \left(i_q^r \right)}{i_q^r} \tag{4.132}$$

Results

Outcomes of the previously described experiments are depicted in Figure 4.7. Both experiments were conducted up to an overload region of $|\underline{i}| = 1.15$. Temperature warnings and the voltage cap of $|\underline{u}|_{max}^{dq}$ were limiting factors.

Simulation results of [1] reported saturation effects occurring at the rotor's d-axis. These effects became apparent at rated current levels of $i_d = i_q = 1/\sqrt{2}$ and higher. This is confirmed by inspection of the direct axis flux ψ_d and inductance l_d in Figure 4.7. The quadrature axis flux and inductance show no substantial saturation behavior, reasoned by a large airgap in this direction. Increased values of l_d and l_q at lower currents can be attributed to a combination of physical and numerical sources. Due to the self commissioning nature both stator axis components cannot be chosen independently. That leads to a presence of i_q in Equation (4.128) and i_d in Equation (4.131). This is aggravated by calibration dependence of the encoder angle, discussed in Section 2.6, and a division by relatively small current values.

For implementation inductance values at $i_d = i_q = 1/\sqrt{2}$ are taken as constants, indicated as dashed lines in Figure 4.7. The most significant difference between simulation and experiment is given by an increased quadrature flux & inductance value. This can be reasoned by the neglected end-turn region and the corresponding increased stray fluxes within the simulation. The effects discussed in the above paragraph also apply here. Parameter values are reported in Table 4.3. Differences to [1] are indicated in the last column.

Overall the assumption of a magnetically linear motor is justified. A choice of constant inductances is possible and all subsequently described subsystems greatly benefit from this property. For future work a load machine should be used to enable more sophisticated identification methods with less interdependencies. Speeds well above 12 krpm should be targeted to gather a representative set of data for the flux weakening region, cf. Section 4.7. Thereto, a redesign of the motor shaft may be necessary to mount the corresponding claw coupling safely. Then the
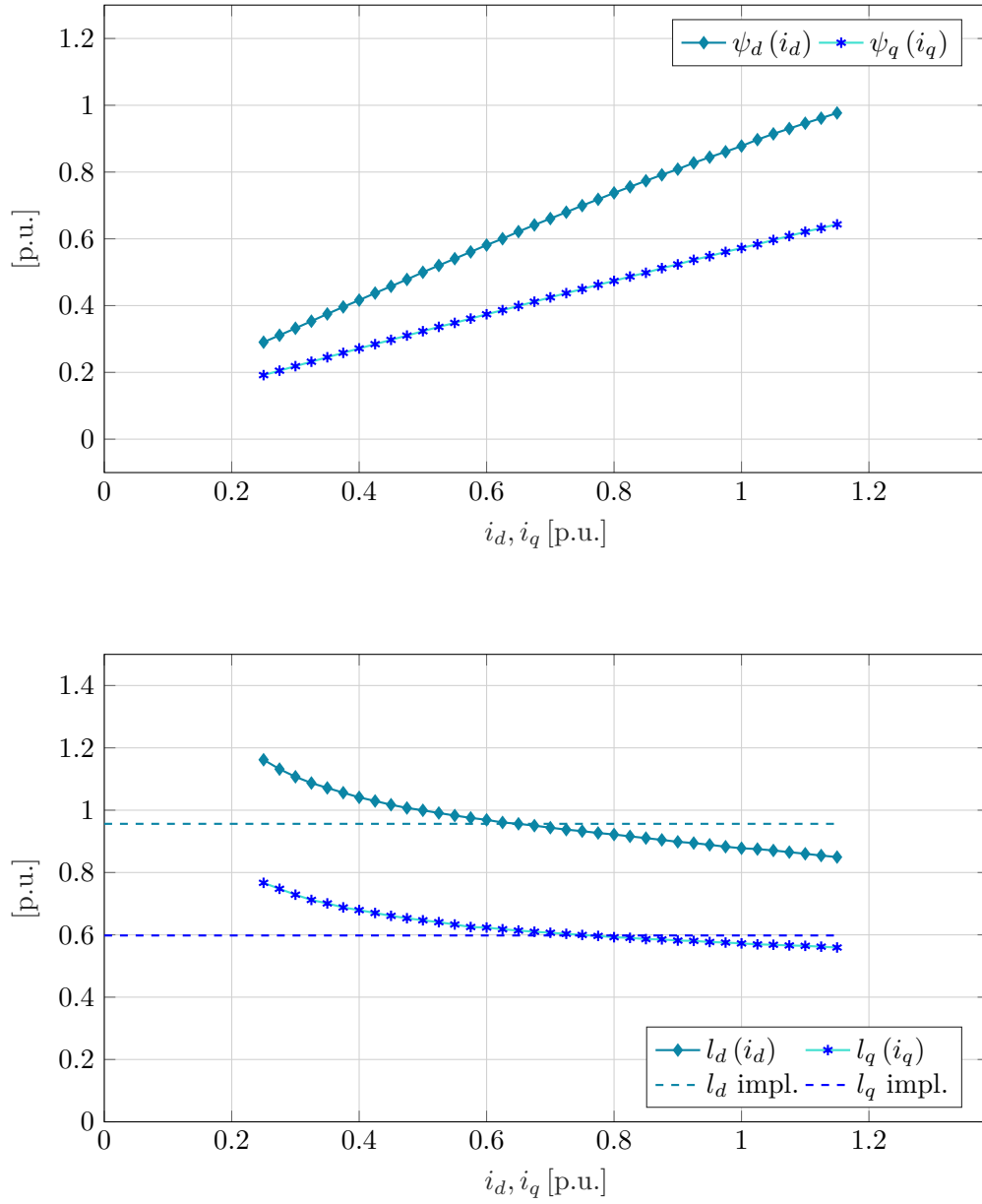
Figure 4.7: Results of parameter identification

Parameter	Symbol		Value		% diff.
			absolute	scaled	
identified					
d-Axis Inductance	L_d	l_d	$425\,\mu\mathrm{H}$	0.956	1%
q-Axis Inductance	L_q	l_q	$266\,\mu\mathrm{H}$	0.598	26%
Stator Resistance (Motor)	R_s^M	r^M	$36\,\mathrm{m\Omega}$	0.0161	0%
Stator Resistance (Inverter)	R_s	r	$55\,\mathrm{m\Omega}$	0.0247	-
Inertia	Θ		$53\,\mu\mathrm{kgm}^2$		-
derived					
Start-Up Time Constant	T_M		$0.31\,\mathrm{s}$		-
Saliency Ratio	ξ		1.6	1.6	-20%

Table 4.3: Identified machine parameters. Differences reported with respect to simulation parameters given in Table 2.5.

discrepancy reported in Table 4.3 can be verified or falsified reliably. Nevertheless, the usage of reported parameter values lead to success to reach high speeds with and without rotary encoder.

The resulting saliency ratio of $\xi = 1.6$ at rated currents is typical for a salient pole synchronous reluctance machine, see Section 2.4. If compared to the preceding work's motor the saliency ratio is 18% higher, cf. [3].

All in all this identification results pose a promising starting point for flux weakening and sensorless operation.

4.6.3 Inertia

After resistance and inductance identification the start-up time constant T_M can be identified using Equation (2.83). At open speed loop a series of known torque pulses was injected to accelerate and brake the motor. The procedure is explained more detailed in the next section. Speed was observed, time was measured in software. A representative value is reported in Table 4.3. The relation of Equation (2.22) was used to calculate the absolute value. Caution is advised when injecting torque pulses as this can damage the motor irreversible.

4.7 Flux Weakening Operation Utilizing a Rotary Encoder

This section proposes an expansion to the implemented speed controller of Section 4.5 to achieve high rotational speeds. Generally speaking, the output t_e^r will be restricted as shown in Figure 4.8 in order to avoid saturation of the inner cascade's control system. In this sense flux weakening can be seen as a kind of anti windup strategy for the inner cascade carried out by the outer cascade.
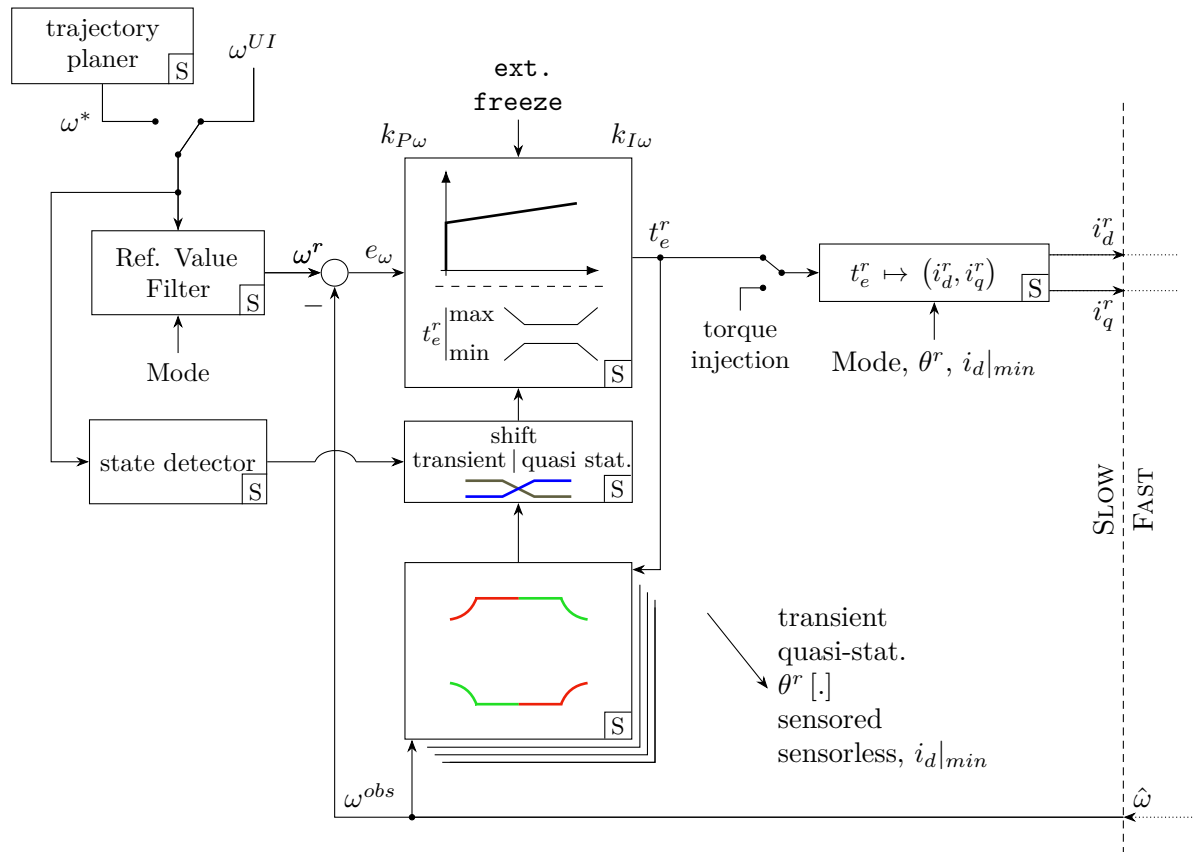
Figure 4.8: Speed controller with flux weakening expansion and torque injection

An introduction of the relevant effects and quantities in this operational stage is given in Section 4.7.1. The strategy will be separated into *transient*, *quasi-stationary* flux weakening and a shifting between the two in Section 4.7.2 and Section 4.7.3. Finally the motor's performance when implementing the proposed matter is presented and discussed in Sections 4.7.4−4.7.6.

4.7.1 General Considerations

A prime advantage of electrical drives is to instantaneously exert torque from standstill. In case of SynRM the amount of torque in scaled format was derived as

$$t_e = (l_d - l_q)\ i_d\, i_q = (l_d - l_q)\, \frac{1}{2}\, i^2 \sin(2\theta)\ . \tag{4.133}$$

During operation thermal constraints usually emerge first in the sense that one cannot increase the motor's current indefinitely in order to yield more torque. This was discussed earlier in Equation (4.110)−Equation (4.113) and resulted in $t_e^r\big|_{min}^{max} = 0.179$. The SynRM is then able to deliver this constant (maximum) torque up to a certain stage where additional limitations apply.

These constraints are given below by the stator voltage equation:

$$\underline{u}^{dq} = \underbrace{\underbrace{r\underline{i}^{dq} + j\omega\underline{\psi}^{dq}}_{\text{quasi}-\text{stationary limit}} + \frac{\mathrm{d}\underline{\psi}^{dq}}{\mathrm{d}t}}_{\text{transient limit}} \ . \tag{4.134}$$

When controlling $\underline{i}^{dq}$ (proportional to torque) to be at its maximum scaled value the only variable on the right hand side of Equation (4.134) is the (electrical) angular velocity ω. As outlined in Equation (2.75), $\underline{\psi}^{dq}$ is assumed to be a linear function of $\underline{i}^{dq}$. The left hand side of Equation (4.134) is ultimately limited by the available inverter bus voltage U_{DC}. This value can in term be optimally exploited when adopting the considerations of Section 4.2.2 to yield $|\underline{u}|^{dq}_{max}$.

Figure 4.9 illustrates the behaviour of torque and voltage as shaft speed is increased. A necessity to decrease flux (viz. torque) arises when the right hand side's absolute value in Equation (4.134) equals $|\underline{u}|^{dq}_{max}$ at the characteristic speed ω^{FW}_{rated}. The motor is then entering the high speed domain where flux weakening (FW) strategies $t^r_e|^{max}_{min}(\omega)$ trade torque for speed, ideally up to the drive train systems maximum mechanical speed ω^{max}.

At this point the question of "*how* to decrease $\underline{\psi}^{dq}$..." arises. Due to reasons discussed in Section 4.5.3 the MMF angle is fixed to $\theta^r = 45\,°_{\text{elec}}$ and flux weakening will be conducted alongside the MTPA line in this thesis. To give the reader a prospect, inspection of Figure 4.13 in Section 4.7.3 is advised. In the following sections this plot will be systematically derived. For sensorless operation however it will serve as a starting point to develop a proper sensorless flux weakening strategy.

The adoption of a proper flux weakening strategy increases the motor's effective speed range considerably. Furthermore it allows for smaller form factors of actual motors when certain mechanical power-requirements have to be met. Very intuitively speaking power, $p_{mech} = t_e\omega$, can be increased by either boosting torque or speed. When allowing higher amount of currents for increased torque this corresponds to larger form factors. For a constant requirement of p_{mech} it is often prudent to specify a "reasonable" rated current and achieve the requirement via increased speed through flux weakening strategies.

Underneath Equation (4.134) two braces indicate that there are in fact two different cases of active voltage limitations:

- The *quasi-stationary* case is defined as a state where the flux's rate of change $\frac{\mathrm{d}}{\mathrm{d}t}\underline{\psi}^{dq}(t)$ can be neglected. This is the case when the shaft is rotating at constant speed or *after* a control command t^r_e has been translated and executed into the corresponding currents viz. $t_e = t^r_e$, see Figure 4.6. The case is also defined to be active when ω and $\underline{i}^{dq}$ change slowly with respect to a time scale of T_{slow}.

- The *transient* case covers all terms in Equation (4.134) and is defined to be active when $\underline{i}^{dq}$ changes fast with respect to a time scale of T_{slow}. This is usually true at the beginning of acceleration and brake maneuvers i.e. when the speed/torque reference value ω^r/t^r_e changes abruptly. The duration of the *transient* flux weakening state is parametrized by T_{trans}, presented in Section 4.7.2

Again considering Equation (4.134) it becomes clear that the speed limit to enter flux weakening will be significantly higher for the *quasi-stationary* case. Attention is drawn to the findings of
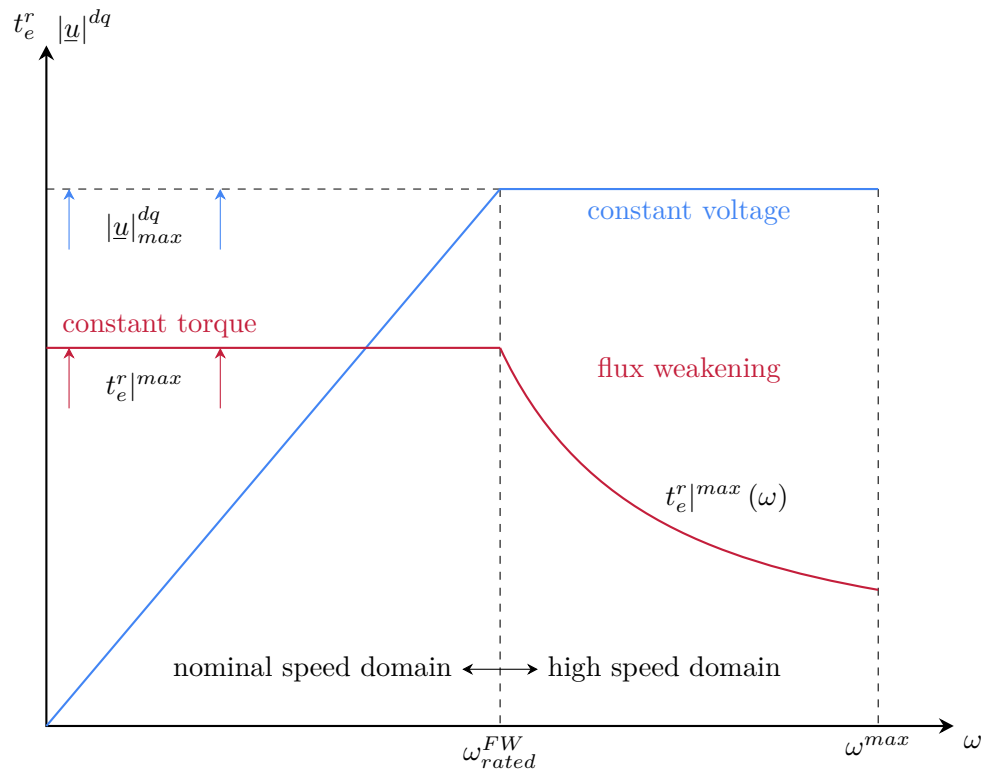
Figure 4.9: Principle of flux weakening and incorporated quantities; First Quadrant (Q1)

t_e^r	min	max
transient	$\widetilde{t}_{min}$	$\widetilde{t}_{max}$
quasi-stationary	$\bar{t}_{min}$	$\bar{t}_{max}$

Table 4.4: Speed controller output limits overview and substitutions

Section 4.2.2:

$$|\underline{u}|_{max}^{dq} = 0.71 \tag{4.135}$$

being $\approx 82\%$ of the theoretical maximum of $\sqrt{3}/2$. This will have a considerable positive impact on overall system's performance. That is an increased nominal speed range and an improved flux weakening capability to achieve very high speeds.

In the following flux weakening methods for both defined cases above will be presented. Then, a way to indicate the active case to subsequently shift between the two will be described. Thereto, four different torque limitations are defined in Table 4.4 for the negative (min.) and positive (max.) output value of the speed controller in both cases.

4.7.2 Transient Voltage Limit

The transient voltage limit becomes active, if the application or the user demands a rough change of speed to accelerate or break at already high velocities. The calculated reference values for the inner cascade $t_e^r \mapsto (i_d^r, i_q^r)$ may be not achievable due to the system's voltage limitation, see Section 4.7.1. If no further precautions are taken the inner cascade will saturate due to a non-realizable reference value and *plant windup* will occur with all accompanying detrimental effects, [55].

To avoid this behavior the speed controller's output needs to be limited in such a way that Equation (4.134) is balanced. That means the electrical drive is *just at* the voltage limit providing the most possible amount of torque under given constraints depending on the current shaft speed.

Identification

The term $\frac{\mathrm{d}}{\mathrm{d}t}\underline{\psi}^{dq}(t)$ is responsible for the division of *transient* and *quasi stationary* voltage limitation cases. It depends on the implemented current controller of Section 4.4 and the deployed/connected machine. To increase the system's modularity and portability for the method proposed, preconditions as follows are considered:

- The transient voltage limitation will be identified using a experimental instead of an analytical approach.

- The motor will be operated in free shaft mode since the maximum speed of available claw couplings for this assembly is about $\omega \approx 0.666$, see Section 2.1.

- As for MTPA in the nominal speed range the MMF angle will be fixed to $\theta^r = 45°_{\text{elec}}$ when adopting sensored flux weakening.

A self commissioning transient voltage limit identification method is proposed and described by pseudo code of Experiment 1. The idea is to "simulate" a spontaneous high torque demand of the upper cascade (sudden accelerate/break). By trial and repeat the exact reference value at which the lower cascade will *start* to saturate is found. This is done by direct injection of a reference value t_e^r for T_{inj} while the shaft is running free. After a specified time T_{rec} the speed feedback loop is closed again, see Figure 4.8.

Figure 4.10 shows a successful iteration at $\omega = 0.75$ displaying the relevant quantities. It can be deducted that after $T_{inj} = 80 \cdot 6 \cdot T_{fast} = 32.16\,\text{ms}$ the actual currents i_d and i_q have settled. This indicates the transient state's end[32]. In the final firmware the transient state duration was chosen to be $T_{trans} = 35\,\text{ms}$. It is important to note that after injection a recovery phase as proposed is mandatory to ensure stability at higher speeds.

Experiment 1 Torque Injection for Transient Voltage Limit Identification

---

Ensure: $\omega^r = \omega_{FWinit}$
Ensure: $\theta^r = 45°_{\text{elec}}$
 $\widetilde{t}_{last} \leftarrow 0.5$
 repeat
  $\widetilde{t}_{tmp} \leftarrow \widetilde{t}_{last}$
  for $T_{inj} = 80 \cdot T_{slow}$ **do**
   $t_e^r \leftarrow \widetilde{t}_{tmp}$ ▷ inject torque
  for $T_{rec} = 1000 \cdot T_{slow}$ **do**
   $t_e^r \leftarrow 0$ ▷ recover
  reconnect ω controller FB path
  if `vcapct` ≤ 0 **then**   ▷ inspect inner cascade
   increase $\widetilde{t}_{tmp}$
  else if `vcapct` > 50 **then**
   decrease $\widetilde{t}_{tmp}$
  else   ▷ accept, if $\leq 10\%$ saturation
   save $\left(\omega^r, \widetilde{t}_{tmp}\right)$
   $\omega^r \leftarrow \omega^r + \varepsilon_{FW}$
  reset `vcapct`
  $\widetilde{t}_{last} \leftarrow \widetilde{t}_{tmp}$
 until $\omega^r = \omega_{FWend}$

The experiment is set to start in the nominal speed range e. g. $\omega_{FWinit} = 0.4$. It is reported for speeds up to[33] $\omega_{FWend} = 1$. A speed-step of $\varepsilon_{FW} = 0.025$ was chosen. This choice simultaneously specifies the resolution in ω-direction of a Lookup-Table (LUT) where the identified pairs $\left(\omega^r, \widetilde{t}_{tmp}\right)$ are stored.

During injection each `vcap` flag defined in Section 4.4.5 is logged by means of a counter `vcapct`.

---

[32]viz. $t_e = t_e^r$

[33]This was in principle an arbitrary choice as "reasonable" high velocity of around $24\,000\,\text{rpm}$. By the time of development the author and supervisor of this thesis wanted to exercise caution as further development goals were to be reached within the sensorless domain.
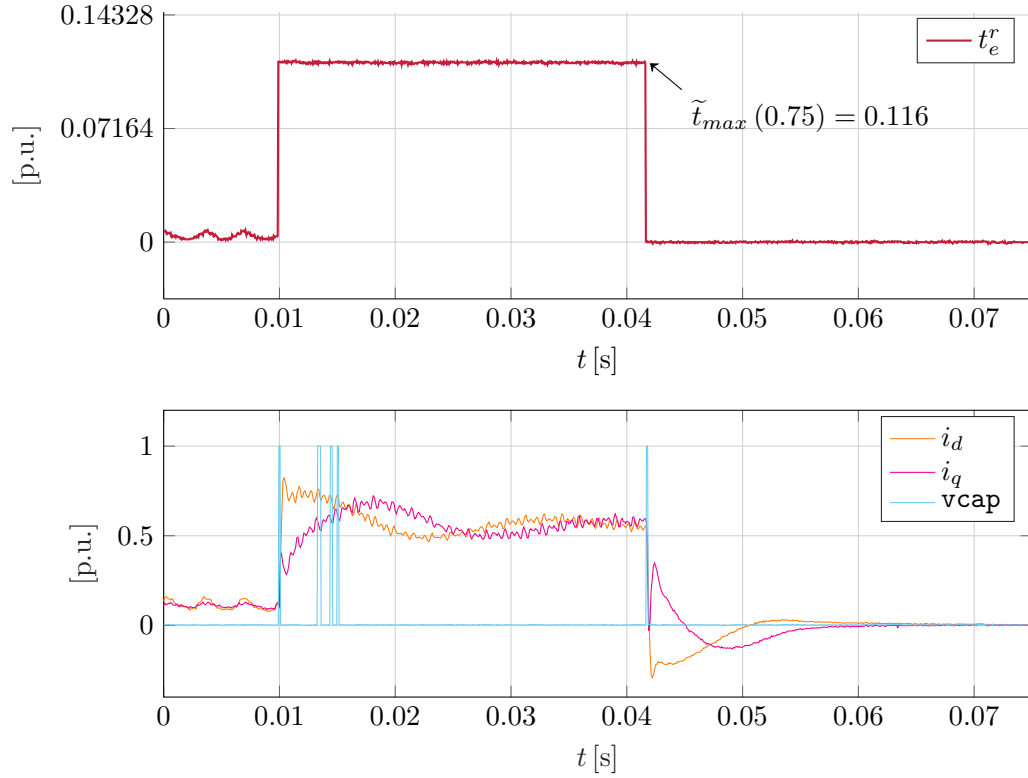
Figure 4.10: Transient limit identification experiment: valid torque injection value

If the inner cascade tips (meaning: entering and leaving) saturation during injection as it is the case in Figure 4.10 the value $\widetilde{t}_{tmp}$ has qualified for flux weakening. This qualitative condition is translated into a quantitative one by:

$$0 < \frac{\mathtt{vcapct} \cdot T_{fast}}{80 \cdot 6\,T_{fast}} \leq \frac{50\,T_{fast}}{80 \cdot 6\,T_{fast}} \approx 10.4\% \; . \tag{4.136}$$

Experiment 1 was conducted manually for all operational regions[34]. The description was given for Q1 but is valid for all other quadrants if torque and/or speed signs are changed appropriately. With proper test equipment the experiment can readily be automated to sweep over an arbitrary range of MMF angles θ^r. This would produce a large amount of identification data[35].

The result of Experiment 1 is depicted in Figure 4.11. Color codes are given with markers for acceleration and break. An indication of positive (clockwise) and negative (counterclockwise) shaft rotation allows to quickly identify each of the four operational regions. An essential figure of merit for the flux weakening control system is the smallest characteristic velocity ω_{rated}^{FW} of Figure 4.9. It marks the start of high speed regime where flux weakening algorithms become

---

[34]quadrants Q1,Q2,Q3,Q4 of the ω/t_e plane
[35]explaining the precondition of $\theta^r = 45°_{elec}$ laid down earlier for manual identification
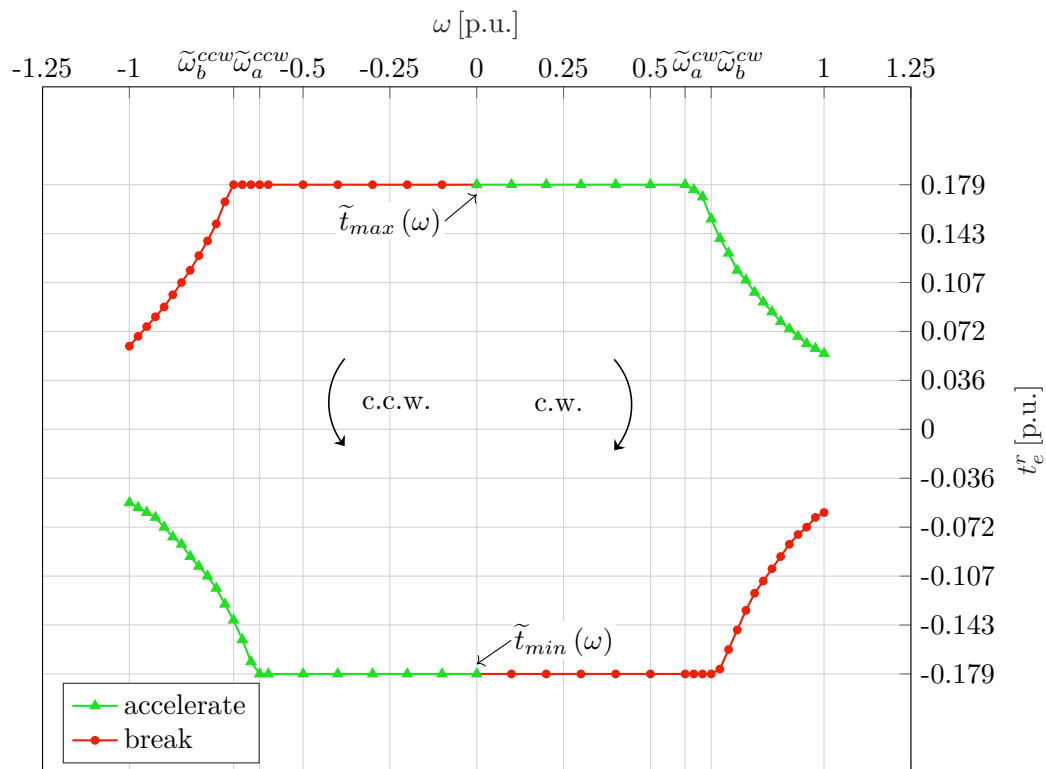
Figure 4.11: Transient torque limitations results; c.w.-clockwise; c.c.w.-counterclockwise

necessary. This velocity was identified to be

$$\omega_{rated}^{FW} = \widetilde{\omega}_a^{cw} = 0.6 \tag{4.137}$$

The experiment showed, that each quadrant is associated with a characteristic velocity, reported in the second column of Table 4.5. In absolute values the speeds for (Q1,Q3) are lower than those of (Q2,Q4). This can be explained by free shaft operation during the injection of t_e^r. When breaking torque values are injected the motor will slow down during T_{inj}, reducing the induced voltage term $j\omega\underline{\psi}^{dq}$. This will cause the inner loop to saturate later (at higher speeds) as it would be the case for accelerating maneuvers.

An in depth description of how $t_e^r|_{min}^{max}(\omega)$ from Figure 4.11 was realized within the speed controller is given in Appendix A.2. Aspects concerning system memory are also covered there.

The proposed experiment will be modified in Section 5.6 for the identification of torque limits for sensorless flux weakening at high speeds but the core ideas are retained. Statements given in Appendix A.2 concerning implementation aspects are even more true for sensorless operation.

4.7.3 Quasi-Stationary Voltage Limit

After the condition $t_e = t_e^r$ is fulfilled as the inner cascade executes the upper cascade's control command the stator voltage equation can be validly formulated as

$$\underline{u}^{dq} = r\underline{i}^{dq} + j\omega\underline{\psi}^{dq} \ , \tag{4.138}$$

$$u_d + ju_q = ri_d - \omega l_q i_q + j\left(ri_q + \omega i_d l_d\right) \tag{4.139}$$

where $\frac{\mathrm{d}}{\mathrm{d}t}\underline{\psi}^{dq}(t)$ is neglected. By inspecting Equation (4.134) and the above equations it can be qualitatively reasoned that henceforth higher speeds of ω will be achievable for given values of $t_e^r|_{min}^{max}(\omega)$ in order to fulfill Equation (4.138). Dual to that a higher amount of torque can be provided when only the less stringent quasi-stationary voltage limit is active for a (quasi[36]-)constant value of ω. So, adopting flux weakening in conjunction with a model-based quasi-stationary limit is likely to make the SynRM operate more efficiently. As previously in Section 4.7.2 the MMF angle is fixed to $\theta^r = 45\,°_{\mathrm{elec}}$ for practical reasons. A generalization will be outlined later.

Derivation, Measurements and Results

The idea of quasi-stationary flux weakening proposed here is based upon restriction of $i = \left|\underline{i}^{dq}\right|$ depending on the current shaft speed ω in order to fulfill Equation (4.138). Thereto, the absolute value of the stator voltage is calculated symbolically and related to its upper bound given by Equation (4.135).

$$\left|\underline{u}\right|^{dq} = \sqrt{u_d^2 + u_q^2} \le \left|\underline{u}\right|_{max}^{dq} \tag{4.140}$$

Substituting Equation (4.139), Equation (4.108)-Equation (4.109), $\theta^r = 45\,°_{\mathrm{elec}}$ and the abbreviations

$$a := l_d^2 + l_q^2 \tag{4.141}$$

$$b := 2r\left(l_d - l_q\right) \tag{4.142}$$

$$c := 2r^2 \tag{4.143}$$

into Equation (4.139) yields

$$\left|\underline{u}\right|^{dq} max \ge \begin{cases} \frac{i}{\sqrt{2}}\sqrt{a\omega^2 + b\omega + c} & \text{for Q1,Q3} \\ \frac{i}{\sqrt{2}}\sqrt{a\omega^2 - b\omega + c} & \text{for Q2,Q4} \end{cases} \tag{4.144}$$

where attention must be paid to the active quadrant when carrying out the above substitutions. As long as the relation Equation (4.144) is fulfilled $i = 1$, $t_e^r|_{min}^{max} = \pm 0.179$, and the motor is within nominal speed range. The quasi-stationary voltage limit is active when Equation (4.144) is read as equation. The corresponding four shaft speeds are found as solutions of the two quadratic equations by substituting $i = 1$, $\left|\underline{u}\right|_{dq}^{max} = 0.71$ and the machine parameters of Section 4.6.

---

[36]cf. Section 4.7.1

Flux Weakening Initial Velocities

Range of Operation	Limitation		Difference
	Transient	Q.stationary	
clockwise (cw)			
accelerate (Q1)	$\widetilde{\omega}_a^{cw} = 0.6$	$\bar{\omega}_a^{cw} = 0.71$	$+18.3\%$
break (Q4)	$\widetilde{\omega}_b^{cw} = 0.675$	$\bar{\omega}_b^{cw} = 0.8$	$+18.5\%$
counterclockwise (ccw)			
accelerate (Q3)	$\widetilde{\omega}_a^{ccw} = -0.625$	$\bar{\omega}_a^{ccw} = -0.725$	$+16.0\%$
break (Q2)	$\widetilde{\omega}_b^{ccw} = -0.7$	$\bar{\omega}_b^{ccw} = -0.825$	$+17.8\%$

Table 4.5: Overview of characteristic flux weakening velocities and difference from transient to quasi-stationary values.

The final deployed values of these characteristic velocities are reported in Table 4.5. There a performance boost of the nominal speed range of at least 16% is indicated when expanding the flux weakening system to adopt quasi-stationary strategies. The reported characteristic velocities in Table 4.5 and implemented flux weakening functions of Table 4.6 differ from the nominal ones as Equation (4.144) possess sensitivities to machine parameters. Even slight errors in identification may cause considerable discrepancies between nominal and real values.

Within the quasi-stationary flux weakening speed range the only degree of freedom to fulfill Equation (4.144) is the absolute value of the current space vector, which in turn can be expressed by

$$i\left(\omega\right) = \frac{\sqrt{2}\left(|\underline{u}|_{max}^{dq}\right)}{\sqrt{a\omega^2 \pm b\omega + c}} \tag{4.145}$$

depending on the active quadrant. Combining Equation (4.145) with the speed controller output expression Equation (4.111) yields the quasi-stationary flux weakening functions as

$$\bar{t}_e|_{min}^{max}\left(\omega\right) = \pm\frac{\left(i\left(\omega\right)\right)^2}{2}\left(l_d - l_q\right) \tag{4.146}$$

$$= \pm\frac{\left(|\underline{u}|_{max}^{dq}\right)^2}{a\omega^2 \pm b\omega + c}\left(l_d - l_q\right) \ . \tag{4.147}$$

Table 4.6 presents the implementation of Equation (4.147) and Figure 4.12 depicts a graphical overview of these functions. In the plot quasi-stationary flux weakening rules from Table 4.6 have been summarized as $\bar{t}_{max}\left(\omega\right) \rightarrow$ (Q1,Q2) and $\bar{t}_{min}\left(\omega\right) \rightarrow$ (Q3,Q4). Again parameter sensitivities lead to a necessity of tuning the nominal version of Equation (4.147). Thereto, a single tuning factor in the numerator of each branch was utilized. A significant performance boost compared to the transient voltage limit branches is evident in Figure 4.12 as it was the presumption at the beginning of the section.
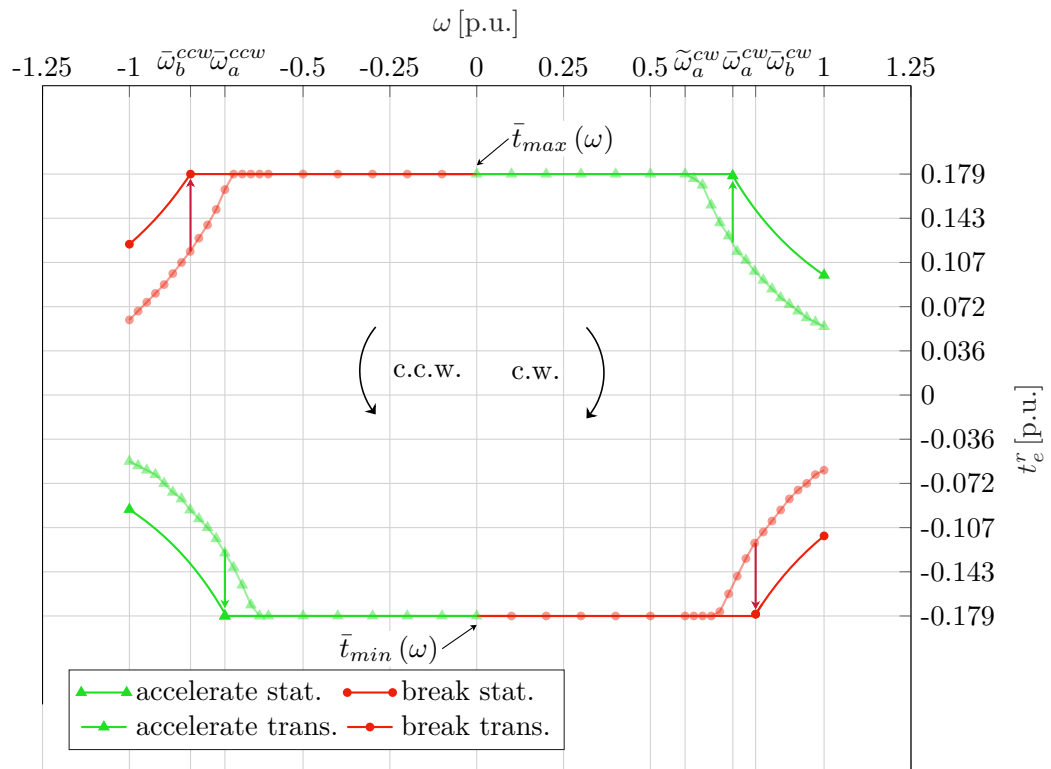
Figure 4.12: Quasi-stationary and transient torque limitations

Stationary FW Torque Limit

Range of Operation	Speed Controller Output $t_e^r\|_{min}^{max}(\omega)$
clockwise (cw)	
accelerate (Q1)	$t_e^r\|^{max} = \begin{cases} 0.179 & \text{when} \quad \omega \leq \bar{\omega}_a^{cw} \\ \frac{0.125}{a\,\omega^2 + b\,\omega + c} & \text{when} \quad \omega > \bar{\omega}_a^{cw} \end{cases}$
break (Q4)	$t_e^r\|_{min} = \begin{cases} -0.179 & \text{when} \quad \omega \leq \bar{\omega}_b^{cw} \\ \frac{-0.138}{a\,\omega^2 - b\,\omega + c} & \text{when} \quad \omega > \bar{\omega}_b^{cw} \end{cases}$
counterclockwise (ccw)	
accelerate (Q3)	$t_e^r\|_{min} = \begin{cases} -0.179 & \text{when} \quad \omega \geq \bar{\omega}_a^{ccw} \\ \frac{-0.116}{a\,\omega^2 + b\,\omega + c} & \text{when} \quad \omega < \bar{\omega}_a^{ccw} \end{cases}$
break (Q2)	$t_e^r\|^{max} = \begin{cases} 0.179 & \text{when} \quad \omega \geq \bar{\omega}_b^{ccw} \\ \frac{0.147}{a\,\omega^2 - b\,\omega + c} & \text{when} \quad \omega < \bar{\omega}_b^{ccw} \end{cases}$

Table 4.6: Overview of stationary FW torque limiting strategies

Current Circle, Voltage Ellipses, Flux Weakening Trajectory

When comparing the "breaking-" with the "acceleration" branches of Figure 4.12 the steeper slope of the latter ones becomes apparent. This can be explained by the following generalization of quasi-stationary flux weakening for SynRM. When calculating the absolute value of Equation (4.139) using Cartesian coordinates for space vector components and relating it to its maximum of $|\underline{u}|_{max}^{dq}$ the following equation can be obtained:

$$i_d^2\left(r^2 + \omega^2 l_d^2\right) + i_q^2\left(r^2 + \omega^2 l_q^2\right) + i_d i_q 2r\omega\left(l_d - l_q\right) - \left(|\underline{u}|_{max}^{dq}\right)^2 = 0 \ . \qquad (4.148)$$

At constant speed an ellipse in the (i_d, i_q) plane is described by Equation (4.148) that restricts the current space vector in order to meet the quasi-stationary voltage limitation. In the current scope all quantities of Equation (4.148) except (i_d, i_q) are to be seen as quasi-constant parameters. A depiction of three such ellipses obtained by a parameter sweep of ω (ascending) is depicted in Figure 4.13 together with the stator current circle fulfilling $|\underline{i}| = 1$. The ellipse's deformation (magnitude of eccentricity) corresponds with the machine's saliency ratio ξ leading to a circle for $\xi = 1$ and a clearly visible elliptic shape for the identified parameters of Section 4.6. Its expanse is positively correlated with available maximum stator voltage $|\underline{u}|_{max}^{dq}$ and *negatively* correlated by the shaft speed ω as depicted in Figure 4.13. A slight ccw tilt angle κ_{tilt} becomes evident when evaluating Equation (4.148) numerically.
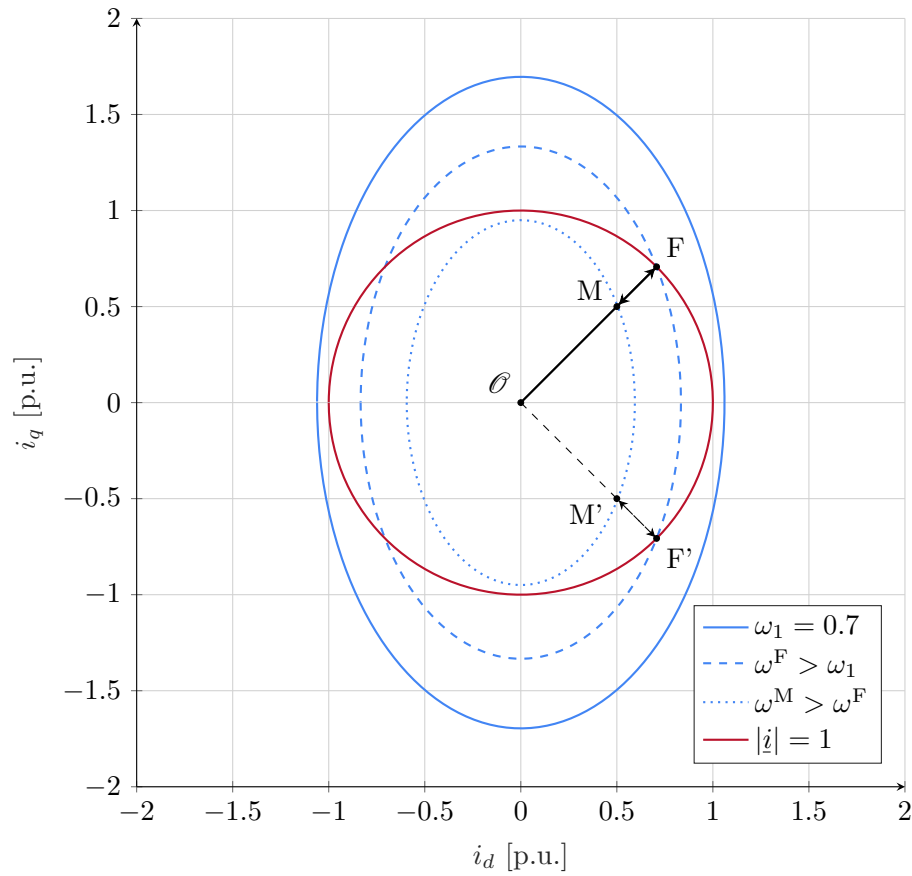
Figure 4.13: Flux weakening strategy: Q1/Q2-solid, Q3/Q4-dashed; Current circle (**red**); Voltage ellipses (**blue**); Valid current space vectors are located within the intersected area of the current circle and (active) voltage ellipse. Tilting not depicted ($r = 0$) to enhance readability.

Voltage Ellipse Tilting Angle

A derivation for a symbolic representation of κ_{tilt} is given in the following. Thereto, the principle axis theorem of linear algebra is applied, see also [61]. First, the following substitutions are applied to Equation (4.148):

$$f_d = r^2 + \omega^2 l_d^2 \tag{4.149}$$

$$f_q = r^2 + \omega^2 l_q^2 \tag{4.150}$$

$$f_{dq} = r\omega \left(l_d - l_q\right) \tag{4.151}$$

$$f_u = \left(|\underline{u}|_{max}^{dq}\right)^2 \tag{4.152}$$

to yield

$$f_d i_d^2 + 2 f_{dq} i_d i_q + f_q i_q^2 - f_u = 0 \tag{4.153}$$

$$\Leftrightarrow$$

$$[i_d \ i_q]^T \underbrace{\begin{pmatrix} f_d & f_{dq} \\ f_{dq} & f_q \end{pmatrix}}_{\mathbf{F}} \begin{bmatrix} i_d \\ i_q \end{bmatrix} - f_u = 0 \ . \tag{4.154}$$

The matrix $\mathbf{F}$ in the quadratic form of Equation (4.154) is to be diagonalized. A parameterization of the rotational matrix for $\mathbf{F}$ will then reveal κ_{tilt}. Eigenvalues λ_1, λ_2 of $\mathbf{F}$ are given by the two solutions of

$$\lambda^2 - \lambda \left(f_d + f_q\right) + f_d f_q - f_{dq}^2 \overset{!}{=} 0 \ . \tag{4.155}$$

As $\mathbf{F}$ is symmetric both eigenvalues will always be real. If Equation (4.153) is to represent an ellipse, conditions are given by $f_u > 0$ and $\lambda_1, \lambda_2 > 0$. For the next step the corresponding eigenvectors $\mathbf{v}_{F1}, \mathbf{v}_{F2}$ are obtained and normalized. The orthonormal rotational matrix $\mathbf{V}$ is defined as:

$$\mathbf{V} = \left(\mathbf{v}_{F1}; \mathbf{v}_{F2}\right) \tag{4.156}$$

These vectors are the major and minor axis of the voltage ellipse. A transformation (rotation) of the original coordinates $[i_d, i_q]$ into coordinates $\left[i_d^v, i_q^v\right]$ that are aligned with those axis is given by

$$\begin{bmatrix} i_d \\ i_q \end{bmatrix} = \mathbf{V} \begin{bmatrix} i_d^v \\ i_q^v \end{bmatrix} \tag{4.157}$$

Equation (4.154) can then be transformed into a standard form for second order curves:

$$\begin{bmatrix} i_d^v & i_q^v \end{bmatrix}^T \mathbf{V}^T \mathbf{F} \mathbf{V} \begin{bmatrix} i_d^v \\ i_q^v \end{bmatrix} - f_u = 0 \ , \tag{4.158}$$

where $\mathbf{V}^T \mathbf{F} \mathbf{V}$ is a diagonal[37] matrix that contains λ_1 and λ_2. The angle κ_{tilt} is obtained by a parameterization of the rotational matrix $\mathbf{V}$ as

$$\mathbf{V} = \begin{pmatrix} \cos(\kappa_{tilt}) & -\sin(\kappa_{tilt}) \\ \sin(\kappa_{tilt}) & \cos(\kappa_{tilt}) \end{pmatrix} \ . \tag{4.159}$$

Further insight of the tilting behavior is gained by inspecting its sensitivity for the stator resistance r and speed ω. If $r = 0$ then $\kappa_{tilt} = 0$ at constant values of l_d and l_q. The sign of κ_{tilt} is determined by the sign of ω. Its magnitude positively correlates with r (linear) and negatively correlates with ω (nonlinear). Values of up to $\pm 3°_{\mathrm{elec}}$ can be observed for the deployed SynRM operating in the nominal and flux weakening region. The sensitivity for r of κ_{tilt} at $\omega = 0.9$ is $s_\kappa \approx r \cdot 4°_{\mathrm{elec}}/(0.1\,[p.u.])$.

MTPA Line Flux Weakening

Referring to the pictured ellipses in Figure 4.13 and above explanations the flux weakening strategy proposed can be reasoned as follows[38]:

- As indicated above all current space vectors in the `MTPA` mode will be alongside the two MTPA lines $\theta^r = \pm 45°_{\mathrm{elec}}$ depending on the demanded torque.

$\mathscr{O} \to \mathrm{F}$ Within nominal speed range current space vectors are restricted to $|\underline{i}| \leq 1$ due to thermal limitations and/or maximum available inverter current. At low speeds, voltage ellipses are outside the maximum torque point F and subsequently shrink as ω increases.

$\mathrm{F} \to \mathrm{M}$ At the characteristic flux weakening velocity ($\bar{\omega}_a^{cw}, \bar{\omega}_b^{ccw}$ in this explanation) the corresponding voltage ellipse intersects with the current circle and indicates the starting point for quasi-stationary flux weakening. By a pivot of κ_{tilt} dependent on the sign of ω differences between the reported values in Table 4.5 as well as different slope-steepness visible in Figure 4.12 can be reasoned. Depending on the quadrant a tilt will let the corresponding ellipse intersect with F or F' "later/earlier" in terms of speed ω accordingly. The equations derived, implemented and reported in Table 4.6 precisely describe the reduction of a current space vector between F and M at the outer bound of a voltage ellipse as it shrinks. This process ends at M where (ideally, only) mechanical limitations become apparent and the SynRM cannot be safely operated above these very high speeds. For the system discussed in this thesis a maximum safe-to-operate speed of $\omega = 1.1$ is proposed[39]. Limits encountered in this region are discussed in the next section.

---

[37]$\mathbf{F}$ is diagonalized by $\mathbf{V}$

[38]explanations for Q1 and Q2 are given, strategies for Q3 and Q4 are depicted by F' and M' and follow accordingly

[39]This is equal to $1.83 \cdot \widetilde{\omega}_a^{cw}$ and $\approx 26\,160\,\mathrm{rpm}$. The sensor limit of $30\,000\,\mathrm{rpm}$ $(1.26@base)$ has been successfully reached but the author doesn't recommend operating the system at this speed level for longer periods.

- As an outlook to sensorless flux weakening it should be emphasized here that many considerations regarding limits noted in this section also apply to sensorless control of SynRM. In Section 5.6 a different strategy to derive $t_e^r|_{min}^{max}(\omega)$ as function of $\underline{i}^{dq}(\omega)$ will be presented. *However it is mandatory for all current space vectors to lie within the intersected area of an active voltage ellipse and the current circle in order to fulfil both thermal and electrical constraints.*

The quasi-stationary flux weakening strategy alongside the MTPA lines given above is only one possible way of operating a salient synchronous machine above the nominal speed level, cf. [8],[1],[59] and Section 4.5.3. The MTPA-line flux weakening strategy covered here has the advantage of being analytical. Hence, it can be easily calculated by the formula of Table 4.6 for an arbitrary value of ω. In Figure 4.12 and Figure 4.16 a solid line indicates the possibility to calculate the quasi-stationary limit at any speed value of interest. Thereby no identifying, saving and searching a LUT is necessary as it was the case in Section 4.7.2 and Appendix A.2. Therefore MTPA-line flux weakening as proposed here is a favorable method for implementation relating to memory usage and computational effort for embedded hardware targets such as the TI-28335 DSC.

Shift from Transient Limit to Quasi-Stationary Limit

In the preceding sections flux weakening strategies for the transient and quasi-stationary case were derived separately. This section describes processes for detection and shifting between transient limit $\left(\widetilde{t}_{min}, \widetilde{t}_{max}\right)$ and quasi-stationary limit $(\bar{t}_{min}, \bar{t}_{max})$. The matter discussed here is represented by a block between the flux-weakening source block and the actual speed controller depicted in Figure 4.8.

quasi-stationary→transient

In this case, the motor shaft is rotating at constant speed and the quasi-stationary limitations are active. The input value of the reference filter (ω^*/ω^{UI} in Figure 4.8) can be sampled as an indication to activate transient limitations immediately[40]. If this is not done the danger of plant windup is given for the same reasons stated in Section 4.7.2. The reference value filter alleviates this, but not completely.

transient→quasi-stationary

It would be inefficient to operate the motor in flux weakening range utilizing only a transient limit as clarified in Section 4.7.3. To ensure a smooth transition the usage of weighting and mixing both limits is proposed. After the expiration of T_{trans} the initial combined speed controller output limitation is given by

$$w_t = 0.9 \tag{4.160}$$

$$w_q = 0.1 \tag{4.161}$$

$$t_e^r|_{min}^{max}(\omega) = w_t \cdot \widetilde{t}|_{min}^{max}(\omega) + w_q \cdot \bar{t}|_{min}^{max}(\omega) \tag{4.162}$$

---

[40]e. g. "value change was greater than 0.25[p.u.] within the last 5 SLOW Tasks" but that can depend on the application, motor and/or mechanical load.

Where w_t and w_q denote weight values for transient and quasi-stationary limits respectively. The weights are updated each SLOW task by

$$w_t \leftarrow w_t - w_{sh} \tag{4.163}$$

$$w_q \leftarrow w_q + w_{sh} \tag{4.164}$$

until $w_q = 1$. A convenient limit shift weight value $w_{sh} = 0.011$ was found via tuning of repeatable speed-test-trajectories given in the top plot of Figure 4.15. The successful execution of this method by the speed controller is shown in Figure 4.14. Interestingly the final value of the sensitive parameter w_{sh} results to a time frame of $T_{shift} = (0.9/0.011) \cdot T_{slow} = 32.9 \, \text{ms} \approx T_{trans}$ for the shifting process. It is suggested to use this finding in other flux weakening subsystems where a transient limit is shifted towards a stationary one.

4.7.4 Sensor-Based Performance

To conduct a repeatable "stress-test" scenario for software and hardware of this prototype system, methods of generating a series of step functions were implemented. This is denoted as *trajectory planer* in Figure 4.8. One of the filtered trajectories that were used to tune the flux weakening module described in this section is visible in the top plot of Figure 4.15. The sensored SynRM control system is able to change its speed from $\omega^{obs} = 1 \rightarrow -1$ within $T_{reverse} = 950 \, \text{ms}$. This corresponds to a maximum achievable acceleration/break rate of $a_{\Delta\omega} = \pm 2.11 [\text{p.u.}]/\text{s} \mathrel{\widehat{=}} \pm 50\,250 \, \text{rpm/s}$. The FAST and SLOW Task routines execute within 43 µs and 9.6 µs. At $T_{PWM} = 67 \, \text{µs}$ this indicates a decent utilization of available resources while retaining reserves.

Additionally inspecting the second plot of Figure 4.15 four quadrant operation is obtained by controlling the torque sign via i_q. As usual breaking maneuvers are more demanding to the control system than accelerating the motor. Flux weakening is clearly indicated by a deliberate reduction of the current space vector components as proposed previously. A slight bending of ω^{obs} when the applied torque is decreased within the high speed domain is also visible.

The maximum available voltage of $|\underline{u}|_{max}^{dq}$ 0.71 is utilized, proven by a characteristic $\vee$ -like shape of the voltage curve in the bottom plot of Figure 4.15 rather than a $\vee\!\vee$ -like shape that occurs without optimization conducted previously.

An overview of the relevant software and hardware parameters configured when driving these speed trajectories is given by Table 4.7, Table 4.8 and Table 4.9. Transient and stationary load tests by applying friction to the shaft were also successfully conducted throughout the development process.

4.7.5 Resulting Characteristic Curve and Projections

The operational region was expanded beyond the base value of $\omega = 1$ that was specified at identification previously in Section 4.7.2. An extrapolation based on the acquired LUT data of Section 4.7.2 was conducted and implemented up to $\omega_{LUT}^{max} = 1.4$. Such a step is not necessary when adopting the analytical quasi-stationary approach of Section 4.7.3 as the formula of Table 4.6 can be evaluated at arbitrary values of ω. Figure 4.16 depicts these adjustments to expand the operational speed range.
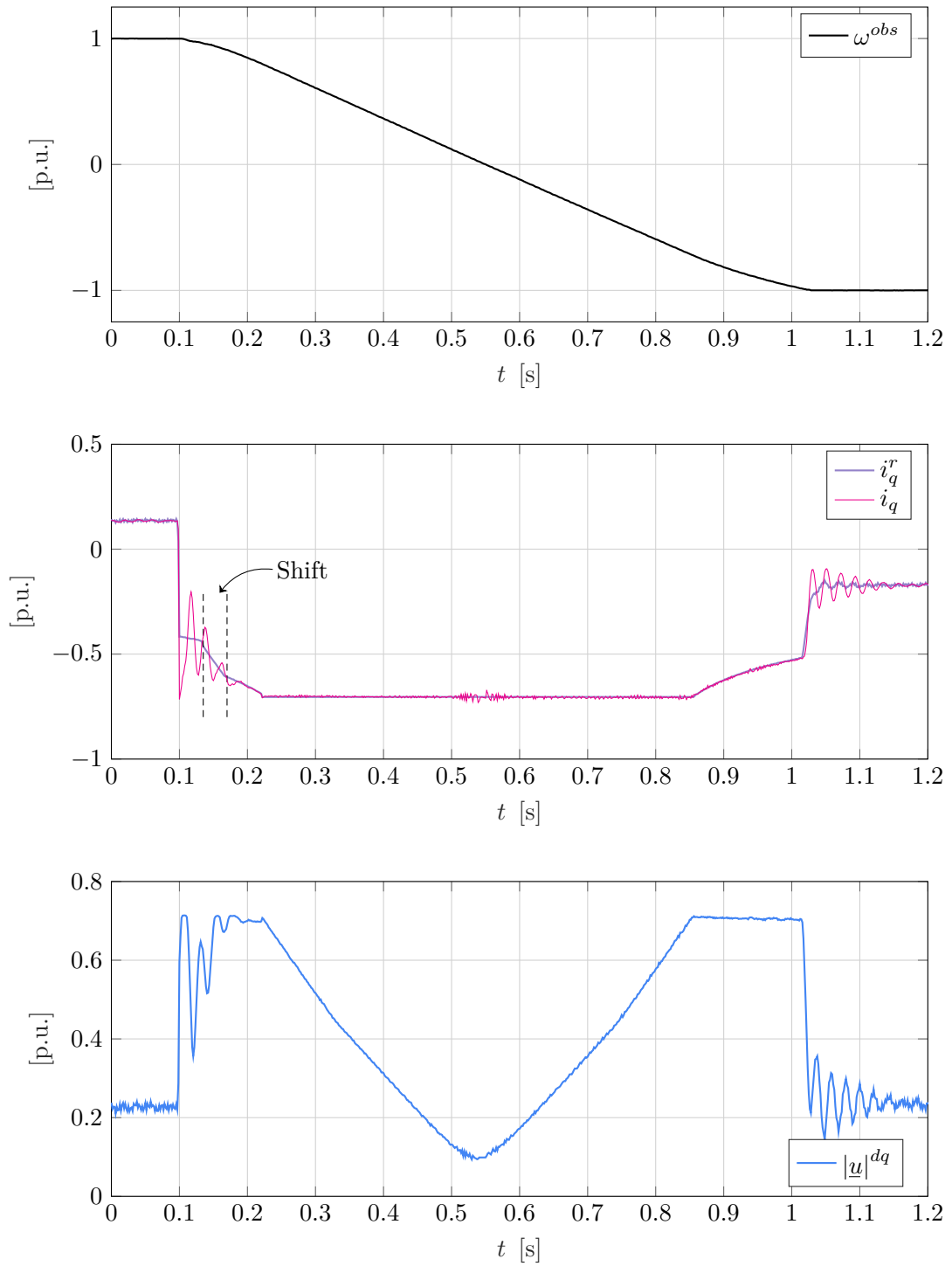
Figure 4.14: Breaking manoeuvre; Shift from transient to quasi-stationary FW torque limit; Transient limit activated from $t = 0.1$s to $t = 0.135$s at Q4 and subsequently shifted for the same amount of time to stationary FW strategy for Q4 as well as for Q3.
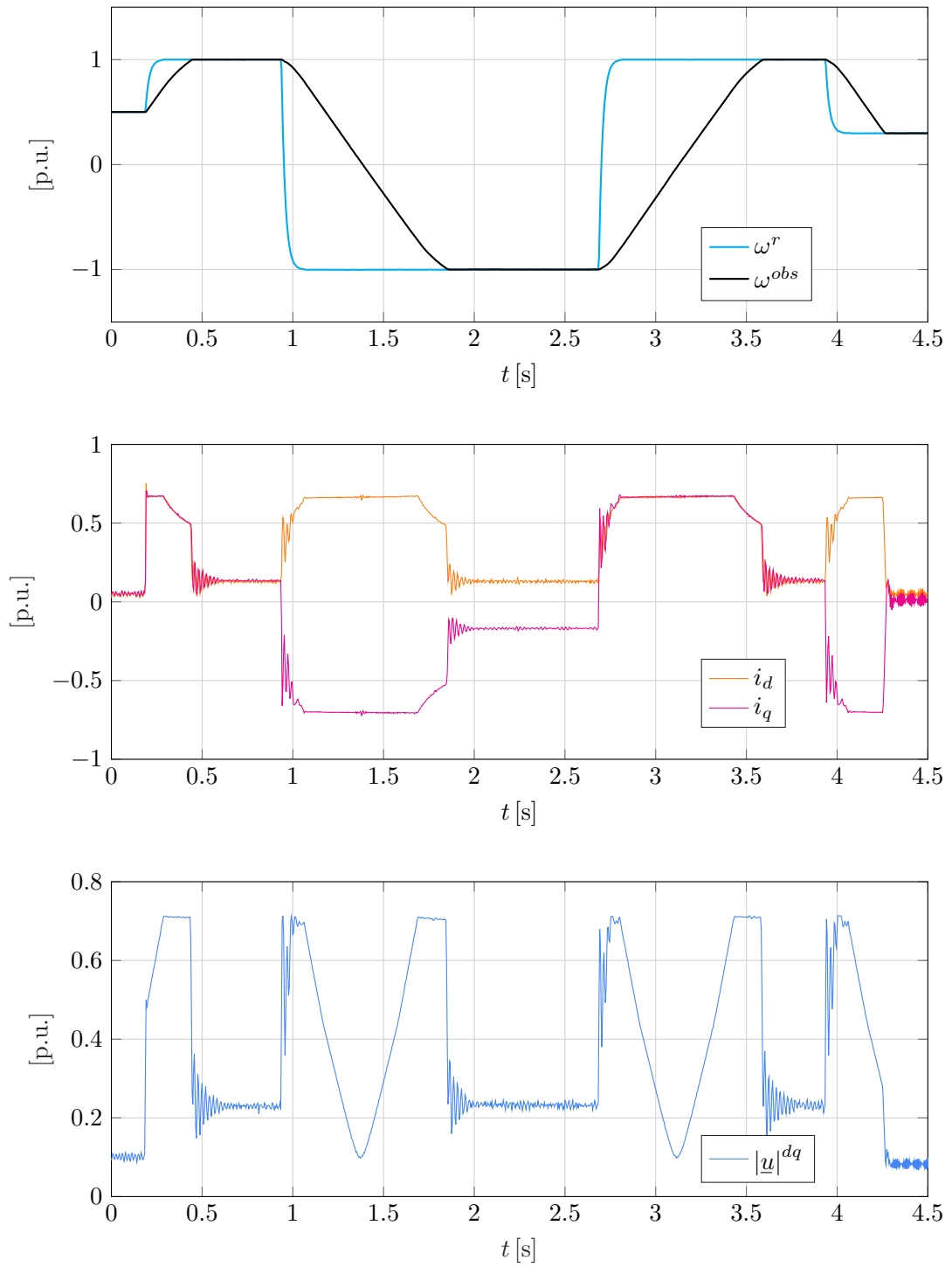
Figure 4.15: Sensor-based performance; Speed reversal manoeuvres, $50\,250\,\mathrm{rpm/s}$ break/accelera-
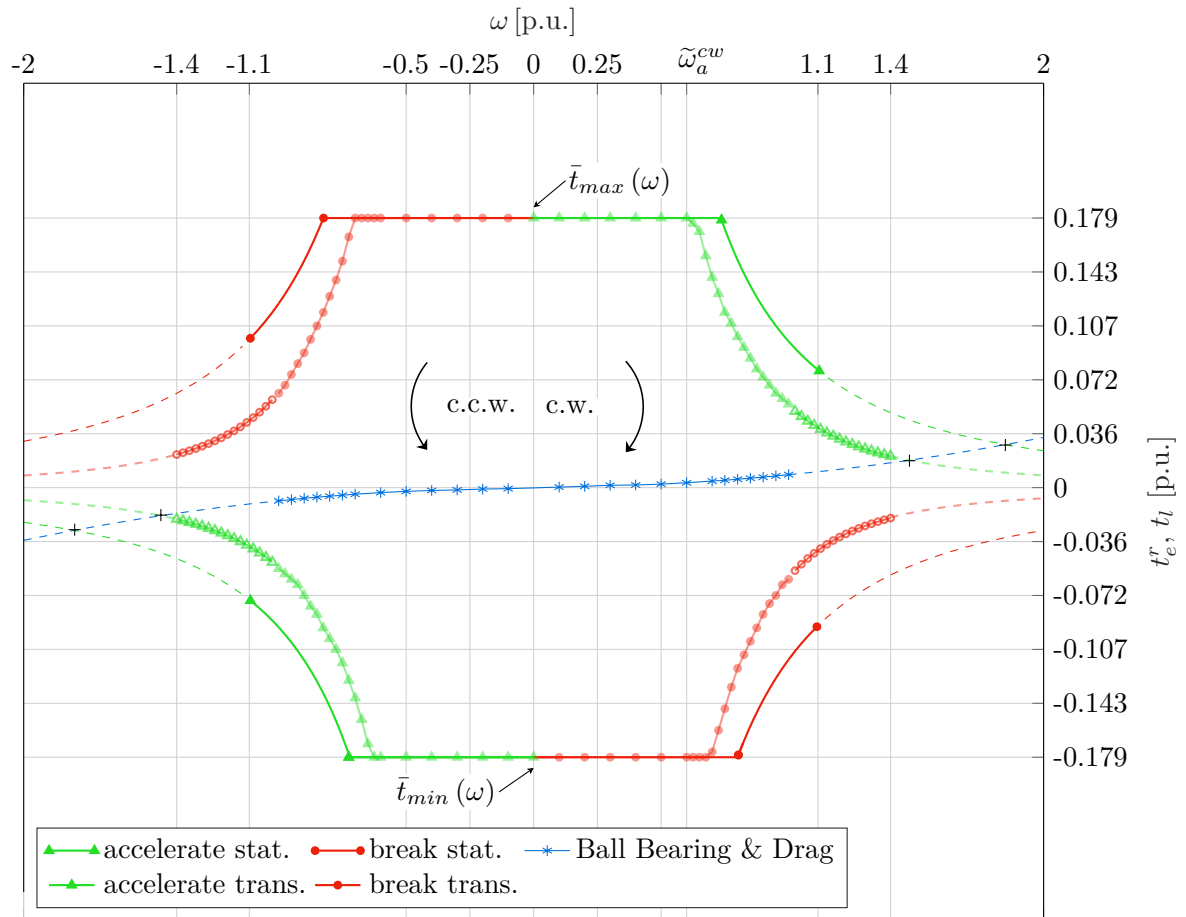tion rate.

Figure 4.16: Overall torque limitations for sensor-based operation, operational range and projections beyond reached values of $\omega = 1.1$, cf. Figure 4.12.

During testing at high velocities rotor drag and ball bearing friction torque became apparent as the speed controller's output t_e^r was monitored. A series of filtered stationary values of this quantity was measured at different speeds under no-load conditions. Using the research results of [62] a unit-based friction model of the structure

$$t_{bbd} = p_2\omega^2 + p_1\omega + p_0 \tag{4.165}$$

was fitted and is depicted in Figure 4.16 wherein dashed lines correspond to projections. It contains a viscous damping component p_1 of the ball bearings, a drag component p_2 of the rotor structure and a coulomb component p_0 for static friction. Intersecting these curves with the transient and stationary flux weakening branches indicated by + symbols yield projected absolute mechanical limitations of approximately[41] 1.47 & 1.82 corresponding to 35 krpm & 43 krpm. These limits can probably be expanded when adopting magnetic bearing for the shaft. A levitating rotor is then absent of viscous damping, i. e. $p1$ gets zero in Equation (4.165).

It is important to emphasize that models at such high speeds heavily depend on a correctly calibrated encoder, see Section 2.6.

4.7.6 Maximum Speed and Limitations

The sensored SynRM control system as proposed can be safely stationary operated up to $\omega^{max} = 1.1 \,\hat{=}\, 26\,160$ rpm. Measuring on a scale normalized to $\widetilde{\omega}_a^{cw}$ this value marks a flux weakening capability of $+83\%$. The sensor limit of $\omega_{enc}^{max} = 1.26 \,\hat{=}\, 30\,000$ rpm can be reached but currently this is not recommended for reasons to be discussed here. Starting from ω^{max} significant oscillations in i_d and i_q occur during reference changes and/or static friction load that are eventually destabilizing the system when operated within in this range. Based on the status quo given by all proposed descriptions, strategies, crucial embedded software settings, hardware fixes and tunings the following possible causes are identified:

Mechanical Limitations
The base plate hosting the motor assembly is placed on a dampening plate. An aluminum cuboid is used as mechanical connection between stator & rotor housing cylinder and base plate. No damping material is used at the contacting surface areas. Additional dampening layers are suggested. Another possible source of this current oscillating effect is the imbalanced rotor inertia. An addition and calibration of balancing shims to the shaft at an appropriate test bench could alleviate this effect. These presumptions are supported by a high acoustic noise level that rises substantially as the motor is accelerated beyond ω^{max}. Torque ripple present due to the motor design [1] is also a possible source of vibrations and noise. During development one pair of ball bearings was also worn down indicating a need for smoother mounting. Another possibility to overcome these characteristics is given by active sensorless magnetic bearing, one of the prospective long-term goals for this system.

Electrical Limitations
The optimum absolute value for the scaled voltage space vector was given in Section 4.2.2 as

---

[41]It should be noted that these values are to be read with an emphasis on the qualitative character of the statement rather than a quantitative one as two extrapolations are intersected.

function of the compulsory pulse window time $T_{PW}^{2a} = 5.98\,\mu s$ to be $|\underline{u}|_{max}^{dq} = 0.71$. This was derived in conjunction with the mandatory measurement agenda at the negative short during the PWM-period. An adoption of current transducers as measurement devices would raise the constraint of measuring inverter quantities at the negative short during the PWM-Period. Then only a mandatory bootstrap-time $T_{BT} \ll T_{PW}$ would restrict the space-vector modulation pulse pattern therefore increasing $|\underline{u}|_{max}^{dq}$. The theoretical maximum for sinusoidal commutation is given by $\sqrt{3}/2$.

An overload of U_{DC} above $60\,V$ would naturally lead to improved flux-weakening capabilities (due to more potent controllers). Investigations of this thesis were conducted at a fix value of U_{DC} for reasons of clarity. If it is taken variable, a rescaling between the current controller's output and the modulator is necessary to relate the actually available DC-link voltage to the demanded scaled $\underline{u}^{dq^r}$.

Control Theoretical Limitations

An inherent dead-time of T_{fast} is always present at discrete time control systems. From signal theory it is known that dead-times of T_D can be approximated as LTI-Transfer functions using an n-th order Padé approximation of the form [14]

$$\mathrm{e}^{-sT_D} = \frac{\left(1 - s\frac{T_D}{2n}\right)^n}{\left(1 + s\frac{T_D}{2n}\right)^n}, \qquad n \to \infty \ . \tag{4.166}$$

For arbitrary values of n Equation (4.166) states that there will be n left-hand-plane(lhp) poles and right-hand-plane(rhp) zeros in the s domain. These translate to n poles within the unity circle and n zeros outside the unity circle when transforming the n-th approximation of Equation (4.166) to an equivalent time discrete system,[54]. This arbitrary number of *additional* lhp-poles and rhp-zeros will have a detrimental effect on the overall control system. Signals present at various points of the closed control loops then may aggravate to instable behavior.

A way to overcome this is to either incorporate Equation (4.166) into the controller design as it was the case in Section 4.4.1 or simply decrease the sample time $T_{fast} = T_{PWM}$. The latter strategy of increasing the PWM-switching frequency is limited by the power-module of the VSI and by the derived reduced computation capabilities of the TI-28335 (less time to execute the same amount of instructions). As a projection the author proposes that an adjustment of $f_{PWM} = 20\,\text{kHz} \to T_{fast} = 1/f_{PWM} = 50\,\mu s$ is feasible for the sensored control mode but not for sensorless operation due to increased computational requirements present in this mode (the execution time is already slightly higher than $50\,\mu s$). A more potent DSC such as the TI-2837xS/D being of the same product family is recommended for future applications.

The Next Step

As became apparent by Section 2.6 the rotary encoder caused several problems until the results of Figure 4.15 were reached (fixation of the pill, corrupted signals and calibration issues). Sensorless motor control systems are superior in this very important aspect because they substitute a system component with a mathematical model. Chapter 5 will discuss how such a system can be implemented and how well it will perform, if compared to the control system implemented in this chapter.

Therefore, all subsequent matter builds upon the findings stated here. This indicates that in order to deploy sensorless field-oriented control successfully a strong basis of reliable software and hardware components is mandatory.

4.8 Parameter Overview

An overview of the relevant Software- and Hardware-parameters is given by the Table 4.7, Table 4.8 and Table 4.9 below. Where applicable, the values can be interpreted in conjunction with Table 2.3. Unless otherwise noted at the appropriate text passage all figures presented in this section were documented using the parameters state here. For increased readability Software parameters were split into Fast and Slow-Task quantities.

Software Setting Overview sensored/m (Fᴀꜱᴛ Task)		
Parameter	Symbol	Value
Fast-Task Period	T_{fast}	$67\,\mu s$
Space Vector Modulator		
PWM Pattern Type		2-Active (shifted)
Compulsory Pulse-Window Time (2a)	T_{PW}^{2a}	$5.98\,\mu s$
PWM-Shift Time (2a)	$T_{PW-shift}^{2a}$	$2.95\,\mu s$
PWM-Dead-Band RED/FED	T_{DB}	$1.25\,\mu s$
Observer and Encoder		
Encoder Dead-Time Correction	$k_{\gamma D}$	2.325
Refresh Rate		T_{fast}
Type		Luenberger [$\mathbf{k}$] 3×3
Closed Loop Poles	$\underline{\mathbf{z}}_{PL}$	$0.975 \cdot \underline{\lambda}_M$
Error Weight: Angle	$k_{L\gamma}$	-0.075
Error Weight: Speed	$k_{L\omega}$	-0.002188
Error Weight: Torque	k_{Lt}	0.27337
Current Controller (i_d)		
Proportional Gain	$k_P^{i_d}$	0.45
Integral Gain	$k_I^{i_d}$	0.016
Max. Reference Value (abs.)	$|i_d^r|^{max}$	1
Max. Output Value (abs.)	$|u_d^r|^{max}$	0.71
Current Controller (i_d)		
Proportional Gain	$k_P^{i_q}$	0.35
Integral Gain	$k_I^{i_q}$	0.015
Max. Reference Value (abs.)	$|i_q^r|^{max}$	1
Max. Output Value (abs.)	$|u_q^r|^{max}$	0.71
Two Degree of Freedom (FF & FB)		
2 DOF Input Quantities		(i_d^r, i_q^r)
Use Differentiator in FF Path		yes
Diff.Pre-Filter Time Const.	τ_{2DOF}	$67\,\mu s$
Max. Combined Output Value	$|\underline{u}|_{max}^{dq}$	0.71

Table 4.7: Motor control system sensored mode; Fast task; Final configuration

Software Setting Overview sensored/m (SLOW Task)

Parameter	Symbol	Value
Slow-Task Period	T_{slow}	402 µs
Speed Controller (ω)		
Proportional Gain	$k_{P\,\omega}$	7.16
Integral Gain	$k_{I\,\omega}$	0.015
Ref.Val. Filter Time Const.	τ_ω	20 ms
Max. Output Value (abs.)	$|t_e^r|^{max}$	0.179
Torque Output Mode		`MTPA`
MMF-Angle	θ	45 °$_{elec}$
Flux Weakening Subsystem		
FW Rated Speed	ω_{rated}^{FW}	0.6
FW Max. Range	ω^{max}	± 1.1(1.83 @rated)
FW Strategy (transient)		LUT (t_e^r)
FW LUT provided Speed Range	ω_{LUT}^{max}	1.4
FW Transient State duration	T_{trans}	35 ms
FW Strategy (stationary)		MTPA-line FW
FW Limit Shift weight	w_{sh}	0.011
FW Limit Shift starting-weights	w_{t0}, w_{q0}	(0.9,0.1)

Table 4.8: Motor control system sensored mode; Slow task; Final configuration

Hardware Setting Overview

Parameter	Symbol	Value
Inverter		
Nominal Bus Voltage	U_{DC}	60 V
Lower Bus Voltage Lim.	$U_{DC}|_{min}$	50 V
Upper Bus Voltage Lim.	$U_{DC}|^{max}$	71.5 V
Trip Phase Current	I_{VSI}^{max}	25.7 A (1.43@base value)
Warning Temperature	ϑ_{Warn}	60 °C
Limit Temperature	ϑ_{Lim}	70 °C
DSC TI-28335		
CPU Usage: $T_{fast}\backslash T_{slow}$, sensored		64.18%\66.57%
RAM Usage (total application)		61.65%

Table 4.9: Hardware parameters

5 Sensorless Field-Oriented Control

This chapter describes methods and functions used to obtain a reliable and robust estimation of the electric shaft position $\gamma_d \to \hat{\gamma}$ and speed $\omega \to \hat{\omega}$. These methods allow the omission of a mechanical shaft encoder in the final system. Nevertheless, a well calibrated sensor is mandatory for the development of such methods since the angular error

$$\gamma_\Delta = \hat{\gamma} - \gamma_{enc} \tag{5.1}$$

gives information about the quality of said estimations. In this thesis a target value of $|\gamma_\Delta| \leq 7.5\,°_{\text{elec}}$ for medium/high speeds was specified. In the low/medium speed range the same value was specified for the standard deviation of the angular error, viz. $\sigma_{\gamma_\Delta} \leq 7.5\,°_{\text{elec}}$. The qualitative terms *low*, *medium* and *high* in the context of this thesis are defined in Section 5.4. To increase clarity and readability of this document a comprehensive overview of used "angular" quantities in this thesis is given in Table 5.1.

Angles Overview	
Quantity	Designation & First Reference
γ, γ_e	general electric angle, Section 2.2
γ_m	mechanical d-axis position,Section 2.3
γ_d	electrical d-axis position,Section 2.3
γ_{enc}	calibrated encoder angle, Section 2.6
$\hat{\gamma}$	Luenberger observer output angle, Section 4.3
$\hat{\gamma}_d$	electric d-axis position estimation, Section 5.2
γ_Δ	angular error, Chapter 5
$\hat{\gamma}_{\text{INF}}$	raw INFORM angle, Section 5.2
$\hat{\gamma}_{\text{BEMF}}$	raw BEMF angle, Section 5.3
$\gamma_{\Delta INF}$	angular error from raw INFORM angle, Section 5.2.2

Table 5.1: Essential angular quantities used in this thesis

Chapter Overview

General functional relationships for sensorless functionality and important timing considerations are discussed in Section 5.1.

At standstill and low/medium shaft speeds the <u>In</u>direct <u>F</u>lux Detection by <u>O</u>nline <u>R</u>eactance <u>M</u>easurement (INFORM) method was deployed. Its concept and application to the SynRM drive system is described in Section 5.2. To ensure the required performance various experiments were conducted and their results are presented in Section 5.2.4.

At medium/high shaft speeds a method based on integration of the induced voltage a.k.a. <u>B</u>ack <u>E</u>lectro<u>m</u>otive <u>F</u>orce (BEMF) was deployed. Design and adoption to a SynRM of this method is discussed in Section 5.3.

Both above mentioned methods were developed independently from each other. A combination strategy of these methods to achieve sensorless operation in all speed regions up to the voltage limit is given in Section 5.4.

In Section 5.5 different sources of influence on the sensorless control system are covered together with necessary modifications. A correctly tuned observer was of essential importance for stability and performance of the overall sensorless system. Current and speed controllers also needed to be detuned to more defensive values and settings.

The ultimate goal of this thesis was to achieve very high speeds in sensorless mode. A strategy to further increase speed under constraints of voltage limitations, angle error and stability is presented in Section 5.6. A torque/speed map as result can be inspected in Section 5.6.3. Performance and compliance to all constraints is proven by representative experiments and is discussed in Section 5.7.

All results (signal trends, plots, data ect.) presented in this chapter were obtained under sensorless control. Therefore, the FOC system utilized the estimated shaft position. The encoder value only served as quality indicator.

5.1 Control Strategy

Figure 5.1 gives a functional overview of the estimation part of the sensorless FOC system. Three blocks are necessary to substitute/replace the mechanical encoder presented in Section 2.6: INFORM, SynRM-BEMF and a Mix & Switch block. Each subsystem is described in detail in the subsequent chapters.

In sensorless control it is always necessary to use a dedicated observer structure[1] to smooth the raw-angle(s) $\hat{\gamma}_{\text{INF}}$ and $\hat{\gamma}_{\text{BEMF}}$ for control. If Park and Inverse Park transformations are carried out using these raw angles only, the system tends to become unstable in most cases. Furthermore, the observer yields an estimation of shaft speed $\hat{\omega}$ that is required for speed control.

At each FAST Task, a prediction for angle and speed is calculated by the observer. This prediction is then used *without further correction* in the *consecutive* FAST task for coordinate system transformations. A correction of the predicted angle is obtained by feeding the difference e_γ between sensorless raw angle and last valid predicted angle into the observer structure as defined in Section 4.3. Therefore, the general sensorless control strategy can be reasoned as predictor-corrector scheme.

---

[1]such as the proposed full order Luenberger Observer or other common approaches from control theory such as Kalman Filter ect.
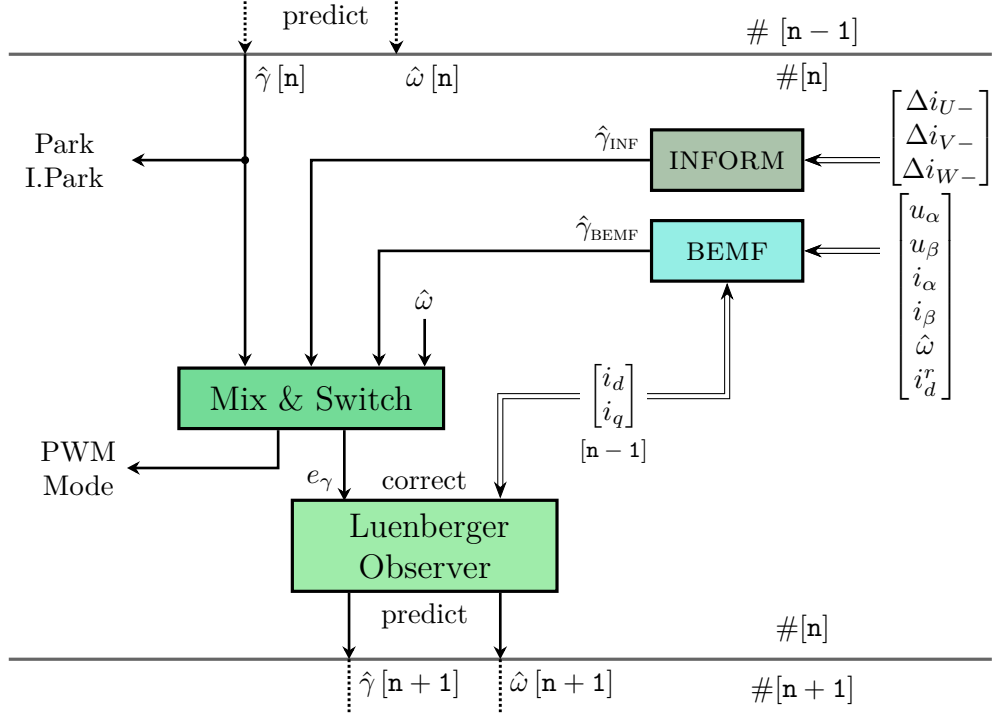
Figure 5.1: Functional overview of sensorless angle and speed estimation. Predictor-Corrector scheme. A schematic discrete time scale in terms of three consecutive FAST Tasks is indicated from top to bottom. The situation in task $\#[\mathtt{n}]$ is highlighted.

At high electric frequencies the exact timing and correct order for evaluating all functional blocks in Figure 5.1 is crucial. Input quantities such as current slopes and $(\alpha\beta)$- currents are measured during or at the end of FAST Task $\#[n-1]$, see measurement agendas in Section 4.2 and Section 5.2.3. The measurements are read out at the beginning of FAST Task $\#[n]$ and used to calculate raw angles from BEMF and INFORM models. As voltages, the currently active current controller output voltages during the preceding FAST Task $\left(u_\alpha^r, u_\beta^r\right)$ are used. Rotor referred current values (i_d, i_q) calculated at the preceding FAST Task $\#[n-1]$ are taken as input values in the actual FAST Task $\#[n]$.

Any combination and strategy other than the one proposed here resulted in unstable behavior of the SynRM drive during testing. This can be explained by a worst-case dead time of $T_{fast} = 67\,\mu s$ when choosing a different sample instant than discussed. In Section 2.6, Equation (2.110) related angular measurement error to sensor dead-time and mechanical shaft speed. Intuitively the same relationship applies when estimating[2] the shaft angle. The above mentioned dead-time of T_{fast} then corresponds to an error of $19.2°_{\text{elec}}$ at $\omega = 1$. This situation only aggravates when calculating the estimated position within the SLOW Task. Therefore it is highly recommended to perform all sensorless related measurements and calculations within the FAST Task to achieve high speeds and low angular error values.

---

[2]viz. "measuring"

5.2 INFORM Method

The <u>In</u>direct <u>F</u>lux Detection by <u>O</u>nline <u>R</u>eactance <u>M</u>easurement (INFORM) method allows for sensorless rotor position detection based upon motor phase current slope measurements. It was invented and developed by o.Univ.-Prof. Dipl.Ing. Dr.techn. Manfred Schrödl during the late 1980's and early 1990's. Since then numerous variants, improvements and expansions have been published, see Section 5.2.1. Essentially, the method utilizes *measurable*[3] induction variations induced by magnetic conductivity changes alongside the circumference of an electric machine. These magnetic conductivity changes in turn are caused by *position dependent* saturations of stator/rotor/yoke, and/or geometrical variations of magnetic conductive material. As discussed in Section 2.4, SynRM are inherently built to comprise "geometrical variations of magnetic conductive material". Therefore, they are promising candidates for the application of the INFORM method.

5.2.1 Classification

A comprehensive theoretical foundation of this method was given in the habilitation thesis of Prof. Schrödl, [63]. Extensive research on the method's application for PMSM[4] was issued in the dissertations [64], [65], [66], [67] and [68].

    Due to the high number of publications a need to classify the deployed INFORM method arises. Referring to the above resources and Section 5.2.2 the implemented INFORM variant can be categorized as follows:

- Small signal variant with sinusoidal commutation[5] of space vectors. This is referred to as "classical-" INFORM.

- As PWM voltage injection function the *3-active pulse pattern* is used in the $\overline{\text{UVW}}$ variant, see Section 5.2.3. This subject matter is protected by the European patent [69]. An INFORM angle $\hat{\gamma}_{\text{INF}}$ is calculated and processed each FAST Task, see Figure 5.1. This recent invention ensures high control bandwidth and also minimizes mechanical vibrations and induced noise by the method. Such effects may arise when dedicated PWM voltage injection functions are used in each phase to obtain $\hat{\gamma}_{\text{INF}}$. Thus, this is also called "silent-" INFORM.

- The angle $\hat{\gamma}_{\text{INF}}$ is obtained as argument of the complex parameter $\underline{c}_{INF}$, derived in the next section. Said parameter is constituted by a (complex) linear combination of measured phase current slope values along three different spatial axes in the $(\alpha\beta)$- reference frame. These measured phase current slopes represent real part values of generalized complex current slopes. This procedure is therefore called "real part evaluation" of the INFORM method

5.2.2 INFORM Algorithm

This section derives a formula to obtain $\hat{\gamma}_{\text{INF}}$ based upon current measurements only. Initially an idealized formula of "classical" INFORM will be derived based on known literature [66],[68] and [6]. This is designated as the *idealized* INFORM method here. Subsequently, it is adapted for application of SynRMs in the scope of this thesis. An assessment whether prior stated design

---

[3]current slopes are measured

[4]Permanent Magnet Synchronous Machines

[5]A Brushless DC- variant of INFORM has also been invented and is described in dissertations [67] and [68].

targets can be met is carried out. The designation for that implemented method in this document is the *realized* INFORM variant.

The Idealized INFORM Method

The method is based upon measuring inductance variations while injecting voltage pulses[6]. Therefore, the use of a VSI is mandatory. During a short time period in the scale of microseconds two anti-parallel voltage space vectors $\underline{u}_1$, $\underline{u}_2 = -\underline{u}_1$ are applied to the motor. The system's response is given by (scaled) stator voltage equations written in an arbitrary coordinate system,

$$\underline{u}_1 = r\underline{i}_1 + \frac{\mathrm{d}\underline{\psi}_1}{\mathrm{d}t} + \mathrm{j}\omega_1\underline{\psi}_1 \tag{5.2}$$

$$\underline{u}_2 = r\underline{i}_2 + \frac{\mathrm{d}\underline{\psi}_2}{\mathrm{d}t} + \mathrm{j}\omega_2\underline{\psi}_2 \stackrel{!}{=} -\underline{u}_1 \tag{5.3}$$

Due to the short time scale the assumptions $\omega_1 = \omega_2$, $\underline{i}_1 = \underline{i}_2$ are justified. By calculating the difference between the above equations, stator resistor voltage losses and induced voltage terms cross each other out[7]. Consequently the method's temperature and speed dependencies are minimized. The remaining terms are split into a complex inductance $\underline{l}_{INF}$ and complex current derivatives:

$$\underline{u}_1 - \underline{u}_2 = 2\underline{u}_1 = \frac{\mathrm{d}\underline{\psi}_1}{\mathrm{d}t} - \frac{\mathrm{d}\underline{\psi}_2}{\mathrm{d}t} := \underline{l}_{INF}\left(\frac{\mathrm{d}\underline{i}_1}{\mathrm{d}t} - \frac{\mathrm{d}\underline{i}_2}{\mathrm{d}t}\right) \tag{5.4}$$

Further calculations can be considerably simplified by introduction of the reciprocal value of $\underline{l}_{INF}$. In [63] it was shown that this complex INFORM admittance can be parametrized as follows:

$$\underline{y}_{INF_{1,2}} := \frac{1}{\underline{l}_{INF}} = \ldots = y_0\, e^{\mathrm{j}(arg(\underline{u}_1))} - \Delta y\, e^{\mathrm{j}(2\hat{\gamma}_{d-1} - 2\cdot arg(\underline{u}_1))} \tag{5.5}$$

The locus of Equation (5.5) is a circle in the complex plane located at $y_0\, e^{\mathrm{j}(arg(\underline{u}_1))}$ with a radius of Δy. The variable quantity $\hat{\gamma}_{d-1}$ denotes the angle between applied voltage shot $\underline{u}_1$ and "axis of highest magnetic conductivity"(called INFORM-axis). In synchronous machines two such axes exist per definition: Either in $\pm$d, or in $\pm$q direction depending on the machine's construction. That means in terms of magnetic conductivity, circumstances repeat every $180\,°_{\mathrm{elec}}$ and subsequently $\underline{y}_{INF_{1,2}}$ has a periodicity of $180\,°_{\mathrm{elec}}$. The fundamental message of Equation (5.5) is that the INFORM admittance $\underline{y}_{INF_{1,2}}$, found by applying voltages pulses, comprises rotor position information.

An illustration and example of Equation (5.5) is given in Figure 5.2. The voltage pulses $\underline{u}_{U+}, \underline{u}_{U-}$ are applied and $\underline{y}_{INF,U\pm}$ is plotted. In this case Equation (5.5) resembles to

$$\underline{y}_{INF,U\pm} = y_0 - \Delta y\, e^{\mathrm{j}(2\hat{\gamma}_d)}\ . \tag{5.6}$$

---

[6]In this context these pulses are often called "shots".
[7]Thereby a "small signal consideration" is applied.

Figure 5.2: INFORM admittance and locus for applied voltage space vectors $\underline{u}_{U+}, \underline{u}_{U-}$. Positive d-axis as INFORM axis depicted. Absence of noise and perfect estimation assumed, viz. $\hat{\gamma}_d = \gamma_d$. A full electric revolution causes $\underline{y}_{INF,\pm U}$ to circle twice. Modified from previous INFORM publications, such as [3].

The INFORM angle is introduced as estimation of the doubled positive d-axis angle,

$$\hat{\gamma}_{\text{INF}} = 2\hat{\gamma}_d . \tag{5.7}$$

According to [66], [68] and [6] the parameters y_0 and Δy can be linked to the machines direct and quadrature axes as

$$l_d = \frac{1}{y_0 \mp \Delta y} \tag{5.8}$$

$$l_q = \frac{1}{y_0 \pm \Delta y} . \tag{5.9}$$

The use of a plus or minus sign depends on the machine under consideration. Above equation also implies that a significant machine saliency $l_d \neq l_q$ is required to successfully use the INFORM method. Otherwise the circle in Figure 5.2 would degenerate towards a point at y_0 and $\underline{y}_{INF,U\pm}$ would no longer comprise rotor position information.

A direct calculation of $\underline{y}_{INF_{1,2}}$ by means of Equation (5.4) would theoretically allow to obtain $\hat{\gamma}_{\text{INF}}$. But the estimation's quality would depend on knowledge of the parameters y_0 and Δy. Therefore, a different approach is usually taken that enables a calculation of $\hat{\gamma}_{\text{INF}}$ using only measured values. The definition of $\underline{y}_{INF_{1,2}}$ together with Equation (5.4) allows to express complex current slopes directly as

$$\Delta \underline{i}_1 - \Delta \underline{i}_2 = \Delta \underline{i}_{1,2} = \underline{y}_{INF_{1,2}} \; u_1 e^{j\gamma_1} \Delta \tau . \tag{5.10}$$

In the above equation the difference quotient was used and both anti-parallel vectors $\underline{u}_1 = u_1 e^{j\gamma_1}$, $\underline{u}_2 = -\underline{u}_1$ are applied for a duration of $\Delta\tau$. In standard two level VSI six non-zero voltage space vectors are available, see Table 2.6. Three pairs of anti-parallel voltage space vectors can be applied to yield three different INFORM admittances. Substituting these anti-parallel pairs into Equation (5.10) yields

$$\Delta \underline{i}_{U\pm} = \underline{y}_{INF,U\pm} \; u e^{j0\,°_{\text{el}}} \, \Delta\tau \tag{5.11}$$

$$\Delta \underline{i}_{V\pm} = \underline{y}_{INF,V\pm} \; u e^{j120\,°_{\text{el}}} \, \Delta\tau \tag{5.12}$$

$$\Delta \underline{i}_{W\pm} = \underline{y}_{INF,W\pm} \; u e^{j240\,°_{\text{el}}} \, \Delta\tau \tag{5.13}$$

In terms of notation Equation (5.5) holds for each of the above equations. It is prudent to relate the above equation set for complex current slope values to real value representations. Thereto, each of the above equation is transformed into a coordinate system whose real axis coincides with the voltage shot's direction. Then the real parts of these quantities are evaluated to yield

$$\Re\{\Delta \underline{i}_{U\pm}\} = \Delta i_{U\pm}^m = u\,\Delta\tau\,[y_0 - \Delta y \cos{(2\hat{\gamma}_d)}] \tag{5.14}$$

$$\Re\{\Delta \underline{i}_{V\pm} \cdot e^{-j120\,°_{\text{el}}}\} = \Delta i_{V\pm}^m = u\,\Delta\tau\,[y_0 - \Delta y \cos{(2\,(\hat{\gamma}_d - 120\,°_{\text{el}}))}] \tag{5.15}$$

$$\Re\{\Delta \underline{i}_{W\pm} \cdot e^{-j240\,°_{\text{el}}}\} = \Delta i_{W\pm}^m = u\,\Delta\tau\,[y_0 - \Delta y \cos{(2\,(\hat{\gamma}_d - 240\,°_{\text{el}}))}] \tag{5.16}$$

The above current slope differences are given by

$$\Delta i_{U\pm}^m = \Delta i_{U+} - \Delta i_{U-} \tag{5.17}$$

$$\Delta i_{V\pm}^m = \Delta i_{V+} - \Delta i_{V-} \tag{5.18}$$

$$\Delta i_{W\pm}^m = \Delta i_{W+} - \Delta i_{W-} \tag{5.19}$$

where Δi_{U+} is the current slope magnitude measured in phase U while $\underline{u}_{U+}$ is applied for a duration of $\Delta\tau$. At least two current values at different time instants ($t_1 < t_2$) need to be measured to obtain $\Delta i_{U+} = i_U\,(t_2) - i_U\,(t_1)$. The other values follow accordingly.

To eliminate the offset values on the right hand side of equations (5.14), (5.15) and (5.16) a complex linear combination is calculated as

$$\underline{c}_{INF}^{ideal} \coloneqq (\Delta i_{U\pm}^m) + (\Delta i_{V\pm}^m) \cdot e^{j240\,°_{\text{el}}} + (\Delta i_{W\pm}^m) \cdot e^{j120\,°_{\text{el}}} \; . \tag{5.20}$$

The quantity $\underline{c}_{INF}^{ideal}$ comprises information of the rotor's position. An evaluation of Equation (5.20) considering equations (5.14), (5.15) and (5.16) yields:

$$arg\{\underline{c}_{INF}^{ideal}\} = 2\,\hat{\gamma}_d \pm 180\,°_{\text{el}} \; . \tag{5.21}$$

Plotting the locus of $\underline{c}_{INF}^{ideal}$ is often done to indicate the quality of the implemented IN-FORM method. These figures ideally depict circles centered around the origin of the complex plane such as shown in Figure 5.7. As stated in the beginning of this section the calculated INFORM axis is $\pm d$ if $l_d > l_q$. To eliminate this uncertainty several methods have been proposed in the above cited dissertations. For salient pole SynRM however, this uncertainty is irrelevant as both d-axes are equal from a magnetic and control theoretical perspective.

The Realized INFORM Variant

The above presented process is adapted for the deployed sensorless control system. Generally speaking several simplifications are implemented that introduce systematic errors if compared to the algorithm above. These effects are *deliberately* accepted in order to gain higher control bandwidth (viz. stator voltage) and reduce computation time.

From a research perspective it is expedient to investigate if such modifications still enable the system to reach goals set up in Chapter 1 and the beginning of this chapter (robust control). Furthermore it is advantageous for future projects to identify, clarify and quantify prior stated trade-off.

The most significant difference compared to the previously presented idealized INFORM method is the use of three instead of six voltage shot space vectors. For the deployed INFORM variant $\underline{u}_{U-}$, $\underline{u}_{V-}$ and $\underline{u}_{W-}$ were used. These three space vectors also serve to adjust a reference voltage space vector $\underline{u}^r$ by means of the so-called 3-active space vector modulation presented in the next section. Using this approach unifies current control and INFORM angle evaluation. In many earlier applications these subsystems were separated. Three pairs of dedicated anti-parallel "shots" as described above were applied interrupting the current controller. As consequences, mechanical vibrations and decreased control bandwidth had to be accepted. The proposed 3-active method is superior in both aspects. The cost in return are variable shot times $\Delta\tau \neq const.$ and decreased maximum stator voltage magnitude $|\underline{u}|_{max}^{dq} < 1/2$.

Figure 5.3 and Figure 5.4 illustrate the use of said space vectors in the complex plane and time domain. Each shot has a different duration and $t_{U-} + t_{V-} + t_{W-} = T_{PWM}$. Due to a mandatory settling time to compensate for transient phenomena at the analogue ADC interface[8] the available current slope measurement time is lower than the pulse width time. The current measurement therefore starts at points I,III,V in Figure 5.4. This measurement time is further decreased by an arbitrary offset from the ending pulse edge to provide a window for ADC measurement and end-of-conversion processing[9] at points II,IV,VI. These offsets are designated as Starting-/Ending Edge Offset t_{SEO}, t_{EEO}, an overview can be found in Table 5.5. Representative for phase U this means the current slope magnitude is measured via two point difference during t_{U-}^m,

$$t_{U-} = t_{SEO} + t_{U-}^m + t_{EEO} \tag{5.22}$$

$$\Delta i_{U-}^m = \frac{1}{2}\left(i_U^m|_{II} - i_U^m|_I\right) \ . \tag{5.23}$$

To connect to the above INFORM equations an average shot time is calculated together with a normalized current slope magnitude $\Delta i_{U-}^{m,n}$,

$$t_{AVG}^m = \frac{t_{U-}^m + t_{V-}^m + t_{W-}^m}{3} \tag{5.24}$$

$$\Delta i_{U-}^m = \Delta i_{U-}^{m,n} \cdot \frac{t_{U-}^m}{t_{AVG}^m} \ . \tag{5.25}$$

---

[8]a value of $\approx 5\,\mu s$ was measured at the inverter
[9]Equation (3.3) yielded $2.2\,\mu s$ for four current samples taken at the end of the slope.
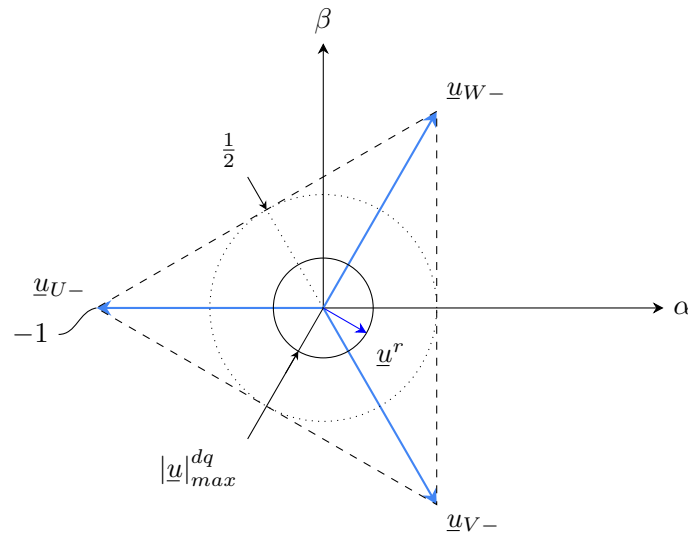
Figure 5.3: Available inverter voltage space vectors for 3-active SVM using negative vectors Maximum orbits (theoretical and practical). Example voltage reference space vector is $\underline{u}^r = 0.22e^{-j30^\circ_{el}}$.

Equation (5.25) is substituted into Equation (5.14) with $\Delta\tau \triangleq t^m_{U-}$. The other phases follow accordingly. Then the same approach is taken as before to yield the complex parameter $\underline{c}_{INF}$ as

$$\underline{c}_{INF} = \left(\Delta i^{m,n}_{U-}\right) + \left(\Delta i^{m,n}_{V-}\right) \cdot \mathrm{e}^{\mathrm{j}240^\circ_{el}} + \left(\Delta i^{m,n}_{W-}\right) \cdot \mathrm{e}^{\mathrm{j}120^\circ_{el}} \tag{5.26}$$

$$= \underbrace{\frac{1}{2}\left(2\Delta i^{m,n}_{U-} - \Delta i^{m,n}_{V-} - \Delta i^{m,n}_{W-}\right)}_{\Re\{\underline{c}_{INF}\}} + \mathrm{j}\underbrace{\frac{1}{2}\left(\sqrt{3}\,\Delta i^{m,n}_{W-} - \sqrt{3}\,\Delta i^{m,n}_{V-}\right)}_{\Im\{\underline{c}_{INF}\}}, \tag{5.27}$$

and finally

$$\hat{\gamma}_{\mathrm{INF}} = arg\{\underline{c}_{INF}\} = \mathrm{atan}\left(\frac{\Im\{\underline{c}_{INF}\}}{\Re\{\underline{c}_{INF}\}}\right). \tag{5.28}$$

At zero speed and zero stator resistance ($r = 0$) both idealized and realized complex IN-FORM quantities $\underline{c}^{ideal}_{INF}$ and $\underline{c}_{INF}$ are equal. Under all other operational circumstances the omission of anti-parallel test shots introduces systematical errors when calculating $\hat{\gamma}_{\mathrm{INF}}$. These errors will depend on speed, current magnitude and temperature, see equations (5.2)-(5.4). A speed dependent error was equalized using a heuristic correction factor. All other errors need to be compensated by the observer. An assessment of the resulting quality is presented in Section 5.2.4.

5.2.3 Three Active Space Vector Modulation

By inspection of Figure 5.4 it becomes clear that a minimum measurement time within all three phases is mandatory in order to obtain reliable current slope values. Ultimately calculated pulse
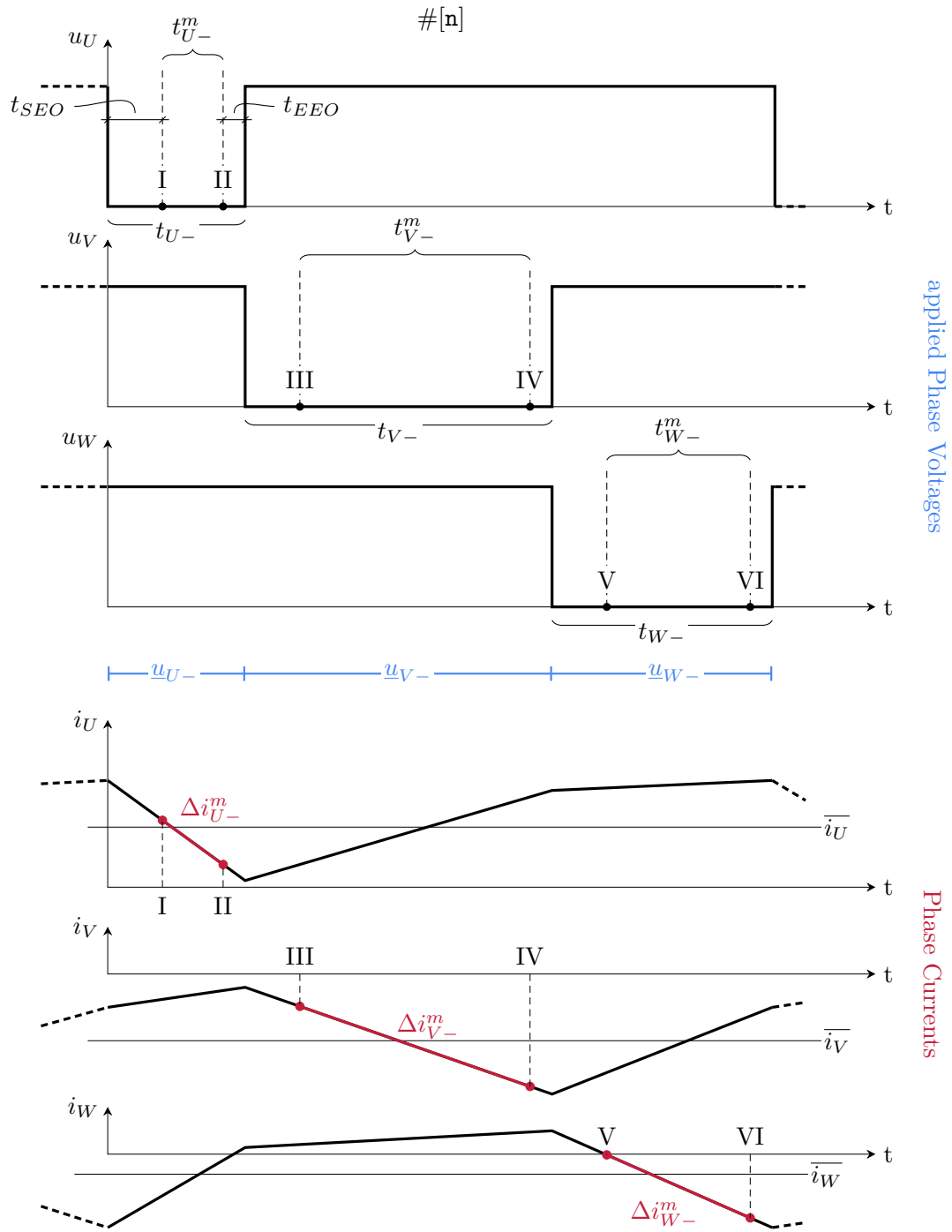
Figure 5.4: Three active SVM and INFORM measurement agenda, applied phase voltages (scaled) and motor response by current slopes. These slopes are semantically correct but exaggerated for this figure. The depicted voltage reference space vector is $\underline{u}^r_{\alpha\beta} = 0.22e^{-j30^\circ_{el}}$. Dead-Band effects from PWM modulator output not shown. Mandatory offsets t_{SEO} and t_{EEO} apply equally within each phase.

width values depend on the current controllers output that ensures $\overline{i_U}, \overline{i_V}, \overline{i_W}$ by application of a combination of $\underline{u}_{U-}, \underline{u}_{V-}, \underline{u}_{W-}$. By restricting the current controllers output in 3-active mode such a minimum pulse width can be ensured. This is laid down in this section.

Principle of Operation

A reference voltage space vector $\underline{u}^r = u_\alpha^r + \mathrm{j}u_\beta^r$ can be represented by a superposition of three positive or negative voltage space vectors:

$$T_{PWM}\underline{u}^r = t_{U\pm}\underline{u}_{U\pm} + t_{V\pm}\underline{u}_{V\pm} + t_{W\pm}\underline{u}_{W\pm} \tag{5.29}$$

$$T_{PWM} = t_{U\pm} + t_{V\pm} + t_{W\pm} \ . \tag{5.30}$$

The 3-active modulation method was introduced in [68] and derived appropriate pulse widths for a combination of $\underline{u}_{U+}, \underline{u}_{V+}, \underline{u}_{W+}$ to realize $\underline{u}^r$:

$$\frac{t_{U+}}{T_{PWM}} = \frac{1}{3} + \frac{2}{3}u_\alpha^r \tag{5.31}$$

$$\frac{t_{V+}}{T_{PWM}} = \frac{1}{3} - \frac{1}{3}u_\alpha^r + \frac{1}{\sqrt{3}}u_\beta^r \tag{5.32}$$

$$\frac{t_{W+}}{T_{PWM}} = \frac{1}{3} - \frac{1}{3}u_\alpha^r - \frac{1}{\sqrt{3}}u_\beta^r \ . \tag{5.33}$$

To implement this method at the TI-28335 ePWM module, compare values need to be calculated from the above equations and linked to output action events[10], see [48]. As in Section 4.2 the "Up-Count Mode" is recommended. Consequently, the carrier signal has a sawtooth-like shape.

The SynRM of this thesis was controlled using the set $\underline{u}_{U-}, \underline{u}_{V-}, \underline{u}_{W-}$. Currents are always measured at low-side bridge shuts. Therefore, a current can only be measured if the corresponding phase is connected to the half bridge's low side[11]. Using negative patterns allows to measure $i_U^m|_I$ and $i_U^m|_{II}$ directly during t_{U-}^m. For each current measurement point (I-VI) in Figure 5.4 the median value of four consecutive samples is taken as measured current, see Section 2.5 and Section 3.4. If $\underline{u}_{U+}, \underline{u}_{V+}, \underline{u}_{W+}$ are used in an alternative configuration, phase currents in phase V and phase W have to be measured during t_{U+}^m. Kirchhoff's law then yields $i_U^m|_{I,II,+}$. In this case eight additional samples are needed. To ensure the *same* minimum pulse width for current slope measurement as in the "negative-shot" case, the space vector's reference magnitude would need to be reduced. This trade-off is quantified at the end of this section. In a nutshell, when using low-side bridge shunts and 3-active space vector modulation the use of $\underline{u}_{U-}, \underline{u}_{V-}, \underline{u}_{W-}$ maximizes the available voltage space vector and thus tends to improve control bandwidth.

The appropriate pulse widths to combine $\underline{u}_{U-}, \underline{u}_{V-}, \underline{u}_{W-}$ are found using the real and imaginary part of

---

[10]such as Gate-Driver switching signals and ADC start of conversion (SOC) commands to realize measurement points I-VI in Figure 5.4

[11]that is: the high side's switching signal is zero, see Figure 5.4

$$T_{PWM} \underline{u}^r = t_{U-} \underline{u}_{U-} + t_{V-} \underline{u}_{V-} + t_{W-} \underline{u}_{W-} \tag{5.34}$$

$$T_{PWM} \left(u_\alpha^r + \mathrm{j} u_\beta^r \right) = t_{U-} \left(-1 \right) + t_{V-} \left(\frac{1}{2} + \mathrm{j} \frac{\sqrt{3}}{2} \right) + t_{W-} \left(\frac{1}{2} - \mathrm{j} \frac{\sqrt{3}}{2} \right) \tag{5.35}$$

and

$$T_{PWM} = t_{U-} + t_{V-} + t_{W-} \;. \tag{5.36}$$

The solution of this linear equation system (3 equations, 3 unknowns) is given by

$$t_{U-}^n = \frac{t_{U-}}{T_{PWM}} = \frac{1}{3} - \frac{2}{3} u_\alpha^r \tag{5.37}$$

$$t_{V-}^n = \frac{t_{V-}}{T_{PWM}} = \frac{1}{3} + \frac{1}{3} u_\alpha^r - \frac{1}{\sqrt{3}} u_\beta^r \tag{5.38}$$

$$t_{W-}^n = \frac{t_{W-}}{T_{PWM}} = \frac{1}{3} + \frac{1}{3} u_\alpha^r + \frac{1}{\sqrt{3}} u_\beta^r \;. \tag{5.39}$$

Constraints and Optimization

Inspection of Figure 5.3 and the above equations (5.37)-(5.39) shows, that the maximum voltage space vector magnitude for sinusoidal commutation is given by $1/2$. In that case each of the pulse widths will be zero once per electric revolution. Such behavior is detrimental if the INFORM angle estimation is to be embedded into 3-active modulation.

To ensure reliable position information estimation, a minimum pulse width T_{PW}^{3a}[12] is necessary. This can be reasoned by inspection of t_{U-}^m in Figure 5.4. If significantly decreased noise may cause erroneous measured current slope values Δi_{U-}^m. The value of this mandatory measurement window is dependent on the machine's inductances (l_d, l_q), rated current, scaled variables, inverter ADC circuitry and noise levels (t_{SEO})[13] and ADC timing parameters (t_{EEO}). Generally speaking, it is in the range of several µs and higher. For this system $T_{meas}^{3a}|_{min} = 4.8\,\text{µs}$ was specified. Consulting Equation (5.22) and Table 5.5 this results in a targeted value of $T_{PW}^{3a} = 12.5\,\text{µs}$.

The goal now is to restrict the modulator's reference value[14] $|\underline{u}^r|$ just as much as needed to ensure T_{PW}^{3a} while aiming for a value as high as possible. Thereto, a constrained optimization problem will be formulated and solved. As objective function the squared absolute value of the reference voltage space vector $\underline{u}^r$ will be used. Inspecting the real and imaginary part of Equation (5.35) gets

$$u_\alpha^r = -t_{U-}^n + \frac{1}{2} \left(t_{V-}^n + t_{W-}^n \right) \tag{5.40}$$

$$u_\beta^r = \frac{\sqrt{3}}{2} \left(t_{W-}^n - t_{V-}^n \right) \;. \tag{5.41}$$

---

[12]that ensures a minimum measurement pulse width $T_{meas}^{3a}|_{min}$

[13]The value reported in Table 5.5 is approx. five times the time constant of the analogue interface circuit and was measured manually at the inverter

[14]$|\underline{u}^r|$ corresponds to the current controllers output $|\underline{u}|_{max}^{\alpha\beta} = |\underline{u}|_{max}^{dq}$

Calculating the squared magnitude yields an objective function that depends on the 3-active pulse widths,

$$\left(|\underline{u}^r|\right)^2 = \left|(u_\alpha^r)^2 + (u_\beta^r)^2\right|^2 \tag{5.42}$$

$$= {t_{U-}^n}^2 + {t_{V-}^n}^2 + {t_{W-}^n}^2 - t_{U-}^n t_{V-}^n - t_{U-}^n t_{W-}^n - t_{V-}^n t_{W-}^n \tag{5.43}$$

$$= f_u^{3a}\left(t_{U-}^n, t_{V-}^n, t_{W-}^n\right) \tag{5.44}$$

Formally a constrained optimization problem can then be formulated as

$$
\begin{aligned}
\underset{\{t_{U-}^n, t_{V-}^n, t_{W-}^n\}}{\text{maximize}} \quad & f_u^{3a}\left(t_{U-}^n, t_{V-}^n, t_{W-}^n\right) \\
\text{subject to} \quad & t_{U-}^n + t_{V-}^n + t_{W-}^n - 1 = 0 \\
& t_{U-}^n \geq t_{PW}^{3a} \\
& t_{V-}^n \geq t_{PW}^{3a} \\
& t_{W-}^n \geq t_{PW}^{3a}
\end{aligned}
\tag{5.45}
$$

and

$$t_{PW}^{3a} = \frac{T_{PW}^{3a}}{T_{PWM}} \tag{5.46}$$

Calculating a solution for an optimization problem with several inequality and equality constraints such as Equation (5.45) can be quite complex, see [53]. Therefore, a reformulation/simplification of Equation (5.45) is desirable. Inspection of Equation (5.43) shows a symmetry between all three pulse widths, viz. the variables are interchangeable. Furthermore it is justified to set only one inequality constraint active, solve the problem and check if the solution satisfies all constraints. Supported by these statements the substitutions $t_{U-}^n = t_{PW}^{3a}$ and $\mathbf{t} = \left[t_{V-}^n, t_{W-}^n\right]^T$ are inserted into Equation (5.45) to obtain the reformulated problem as

$$
\begin{aligned}
\underset{\mathbf{t}}{\text{maximize}} \quad & f_u^{3a}\left(t_{PW}^{3a}, \mathbf{t}\right) \\
\text{subject to} \quad & g\left(\mathbf{t}\right) = t_{PW}^{3a} + t_{V-}^n + t_{W-}^n - 1 = 0
\end{aligned}
\tag{5.47}
$$

In Equation (5.47) the number of variables has been reduced to two and only one equality constraint remains. Problems of this type can be solved using an ansatz with Lagrange multipliers,

$$L\left(\mathbf{t}, \lambda\right) = f_u^{3a}\left(t_{PW}^{3a}, \mathbf{t}\right) + \lambda g\left(\mathbf{t}\right) \tag{5.48}$$

with $L\left(\mathbf{t}, \lambda\right)$ as Lagrangian function replacing the objective function and λ as Lagrange multiplier. According to [53] necessary conditions for optimality of Equation (5.48) are given by

$$\left(\frac{\partial}{\partial \mathbf{t}} L\right)^T\left(\mathbf{t}^*, \lambda^*\right) = \left(\nabla f_u^{3a}\right)\left(\mathbf{t}^*\right) + \left(\nabla g\right)\left(\mathbf{t}^*\right)\lambda^* \overset{!}{=} \mathbf{0} \tag{5.49}$$

$$\left(\frac{\partial}{\partial \lambda} L\right)^T\left(\mathbf{t}^*, \lambda^*\right) = g\left(\mathbf{t}^*\right) \overset{!}{=} 0 \tag{5.50}$$
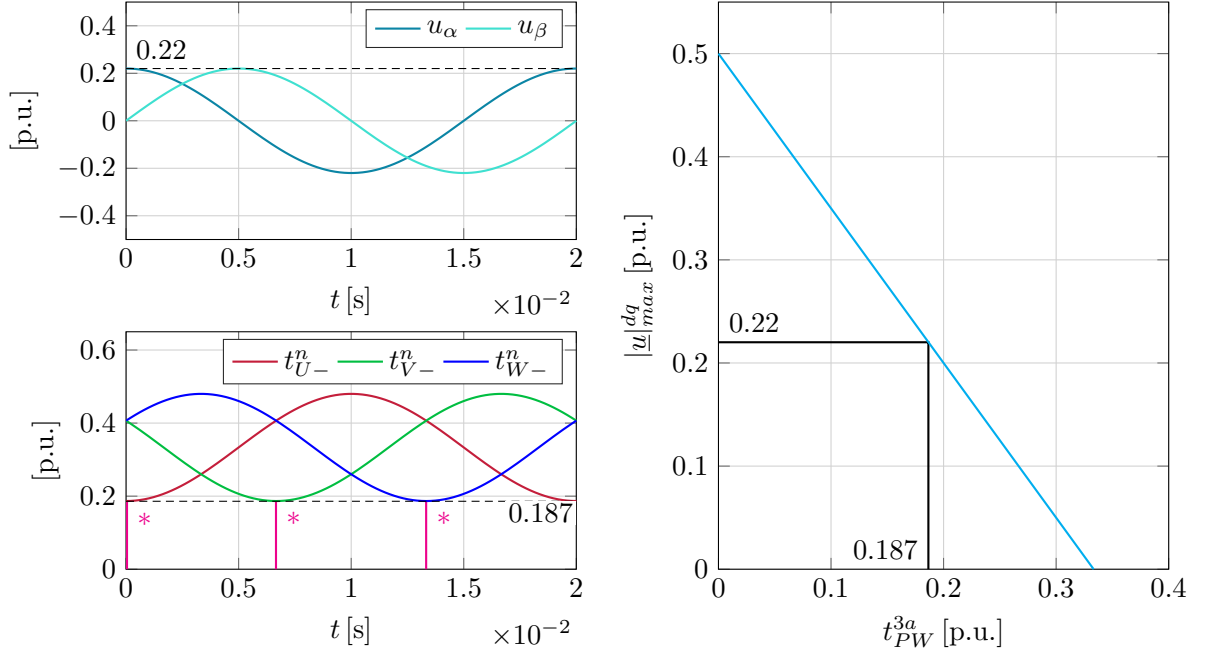
Figure 5.5: Three active modulation method (left) for $\underline{u}^r = 0.22\mathrm{e}^{\mathrm{j}2\pi 50 t}$ and restriction formula Equation (5.54) (right). Stars (*) indicate solutions of Equation (5.51)

where the operator ∇ in this context is read as $\left(\frac{\partial}{\partial t^n_{V-}}, \frac{\partial}{\partial t^n_{W-}} \right)^T$. A symbolic solution of equations (5.49) and (5.50) is found as

$$\mathbf{t}^* = \begin{bmatrix} 0.5 - 0.5\, t^{3a}_{PW} \\ 0.5 - 0.5\, t^{3a}_{PW} \end{bmatrix} \tag{5.51}$$

$$\lambda^* = 0.5 - 1.5\, t^{3a}_{PW} \tag{5.52}$$

On the top left of Figure 5.5 a complete revolution of the reference voltage space vector $\underline{u}^r = 0.22\mathrm{e}^{\mathrm{j}2\pi 50 t}$ is plotted in $(\alpha\beta)$-components. The necessary normalized pulse widths to modulate this space vector are obtained via equations (5.37)-(5.39) and plotted on the bottom left. By comparing Equation (5.51) with Figure 5.5 it can be concluded that this extremum occurs once each phase per revolution. The interpretation is as follows: The solution given by equations (5.51),(5.52) yields the combination of normalized pulse widths, where inequality constraints of Equation (5.45) become active. In a mathematical sense a maximum *possible* voltage space vector magnitude that ensures a minimum pulse width is obtained (in those critical points and all others). Substituting Equation (5.51) back into Equation (5.42) yields the expression

$$f^{3a}_u \left(t^{3a}_{PW}, \mathbf{t}^* \right) = \left(|\underline{u}|^{dq}_{max} \right)^2 = \left(\frac{1}{2} - \frac{3}{2} t^{3a}_{PW} \right)^2 . \tag{5.53}$$

Taking the square root results in the targeted relationship between minimum pulse width and maximum space vector magnitude:

$$|\underline{u}|_{max}^{dq} = \frac{1}{2} - \frac{3}{2} t_{PW}^{3a} \tag{5.54}$$

This relationship is plotted on the right side of Figure 5.5. Implemented values of $t_{PW}^{3a} = \frac{12.5\,\mu s}{67\,\mu s} = 0.187$ and $|\underline{u}|_{max}^{dq} = 0.22$ are also indicated. It becomes clear that the relation $t_{PW}^{3a} < \frac{1}{3}$ needs to be fulfilled to result in meaningful values and qualify the solution Equation (5.51) to solve Equation (5.45). The formula given by Equation (5.54) is also valid for 3-active space vector modulation using positive voltage space vectors $\underline{u}_{U+}, \underline{u}_{V+}, \underline{u}_{W+}$.

It can be used for any implementation of field-oriented control where 3-active modulation is deployed.

The 3-active modulation method profits from longer PWM periods as normalized values of t_{PW}^{3a} tend to be small in this case. It is interesting to note, that this relationship is equal to λ^* in Equation (5.52). In the mathematical theory of optimization Lagrange multipliers can be interpreted as sensitivities of corresponding optimum values, see [53]. This is confirmed by comparing Equation (5.54) with Equation (5.52).

A possible challenge when using 3-active modulation is given by increased DC-link current ripple. These slopes can cause unacceptable losses (overheat) at the inverter's DC-link capacitors, especially for lower PWM frequencies. This fact should always be considered when 3-active modulation is used.

To conclude this section the use of negative voltage space vectors shall be compared to the possible use of positive voltage space vectors. When using the set $\underline{u}_{U+}, \underline{u}_{V+}, \underline{u}_{W+}$ in combination with low-side bridge shuts, phase currents cannot be measured directly. Compared to the implemented case $4 + 4$ additional[15] samples need to be taken. Consulting Equation (3.3) the measurement period per pulse would be increased by $1.92\,\mu s$. If current slopes of the same duration as before should be measured, the minimum pulse width has to be increased by this value. Using Equation (5.54) for that case yields a maximum voltage space vector magnitude of 0.175. This is a reduction of $\approx -20\%$ compared to the usage of $\underline{u}_{U-}, \underline{u}_{V-}, \underline{u}_{W-}$. Consequently, for maximum utilization of available voltage the usage of negative voltage space vectors is preferred.

5.2.4 Performance in the Low Speed Domain

This section presents measurement results from experiments of the implemented INFORM variant presented in Section 5.2.2. As this is an estimation of the double-electric angle the quality of $\hat{\gamma}_{\mathrm{INF}}$ is assessed in this thesis as

$$\gamma_{\Delta INF} = (\hat{\gamma}_{\mathrm{INF}} - 2\gamma_{enc})/2 \tag{5.55}$$

This angular error from the raw INFORM angle is also interpreted as statistical quantity to assess estimation quality. Given N samples, mean[16] and standard deviation are calculated as

---

[15]referring to the beginning of this section and Figure 5.4

[16]During investigations mean and median value coincided by less than half an electrical degree.

Inform assessment at various speeds and loads
(ref): see also Figure 5.6

ω [p.u.]	t_e [p.u.]	$id = iq$ [p.u.]	$\overline{\gamma_{\Delta INF}}$ [°$_{elec}$]	$\sigma_{\gamma_{\Delta INF}}$ [°$_{elec}$]	(ref.)
0.05	0	0.06	0.33	1.73	i
0.05	0.045	0.355	-4.43	4.28	ii
0.05	0.12	0.575	-5.6	7.54	iii
0.05	0.185	0.718	-7.4	12	iv
0.1	0	0.06	0.59	1.7	v
0.1	0.035	0.31	-3.83	3.74	vi
0.1	0.088	0.49	-4.03	5.69	vii
0.1	0.138	0.62	-2.9	8.43	viii
0.15	0	0.07	0.59	1.74	ix
0.15	0.048	0.37	-4.5	4.6	x
0.15	0.0876	0.49	-5.8	6.4	xi
0.15	0.181	0.716	-6.2	10.7	xii

Table 5.2: Representative INFORM measurements at various speeds and load torque values (Q1)

$$\overline{\gamma_{\Delta INF}} = \frac{1}{N}\sum_{n=1}^{N} \gamma_{\Delta INF_n} \tag{5.56}$$

$$\sigma_{\gamma_{\Delta INF}} = \sqrt{\frac{1}{N-1}\sum_{n=1}^{N} |\gamma_{\Delta INF_n} - \overline{\gamma_{\Delta INF}}|^2} \tag{5.57}$$

In each experiment, data for at least two electrical periods was captured and processed in MATLAB. Quantities were either represented in 32-bit I8Q24 or I4Q28 format. Values for angular error were rescaled to [°$_{el}$]. To test the system under load, a load torque was applied to the shaft by means of friction. Therefore, no exact target load conditions were feasible. For future work a second motor and/or eddy current brake is recommended.

Range of Operation and Representative Experiments

The INFORM method excels other sensorless position estimation methods at very low speeds and standstill. Experiments with speed control turned off and manually rotating the shaft proved the functionality of the implemented variant. When applying the voltage limit derived in Section 5.2.3 and modifications from Section 5.5 speeds up to $\omega = \pm 0.225$ (± 5350 rpm) are achievable with proper control dynamics. Constant speeds as low as ± 60 rpm (± 1 Hz $_{mech}$) are feasible until static friction effects become dominant.

A series of experiments was conducted at different speed and load torque values (Q1). The results are presented in Table 5.2. The parameter $\underline{c}_{INF}$ from Equation (5.26) corresponding to each row (viz. experiment) is depicted in Figure 5.6. For each speed value four different load conditions were investigated: no load, low/medium load, medium/rated load, overload.

At no load the system showed excellent performance for all tested speeds as $\overline{\gamma_{\Delta INF}}$ is below the sensor's resolution of $\frac{360}{1024}2\,^{\circ}_{\mathrm{elec}} \approx 0.7\,^{\circ}_{\mathrm{elec}}$. The complex parameter $\underline{c}_{INF}$ resembles a circular ring visible in the first row of Figure 5.6. The thickness of this ring depends on the measurement's signal-to-noise ratio. Signal traces and the locus of $\underline{c}_{INF}$ for $\omega = 0.1$ and no load is also shown in Figure 5.7. The time signal of $\gamma_{\Delta INF}$ and a its frequency distribution resembling a Gaussian probability density function are shown in Figure 5.8. Both plots were captured at the same operational conditions as (v) in Table 5.2 but the primary data is different from the table's primary data.

Under load the quality of $\hat{\gamma}_{\mathrm{INF}}$ decreased gradually. This mainly depended on torque magnitude instead of speed, clearly indicated by Figure 5.6 (rows 2-4). As motor currents increased with t_e two concentric circular shapes having an iris in the middle become apparent in the locus plots. The width of said iris decreases as load increases. For stable operation, the origin in the complex plane must be encircled. As discussed in Section 5.2.2 and expected, the omission of anti-parallel test voltage shots lead to systematic errors present in $\hat{\gamma}_{\mathrm{INF}}$. A heuristic compensation using speed and torque dependent equalization functions was implemented but didn't improve the performance substantially. This behavior was also expected from other sensorless control systems where INFORM variants were deployed. At medium/rated load quality indicators $\overline{\gamma_{\Delta INF}}$ and $\sigma_{\gamma_{\Delta INF}}$ were already within the targeted range of $7.5\,^{\circ}_{\mathrm{elec}}$. Again representative plots for these operating points are given by Figure 5.9 and Figure 5.10.

The last row of Figure 5.6 indicates the behavior for torque values higher than the rated torque (overload). The iris still encircles the origin but quality indicators show substantial angle errors, see Table 5.2. However, the fact that stable operation is possible despite of angular error spikes of $30\,^{\circ}_{\mathrm{elec}}$ and more is impressive and underlines the robustness capabilities of the INFORM method.

In the final configuration of the sensorless FOC system current values of the same magnitude as given in rows 2-3 in Figure 5.6 occur. The corresponding quality indicators were within the targeted $7.5\,^{\circ}_{\mathrm{elec}}$ margin. Acceleration from standstill to very high speeds as well as braking maneuvers to standstill are presented in Section 5.7 together with speed reversals. From these outcomes and the results presented here the *research question* formulated in Section 5.2.2 can be answered with a clear "yes". Yes, using a negative 3-active pattern to indirectly measure current slopes for INFORM without anti-parallel voltage test vectors to control SynRM yields fairly good performance. The usage of Equation (5.54) is critical to accomplish a wide range of operation while ensuring enough time to measure current slopes.

Further improvements of the angular error are possible if a dedicated voltage shot test pattern is used as discussed in [68], [66], [67] and [6] incorporating anti-parallel shots. When that approach is taken a decrease in control bandwidth in the low speed region as well as mechanical noise has to be accepted. The usage of positive 3-active voltage space vectors together with a systematic compensation is topic of ongoing research at the department of electrical drives at TU Wien. As laid down in Section 5.2.3 this would lead to a decrease in maximum usable inverter voltage and increase computational demands. Therefore, the chosen solution can be considered as "best one" to meet the targeted goals (high voltage reserves, high speed, decent quality).

At the end of this section it should be emphasized that the INFORM method is superior to many other sensorless methods at low speeds and standstill. Other possible approaches are often called "high frequency voltage pulse injection", see [70]. These methods require the knowledge of machine parameters, which is not the case[17] when using INFORM . Additionally these methods almost always introduce high levels of acoustical noise, which can be avoided using silent INFORM.

---

[17]Note that only three phase currents needed to be measured to be used in Equation (5.28).

increased speed (ω)
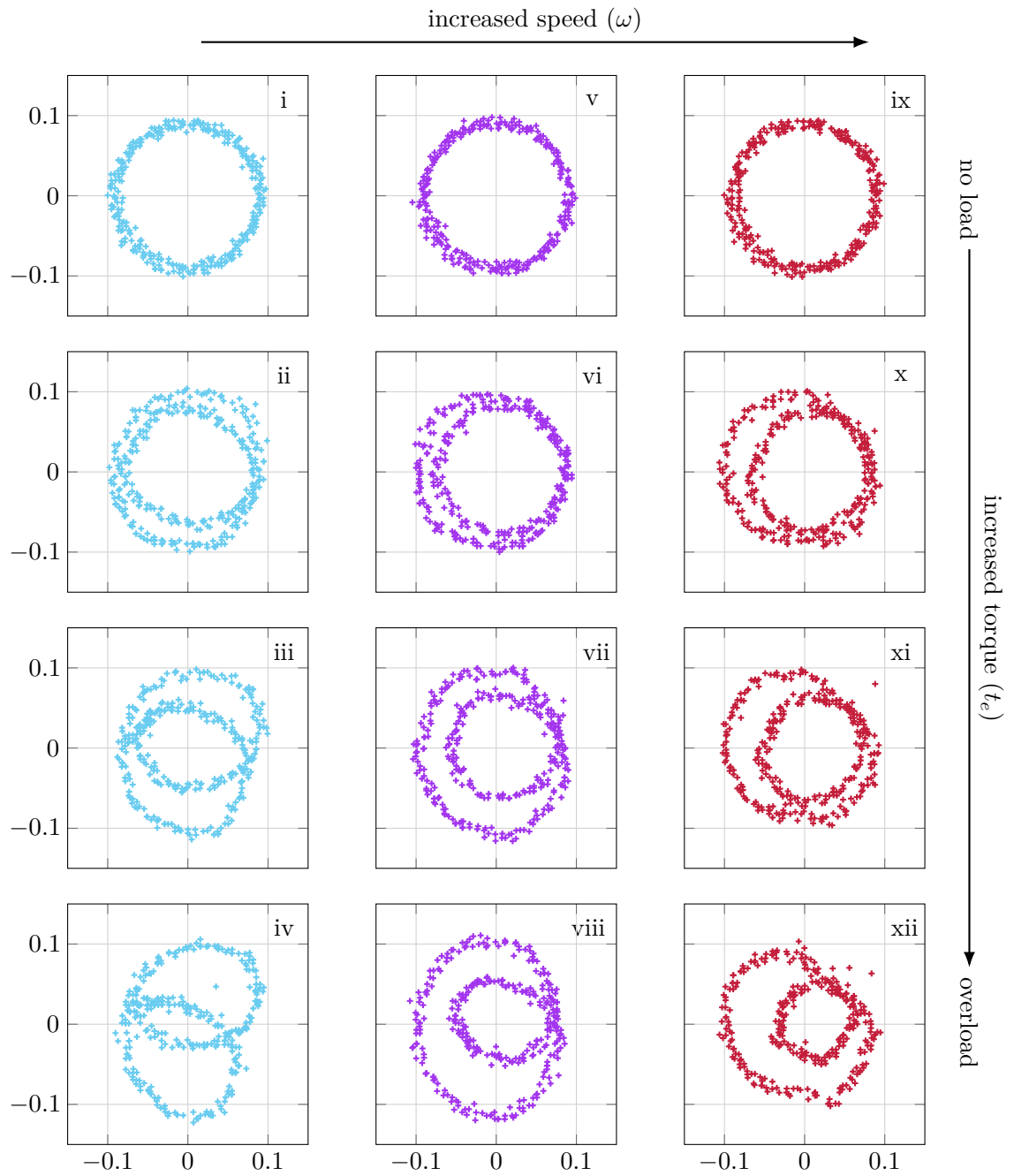
Figure 5.6: INFORM orbits at a glance; Operational Region Q1; Horizontal axis directions correspond to $\Re\{\underline{c}_{INF}\}$ [p.u.], vertical axis directions correspond to $\Im\{\underline{c}_{INF}\}$ [p.u.]. Statistical data and experiment conditions for each plot is given in Table 5.2
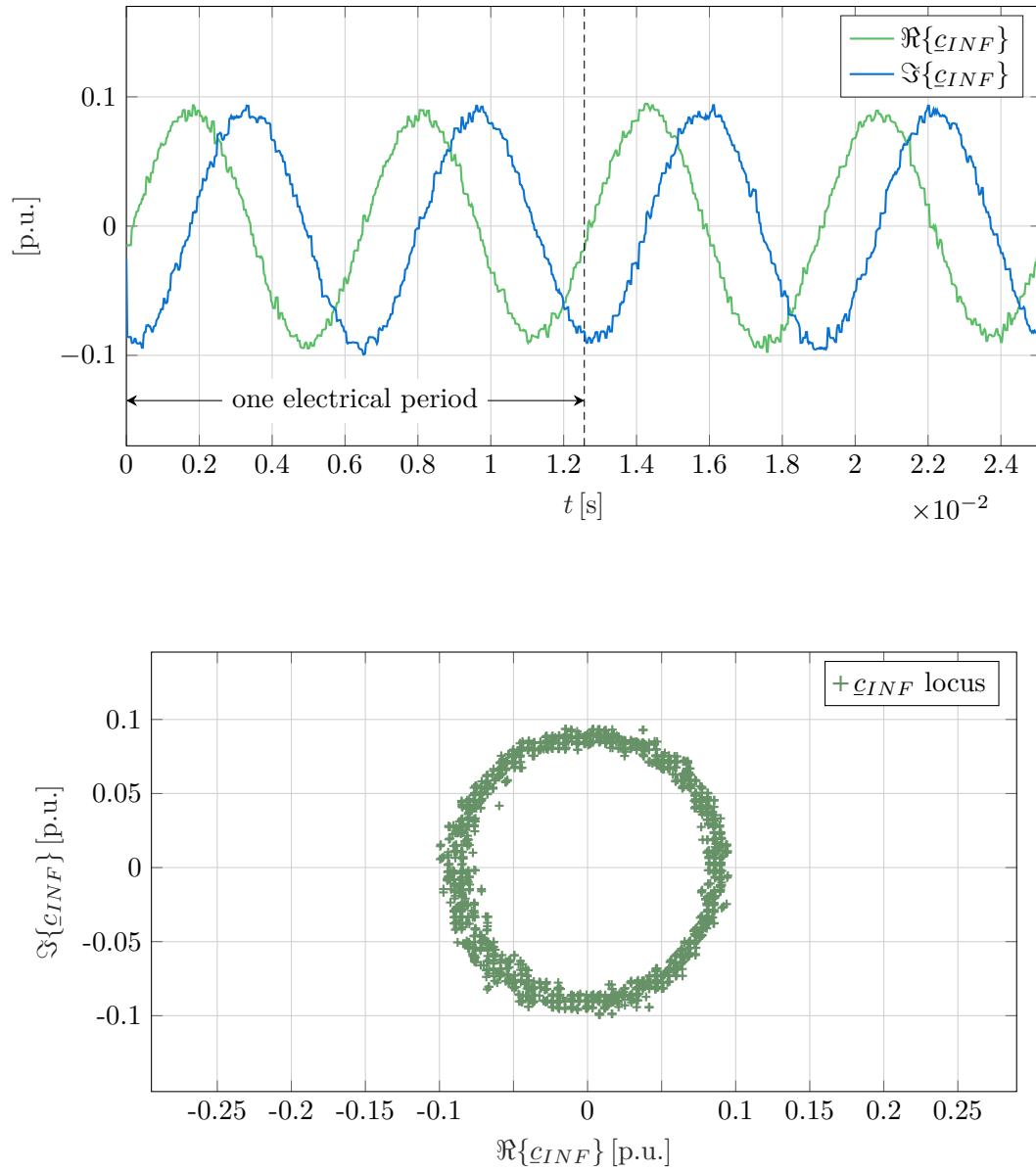
Figure 5.7: Time signals and locus of $\underline{c}_{INF}$ for $\omega = 0.1$ and no load conditions. Very good performance indicated as sinusoidal signals and a circular ring with significant radius are apparent. Primary data taken for this plot is different from Table 5.2 and Figure 5.6.
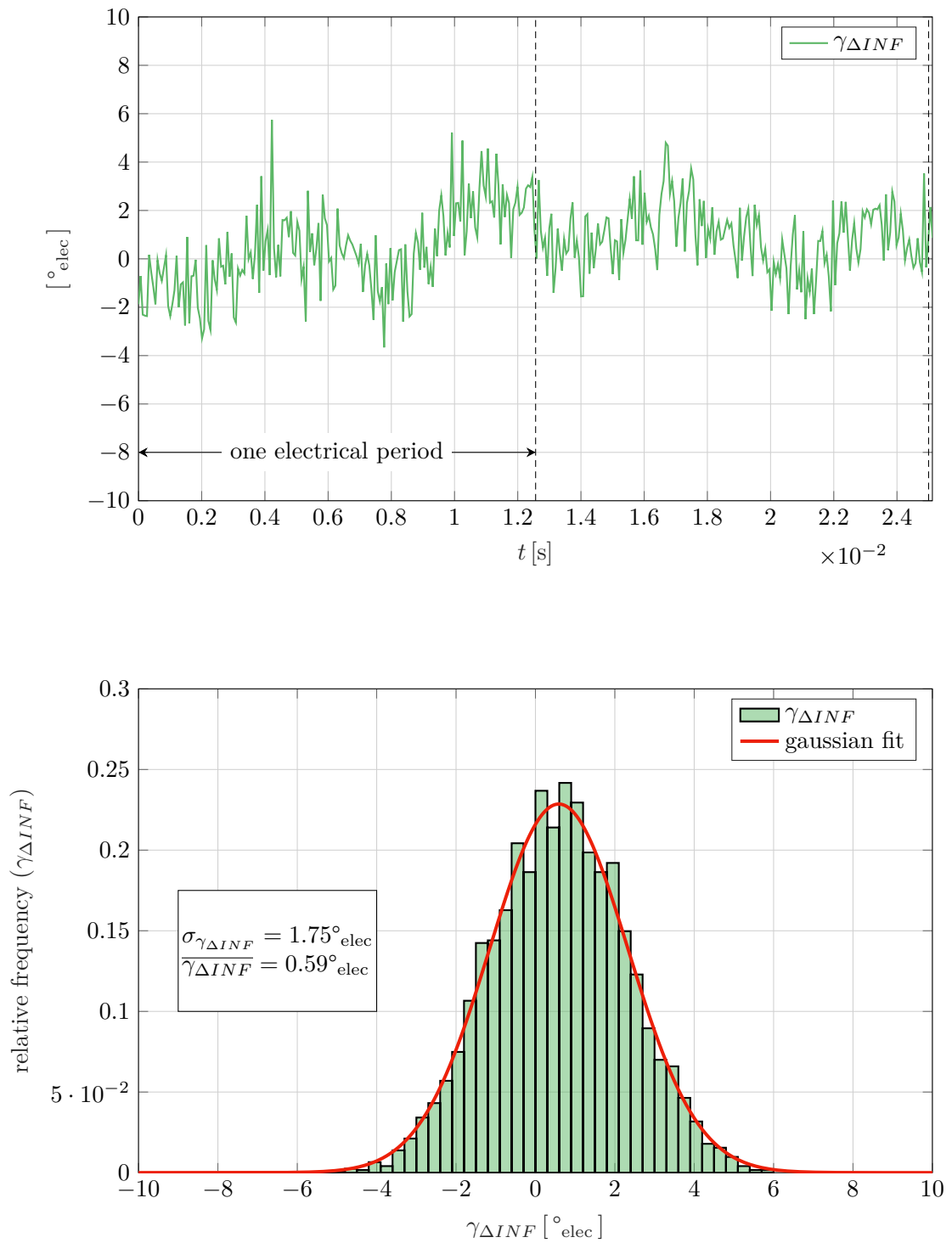
Figure 5.8: Time signal and frequency distribution of $\gamma_{\Delta INF}$ for $\omega = 0.1$ and no load conditions. Two electrical periods shown. Sample size $= 4096$; bin size $= 0.3^{\circ}_{el}$. Primary data taken for this plot is different from Table 5.2 and Figure 5.6. Current measurement noise that lead to a circular-ring shaped locus of $\underline{c}_{INF}$ results in a Gaussian shaped frequency distribution of $\gamma_{\Delta INF}$ as expected.
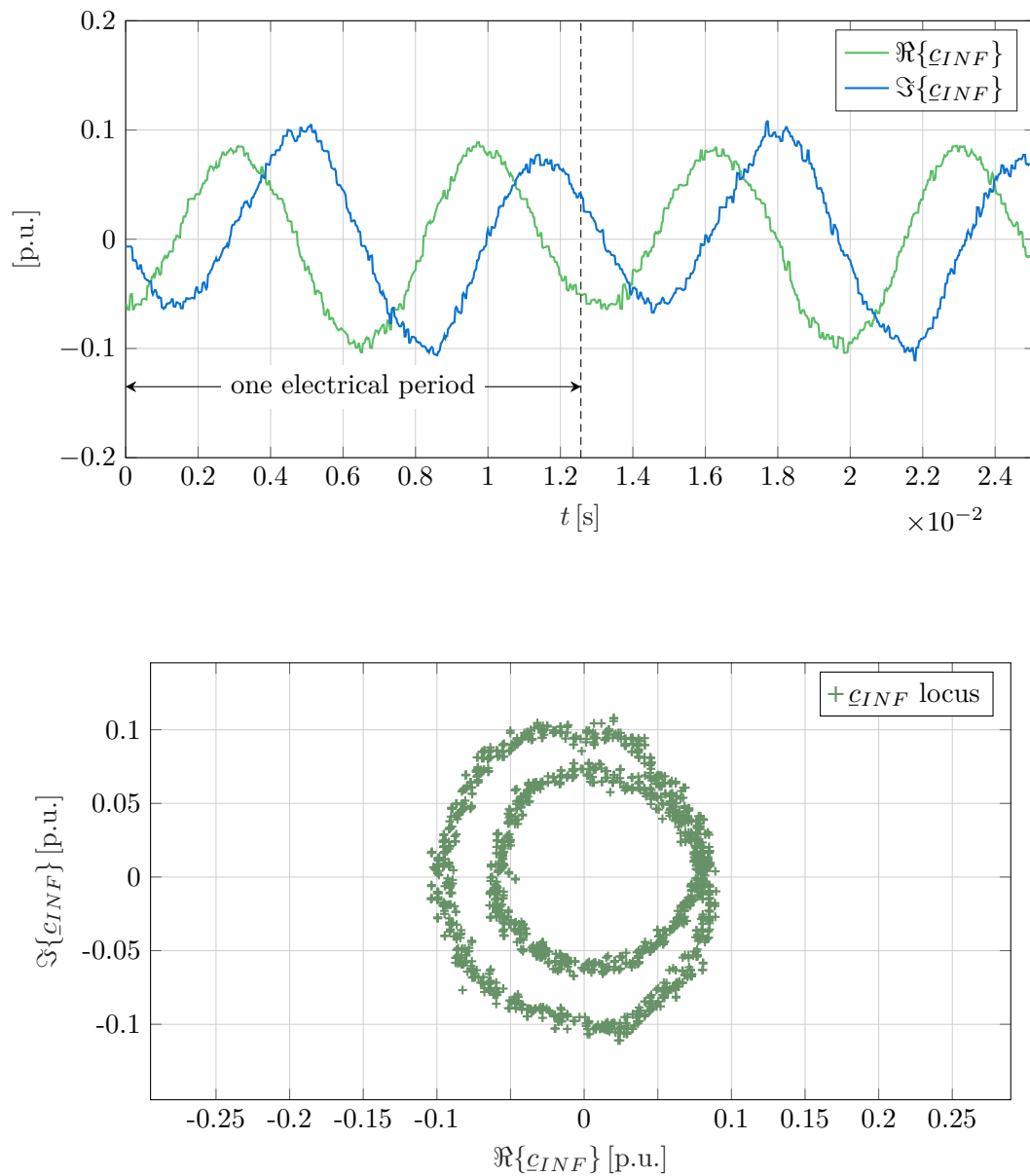
Figure 5.9: Time signals and locus of $\underline{c}_{INF}$ for $\omega = 0.1$ and $t_e = 0.076$. Due to non sinusoidal time signals the locus resembles two concentric circle-like traces with an iris in the middle. This was expected from the chosen implementation as no anti-parallel voltage test pulses are used to save computation time and gain control bandwidth (silent INFORM). However, indicated performance is within targeted margins. Primary data taken for this plot is different from Table 5.2 and Figure 5.6.
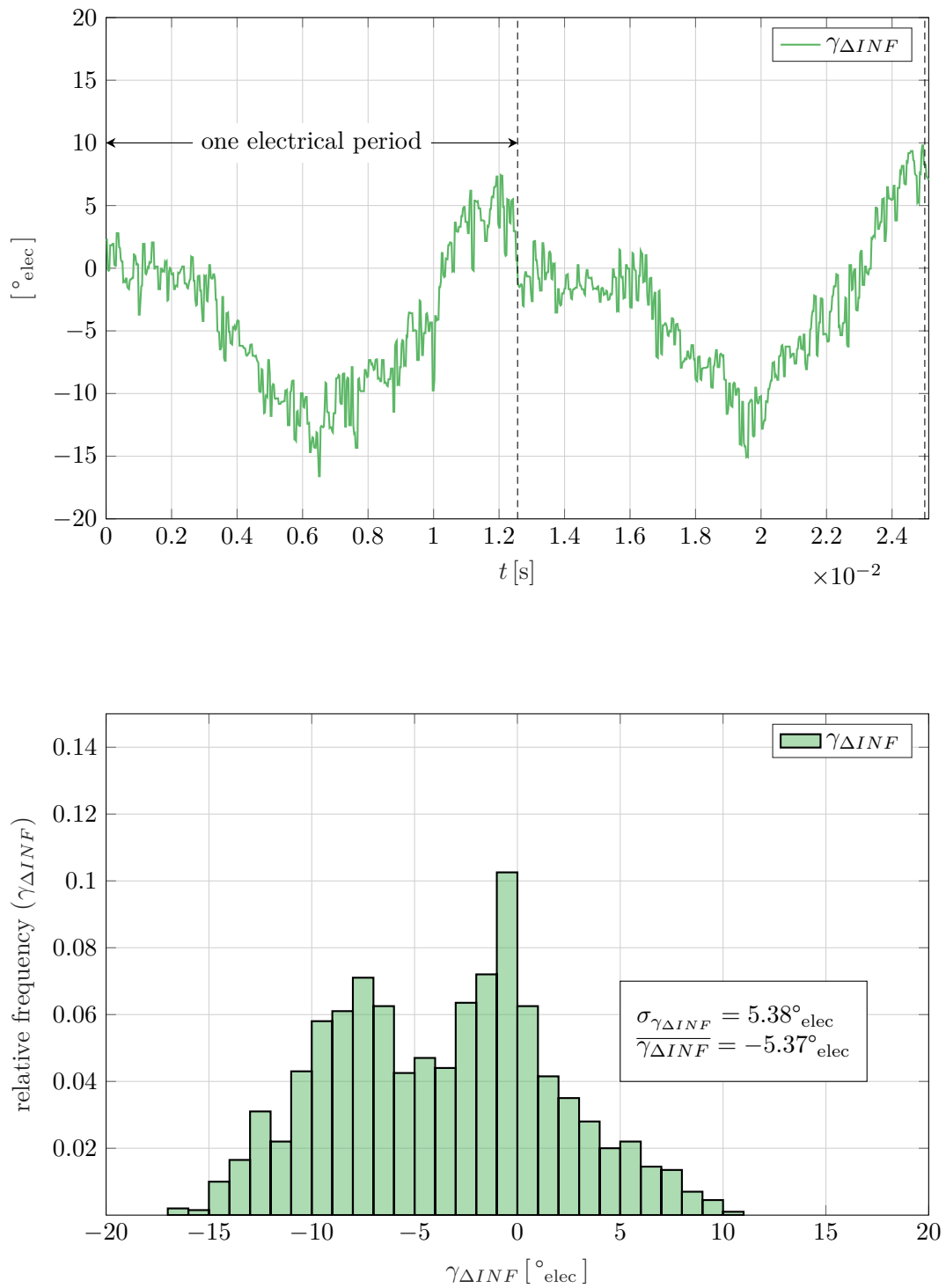
Figure 5.10: Time signal and frequency distribution of $\gamma_{\Delta INF}$ for $\omega = 0.1$ and $t_e = 0.076$. Two electrical periods shown. Sample size = 4096; bin size = 0.3°_{el}. The locus shape of $\underline{c}_{INF}$ visible in Figure 5.9 results in a frequency distribution with two prominent peaks for $\gamma_{\Delta INF}$. Indicated performance is within targeted margins (7.5°_{el}). Primary data taken for this plot is different from Table 5.2 and Figure 5.6.
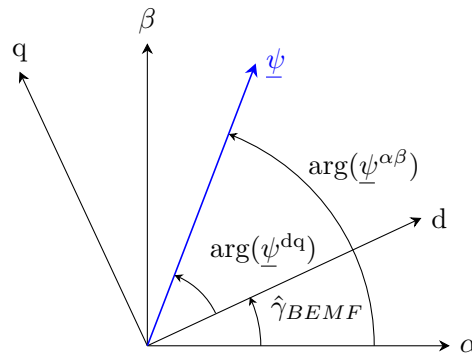
Figure 5.11: Regarding <u>B</u>ack <u>E</u>lectro<u>m</u>otive <u>F</u>orce based sensorless position estimation

5.3 SynRM-BEMF Method

This section describes the adoption of a sensorless position estimation method for the use in high speed operation of SynRMs. Said method relies on the evaluation of the induced voltage, hence the name. Algorithms of this type are widespread in the field of sensorless control of electric machines. They all share the basic idea (integration of stator voltage) and differ mostly in their implementation and tuning aspects. Therefore, this section is organized in the same way, starting with an outline of the method in Section 5.3.1. Several different variants of this idea were implemented and tested. In Section 5.3.2 the final result of this "trial and error" process is presented. A series of representative experiments concludes the presentation in Section 5.3.3.

5.3.1 SynRM-BEMF Algorithm

The idea of the <u>B</u>ack <u>E</u>lectromotive <u>F</u>orce based sensorless position estimation is simple and can be reasoned by inspection of Figure 5.11. To estimate the d-axis position, the machine's flux linkage argument is calculated twofold in $(\alpha\beta)$- and (dq)-coordinates. Then, both values are subtracted to yield

$$\hat{\gamma}_{\text{BEMF}} = \arg\left(\underline{\psi}^{\alpha\beta}\right) - \arg\left(\underline{\psi}^{\text{dq}}\right) \ . \tag{5.58}$$

Calculation of $\underline{\psi}^{\alpha\beta}$ is achieved by integration of the (scaled) stator voltage Equation (2.53) in $(\alpha\beta)$-coordinates,

$$\underline{\psi}^{\alpha\beta} = \int \left(\underline{u}^{\alpha\beta} - r\underline{i}^{\alpha\beta}\right) \mathrm{d}t \ , \tag{5.59}$$

$$\arg\left(\underline{\psi}^{\alpha\beta}\right) = \mathrm{atan}\left(\frac{\psi^{\beta}}{\psi^{\alpha}}\right) \ . \tag{5.60}$$

where currents are measured in the preceding FAST task and voltages are taken from the current controller's output, viz. $\underline{u}^{\alpha\beta} = \underline{u}_r^{\alpha\beta}$. The (dq) flux linkage is obtained under the assumption of constant inductances identified in Section 4.6.2 and "last known" direct- and quadrature-axis currents (i_d, i_q) , see Section 5.1:

$$\arg\left(\underline{\psi}^{\mathrm{dq}}\right) = \mathrm{atan}\left(\frac{l_d i_d}{l_q i_q}\right) \ . \tag{5.61}$$

5.3.2 Implementation- and Calibration-Aspects

The flux linkage $\underline{\psi}$ that induces Back Electromotive Force is to be provided by current controllers, as SynRMs are completely free of permanent magnet material. A minimum flux linkage space vector amplitude needs to be ensured in order to keep this sensorless model "alive" (viz. produce EMF). This is done by operating the motor in the `vpsm(id)` mode as presented in Section 4.6.2. Depending on the motors torque demand, the speed controller will further switch between `MTPA` and `vpsm(id)` mode. More details are found in Section 5.5. In the `vpsm(id)` case the flux linkage amplitude is then given by $l_d \cdot i_d|_{min}$. For development $i_d|_{min}$ was initially set to 0.75 as higher values tended to improve stability. Required values for this quantity remain high for this specific machine[18] as its airgap $\delta = 1\,\mathrm{mm}$ is relatively large, resulting in small scaled inductances. A trade-off is reasoned when keeping in mind that permanent magnets (ferrite or rare-earth type) in rotors allow for $i_d|_{min} = 0$.

The final implementation of the algorithm presented in Section 5.3.1 is discussed in subsequent paragraphs. As the flux linkage is calculated twofold, $(\alpha\beta)$ and (dq) evaluation are discussed separately.

Stator Fixed ($\alpha\beta$) Flux Linkage Evaluation

From a mathematical perspective the task of calculating Equation (5.59) is equivalent to numerically solving an ODE. Many methods exist to calculate the integral $\int\left(\underline{u}^{\alpha\beta} - r\underline{\imath}^{\alpha\beta}\right)\mathrm{d}t$, e. g. single-step or multi-step methods that can either be explicit or implicit. However, in embedded control however several restrictions apply when choosing the proper algorithm. In the SynRM control system under consideration the step-size a.k.a sample time is fixed to T_{fast}. This excludes variable step size methods. Due to the real-time nature of control, implicit methods are also excluded. Limited computation time and available memory space should also be considered.

Therefore, the optimal method for implementation should be computationally lightweight and have a predictable (known) error that allows for compensation. This leads to the choice of a first order low-pass filter to approximate integrating behavior above a set cutoff-frequency. An estimation of the stator fixed flux linkage is obtained using,

$$\hat{\underline{\psi}}^{\alpha\beta} \approx G_{\mathrm{BEMF}}\left(\underline{u}_r^{\alpha\beta} - r\underline{\imath}^{\alpha\beta}\right) \cdot \frac{1}{\left|G_{\mathrm{BEMF}}\left(\underline{u}_r^{\alpha\beta} - r\underline{\imath}^{\alpha\beta}\right)\right|} \ , \tag{5.62}$$

$$G_{\mathrm{BEMF}}\left(s\right) = \frac{1}{1 + sT_{\mathrm{BEMF}}} \ . \tag{5.63}$$

Equation (5.63) is implemented by the exponential moving average[19] algorithm, see Equation (3.10). An important remark has to be made here before describing the filter's design process

---

[18] As described at the beginning of this thesis, the long-term goal is to build a prototype supported by magnetic bearings with levitating rotor. Therefore, the airgap needs to be of this magnitude.

[19] Therefore Forward Euler approximation with small step-size is utilized.

and phase tuning. The relationship of Equation (3.10) and a direct *direct discretization*[20] from s to z domain only holds for $\frac{1}{T_{fast}} = f_{sample} \gg f_{el}$. For the given system this is true because $f_{el} < 1\,\text{kHz}$ and $f_{sample} \approx 15\,\text{kHz}$. Hence, instead of designing in the s-domain and switching to the z-domain, the theoretically correct way is to adopt the so called Tustin-Transformation presented in [54]. Therefore, the workflow is $s \to q$, design your systems in q, and $q \to z$ for implementation. For current controllers and SynRM-BEMF method realization this was investigated without any noticeable differences[21], so direct discretization is adopted here.

Based on the findings of Section 5.2.4 the target speed above which SynRM-BEMF shall work was set to $\omega_{\text{BEMF}}^{work} = 0.2$. Experiences from previous projects lead to a choice of $\Omega_{g,\text{BEMF}} = \omega_{\text{BEMF}}^{work} \Omega_B / 1.5$ for the cutoff frequency and thus $T_{\text{BEMF}} = \Omega_{g,\text{BEMF}}^{-1} = 1.5\,\text{ms}$ as filter time constant. Using Equation (3.11) lead to $\alpha_{\text{BEMF}} = 0.9572$. The phase lag introduced by the low pass filter of Equation (5.63) is approximately (see preceding paragraph) given by

$$\varphi_{lpf}\left(\hat{\omega}\right) \approx -\text{atan}\left(\hat{\Omega}\,T_{\text{BEMF}}\right) = -\text{atan}\left(7.5\,\hat{\omega}\right)\;, \tag{5.64}$$

where scaling values were substituted. An ideal integrator yields a phase lag of $90\,^{\circ}{}_{\text{elec}}$. At the desired working speed for SynRM-BEMF the phase error between this semantically correct value and $\text{atan}\left(\hat{\psi}_\beta / \hat{\psi}_\alpha\right)$ is still substantial and needs to be compensated. Thereto, in a first step the error is calculated as:

$$e_{lpf}\left(\hat{\omega}\right) = 90\,^{\circ}{}_{\text{elec}} - \left|\varphi_{lpf}\left(\hat{\omega}\right)\right|\;. \tag{5.65}$$

This error in turn could be subtracted from $\text{atan}\left(\hat{\psi}_\beta / \hat{\psi}_\alpha\right)$ to yield a corrected phase as a result. However during testing this approach alone did not meet the targeted performance of $|\gamma_\Delta| < 7.5\,^{\circ}{}_{\text{elec}}$. A strong dependence of the type $\gamma_\Delta\left(i_d^r\right)$ was discovered during testing in both no-load and load situations at various speeds.

An important remark: How can i_d^r be properly realized to produce flux linkage $\underline{\psi}$ that enables sensorless control via SynRM-BEMF method? To realize i_d^r the controller needs to know the d-axis location $\hat{\gamma}$. On the other hand it is just about to estimate that very location using flux linkage and current space vector in Equation (5.61). The absence of permanent magnet material (and therefore absence of $\psi_d^{PM} = const.$) introduces challenges for sensorless control of SynRM. As it becomes apparent the "problem chases its own tail" here and the proposed model/approach faces limitations. This short discussion also excluded the fact that all these calculations of a raw SynRM-BEMF angle $\hat{\gamma}_{\text{BEMF}}$ heavily depend[22] on the (adapted/tuned) observer when assessing dynamic performance. The adoption of advanced techniques is strongly recommended for future work using a more computationally potent DSC. Examples of these techniques are Sliding-Mode Observers or Model-Reference-Adaptive Observers, Extended Kalman Filter, see [51], [71],[40] and [72].

---

[20]see also Section 4.4

[21]However, recap that the observer design directly in the z-domain was critical for the overall system's stability, see Section 4.3 and Section 5.5.

[22]This means even more parameter dependencies. Observer subsystem is covered in Section 4.3 and Section 5.5

However, with the system at hand (limited computation capacity) and with respect to the scope of this thesis, the proposed method shall be used. Experimental but systematic calibration of erroneous effects shall exploit resources at hand to yield a good result. After many iterations and variations[23] of this method the following calibration strategy lead to a stable and efficient operation:

- Modifications to current and speed controllers and the observer according to Section 5.5 have to be active.

- As the phase error e_{lpf} has its highest value at $\omega_{\text{BEMF}}^{work} = 0.2$ for SynRM-BEMF operational region, the calibration was initially carried out in this point first. After calibration at this most sensitive speed value other speed/load conditions were tested. It became evident that the performance at all higher shaft speeds with or without load (fortunately) was within targeted margins.

- At $\omega = 0.2$ and no load ($i_q \approx 0$), i_d^r was adjusted while γ_Δ was inspected. A multiplicative tuning factor $\hat{\kappa}$ was applied to e_{lpf} before subtracting it from $\operatorname{atan}\left(\hat{\psi}_\beta / \hat{\psi}_\alpha\right)$. In other words the term

$$\operatorname{atan}\left(\hat{\psi}_\beta / \hat{\psi}_\alpha\right) - e_{lpf}\left(0.2\right)\hat{\kappa} \tag{5.66}$$

was adjusted by means of $\hat{\kappa}$ to yield $\gamma_\Delta \overset{!}{=} 0$.

- This resulted in several pairs of values $(i_d^r, \hat{\kappa})$. The goal was to find a simple functional relationship between i_d^r and $\hat{\kappa}$ such that $\gamma_\Delta \approx 0$. Thereto, a least square linear function was parametrized as $\mathbf{p} = [k_{ph} \ d_{ph}]^T$ and fit to the available data set (overdetermined system of equations) as follows:

$$\mathbf{S}_N \mathbf{p} = \hat{\kappa}_N \tag{5.67}$$

$$\begin{bmatrix} i_{d_1}^r & 1 \\ i_{d_2}^r & 1 \\ i_{d_3}^r & 1 \\ \vdots & \vdots \\ i_{d_N}^r & 1 \end{bmatrix} \begin{bmatrix} k_{ph} \\ d_{ph} \end{bmatrix} = \begin{bmatrix} \hat{\kappa}_1 \\ \hat{\kappa}_2 \\ \hat{\kappa}_3 \\ \vdots \\ \hat{\kappa}_N \end{bmatrix} \qquad \text{such that} \quad \gamma_\Delta \overset{!}{=} 0 \tag{5.68}$$

$$\mathbf{p} = \begin{bmatrix} k_{ph} \\ d_{ph} \end{bmatrix} = \left(\mathbf{S}_N^T \mathbf{S}_N\right)^{-1} \mathbf{S}_N^T \hat{\kappa}_N \tag{5.69}$$

Final values obtained were $k_{ph} = 0.63$, $d_{ph} = 0.053$. It is emphasized here that these two quantities are very sensitive parameters. During development the motor's ball bearings were replaced due to wear. After a new commissioning of the system the above process had to be repeated as the old values[24] did not work anymore. When reversing the motor's speed, the sign of both parameters must also be negated.

---

[23]A non exhaustive list: Placing SynRM-BEMF in SLOW Task and extrapolating the angle in FAST Task; Changing data format to other than I4Q28 ; Design in q domain as described above; Iterating through current and voltage values between $\#[n-1]$ and $\#[n]$ other than proposed in Section 5.1; Application of additive and multiplicative tuning factors other than presented. Adoption of multi-step integrating methods.

[24]To give the reader an impression of their range, the old values were: $k_{ph} = 0.83$, $d_{ph} = -0.076$.

After explaining this calibration method the process to correctly evaluate the stator fixed flux linkage can be summarized as follows. The stator flux linkage is obtained via LPF operation given in Equation (5.62). The systematic error due to this operation is obtained by Equation (5.65). Referring to the above described process this error is altered by

$$s_\omega = \text{sign}(\hat{\omega}) \tag{5.70}$$

$$\kappa_{ph}(\hat{\omega}, i_d^r) = s_\omega (k_{ph} i_d^r + d_{ph}) \tag{5.71}$$

$$e_{ph}(\hat{\omega}, i_d^r) = e_{lpf}(\hat{\omega}) \cdot \kappa_{ph}(\hat{\omega}, i_d^r) \ . \tag{5.72}$$

This tuned phase error $e_{ph}(\hat{\omega}, i_d^r)$ is used to obtain the $(\alpha\beta)$ flux linkage angle for SynRM-BEMF angle estimation,

$$\arg\left(\underline{\hat{\psi}}^{\alpha\beta}\right) = \text{atan}\left(\frac{\hat{\psi}_\beta}{\hat{\psi}_\alpha}\right) - e_{ph}(\omega, i_d^r) \tag{5.73}$$

Rotor Fixed (dq)-Flux Linkage Evaluation

Constant inductances (l_d, l_q) are assumed. Current values (i_d, i_q) calculated in the preceding FAST task are used, see Section 5.1. The use of other current values destabilized the system. It is possible to adopt inductance LUTs to incorporate saturation effects at this stage, but as the motor showed nearly magnetic linear behavior in Section 4.6 this was omitted. Furthermore, this would only introduce additional complexity to an already heavily tuning and calibration dependent method. Hence, Equation (5.61) is utilized to obtain the rotor referenced flux linkage angle.

Resulting Raw BEMF Angle

From the preceding text of this section the calculation of the raw SynRM-BEMF based angle estimation can be summarized as follows:

$$\hat{\gamma}_{\text{BEMF}} = \text{atan}\left(\frac{\hat{\psi}_\beta}{\hat{\psi}_\alpha}\right) - e_{ph}(\omega, i_d^r) - \text{atan}\left(\frac{l_d i_d}{l_q i_q}\right) \tag{5.74}$$

This quantity is fed to the observer as corrector term, depicted in Figure 5.1, to yield $\hat{\gamma}$ as sensorless "control" angle used for Park and Inverse Park transformations.

5.3.3 Performance in the High Speed Domain

Characteristic signals and performance of the implemented SynRM-BEMF estimation method in conjunction with the tuned observer of Section 5.5 are presented here. To assess the quality γ_Δ

was used instead of a difference between the raw value $\hat{\gamma}_{\text{BEMF}}$ and γ_{enc}. At high speeds relevant information is gained by inspection of γ_Δ and $\hat{\gamma}$ rather than statistical investigations.

Figure 5.12 shows angles, currents and angle-error signals for a quasi-stationary operating point at $\omega = 0.9$, deep within sensorless flux weakening region. The angular error is within the set target of $7.5\,°_{\text{elec}}$. One source for the remaining deviation can be found when recapitulating the preceding section that introduced various uncertainties by (necessary) empirical tunings that aggravate in magnitude at high speed. Another source is given by a (possible) imprecise calibration of the encoder, see Section 2.6. At high speeds dead time compensation by means of Equation (2.114) becomes very sensitive to $k_{\gamma D}$.

Dynamic performance of the implemented method is indicated by various figures presented in the remaining sections of this chapter. That is figures 5.18, 5.19, 5.20, 5.24, 5.25 and 5.26.

After successfully identifying and implementing the sensorless flux weakening subsystem the value for $i_d|_{min}$ at $\omega_{\text{BEMF}}^{work}$ could be reduced from 0.75 to 0.71.

Altogether the calibrated SynRM-BEMF method of Equation (5.74) combined with the tuned observer of Section 5.5 eventually yielded very good performance. However, this specific path of development proved to be complex and involved a lot[25] of experimental tuning. The contribution of this work regarding the aspect of high speed sensorless control for SynRMs using a SynRM-BEMF model is the systematic calibration process presented in Section 5.3.2. The author suggests/presumes that this method works best for salient pole SynRM with (nearly) linear magnetic behaviour.

5.4 Transition Between Sensorless Models

Both INFORM and SynRM-BEMF methods were developed and tested independently from each other. To ultimately obtain a completely sensorless system a transition between these methods needed to be designed and implemented. The dissertation [66] covers this topic extensively in the case of PMSMs. Other than in this thesis a dedicated test voltage shot sequence was used for INFORM implementation. Therefore the scientific content of this section can be named as investigation and adoption of Silent-INFORM $\Leftrightarrow$ BEMF transition for salient pole SynRM. A SynRM controlled in `vpsm(id)` mode resembles a PMSM. This is why ideas and results proposed in [66] are also used and expected for the SynRM sensorless control system. There is also a strong foundation of experience covering this topic at the Department of Electrical Drives and Machines (TU Wien) built from previous topics using PMSMs, which supports the proposed strategy.

5.4.1 Trade-offs for Transition

Figure 5.14 depicts a semantically correct estimation quality trend for both discussed sensorless methods. Therefore the INFORM method should be used at velocities from standstill up to a point where standard deviations intersect. A velocity band where both estimations are mixed and fed to the observer is suggested due to model and/or parameter uncertainties. The (silent)

---

[25]If compared to the three current slope values for INFORM , the proposed SynRM-BEMF method involves more than 10 measured quantities or tuning factors. Obviously, a rather simple idea/model given by Equation (5.58) is traded for increased effort in tuning.
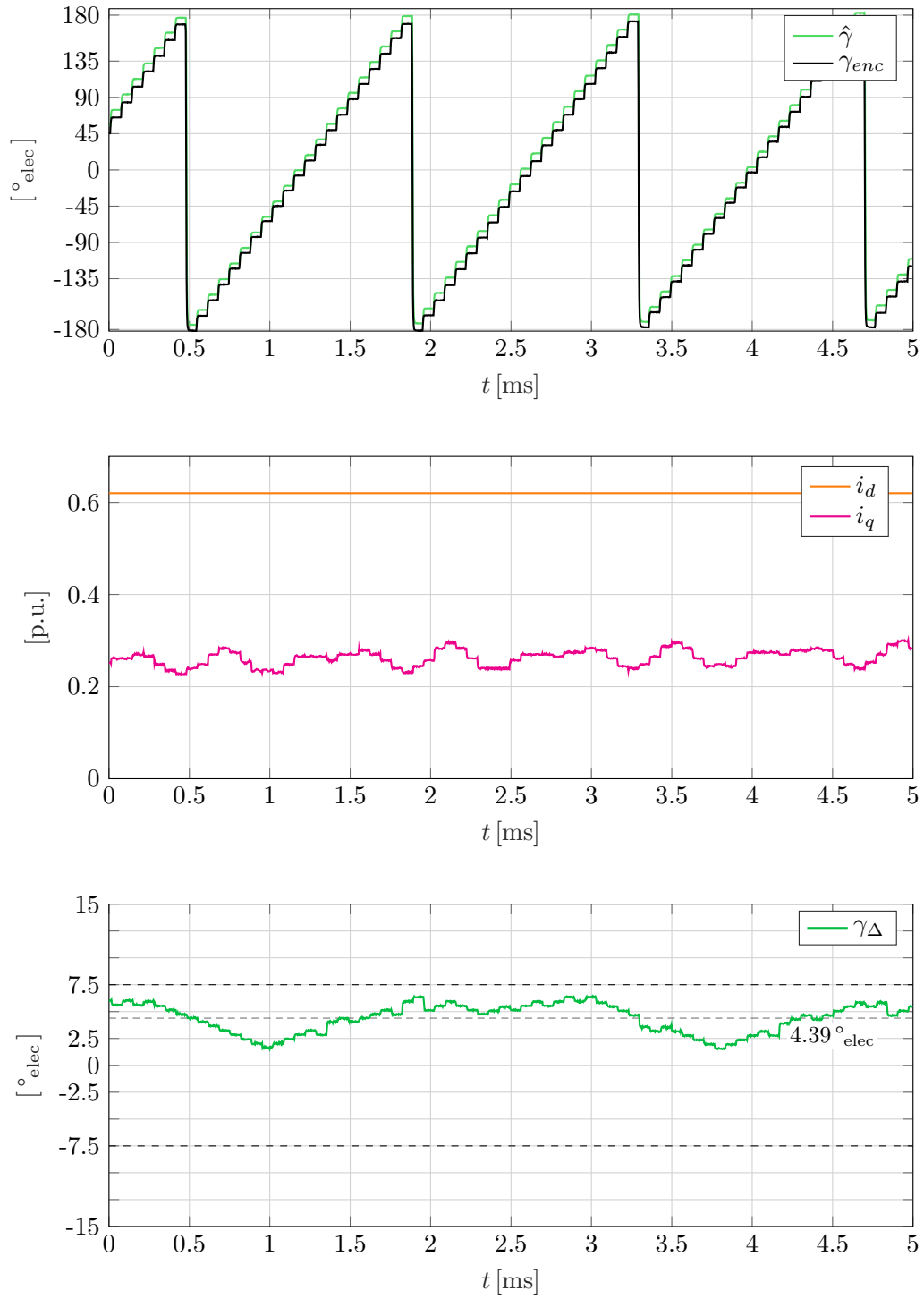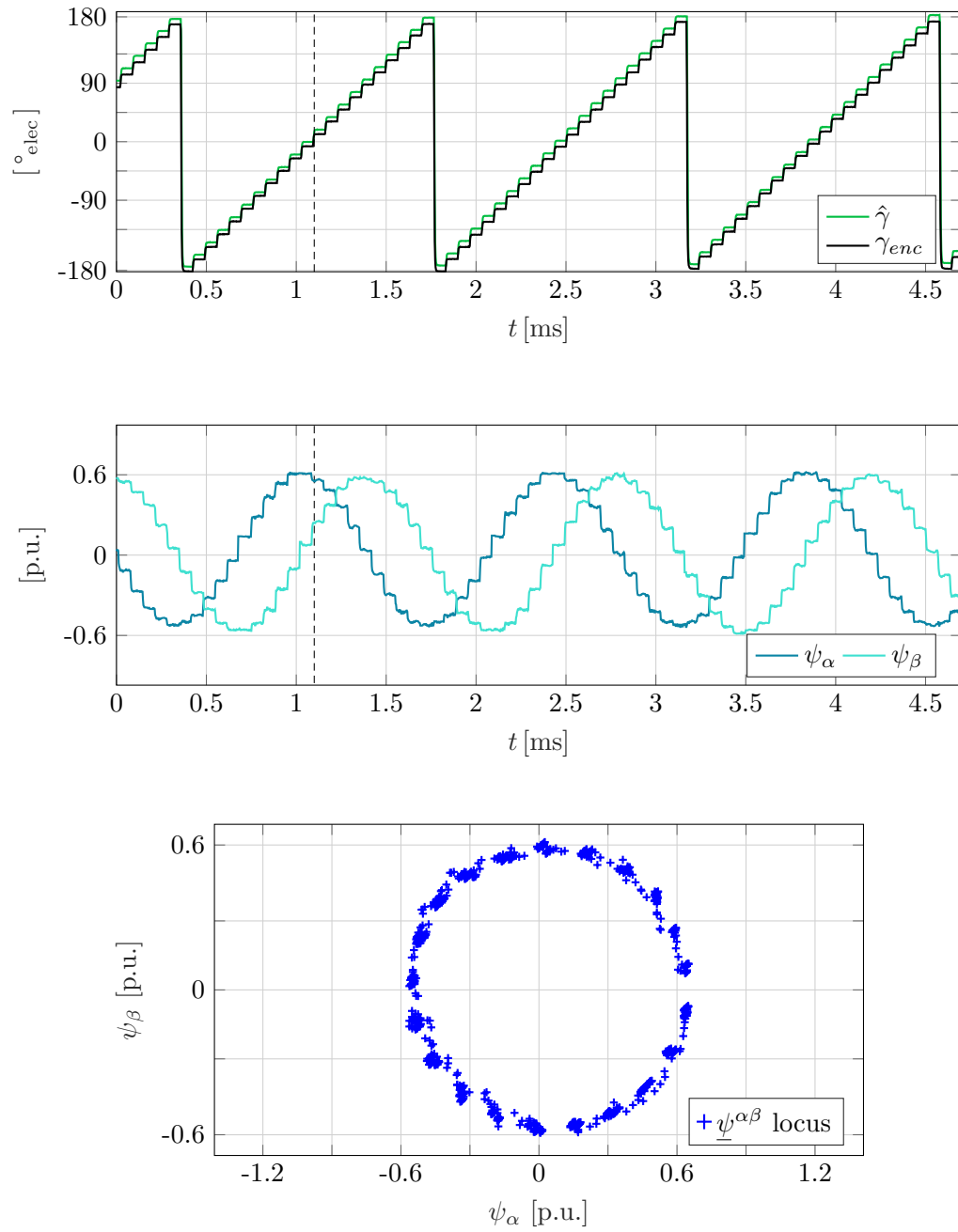
Figure 5.12: SynRM-BEMF performance at load: $\omega = 0.9$, $t_e = 0.06$, $i_d = 0.62$, $i_q = 0.266$ (deep flux weakenig 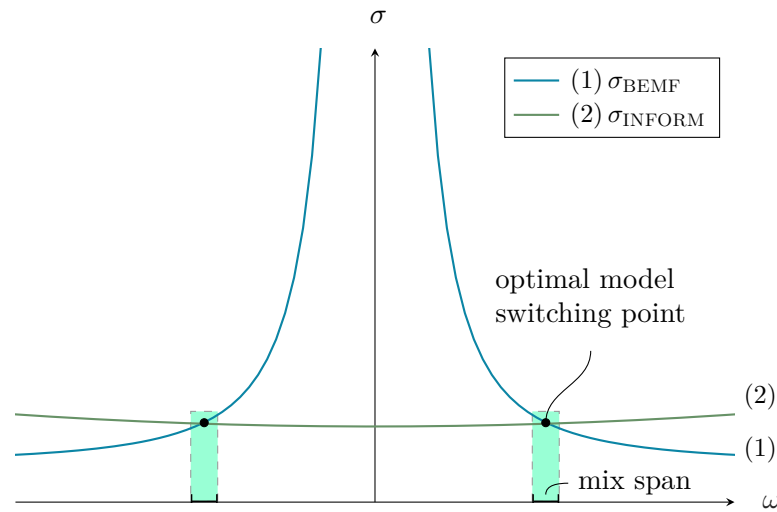range at corresponding load limit); Harmonics visible in i_q due to non-perfect winding distributation as simulated in [1]; Angle error within targeted limits.

Figure 5.13: SynRM-BEMF performance at load: $\omega = 0.9$, $t_e = 0.06$, $i_d = 0.62$, $i_q = 0.266$ (deep flux weakenig range at corresponding load limit);

Figure 5.14: Semantically correct standard deviation trends for INFORM and SynRM-BEMF
methods, inferred from [66]. A mixing speed-span covering the optimal switching
point ensures smooth transition.

INFORM method requires 3-active space vector modulation presented in Section 5.2.3. This
work related the compulsory pulse width required for current slope measuring to $|\underline{u}|^{dq}_{max}$ in Equation (5.54). The proposed SynRM-BEMF method in the previous section works with both 3-active
and 2-active space vector modulation. As discussed in Section 4.2 and shown in Equation (4.23),
the maximum current controller output $|\underline{u}|^{dq}_{max}$ in the 2-active case is substantially[26] higher than
in the 3-active case. On the other hand the SynRM-BEMF method requires the motor to operate
in `vpsm(id)/MTPA` mode as a certain $i_d|_{min}$ is needed to keep the estimation method running.
Thereby it is irrelevant if the motor is loaded or not. Even if the motor is not loaded, ohmic
losses will occur in `vpsm(id)`. When INFORM is used the motor is allowed operate in "pure"
`MTPA` mode.

5.4.2 Transition Strategy

By the above subsection a trade-off between efficiency, control dynamics and estimation quality became evident. This lead to the transition strategy depicted in Figure 5.15. The INFORM method
is used up to a reasonable high speed $\omega_{mix}|^{start}$ to adopt `MTPA` operation. At the end of this
"low"-speed range i_d is ramped up linearly to reach $i_d|_{min}$ to support the SynRM-BEMF method,
see also Figure 5.21 in Section 5.6.3.

Both raw sensorless angles are mixed by means of linear weights[27] similar to the mixing
of transient and quasi-stationary torque limits conducted in Section 4.7.3. Therefore, IN-
FORM operation will start to fade out at $\omega_{mix}|^{start}$ until the motor is completely controlled by
the SynRM-BEMF method at $\omega_{mix}|^{start} + \Delta\omega_{mix}$. In the scope of this thesis that is designated
as the start of "medium" speed range. Note that according to Table 5.6, this speed was set to be

---

[26]0.71 vs. 0.22, see Table 5.5

[27]this is an accepted method in state of the art, see also patent [73] page 14, Figure 5B
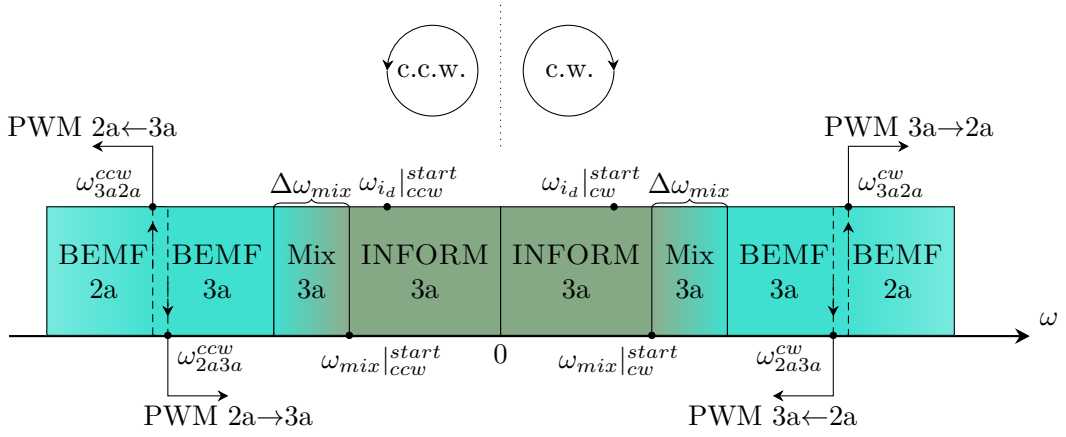
Figure 5.15: Symbolic mixing and switching illustration presenting relevant states, methods and parameters, see also Table 5.6 and Figure 5.21

0.185(CW)/-0.17(CCW). This corresponds also to recommended values, gained by experience from the institute's prior projects, see [74].

To increase the current controller's output, space vector modulation (and thus PWM patterns) must be switched from 3-active to 2-active. The implementation of this PWM-pattern switching process is challenging but possible at the TI-28335[28]. A thorough consultation of [48] is recommended. The adoption of a hysteresis is advised to avoid bouncing between PWM patterns. A "hard-switch" (no pattern mixing) between the two patterns is conducted.

At a certain shaft speed while running in 2-active SynRM-BEMF mode the torque output of the speed controller needs to be restricted due to stator voltage limitations. This starting point of sensorless flux weakening marks the beginning of the so-called "high speed" range in this thesis.

Values for all above mentioned quantities were determined experimentally after considering the findings of Section 5.2 and Section 5.3. A full report of the deployed values is given in Section 5.8 and Table 5.6 in particular.

An interesting effect for quasi-stationary operation at shaft speeds within the angle-mixing span is reported in Figure 5.16. Even at high load torque the system shows excellent performance in terms of stability and angular error quality. The mean value of γ_Δ is nearly zero. This is different from speeds where the motor is controlled using the SynRM-BEMF method only, see Figure 5.12. At later development stages the "medium" speed range proved to be the most sensitive/critical one. This can also be reasoned by inspection of the oscillations after the mixing band visible in Figure 5.24, Figure 5.25, Figure 5.26.

As a scientific result, the adoption of ideas from [66] for Silent-INFORM and salient pole SynRMs yields very good results. The performance within the mixing band was much better than expected. A mandatory prerequisite to adopt the above strategy is to implement clean and reliable switching process between 3-active and 2-active PWM patterns at the TI-28335.

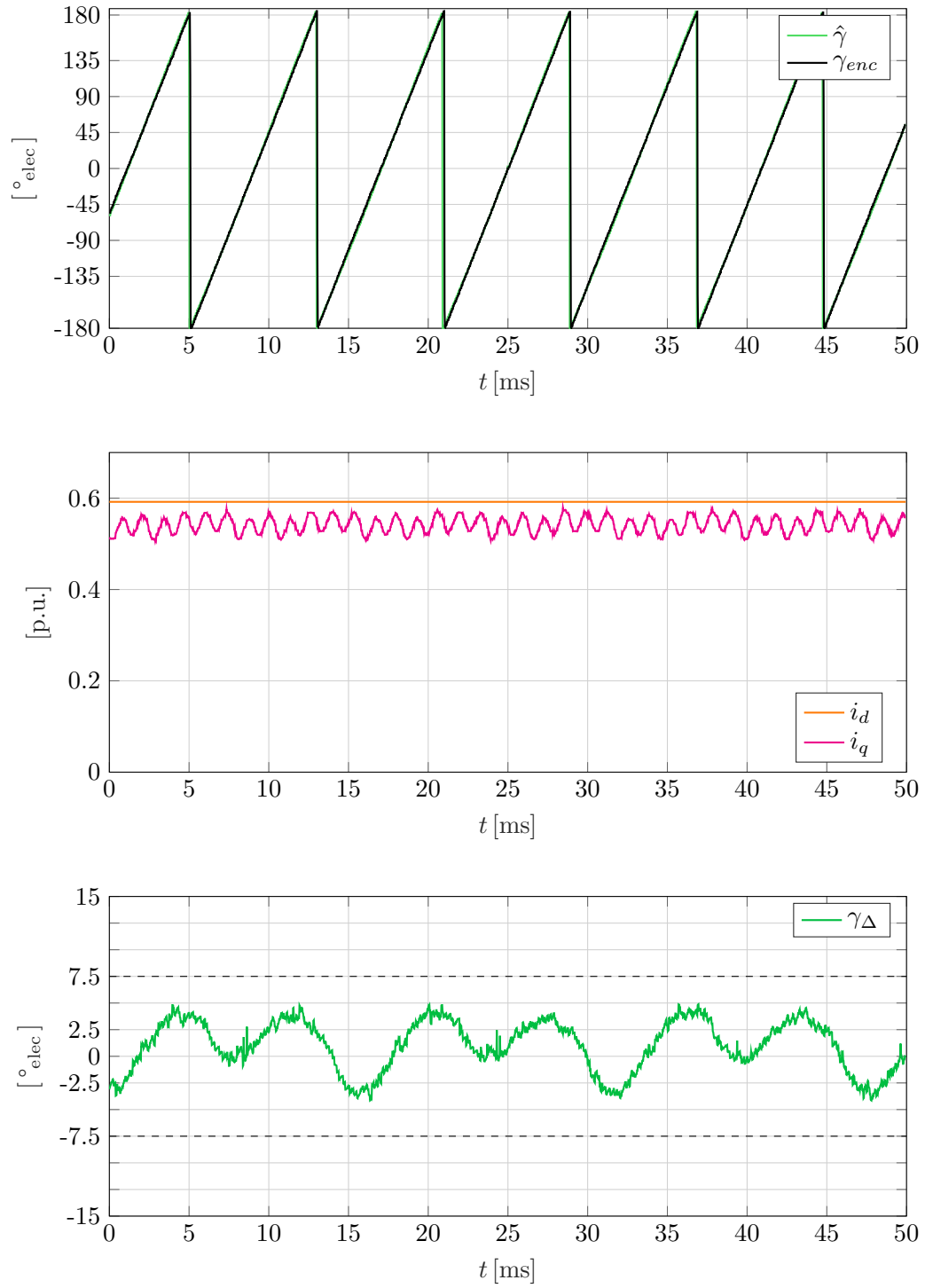[28]and therefore also at other members of the C2000 DSC family.

Figure 5.16: Performance of the mixing subsystem under load: $\omega = 0.167$, $t_e = 0.116$. The angular error's mean is nearly zero. Its magnitude depends on the load torque magnitude.

5.5 Necessary System Modifications for Sensorless Operation

To successfully support both previously described sensorless methods, current- and speed controllers as well as the Luenberger observer need to be tuned with new parameters. Generally speaking, these new settings are of a more "defensive/conservative" nature if compared to the initial ones given in Section 4.8. The respective basic subsystem's structure as presented in Section 4.3 (Observer), Section 4.4 (Current Controllers) and Section 4.5 (Speed Controller) remains unaltered.

In the following, each subsystem is covered separately to enhance readability. However, in a closed loop control system such as the SynRM drive several interdependencies exist between subsystem components. Therefore, the effects discovered and proposed here shall *not* be considered as hard causal "if-then" relationships, true for any system where the respective block is implemented. Correlations outlined and quantified in the following are always to be seen in the context of *this* specific system, having the prior presented specific combination of subsystems[29]. More detailed investigations for each block in turn are only possible in an "open loop" setup[30] that requires a telemetry machine and a load machine.

5.5.1 Current Controller Modifications

The initial current controller design of Section 4.4 comprised a feedforward and a feedback path (two degree of freedom control). Differentiating the reference values (i_d^r, i_q^r) within the FF branch lead to an improvement in transient performance. This became apparent by inspecting the rise and settling time of the measured currents compared to the feedback-only current controller. But these favorable characteristics are traded by current overshoots when the reference values are differentiated. The overshoot's magnitude is influenced by the differentiators pre-filter's time constant τ_{2DOF}, the speed controllers proportional gain $k_{P\omega}$ and the speed controllers reference value filter's mode.

For sensorless control this differentiating part was set to zero, because with this setting issues emerged at both very low and very high speeds. At very low speeds, when the motor is running sensorless in `MTPA` mode facilitated by an INFORM estimation, the sign of i_q^r changes frequently. This is visible in the right half of the 2$^{\text{nd}}$ plot of Figure 5.25 and may be accounted to static friction effects of the ball bearings and/or also harmonics introduced by a non-perfect sinusoidal field excitation curve, see Section 2.3. The speed controller is working as intended, see Equation (4.109), but in combination with the current controller's differentiating part stated operating point results in substantial overshoots in i_q. This in turn degrades INFORM performance considerably. By turning off the differentiator described effects disappear.

At very high speeds within flux weakening range overshoots in measured currents introduce/amplify oscillations in $\hat{\gamma}_{\text{BEMF}}$. This lead to a complete omission of the differentiating branch within the FF part of the current controller for sensorless operation.

---

[29]This is especially true for the interplay between observer, speed Controller and INFORM & BEMF subsystems.

[30]As explained in Section 2.1 the system under consideration comprises one machine that is loaded by means of friction rather than a setup comprised of two motors. To recap: the main reason was given by the fact that the available coupling could not support shaft speeds higher than $\omega \approx 0.63$.

5.5.2 Luenberger Observer Modifications

Within the sensorless system "measured" angles in the scope of the proposed Luenberger observer are the calculated raw values from the preceding sections. Further, in Equation (4.37) the angle difference $\hat{y}_k - y_k$ becomes

$$\hat{y}_k - y_k := \begin{cases} 2\,\hat{\gamma} - \hat{\gamma}_{\text{INF}} & \text{when } \omega < \omega_{mix}|_{cw}^{start} \\ \hat{\gamma} - \hat{\gamma}_{\text{BEMF}} & \text{when } \omega > \omega_{mix}|_{cw}^{start} + \Delta\omega_{mix} \\ \hat{\gamma} - \text{mixed}\,\{\hat{\gamma}_{\text{INF}}, \hat{\gamma}_{\text{BEMF}}\} & \text{when } \omega \in [\omega_{mix}|_{cw}^{start} \dots \omega_{mix}|_{cw}^{start} + \Delta\omega_{mix}] \end{cases} \tag{5.75}$$

During the development of the BEMF method from Section 5.3 the following conclusions were drawn that eventually yielded the final configuration of the deployed observer:

1. Due to model uncertainties, sensitivities to calibration and measurement noise, a tuning of the observer towards a more defensive setting is mandatory. The raw values $\hat{\gamma}_{\text{BEMF}}$ and $\hat{\gamma}_{\text{INF}}$ need to be smoothed in order to establish a stable and robust FOC operation. The initial design parameter $\underline{z}_{PL} = 0.975 \cdot \underline{\lambda}_M$ used in Ackermann's formula results in error weights that amplify above effects too much and eventually lead to an unstable system.

2. Choosing $\underline{z}_{PL} = 0.999 \cdot \underline{\lambda}_M$ leads to a set of error weights that are reduced in magnitude and consequently reduce noise from sensorless estimations. The system becomes stable up to speed values where the voltage limit becomes active (base speed range of SynRM-BEMF method, see Section 5.6). Based on the findings of Section 4.7 the flux weakening region is estimated to start at about $\omega \approx 0.5\dots 0.7$.

3. The dynamics of this stable, defensive Luenberger observer is decreased, if compared to the prior setting. When driving the control system with (first order LPF filtered) speed reference values as discussed in Section 4.5.2, tracking errors visible in γ_Δ will occur while torque is applied to the motor. For speed reversals and several other trajectories the sensorless system becomes unstable. "The observer is too slow" to eliminate these tracking errors, but it has to be "that slow" to ensure stability, see points 1. & 2.
   Therefore, the speed controller must also be adapted to this defensive, stable observer which is discussed in the next Section 5.5.3. To estimate the shaft's torque in order to eliminate tracking errors, the Luenberger observer was expanded[31] by a third state $\hat{t}_l$

The initially obtained error weight coefficients $(k_{L\gamma}, k_{L\omega}, k_{Lt})$ for $\underline{z}_{PL} = 0.999 \cdot \underline{\lambda}_M$ were further *manually* adjusted to meet the target of $|\gamma_\Delta^{max}| \leq 7.5°_{\text{elec}}$. Their final values are reported in Table 5.5. Two findings shall be highlighted here.

- The difference between a suitable, functioning design and an unstable one in terms of $\underline{z}_{PL}$ is just 2.5%. This highlights the importance of designing and tuning the observer within the time discrete z-domain rather than adopting direct-discretization of s-domain designs, see also the discussions in Section 5.3.2 and Section 4.4.2.
  After manually tuning the error weight coefficients an investigation of the observer's closed loop error system poles is obligatory to ensure operation within theoretically stable margins.

---

[31]Up to this point of development it comprised only two states (angle and speed). In this thesis, only the final version is presented and discussed.

With definitions of Section 4.3 and reference to [54] the observer's closed loop error system poles are obtained via

$$\underline{\lambda}_e = \text{eig}\left(\mathbf{\Phi} + \mathbf{k_L}\mathbf{c^T}\right) \tag{5.76}$$

and are reported as

$$\underline{\lambda}_{e,1} = 0.99780\cdots + \text{j}0.05837\cdots \tag{5.77}$$

$$\underline{\lambda}_{e,2} = 0.99780\cdots - \text{j}0.05837\cdots \tag{5.78}$$

$$\underline{\lambda}_{e,3} = 0.99999980\cdots \tag{5.79}$$

This confirms stability and highlights the very narrow band for these parameters where proper system performance can be achieved. It would have been practically impossible to find this band by directly tuning the error weights alone. Challenges and limitations for the approach with Luenberger observers are also indicated. For future work an adapted scaling and/or the usage of a Kalman Filter variant[32] is suggested.

- The final value for the estimated load torque's error weight is $k_{Lt} = 10^{-5}$. This *numeral is only representable if 32-bit* `IQmath` *data formats*[33] *are used.* The topic of data formats and numerical representation is also comprehensively discussed in [43, Chapter 8]. There the adoption of a format higher than I13Q19 is recommended for sensorless control. As discussed in Section 3.2, the formats I4Q28 (observer) and I8Q24 (current/speed Control) were deployed in this thesis.

5.5.3 Speed Controller Modifications

To enable high performance sensorless operation the following three modifications to the speed controller were necessary:

Torque Realization Mode: vpsm(id)/MTPA

This paragraph is to be seen as expansion to the torque realization strategies presented in Section 4.5.3. When operating the motor in sensorless mode, a certain value of $i_d|_{min}(\omega)$ has to be established for SynRM-BEMF operation, see Section 5.3 and the discussion in Section 5.6. This is achieved by adopting the `vpsm(id)` mode. Depending on the torque demand t_e^r calculated by the speed controller the `MTPA` mode is adopted if possible ($i_d|_{min}(\omega)$ or higher is then still fulfilled).

That is, if

$$t_e^r > (l_d - l_q)\left(i_d|_{min}(\omega)\right)^2 \tag{5.80}$$

is true, the motor runs using the `MTPA` mode of Section 4.5.3. If the torque demand is too low and the above relationship is not fulfilled, the `vpsm(id)` is adopted using

$$i_d^r = i_d|_{min}(\omega) \tag{5.81}$$

$$i_q^r = \frac{t_e^r}{(l_d - l_q)\,i_d|_{min}(\omega)} \tag{5.82}$$

---

[32]stationary, time-variant, extended, unscented, cf. [72]
[33]To be specific, I15Q17 or higher resolution for this parameter.

The identification of the function $i_d|_{min}(\omega)$ is carried out in the next section. The result is shown in Figure 5.21. Using this operational mode the MMF angle θ will lie within the interval $[-45\,°_{\text{elec}} \ldots 45\,°_{\text{elec}}]$.

Ramp Filter Mode for Reference Values

A decrease of the speed controller's dynamic is necessary in order to adjust to the robust sensorless observer as discussed in Section 5.5.2. To suppress tracking errors in γ_Δ, input values will be restricted by means of a ramp-generator[34]. Only a certain rate-of-change at the filter's output will be allowed. Testing the final system configuration including sensorless flux weakening was carried out to find the maximum possible rate of change for ω^r. An appropriate setting of $SR_\omega^{max} = 1.29\frac{\text{p.u.}}{\text{s}}$ was obtained. This ramp output in turn is again low-pass filtered by Equation (3.10) using $\tau_{SR} = 50\,\text{ms}$ to smooth kinks at the beginning and end of each ramp.

Therefore, a new mode is added to the "Reference Value Filter" block on the left side of Figure 4.8. This mode is activated for standard sensorless operation of the SynRM drive. The signal input/output relationship can be inspected in the top plots of Figure 5.24, Figure 5.25 and Figure 5.26. The first-order LPF mode is still used for development and identification purposes in sensorless operations, see Figure 5.18 and Figure 5.20.

The reader is referred to Section 4.5.2 and Equation (4.105) in particular, where control theoretical trade-offs between ω^r and t_e^r are discussed.

Proportional and Integral Gain

The prior presented filtering mode for reference values is an adjustment of the reference value path. The feedback path also needs to be tuned towards a more defensive setting in order to adapt to the (reconfigured) stable sensorless observer of Section 5.5.2. This resulted in $k_{P\,\omega} = 7.16 \rightarrow 2.864$ and $k_{I\,\omega} = 0.015 \rightarrow 0.007$. The proportional gain $k_{P\,\omega}$ is more critical in this context, as discussed in the prior two sections.

During the creation of this document an interesting relationship was discovered: If the transient time T_{trans} from Section 4.7.2 is substituted into the symmetrical optimum design rule Equation (4.104) values of the same magnitude as printed above can be obtained. This finding could be beneficial for the design of future sensorless SynRM control systems.

By decreasing $k_{I\,\omega}$ to 0.007 overshoots in $\hat{\omega}$ can be avoided. This was one of the very last tunings that were made to the control system. The difference between the settings 0.015 vs. 0.007 can be reasoned by comparing the top plots of Figure 5.24 and Figure 5.26.

5.6 Flux Weakening Operation Utilizing Estimated Shaft Positions

In the following a strategy of how to operate a sensorless controlled SynRM in the flux weakening region is proposed in Section 5.6.1. Identification methods that obtain proper settings and limits

---

[34]A step at the input will therefore result as a ramp to the desired value at the output of the filter, which resembles integrating behavior during the transition between two distinct input-reference values.

to realize that strategy are presented in Section 5.6.2. As result of this process, output torque limitation functions $\bar{t}_e^{sl}|_{min}^{max}(\omega)$ are derived that allow for four quadrant high speed sensorless operation. Properties and implications of these functions are discussed in Section 5.6.3. The overall resulting system performance in sensorless mode is then assessed in the next Section 5.7.

The subject matter discussed here builds upon all prior presented subsystems from Chapter 4 and Chapter 5. The reader is advised to consult the preceding sections, especially Section 4.7.

5.6.1 Constraints, Trade-offs and Sensorless Flux Weakening Strategy

The limitations and trade-offs of four quantities characterize the sensorless flux weakening region: Maximum current space vector $|\underline{i}|$, maximum voltage space vector $|\underline{u}|_{max}^{dq}$, minimum direct axis current $i_d|_{min}(\omega)$, and angular error γ_Δ. Consequently, sensorless FW can be considered as constrained optimization task[35].

Current and Voltage Constraints

Just as in the sensor-based case, current limitations due to thermal constraints and voltage limitations due to a finite available bus voltage U_{DC} need to be considered. Current space vectors that realize a given torque command t_e^r from the speed controller need to lie within the intersected area of the current circle and voltage ellipse(s), visible in Figure 5.17. As the speed increases the voltage ellipse shrinks, see Section 4.7. Due to necessity of 3-active space vector modulation for silent INFORM the maximum output voltage is given by $|\underline{u}|_{max}^{dq} = 0.22$, see Equation (5.54). Relating to Figure 5.17, much smaller voltage ellipses would result. This limitation can be avoided by an intelligent transition strategy and a proper choice of switching speeds, see Section 5.4. Then, the maximum output voltage becomes $|\underline{u}|_{max}^{dq} = 0.71$ as was derived in Equation (4.23).

Constraints Induced by Sensorless Models

The SynRM-BEMF method requires a specific $i_d|_{min}(\omega)$ for stable operation. The choice of this quantity is of central importance for the sensorless control system at high speeds. Due to interdependencies discussed in Section 5.5 and the structure of the calibrated SynRM-BEMF method that was covered in Section 5.3.2, solely experimental and heuristic statements can be made here. As the proposed subject matter of this section is assumed to be novel in the field, this is a natural scientific approach: Observations gathered by experiments are the beginning of each scientific analysis.

Given the sensorless SynRM system with all applied modifications discussed in Section 5.5, an increase of $i_d|_{min}(\omega)$ leads to:

- ...a reduction in γ_Δ and consequently improved sensorless estimation quality and increased stability.

- ...an increased voltage demand in both load and no-load conditions and ultimately reduced motor efficiency.

---

[35]speed/torque/power (depending on the objective) is to be maximized under aforementioned constraints
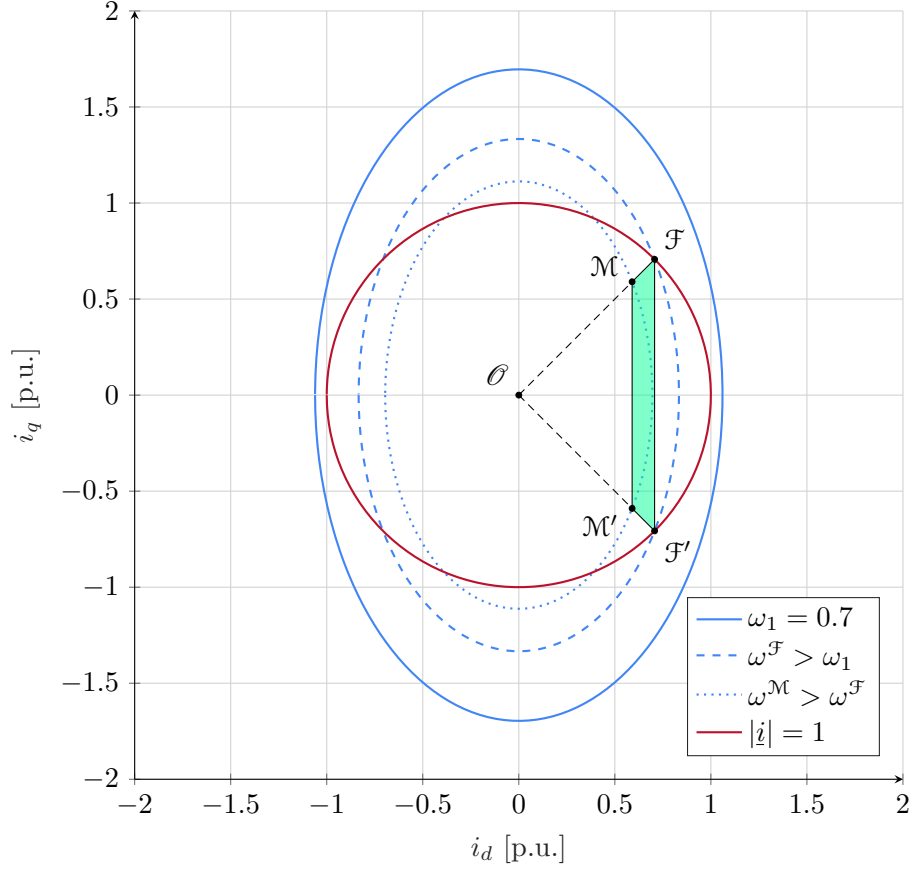
Figure 5.17: Sensorless flux weakening strategy; Current circle (**red**); Voltage ellipses (**blue**); Ideal stability trapezoid established by $i_d|_{min}(\omega)$ (**green**) ; Valid current space vectors are located within the intersected area of current circle, (active) voltage ellipse and stability trapezoid. Tilting not depicted ($r = 0$) to enhance readability.

Therefore, a *trade-off between stability/quality vs. efficiency is discovered.* Testing revealed that the most critical speed (ω) operating point is $0.185\,(\text{CW})\,/-0.17\,(\text{CCW})$ viz. the start of the SynRM-BEMF operational region, see Section 5.4.2. At these speeds values of $i_d|_{min} > 0.35$ are allowed, but introduce substantial angular errors for lower values. To meet the target of $|\gamma_\Delta| \leq 7.5\,°_{\text{elec}}$ a choice of $i_d|_{min} \geq 0.707$ is necessary.

It shall also be highlighted here that "adjusting the target" $|\gamma_\Delta| \leq 7.5\,°_{\text{elec}}$ to higher values in order to allow for a lower $i_d|_{min}(\omega)$ is misleading. At high speeds angular errors as high as $7.5\,°_{\text{elec}}$ may already prove to be problematic for stability. In [66] the requirement of $\sigma_{\gamma_\Delta} \leq 5\,°_{\text{elec}}$ is mentioned for industrial application. The final version of the sensorless SynRM drive system satisfies this requirement in the high speed region, visible in the bottom plots of Figure 5.24, Figure 5.25 and Figure 5.26.

Sensorless Flux Weakening Strategy

The following reasoning and proposed FW strategy for sensorless operation is a variant of the quasi-stationary sensor-based FW strategy discussed in Section 4.7.3. Generally speaking, operation in `MTPA` mode is targeted as often as possible, while ensuring $i_d|_{min}(\omega)$ at medium and high speeds through `vpsm(id)` mode depending on the demanded torque t_e^r.

Referring to the pictured ellipses in Figure 5.17 and above explanations the sensorless flux weakening strategy proposed can be reasoned as follows[36]:

$\mathscr{O} \to \mathscr{F}$ In the low speed region the SynRM is operated purely in `MTPA` mode facilitated by IN-FORM angle estimation as described in Section 5.2. The realization of $i_d|_{min}(\omega)$ is not necessary until the interval $\left[\omega_{id}|^{start} \ldots \omega_{id}|^{end}\right]$ where said quantity is ramped up from $0 \to 0.707$, visible in Figure 5.21, to prepare for a possible change to SynRM-BEMF mode. This ramp-up state is not depicted in Figure 5.17.

$\mathscr{F} \to \mathscr{M}$ At the characteristic flux weakening velocity ($\widetilde{\omega}_a^{cw}$ and $\widetilde{\omega}_b^{cw}$ given in Table 5.3) the corresponding voltage ellipse intersects the current circle under the constraint of $i_d|_{min}(\widetilde{\omega}_a^{cw}, \widetilde{\omega}_b^{cw})$. This indicates the starting point for sensorless flux weakening. Depending on the speed controllers output (torque demand) t_e^r and the identified functions $i_d|_{min}(\omega)$ and $\bar{t}^{sl}|_{min}^{max}(\omega)$ current space vectors will be located within the green trapezoid indicated in Figure 5.17. A higher torque demand leads to an increased MMF angle, see the description of output modes in Section 5.5.3.

$\mathscr{M}$ This FW process ends at $\mathscr{M}$ where the SynRM sensorless control system ultimately faces one or more of the following (insurmountable) limitations[37]: Voltage limit vs. $i_d|_{min}(\omega)$, mechanical limitations, dead time effects, angular error or stability issues. As prospect to the results a maximum sensorless safe-to-operate speed of $\omega = 1$ can be reported. This corresponds to $\approx 24\,000\,\text{rpm}$ and $1.81 \cdot \widetilde{\omega}_a^{cw}$.

- Speaking about all four operational quadrants, the resulting (optimum) current space vector region in the (i_d, i_q) plane of Figure 5.17 is therefore given by the unification of the dashed MTPA lines $\overline{\mathscr{O}\mathscr{F}}/\overline{\mathscr{O}\mathscr{F}'}$ (low speeds) and the green trapezoid $\overline{\mathscr{M}\mathscr{F}\mathscr{F}'\mathscr{M}'}$ (medium & high speeds).
  This reasoning is without consideration of the ramp-up state for $i_d|_{min}(\omega)$, visible in Figure 5.21. If this state is included the above explained region expands by the triangle $\overline{\mathscr{O}\mathscr{F}\mathscr{F}'}$ during the speed interval $\left[\omega_{id}|^{start} \ldots \omega_{id}|^{end}\right]$ (not depicted in Figure 5.17).

- The reader is referred to Section 4.7.3 where an apparent tilting of voltage ellipses by κ_{tilt} is discussed. Additionally it is important to note that the above stated trapezoid does not include constraints that may become apparent by targeting $|\gamma_\Delta| \leq 7.5\,°_{\text{elec}}$. Therefore, the depicted green area above is the maximum possible area for current space vectors given by the above range of $i_d|_{min}(\omega)$. An introduction of such an additional limit as well as pivot effects of the ellipses are likely to further restrict the trapezoid. This will be investigated in the remaining sections.

---

[36]explanations are valid for Q1 and Q2 , strategies for Q3 and Q4 follow accordingly.
[37]cf. Section 4.7.6

5.6.2 Sensorless Torque Injection

Identification of the function $i_d|_{min}(\omega)$ with values "as low as possible" while ensuring stability and $|\gamma_\Delta| \leq 7.5\,°_{\text{elec}}$ is compulsory to realize the strategy presented in the previous section. In addition to that torque limitation functions $\bar{t}_e^{sl}|_{min}^{max}(\omega)$ need to be obtained (flux weakening) as the voltage ellipse in Figure 5.17 shrinks if the shaft speed is increased. Due to reasons given above (interdependencies, absence of a second motor) a purely experimental approach is taken and one[38] set of torque limitation functions $\bar{t}_e^{sl}|_{min}^{max}(\omega)$ is obtained.

Test Trajectory for Sensorless Tuning

A prerequisite for the start of the identification process is the successful execution of the trajectory depicted in Figure 5.18. As described in Section 5.5, several modifications needed to be implemented to current/speed-controllers and the observer. The trajectory in the top plot was taken to develop prior described settings. Configured[39] values of $i_d|_{min} < 0.35$ would result in unstable behavior for small reference changes depicted in the left half of the top plot of Figure 5.18. The value of $\omega^r = 0.65$ is an educated guess for the characteristic flux weakening speed based upon the findings of Table 4.5 in Section 4.7.3. A strong sensitivity of the type $\gamma_\Delta(i_d|_{min})$ can be reported. The choice of $i_d|_{min} = 0.75$ yielded acceptable angular errors for acceleration in the medium speed range[40]. At medium speed breaking maneuvers the angular error is outside the targeted margin. This will be improved after adopting sensorless flux weakening.

Identification Experiments and Qualification Rules

The sensorless torque injection experiments are carried out in the same manner as the torque injection process for transient sensor-based voltage limits, described in Section 4.7.2. That means timings and control structure are the same as before with additional properties:

- The speed controller runs in the mixed `vpsm(id)`/MTPA mode, see Section 5.5.3.

- Additionally to output torque $t_e^r(\omega^r)$ and speed ω^r, the minimum direct current $i_d|_{min}(\omega^r)$ is also adjusted to gain flux weakening functions $\bar{t}^{sl}|_{min}^{max}(\omega)$ and $i_d|_{min}(\omega)$

- The condition given in Equation (4.136) is adjusted to: Maximum saturation time $< 10\%$. Inactivity of `vcap` is accepted. Several additional conditions were specified, see below.

As representative example, Figure 5.19 shows a successful iteration for the experiment. Conditions for $t_e^r(\omega^r)$ and $i_d|_{min}(\omega^r)$ candidate values to qualify for flux weakening were specified[41] as:

(i) The injection process per se has to be stable.

(ii) `vcap` saturation time percentage is below $\approx 10\%$.

---

[38]contrary to the transient/quasi-stationary approach in Section 4.7

[39]Several values for $i_d|min$ were applied, see the discussion for trade-offs below.

[40]The target of $i_d|_{min} = 0.707$ as highest possible value was formulated, to comply with the MTPA point at the current circle in Figure 5.17. After identification this goal could be achieved.

[41]Explanations are given for Q1,Q4. The quadrants Q2,Q3 follow accordingly

(iii) $|\gamma_\Delta| \leq 7.5\,°_{\text{elec}}$.

(iv) stable accelerate condition: Given a possible set of $\{t_e^r(\omega_{tmp}^r){>}0\ ,i_d|_{min}(\omega_{tmp}^r)\}$. A speed reference change (LPF-Mode) to $\omega_{tmp}^r + 0.1$ is performed. The conditions (i)-(iii) apply.

(v) stable brake condition: Given a possible set of $\{t_e^r(\omega_{tmp}^r){<}0\ ,i_d|_{min}(\omega_{tmp-1}^r)\}$ (braking torque and direct axis current from last identification step). A speed reference change (LPF-Mode) to $\omega_{tmp}^r - 0.1$ is performed. The conditions (i)-(iii) apply.

When conducting these experiments $i_d|_{min}$ is tuned first. Then, in most cases, $|\gamma_\Delta| > 7.5\,°_{\text{elec}}$ will result. As compensation, the torque's magnitude is reduced in order to yield $|\gamma_\Delta| \leq 7.5\,°_{\text{elec}}$. Therefore, a reduction of $i_d|_{min}$ is prioritized over a reduction of $\bar{t}^{sl}|_{min}^{max}$. A monotonous decreasing trend for $i_d|_{min}(\omega)$ is targeted while adjusting test values.

When the experiment was conducted, condition (ii) from above (voltage limit) was inactive for the majority of identified values $\{\bar{t}^{sl}|_{min}^{max}(\omega)\ ,i_d|_{min}(\omega)\}$. The shaft speed where voltage limitations become permanently active when injecting torque due to a certain value of $i_d|_{min}$ marks the ultimate limit for sensorless control. For the SynRM drive system this was measured as $\omega_{sl}^{max} = \pm 1.05$ and $i_d|_{min}(\omega_{sl}^{max}) \approx \pm 0.6$, see Figure 5.21, Figure 5.22 and the discussion in Section 5.6.3.

Experiment results are presented and discussed in the next section. Values for $\bar{t}^{sl}|_{min}^{max}(\omega)$ and $i_d|_{min}(\omega)$ are again implemented by means of LUTs and piecewise linear interpolation, as described in Appendix A.2. Referring to Figure 4.8, these LUTs are evaluated according to the speed controller's respective active operational mode.

If the results of the sensorless FW identification process are implemented at the speed controller, considerable improvements become evident when executing the test trajectory from Figure 5.18 again. This is indicated in Figure 5.20.

5.6.3 Sensorless Characteristic Curve and Projections

The results of the identification process described in the previous section are depicted in Figure 5.21 for $i_d|_{min}(\omega)$ and Figure 5.22 for $\bar{t}^{sl}|_{min}^{max}(\omega)$.

Referring to Figure 5.21, values of $i_d|_{min}(\omega)$ start relatively high at the medium speed range. The identification procedure yielded a highest value of 0.75. Later, it was manually reduced to 0.707 to "reach" the MTPA point at the current circle at $(i_d^r, i_q^r){=}(0.707, 0.707)$. Performance tests in the next Section 5.7 showed that after this adjustment all targets are still met with a high degree (see the discussion there). The parameters $\omega_{id}|^{start}$, $\omega_{id}|^{end}$ (c.w. and c.c.w.) have to be coordinated with the mixing and switching subsystem presented of Section 5.4 and visualized in Figure 5.15. It is desirable to narrow the band where $i_d|_{min}(\omega)$ is ramped up, but a "sufficient broad" band where angles of the INFORM and SynRM-BEMF methods are mixed ensures a smooth transition. For this thesis the margin of this mixing band was chosen to be 0.1 for robustness reasons.

The resulting torque restriction functions $\bar{t}^{sl}|_{min}^{max}(\omega)$ are depicted in Figure 5.22 together with the results of the sensor-based case. The characteristic speed values that indicate the start of flux weakening are reported in Table 5.3. Compared to the (transient) sensor-based case, the
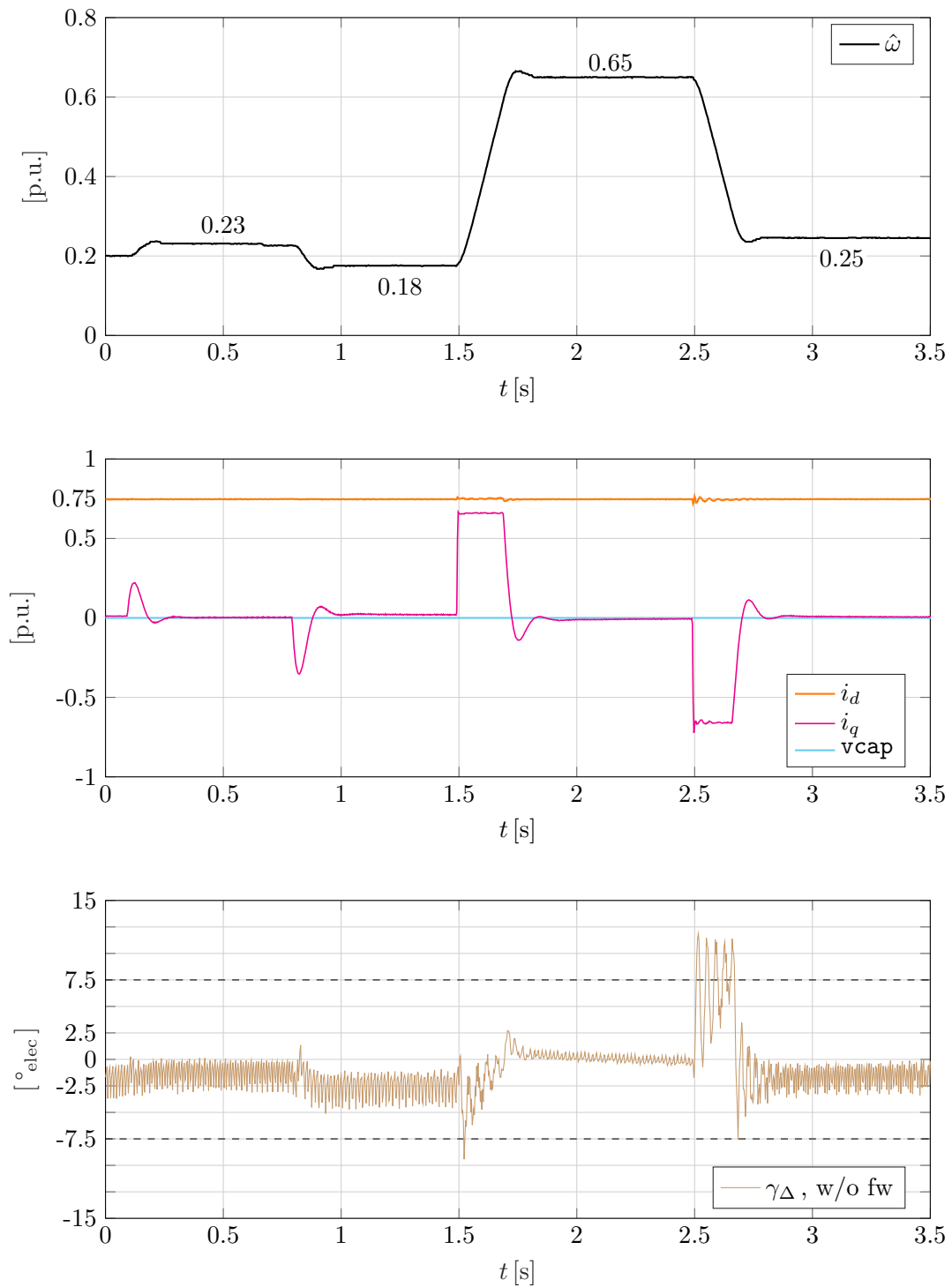
Figure 5.18: Test trajectory to tune current/speed controllers, observer and calibrate SynRM-
Bemf subsystem. LPF as reference value filter used as operational constraints are
eased due to $\omega > 0$ (Q1,Q4) viz. no speed reversals. Angle error target $|\gamma_\Delta| \leq 7.5\,°_{\text{elec}}$.
Slight reference value changes depicted in the left half of the top plot may also
destabilize the system if $i_d|_{min} < 0.35$. For higher speeds the voltage cap becomes
active as sensorless FW is not deployed (yet). MMF angle $\theta < 45\,°_{\text{elec}}$.
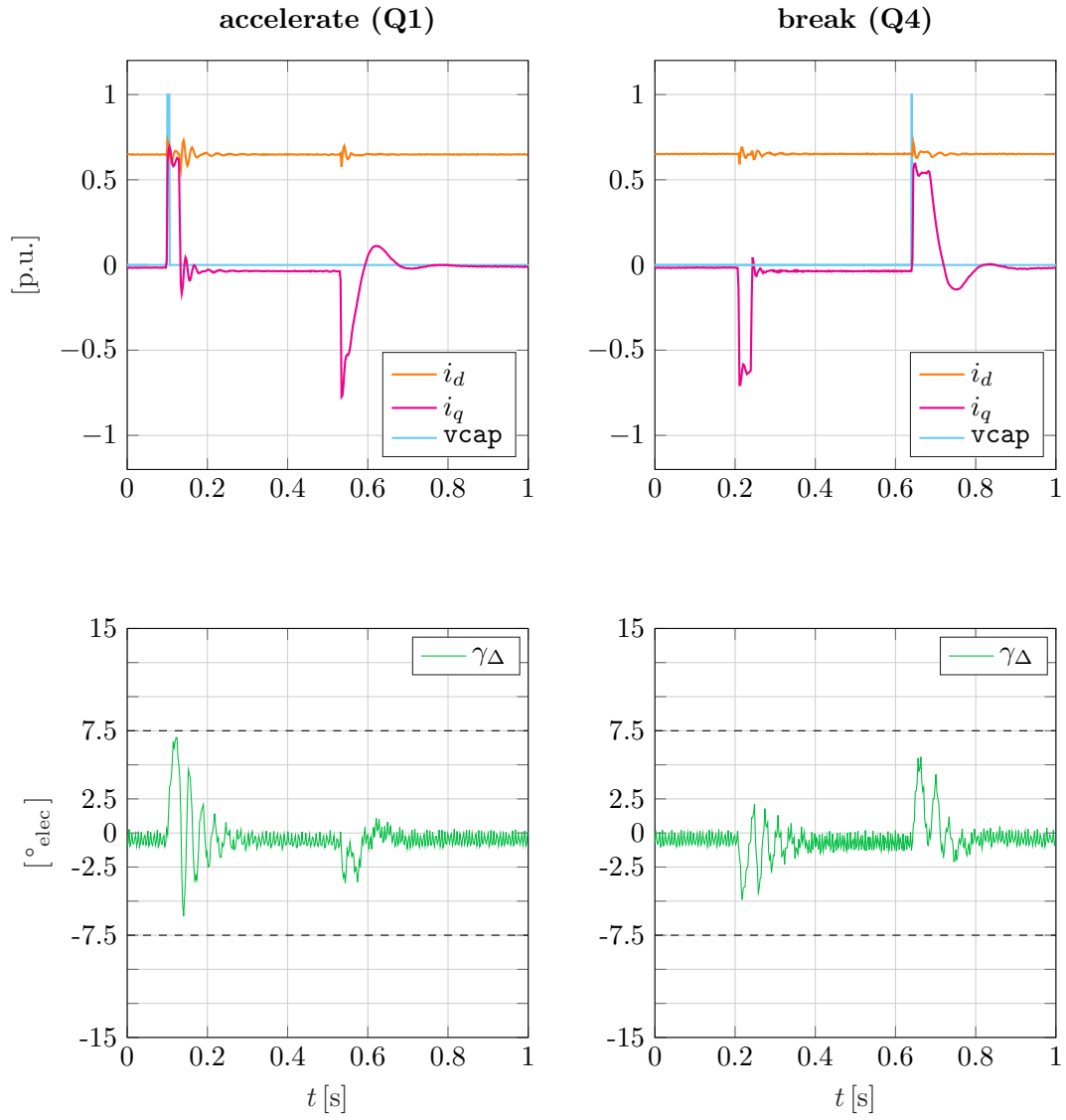
Figure 5.19: Successful iteration for sensorless torque injection and recovery; Voltage limitations are less often active than $|\gamma_\Delta| \leq 7.5\,°_{\text{elec}}$; $\omega = 0.75$, $i_d|_{min}(0.75){=}0.65$, $\bar{t}^{sl}_{max}(0.75){=}0.147$, $\bar{t}^{sl}_{min}(0.75){=}-0.129$
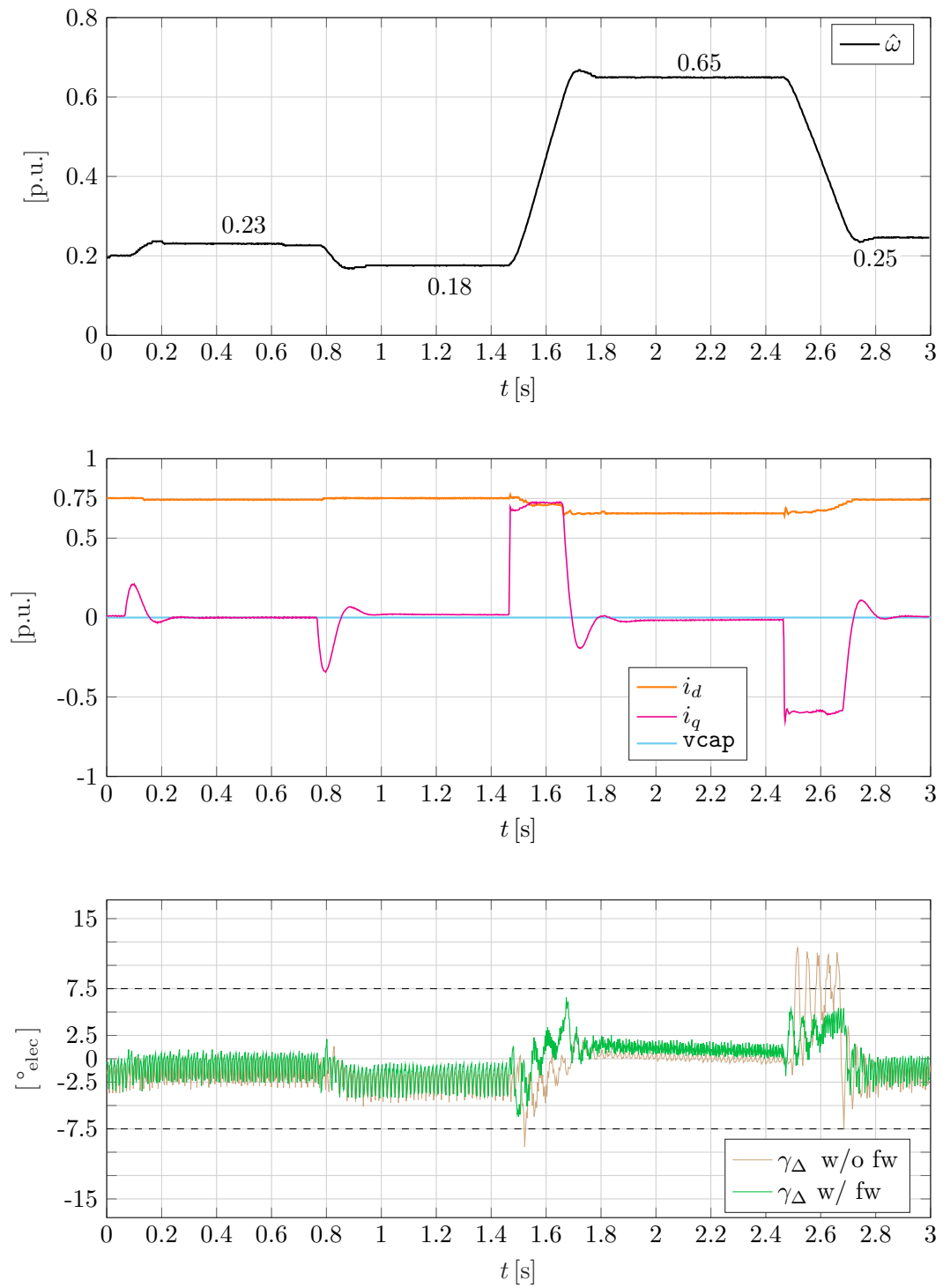
Figure 5.20: Test trajectory after FW identification process by means of torque injection. Substantial improvements for estimation accuracy and efficiency (MTPA) indicated. The depicted speed range can be reasoned as (approximate) "base" speed range for SynRM-BEMF operation.
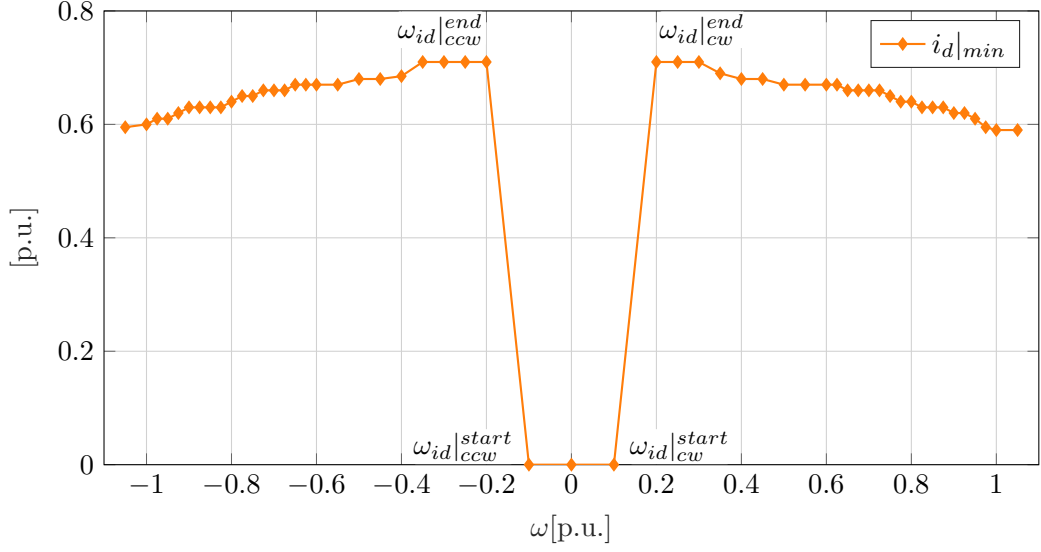
Figure 5.21: Identified and tuned flux weakening function $i_d|_{min}(\omega)$.

Range of Operation	Velocity
clockwise (cw)	
accelerate (Q1)	$\boxed{\widetilde{\omega}_a^{cw} = 0.55}$
break (Q4)	$\widetilde{\omega}_b^{cw} = 0.2$
counterclockwise (ccw)	
accelerate (Q3)	$\widetilde{\omega}_a^{ccw} = -0.575$
break (Q2)	$\widetilde{\omega}_b^{ccw} = -0.2$

Table 5.3: Sensorless flux weakening initial velocities, $|\gamma_\Delta^{max}|=7.5\,°_{\text{elec}}$

characteristic acceleration speeds are only slightly slower than the values reported in Table 4.5. If comparing the torque-restriction branches for acceleration (cyan vs. green in Figure 5.22), the sensorless values are higher than the transient sensor-based values. This can be reasoned by the fact that in the sensorless case the transient term $\frac{d\psi_d}{dt} \approx 0$ as $i_d|_{min}$ is "already" present in the motor. Therefore, torque injection will result in a transient term $\frac{d}{dt}\underline{\psi}^{dq}(t)$ in Equation (4.134) that consists mainly the quadrature axis component and therefore being smaller than in the sensor-based case.

During identification the maximum break torque values had to be reduced substantially to comply to the target of $|\gamma_\Delta| < 7.5\,°_{\text{elec}}$.

At very high speeds the target of $|\gamma_\Delta| < 7.5\,°_{\text{elec}}$ limits the maximum sensorless output torque considerably. Test cases of Section 5.7 showed, that the motor can be safely operated in the range of $\omega = \pm 1$. This result being the precisely the chosen base value of Section 2.2 is coincidence. Adopting the proposed flux weakening methods the sensorless base speed range
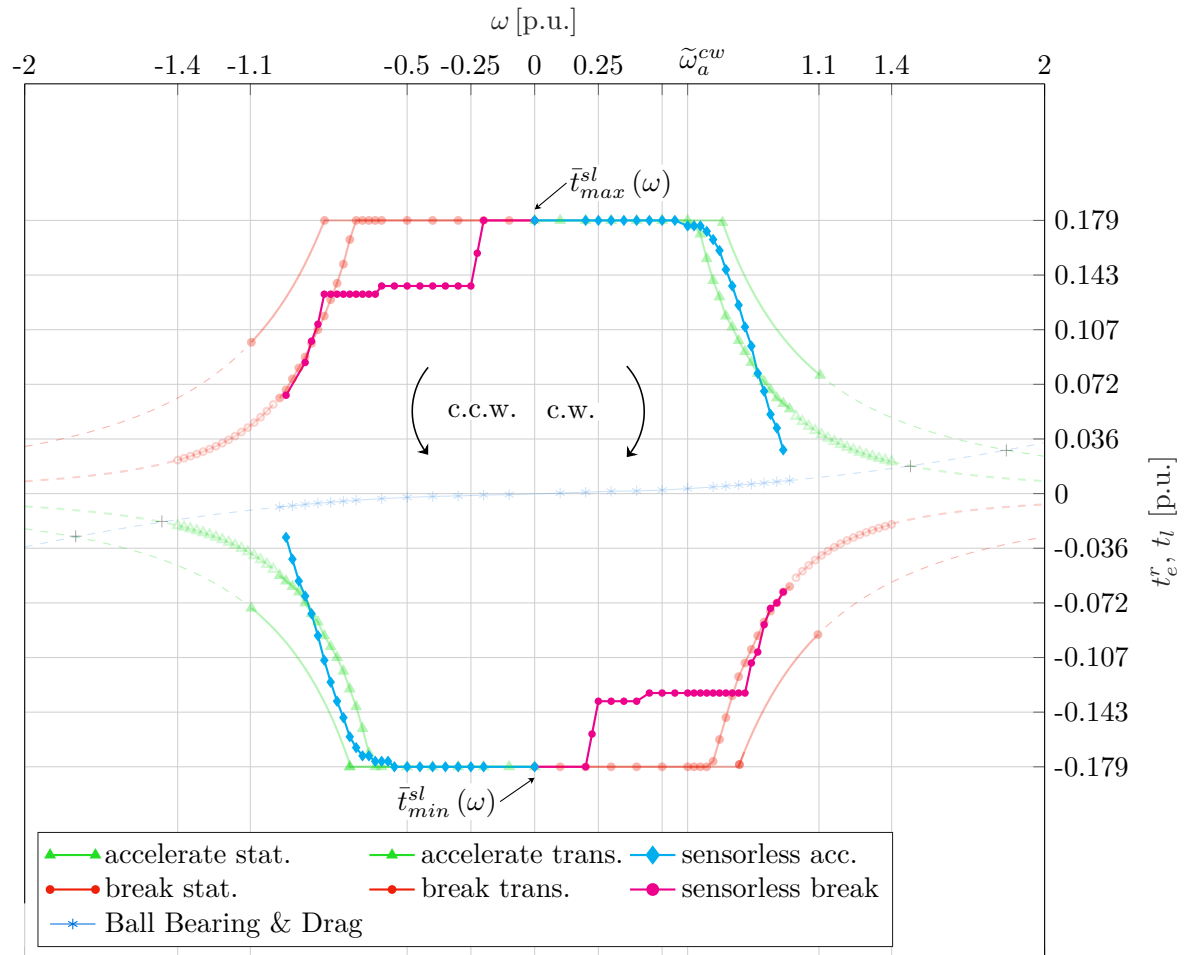
Figure 5.22: Overall transient torque limitations for sensorless operation, comparison to Figure 4.16 (transient & quasi-stationary limitations in sensored mode); Operational range and projections. Full torque availability within the INFORM region. A reduction of the maximum braking torque at medium speed regions was necessary to fulfill $|\gamma_\Delta| < 7.5°_{\text{elec}}$.

$\omega \in [-0.55 \dots 0.55]$ can be increased by 81%. When projecting the cyan acceleration term in Figure 5.22 an intersection with the aerodynamic/ball-bearing-friction branch becomes imminent. Even by an adoption of magnetic bearings the maximum possible projected sensorless speed is much lower compared to the sensored mode. An extrapolation yields a possible intersection at $\omega = 1.05$ this corresponds to $25\,074$ rpm.

A combination of the flux wekening functions of Figure 5.21 and Figure 5.22 reveals the resulting allowed *optimal region* for current space vectors. This shape in the case of Q1/Q4 can be inspected in Figure 5.23. The term optimal region in this context means that by using these current space vectors all four conditions mentioned at the beginning of this section,

- $|\underline{i}| \leq 1$

- $|\underline{u}|_{max}^{dq} \leq \{0.22(3a), 0.71(2a)\}$

- $i_d \geq i_d|_{min}(\omega)$

- $t_e^r \leq \bar{t}^{sl}|_{min}^{max}(\omega)$ to yield $|\gamma_\Delta| \leq 7.5\,°_{\text{elec}}$

for sensorless high speed operation are met (constrained optimization). A comparison of the resulting stability region shape of Figure 5.23 with the initially presented ideal trapezoidal stability region of Figure 5.17 allows for another interesting observation: The difference between the trapezoid of Figure 5.17 and the shape of Figure 5.23 is caused by the last of the four listed above conditions (angular error and torque limitation) in combination with the `vpsm(id)/MTPA` mode. Different values of $|\gamma_\Delta^{max}|$ will lead to different shapes. Narrower shapes for a lower value than $7.5\,°_{\text{elec}}$ are expected.

The resulting allowed region for current space vectors in Figure 5.23 supporting full speed range[42] at sensorless operation can be summarized as follows:

- low speed region: (dashed) MTPA lines $\overline{\mathcal{O}\mathcal{F}_1}/\overline{\mathcal{O}\mathcal{F}_1'}$

- transition region (mix & i_d ramp-up): triangle $\overline{\mathcal{O}\mathcal{F}_1\mathcal{F}_1'}$ during $\left[\omega_{id}|^{start} \dots \omega_{id}|^{end}\right]$

- medium/high speed region: shapes $\overline{\mathcal{F}_1\mathcal{F}_1'\mathcal{F}_2'\mathcal{F}_2}$ for Q1,Q4. Appropriate shapes for Q2,Q3 are of a i_d-axis mirrored appearance with different corner points.

The shape of the sensorless characteristic curves in Figure 5.22 can be accounted to the SynRM machine model in combination with conditions (i)-(v) in Section 5.6.2, rather than a physical model *alone* as was the case in sensor-based operation.

Quasi-Stationary Sensorless Torque Limitation in FW

The quasi-stationary sensorless torque limit was not identified experimentally. In principle it would be possible to proceed with the same strategy as described in Section 4.7.3 under the consideration of the $i_d(\omega)|_{min}$ requirement for sensorless operation. Because of the `vpsm(id)` mode, no significant difference from the transient behavior is assumed. Thus, resulting curves similar to the transient sensorless flux weakening characteristics from Figure 5.22 with only a small shift towards higher speeds are expected. Detailed analysis of shape and magnitude are items to be investigated in future work. Further, for this experiment the utilization of a second load machine is proposed to truly enable a stationary machine operation.

---

[42]For a clarification on *low, medium and high* cf. Section 5.4.1 and Section 5.8.
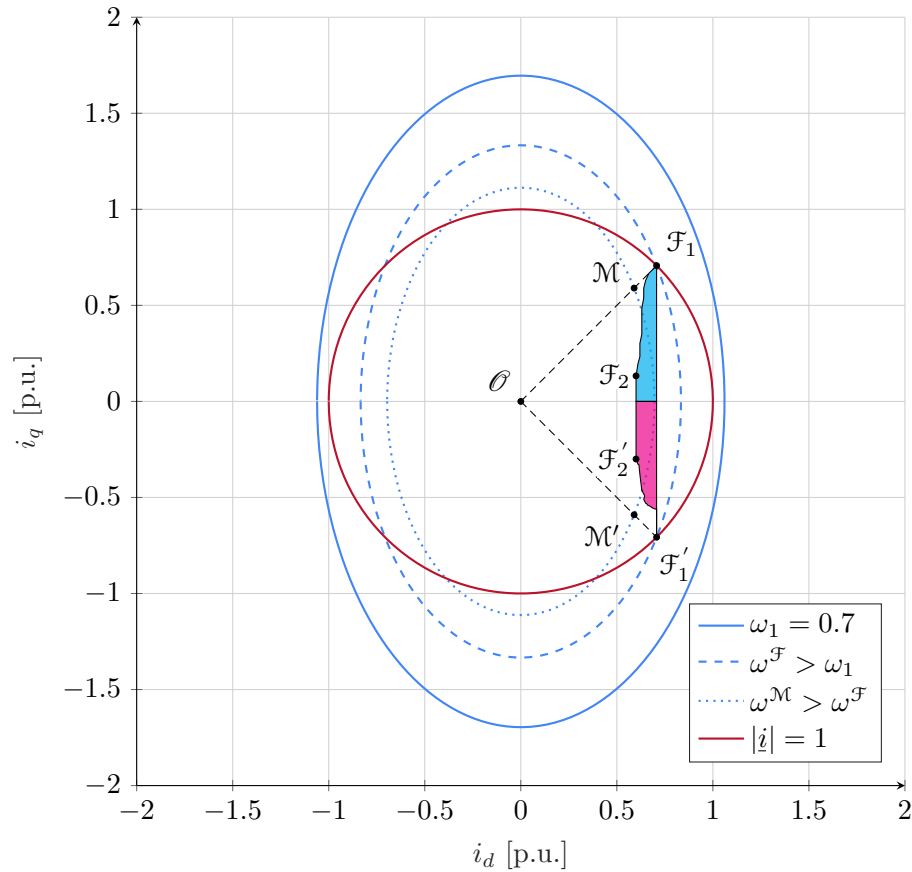
Figure 5.23: Sensorless flux weakening strategy with resulting stability region; Current circle (**red**); Voltage ellipses (**blue**); Stability region established by identified $i_d|_{min}(\omega)$ and $\bar{t}^{sl}|_{min}^{max}(\omega)$ (**cyan(Q1)** and (**magenta(Q4)**) ; Valid FW current space vectors are located within the intersected area of current circle, (active) voltage ellipse and the identified stability shape. The difference between the indicated shape and the green trapezoid of Figure 5.17 is caused by the additional constraint of $|\gamma_\Delta| \leq 7.5\,°_{elec}$. Tilting not depicted ($r = 0$) to enhance readability.

5.7 Performance and Comparison to Sensor-Based Operation

The functionality and overall sensorless system performance including all prior presented methods is presented in this section.

The Fast and Slow Task routines execute within $50.8\,\mu s(3a)^{43}/42.6\,\mu s(2a)$ and $10\,\mu s$ (3a)/ $13.4\,\mu s(2a)^{44}$ respectively. This again indicates decent computational performance while retaining reserves for additional features. If compared to the values of the sensor-based system given in Section 4.7.4 the omission of a sensor only "costs" 11% additional CPU usage[45] for this hardware target, see Table 4.9 and Table 5.8. It shall be emphasized here that in order to obtain these results considerable effort was necessary to fully exploit the DSC 28335, see recommendations in Section 3.1.

The maximum safe-to-operate velocity was already reported in Section 5.6.1 as $\omega_{sl}^{max} = 1.0$, a decrease of 9% if compared to ω^{max} from Section 4.7.6. Nevertheless, this is a very good value because based on the sensorless characteristic velocity the speed could be increased by 81% using flux weakening methods of Section 5.6. That in turn is about the same value as in the sensor-based case. Regarding ultimate limitations, the same considerations as presented in Section 4.7.6 apply together with a trade-off $i_d|_{min}(\omega)$ vs. voltage cap that was reported in Section 5.6.2 to occur at $\omega = 1.05$.

In Figure 5.24 the system's capability to perform an acceleration starting from standstill up to about $24\,000$ rpm is demonstrated. The top plot indicates a "guidance" of the estimated shaft speed $\hat{\omega}$ within a narrow band of the ramp-filtered reference value ω^r. Later, a visible overshoot was corrected by a decrease of $k_{I\,\omega} = 0.015 \to 0.007$. The reader is referred to Section 5.5 that reasoned the necessity to adjust the reference value due to the (new) robust observer settings. In the middle plot, a successful execution of the current conditioning strategies explained before is visible. At low speeds, MTPA is possible until the demand for $i_d|_{min}$ violates Equation (5.80) and the torque realization mode changes to `vpsm(id)`. This is indicated after the first vertical dashed line, a ramp up of the direct axis current is clearly visible. Then, a high demand in $i_d|_{min}$ dominates over the torque demand that is restricted due to filtered reference values of ω^{UI}. Eventually the steep flux weakening function indicated in Figure 5.22 substantially decreases output torque at very high speeds. Standard deviation σ_{γ_Δ} and $|\gamma_\Delta|$ are withing targeted margins.

A deceleration from maximum speed to complete standstill is depicted in Figure 5.25. The same explanations from the above paragraph apply. For this plot (and the following one) the speed controllers integrator was tuned to $k_{I\,\omega} = 0.007$.

Four quadrant operation and speed reversal trajectories are depicted in Figure 5.26. The reader is advised to compare this plot with Figure 4.15, where the same sequence of reference values was used. These two nearly similar test cases also allow for a direct comparison between sensor-based and sensorless control systems. Again the maximum available stator voltage is nearly fully utilized, indicated by a characteristic $\bigvee$-like shape of the voltage curve, seen in the middle plot. Identification conducted in Section 5.6.2 was often limited by angular error first rather than the voltage limit. This can also be seen in the trend of $|\underline{u}|^{dq}$, but these apparent voltage reserves also serve as robustness margin for sensorless control. By inspection of the gathered data

---

[43]six ADC measurement points in 3a vs. one ADC measurement point in 2a
[44]increased effort due to flux weakening routines and LUT search
[45]the absolute computation time increased by $\approx 18\%$ based on the sensor-based system values.
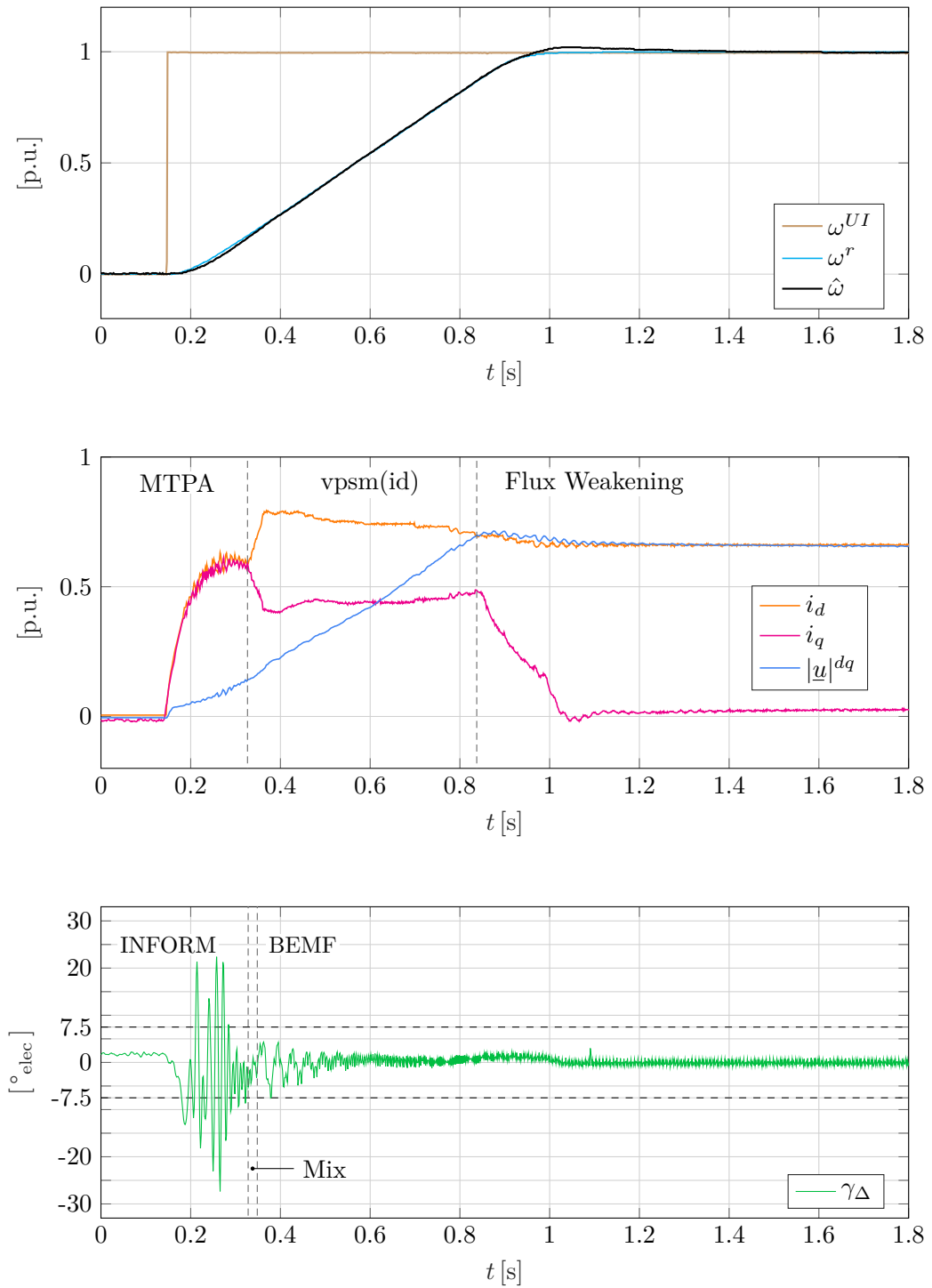
Figure 5.24: Sensorless acceleration benchmark for $\omega^{UI} = 0 \to 1$ (Q1). Execution of the speed command within $< 1\,\mathrm{s}$. All subsystems working as intended, all quality targets met.
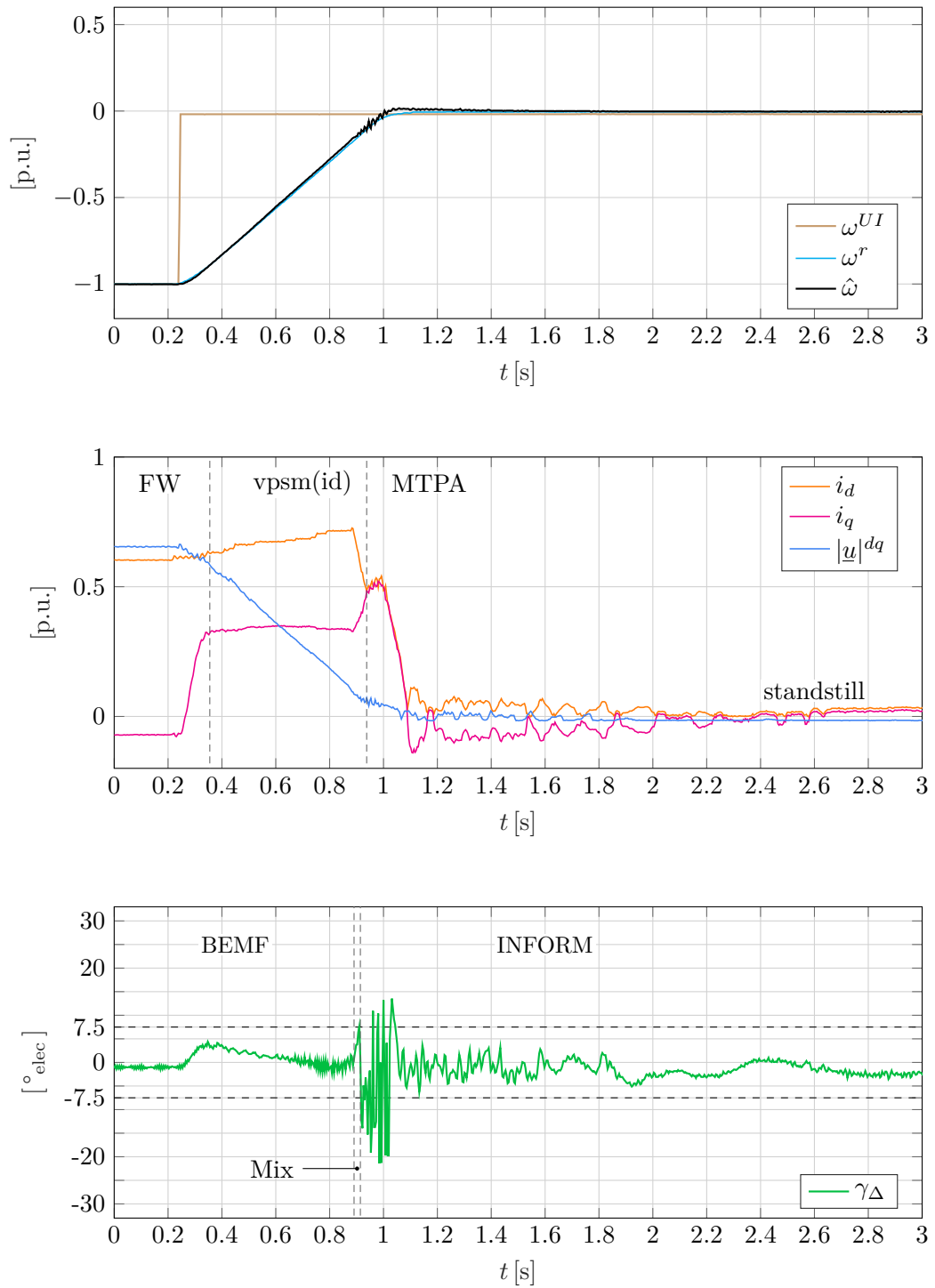
Figure 5.25: Sensorless break benchmark for $\omega^{UI} = -1 \rightarrow 0$ (Q2). Execution of the break command within $\approx 2\,\mathrm{s}$. All subsystems working as intended, all quality targets met.
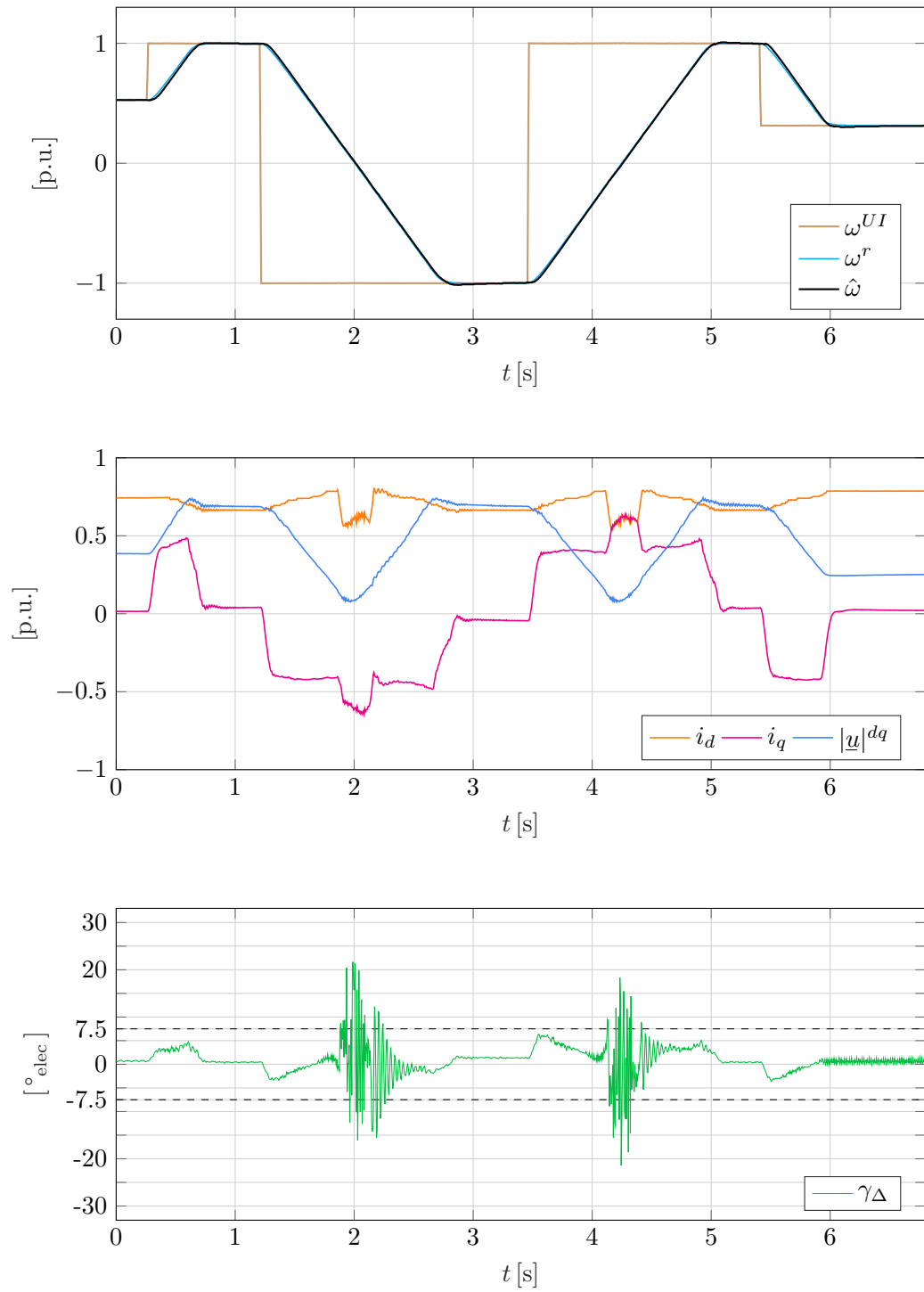
Figure 5.26: Sensorless performance; Speed reversal maneuvers; 31 700 rpm/s break/acceleration rate; all subsystems working as intended, all quality targets met.

a reversal time of $T_{reverse}^{sl} = 1.5\,\mathrm{s}$ can be reported. This corresponds to a maximum achieved acceleration/brake rate of $a_{\Delta\omega} = \pm 1.\dot{3}\,[\mathrm{p.u.}] \,\widehat{=}\, \pm 31\,700\,\mathrm{rpm/s}$, a reduction of 36% compared to the sensor-based case. The main reason for this decrease is given by a reduced torque t_e / torque demand t_e^r, present at the shaft / speed controller's output. To quantify this, a difference of roughly -20% can be reported in the peak torque[46] value[47] if comparing the trajectories of Figure 4.15 and Figure 5.26. Initially this decrease is caused by the ramp filtered (viz. restricted) reference value ω^{UI}. But the core reason is again given by the more defensive observer settings discussed in Section 5.5 that enabled sensorless operation in the first place. Therefore, future system improvement efforts should target the observer subsystem first. The angular error signal printed in the bottom plot of Figure 5.26 indicates very good estimation quality. The absolute angular error is even below $5\,°_{\mathrm{elec}}$ most of the time for medium and high shaft speeds. The most critical stage with current settings deployed is clearly the transition from INFORM to SynRM-BEMF at Q3. These oscillations were introduced/amplified by a deliberate manual reduction of $i_d|_{min}\,(-0.2) = 0.75 \to 0.707$ to reach the MTPA point at $|\underline{i}| = 1$. Both control systems are capable of disturbance rejection of a load torque in order to maintain desired speed values ω^{UI}.

Quantity/Property	Difference
CPU Usage	$+11\%$
max. speed ω^{max}	-9%
max. extrapol. speed $\omega_{extrapl}^{max}$	-28.6%
acc. rate (whole range) $a_{\Delta\omega}$	-36%
peak torque (transient) $|t_e^{max}|$	-20%
efficiency	load dependent

Table 5.4: Comparison between selected sensorless and sensor-based control system specs, see also Section 4.7.4

It is insightful to highlight the trade-offs between sensor-based and sensorless control of the considered SynRM drive system. This is done in Table 5.4. A clear message is also delivered: If the sensor is to be substituted by a mathematical model, certain dynamic trade-offs have to be accepted for robust and stable performance. The core component which influences these trade-offs is the observer subsystem, and *not* the speed controller. Additional computational requirements are within reasonable margins and will shrink as new hardware target systems become more potent, such as the DSC-28379D vs. the deployed DSC-28335[48]. The maximum speed range is not substantially limited by sensorless methods used per se. It is restricted by the mechanical setup (vibrations) and voltage limitations vs. $i_d|_{min}\,(\omega)$. The dependency of $i_d|_{min}\,(\omega)$ is in turn mainly influenced by the machines airgap δ and not by deployed sensorless methods. The speed difference reported in Table 5.4 also reflects this and is regarded as very good value. It is recommended to operate the sensorless control system under load, as no-load

---

[46]The peak torque in sensorless operation occurs during the labeled "MTPA" time frame in Figure 5.26.

[47]The peak torque of the sensorless system occurs during MTPA operation.

[48]800 MIPS vs. 150 MIPS at roughly the same financial cost

operation *also* requires $i_d|_{min}(\omega) > 0$ and produces ohmic losses.

The presented sensorless control system of this chapter allows the operation of a brushless electric machine absent of permanent magnet material and position sensor at arbitrary speeds from $\approx [-24000\text{rpm} \dots 0 \dots 24000\text{rpm}]$ (including standstill). All in all, the performance indicated in Figure 5.26 is very good, considering the proposed matter as first investigation on sensorless flux weakening of SynRMs with INFORM and SynRM-BEMF methods.

5.8 Parameter Overview

Similar to Section 4.8 this section presents the final setting of all the relevant software and hardware parameters at a glance in Table 5.5, Table 5.6, Table 5.7 and Table 5.8. Differences between the sensored mode and the sensorless mode are marked with [†]symbols as are completely novel new quantities. As in Section 4.8, if not otherwise noted at the appropriate text passage all figures presented in this section were documented using the parameters state here.

By printing these essential control system parameters the author hopes to give the reader a comprehensive overview to ease future developments of such control systems.

Software Setting Overview sensorless/m (FAST Task)		
Parameter	**Symbol**	**Value**
Fast-Task Period	T_{fast}	67 µs
Space Vector Modulator		
PWM Pattern Types[†]		2-active (shifted) & 3-active ($\overline{\text{UVW}}$)
Compulsory Pulse-Window Time (2a)	T_{PW}^{2a}	5.98 µs
PWM-Shift Time (2a)	T_{Sh}	2.95 µs
Compulsory Pulse-Window Time (3a)[†]	T_{PW}^{3a}	12.5 µs
Starting Edge Offset[†]	t_{SEO}	5.5 µs
Ending Edge Offset[†]	t_{EEO}	2.2 µs
PWM-Dead-Band RED/FED	T_{DB}	1.25 µs
Observer and Encoder		
Encoder Dead-Time Correction	$k_{\gamma D}$	2.325
Refresh Rate		T_{fast}
Type		Luenberger [k] 3×3
Closed Loop Poles[†]	$\underline{\mathbf{z}}_{PL}$	$0.999 \cdot \underline{\lambda}_M$ (tuned)
Error Weight: Angle[†]	$k_{L\gamma}$	-0.0044
Error Weight: Speed[†]	$k_{L\omega}$	-0.004
Error Weight: Torque[†]	k_{Lt}	10^{-5}
Current Controller (i_d)		
Proportional Gain	$k_P^{i_d}$	0.45
Integral Gain	$k_I^{i_d}$	0.016
Max. Reference Value (abs.)	$|i_d^r|^{max}$	1
Max. Output Value (abs.)[†]	$|u_d^r|^{max}$	0.71(2a)/0.22(3a)
Current Controller (i_d)		
Proportional Gain	$k_P^{i_q}$	0.35
Integral Gain	$k_I^{i_q}$	0.015
Max. Reference Value (abs.)	$|i_q^r|^{max}$	1
Max. Output Value (abs.)[†]	$|u_q^r|^{max}$	0.71(2a)/0.22(3a)
Two Degree of Freedom (FF & FB)		
2 DOF Input Quantities		(i_d^r, i_q^r)
Use Differentiator in FF Path[†]		no
Diff.Pre-Filter Time Const.[†]	τ_{2DOF}	N/A
Max. Combined Output Value[†]	$|\underline{u}|_{max}^{dq}$	0.71(2a)/0.22(3a)

Table 5.5: Motor control system sensorless mode; Fast task; Final configuration

Software Setting Overview sensorless/m (FAST Task) (cont.)

Parameter	Symbol	Value
Fast-Task Period	T_{fast}	$67\,\mu s$
Sensorless Angle Mixing Subsystem[†]		
Start of Operation Speed[†]	$\omega_{\mathrm{BEMF}}^{work}$	± 0.2
LPF Cuttoff Speed[†]	$\omega_{g,\mathrm{BEMF}}$	$\frac{2}{3}\omega_{\mathrm{BEMF}}^{work}$
i_d^r Autotune(Phase) Gain[†]	k_{ph}	0.63
i_d^r Autotune(Phase) Offset[†]	d_{ph}	0.053
$i_d\|_{min}$ at $\pm\omega_{\mathrm{BEMF}}^{work}$[†]		0.707
Sensorless Angle Mixing Subsystem[†]		
Angle Mixing Strategy[†]		linear weights
PWM Switch Strategy[†]		hard switch after mix
Velocity Span (cw+ccw)[†]	$\Delta\omega_{mix}$	0.03
CW Mix Start Velo.[†]	$\omega_{mix}\|_{cw}^{start}$	0.155
CW 3a→2a Sw.Velo.[†]	ω_{3a2a}^{cw}	0.2
CW 2a→3a Sw.Velo.[†]	ω_{2a3a}^{cw}	0.19
CCW Mix Start Velo.[†]	$\omega_{mix}\|_{ccw}^{start}$	-0.14
CCW 3a→2a Sw.Velo.[†]	ω_{3a2a}^{cw}	-0.2
CCW 2a→3a Sw.Velo.[†]	ω_{2a3a}^{cw}	-0.18

Table 5.6: Motor control system sensorless mode; Fast task; Final configuration (cont.)

Software Setting Overview sensorless/m (SLOW Task)

Parameter	Symbol	Value
Slow-Task Period	T_{slow}	$402\,\mu s$
Speed Controller (ω)		
Proportional Gain[†]	$k_{P\,\omega}$	2.864
Integral Gain[†]	$k_{I\,\omega}$	0.015/0.007
Ref.Val. Filter Max. Slew Rate[†]	SR_ω^{max}	$1.29\frac{\text{p.u.}}{\text{s}}$
Ref.Val.Outp. Filter Time Const.[†]	τ_{SR}	$50\,\text{ms}$
Max. Output Value (abs.), INFORM[†]	$|t_e^r|_{INF}^{max}$	0.179
Max. Accelerate Output Val., BEMF[†]	$|t_e^r|_{BEMF}^{acc}$	0.179
Max. Break Output Val., BEMF[†]	$|t_e^r|_{BEMF}^{br}$	-0.136
Torque Output Mode[†]		`vpsm/polar(MTPA)`
MMF-Angle[†]	θ	$\leq 45\,°_{\text{elec}}$
Flux Weakening Subsystem		
FW Rated Speed[†]	ω_{rated}^{FW}	0.55
FW Max. Range[†]	ω^{max}	$\pm 1.0(1.82\,\text{@rated})$
FW Strategy[†]		$\text{LUT}\,(t_e^r, i_{d_{min}})$
FW Identification Constraint[†]	$|\gamma_\Delta^{max}|$	$7.5°_{\text{elec}}$
FW LUT provided Speed Range[†]	ω_{LUT}^{max}	1.05
Direct Axis Current Conditioning[†]		
Start Velocity (cw&ccw)[†]	$\omega_{id}|^{start}$	± 0.1
End Velocity (cw&ccw)[†]	$\omega_{id}|^{end}$	± 0.2

Table 5.7: Motor control system sensorless mode; Slow task; Final configuration

Hardware Setting Overview

Parameter	Symbol	Value
Inverter		
Nominal Bus Voltage	U_{DC}	60 V
Lower Bus Voltage Lim.	$U_{DC}|_{min}$	50 V
Upper Bus Voltage Lim.	$U_{DC}|^{max}$	71.5 V
Trip Phase Current	I_{VSI}^{max}	25.7 A (1.43@base value)
Warning Temperature	ϑ_{Warn}	60 °C
Limit Temperature	ϑ_{Lim}	70 °C
DSC TI-28335		
CPU Usage: $T_{fast}\backslash T_{slow}$; s.l. 3a		75.52% \ 78.01%
CPU Usage: $T_{fast}\backslash T_{slow}$; s.l. 3a mix		75.52% \ 78.01%
CPU Usage: $T_{fast}\backslash T_{slow}$; s.l. 2a		63.58% \ 66.92%
RAM Usage (total application)		61.65%

Table 5.8: Hardware parameters, sensorless mode

6 Conclusions, Contributions and Outlook

At the beginning of this thesis in Chapter 1, three research topics were formulated to define its scope. In Chapter 2 all important hardware components were described and mathematical models were derived. The DSC's architecture and essential used numerical methods were presented in Chapter 3.

This chapter summarizes the scientific core matter of this thesis, mainly given by Chapter 4 and Chapter 5. After a summary of each chapter, findings and contributions to research topics stated in Chapter 1 are highlighted. Finally, suggestions for improvements and future work are given.

6.1 Sensor-based Part: Summary & Discussion

Chapter 4 covered the sensor-based operation of the deployed SynRM. Figure 4.1 in Section 4.1 gave a complete system overview.

Section 4.2 gave an "integrated" analysis of classical 2-active space vector modulation. Quantities of the real target hardware and a measurement agenda for low-side bridge shunts were included to derive a rule to restrict $|\underline{u}|^{dq}_{max}$ as a function of the compulsory pulse window time T^{2a}_{PW}. The result of this process was Equation (4.23). This way a method was found to optimally adjust the 2-active PWM pattern for a maximum possible voltage space vector while ensuring T^{2a}_{PW}.

Section 4.3 emphasized the importance of designing and tuning an observer directly in the time-discrete domain based on the mechanical system model. A Luenberger observer was designed using Ackermann's formula. Deploying this subsystem inside the FAST Task was recommended.

Section 4.4 gave a straightforward PI-tuning rule for the decoupled current controllers comprising dead-time as an additional design parameter. A flatness based two degree of freedom approach was proposed to significantly boost the controller's performance in terms of dynamic response and disturbance rejection. A link to the classical decoupling-method was established. Due to this additional feedforward branch a setting of "no-overshoot" was recommended for feedback current controllers. The usage of reference currents (i^r_d, i^r_q) from the upper cascade in the feedforward path proved to be critical in gaining access to the high speed regime.

Section 4.5 discussed how a reliable speed controller can be obtained for SynRMs and reasoned the importance of a reference value filter in order to avoid detrimental system behavior. A link to the inner cascade was given by a presentation of operational modes (`MTPA vpsm(id)`) to realize a demanded torque.

Section 4.6 identified the machine parameters and related them to those obtained by the simulations in Section 2.4.5. The usage of reported identified parameters yielded success. However,

the adoption of advanced identification methods comprising a load machine and a telemetry machine is recommended to investigate discrepancies compared to the simulation.

Section 4.7 covered the topic of flux weakening for SynRM. Therein, strategies to utilize both a transient and quasi-stationary voltage limit alongside the MTPA line of Figure 4.13 were proposed and implemented. Other methods such as MTPV were not considered due to lack of knowledge regarding flux maps. To give a good overview on the subject, current circle and voltage ellipses indicating thermal and electrical limitations were printed in Figure 4.13. Referring to the additional material in Appendix A.2 a trade-off for ε_{FW} in terms of accuracy vs. identification-time(cost) & memory requirements was found and implications for the discussed system were derived.

Section 4.7.4 presented the final sensor based control system and proposed benchmark values for a comparison with the sensorless control system in Chapter 5. An acceleration/break rate of $a_{\Delta\omega} \pm 50\,250$ rpm/s including the flux weakening region highlighted the validity of all prior approaches and indicated decent performance. The systems response to a characteristic test trajectory was given in Figure 4.15

Section 4.7.5 and Section 4.7.6 discussed the upper bounds for the system in its current state. Causes and possibilities for further improvements regarding mechanical, electrical and control theoretical aspects were discussed. A safe maximum stationary velocity of $\omega^{max} = 26\,160$ rpm was reported for sensored operation. The motor's characteristic torque/speed curve was presented in Figure 4.16.

Discussion

THESIS TOPIC 1:

The salient pole synchronous reluctance machine, simulated in [1] shall be assembled. A proper test bench that incorporates this machine should be built. Together with a provided voltage source inverter, basic field-oriented control should be implemented. The simulated machine's characteristics & parameters should be verified. That is: Magnetic linearity, stator resistor, direct- and quadrature axis inductances.

$\rightarrow$ The **built and operated machine behaved as was to be expected from simulations** in Section 2.4.5. Both direct and quadrature axis fluxes showed a nearly linear trend over the operational range as reported in [1], see Figure 4.7. The **adoption of constant inductance values was justified** as was to be expected for this machine type given the relative large airgap of its design. A parameter difference of l_q if compared to the simulation occurred. Possible sources were stated as: Simple self-commissioning character of the applied identification method (Section 4.6); Calibration of rotary encoder (Section 2.6); Current measurement noise; Discrepancy between simulated & built machine and a combination thereof. However, the **usage of values reported in Table 4.3 generated a good performance** as presented at the end of Chapter 4 and Chapter 5.

<div align="center">

Thesis Topic 2:

</div>

To reach high mechanical shaft speeds, flux weakening methods shall be adopted. Suitable methods should be chosen for both sensor-based and sensorless operation. If possible the chosen strategy should be split into a "transient" and "quasi-stationary" part and a method to switch between the two should be established. Operational speeds as high as possible should be reached safely. Challenges encountered to reach these speeds as well as ultimate limits should be investigated, quantified, solved and documented.

→ This topic has to be discussed from an engineering perspective first before proposing the scientific findings. Concerning *hardware*, a proper breadboard set-up was crucial. For the provided components this meant adding a thick rubber mat below the base plate as **passive dampening** and fixating the magnetic pill with a shrinking tube. In addition to that the position signal of the sensor got corrupted, possibly due to cross-talk or other breadboard set-up related characteristics. Without the **adoption of *input qualification* as feature of the TI-28335** overall system's performance would have been poorly in the sensored mode. Also, no correct reference angle would have been available to assess the sensorless control system's performance. Especially for high speed operation, a **proper sensor dead-time compensation** of the delivered sensor signal using the parameter $k_{\gamma D}$ in Equation (2.114) was of great importance. This was comprehensively covered in Section 2.6. The current measurement showed substantial noise levels that were successfully mitigated by oversampling and calculating the median, see Section 2.5.

Almost all aspects of this, the previous and the subsequent chapter needed to be tested, validated, altered, tested again and so on, until a stable and proper solution was found. Therefore, another very important precondition is given by the adoption of a modular *software framework* comprising clearly defined interfaces and clean, reproducible routines[1]. Recommendations to exploit the 28335's resources were given in Chapter 3.

The method of **MTPA-line flux weakening** was chosen in prospect of the upcoming sensorless method's structure, as the SynRM-BEMF method requires the motor to run in `vpsm(id)/MTPA` mode.

→ Based upon these foundations **the following findings and strategies are proposed as mandatory** for reaching high velocities when operating the SynRM of this thesis:

- f_{PWM} should at least be 15 kHz or higher. This is beneficial for both space-vector-modulation's resolution as well as dead-time behavior. A trade-off concerning computational capabilities has to be considered, cf. Section 4.7.6

- Fast and Slow task should be synchronized and $T_{slow} \geq 6 \cdot T_{fast}$ otherwise non reproducible jitter may occur that destabilizes the control structure.

- An observer subsystem should be placed within the Fast task. Otherwise dynamic performance will degrade by a factor of $T_{slow}/T_{fast} = 6$. A model-based observer together with systematic design rules form the basis of proper tuning the coefficients to their final settings. The observer should be directly designed at the time-discrete domain.

- As preferred data format I8Q24 or `float` should be deployed. Angles should be represented by I4Q28 . This proves to be especially important for sensorless observers, cf. [43, p. 180].

---

[1] such as the trajectory planer, cf. Section 4.7.4

- The measurement agenda of the 2-active pattern should be placed at the *end* of the preceding Fast task and evaluated at the actual Fast task's *beginning* in order to minimize dead-time effects caused by a delay between measurement and evaluation. This was shown in Section 4.2, Figure 4.4.

- To fully utilize the available bus voltage and expand the range of ω_{rated}^{FW} further, Equation (4.23) should be used. The modulator's property of "single reference update & measurement" allows for a PWM pattern shift of $T_{PW}^{2a}/2$ that additionally increases the maximum output voltage. This can be applied in any future motor control application with 2-active space vector modulation with single reference update.

- For the current controller's feedforward-path the speed controller's reference values i_d^r and i_q^r must be used rather than the measured values. The current controller's feedback path should not show overshoot in their step responses.

- A restriction to the reference value of the speed controller has to be applied, cf. Section 4.5.2. For sensored operation a LPF was sufficient.

- When reaching the voltage limitation, a separation into transient and quasi-stationary flux weakening strategy is efficient. An automatable method to identify the transient torque limit when running with free shaft is given in Section 4.7.2. Equation (4.136) states an output saturation time of ten percent from T_{tran} to qualify as transient limit value. A lower bound for the resolution of the ω grid is given by $\varepsilon_{FW} = 0.025$. To fully harness the inverter's bus voltage available a quasi-stationary field weakening strategy is mandatory. An analytical approach alongside the two MTPA lines as presented in Table 4.6 allows for a considerable flux weakening speed of 1.83 times the characteristic velocity $\omega_{rated}^{FW} = 0.6$.

- When adopting two flux weakening strategies the need of a proper shifting between them arises. Thereto, one possible and successfully tested method is given by linearly weighting both limits after the transient time has expired. The choice of $T_{shift} = T_{trans}$ generated valuable results.

The topic's part regarding limitations was extensively answered in Section 4.7.6.

6.2 Sensorless Part: Summary & Discussion

Chapter 5 first listed all used angular quantities for reasons of clarity. As quality indicator the angular error γ_Δ was defined. The strategy to use INFORM and SynRM-BEMF methods was outlined.

Section 5.1 emphasized the proper choice of sample values (current vs. previous task), as this is not trivial any more for very high speeds. Only the combination of measured and estimated values stated in Section 5.1 and depicted in Figure 5.1 lead to stable behavior.

Section 5.2 summarized the "ideal" INFORM method and compared it to the deployed silent INFORM variant with three active negative space vectors only to control a salient pole SynRM. A scientific analysis was carried out to answer the question whether this approach still yields acceptable results or not and how high the trade-off is. This was documented in Table 5.2 and

Figure 5.6. The short answer is "yes". The trade-off is a load dependent angular error that can be quantified as $\sigma_{\gamma_{\Delta INF}} \approx 7.5\,°_{\text{elec}}$ at full load.

The 3-active space vector modulation method was also deployed and related to inverter parameters such as analogue measurement interface time constants and compulsory measurement windows. An advanced analysis lead to the important formula of Equation (5.54) that henceforth enables the user to exactly calculate the absolute voltage space vector in order to guarantee a measurement window for current slopes.

All in all, the INFORM method worked very well for the SynRM.

Section 5.3 presented the deployed sensorless method for medium and high speeds. Challenges introduced by the machines property of "absent permanent magnet material" were highlighted. A method to overcome these challenges was given by the calibration process at the most critical point (start of operation), described with Equation (5.67).

Section 5.4 adopted and investigated transition methods discussed in [66] regarding their usage for SynRMs. From a scientific perspective: Said methods worked well. This can be explained by the fact that a SynRM operated in `vpsm(id)` mode can be considered as a "quasi" PMSM. A proper design and calibration of the SynRM-BEMF method was necessary for a smooth transition. Very good performance within the mixing band of both models was reported in Figure 5.16. A PWM mode hard switch was possible.

Section 5.5 discussed necessary tunings and analyzed relations between implemented subsystems. The Luenberger observer was identified as the most important subsystem for sensorless control in Section 5.5.2. A high sensitivity of the system's stability regarding the closed-loop error system poles was emphasized. A design within the time-discrete domain (and subsequent manual tuning) lead to success. The speed- and current controllers needed to be adapted to this more defensive observer.

Section 5.6 presented the sensorless flux weakening strategy that enabled operation at high shaft speeds. Transient torque limitations were investigated. Quasi-stationary torque limitations required a load machine that was not available for high speeds. The subject matter was also interpreted from a mathematical perspective as "constraint optimization task", see Figure 5.17 and Figure 5.23. This approach enables a comprehensive system performance assessment for future scientific research. The strategy is a hybrid form of the prior MTPA-line flux weakening, ensuring $i_d|_{min}(\omega)$. Eventually this specific flux weakening method yielded $\theta \leq 45\,°_{\text{elec}}$. This is in contrast to MTPV where $\theta \geq 45\,°_{\text{elec}}$ within the flux weakening region.

Methods how to identify flux weakening functions $\bar{t}^{sl}|_{min}^{max}(\omega)$ and $i_d|_{min}(\omega)$ were documented in Section 5.6.2. The resulting characteristic torque/speed curve and the function $i_d|_{min}(\omega)$ were presented and analyzed in Section 5.6.3.

Section 5.7 presented the final sensorless control system and compared it to the sensor-based system. An acceleration/break rate of $a_{\Delta\omega} \pm 31\,700\,\text{rpm/s}$ was reported. A maximum safe-to-operate speed of $\Omega_{sl}^{max} = 23\,880\,\text{rpm}$ was specified. All prior approaches were validated. This can be inspected within Figure 5.24, Figure 5.25 and Figure 5.26. The system showed very good performance within all operational regions and given limitations.

Discussion

<div align="center">THESIS TOPIC 3:</div>

Sensorless operation at standstill and low speeds shall be achieved by using an INFORM variant with embedded voltage test shots (3 active space vector modulation). Thereto, currents should be measured at low-side bridge shunts of the used inverter. At medium to high speeds a method based on the integration of the stator voltage space vector (SynRM-BEMF) shall be implemented. Both methods should be assessed independently, with prior defined quality criteria. Challenges encountered to reach these criteria as well as ultimate limits should be investigated, quantified, solved and documented. A proper way to switch observer models as well as PWM patterns should be established.

$\rightarrow$ **The outcome of this thesis is that a salient pole SynRM that with linear magnetic behavior is very well accessible to high performance sensorless operation**. A quantification can be readily stated as $\Omega_{sl}^{max} = 23\,880$ rpm at $\gamma_\Delta \leq 7.5\,°_{\mathrm{elec}}$.

The **most critical quantity of this sensorless system is** $i_d|_{min}(\omega)$. The **most critical subsystem is the observer**. **Good efficiency is the most challenging task for this system** and other pure reluctance machines, as no permanent magnet provides flux to be used for sensorless models. As the system does not need either magnets nor sensors and uses a common 150 MHz processor to run sensorless models, some compromises in terms of performance are logical. Further substantial improvements may be reached by hardware modifications, discussed in the next Section 6.3.

6.3 Possible Future Work

During the development process, limitations and potential improvements were identified. The list provided below represents fields of future work:

- Usage of a different observer design procedure. Thereby a 3×3 stationary Kalman filter obtained by solving a stationary Ricatti equation can serve as a first starting point. Its design as well as expansions into non-linear forms are described in [72].

- Balancing of the rotor shaft may reduce mechanical vibrations and observed current oscillations at high speeds.

- Usage of variable DC-link voltage and adoption of higher PWM switching frequency (requires more potent hardware). This can reduce current ripples and increase control bandwidth.

- Implementation of different flux weakening strategies (at least in sensor based mode) such as MTPV. These strategies require knowledge of flux maps.

- Construction of a complete test set-up with comprising a load machine. With the software and this document at hand a proper load machine is available. A very important aspect thereby is a suggested reconstruction of the motor shaft to support claw couplings that allow for high speeds.

- Identification of both SynRM's flux maps obtained at high speeds and comparison to simulation (once the test set-up is completed).

- Investigations regarding motor's torque ripple and voltage harmonics, followed by a comparison to [1].

- System integration: Construction of a prototype comprising AMBs from [7] and the recently built multiphase inverter of [5]. This inverter features the currently most powerful C2000 device: 28379D. This means that the developed software of this thesis would be compatible with the new inverter's target hardware. It was stated in Chapter 1, that such a system integration was one of the main motivations of this thesis in the first place. A previous version of such a prototype was presented and discussed in [75]. There, operational speeds of up to 10 000 rpm were reported. Regarding motor control and provided speed range, this thesis delivers the capability to increase that maximum speed for the next prototype version substantially.

A Additional Information and Documents

A.1 Patent Scan from Austrian Patent Office

In Figure A.1 a search report issued by the Austrian Patent Office (Österreichisches Patentamt ÖPA) is depicted. As the report was issued in German a brief description is given here. The classification will also be briefly explained as some of the cited patents.

A.1.1 Classification

The first three lines/boxes of the report from Figure A.1 concern classification of the subject matter that was filed at the ÖPA. The patent examiner was instructed to emphasize on systems which switch between two sensorless methods and (ideally) comprise synchronous reluctance machines.

In general, one of the first steps in patent search and examination processes is to classify the subject matter as this greatly enhances efficiency of the subsequent search. In Austria, two classification schemes are common: International Patent Classification (IPC) and Cooperative Patent Classification (CPC). The more detailed CPC is the official classification scheme by both the European Patent Office (EPO) and the US Patent and Trademark Office (USPTO). It is used to structure mankind's technological entirety according to the following hierarchy:

- Section
  - Class
    * Subclass
      ▷ Group
        · Subgroup

In Figure A.1 one of the classification symbols regarding control is **H02P 21/0021**. Referring to the CPC scheme of **H02P**, [76] this means:

- *ELECTRICITY*
  - *GENERATION; CONVERSION OR DISTRIBUTION OF ELECTRIC POWER*
    * *CONTROL OR REGULATION OF ELECTRIC MOTORS, ELECTRIC GENERATORS OR DYNAMO-ELECTRIC CONVERTERS; CONTROLLING TRANSFORMERS, REACTORS OR CHOKE COILS*
      ▷ *Arrangements or methods for the control of electric machines by vector control, e. g. by control of field orientation*
        · *{using different modes of control depending on a parameter, e. g. the speed}*

Recherchenbericht zu **KN 16122902/UNI/2016/1**

österreichisches
patentamt

Klassifikation des Anmeldungsgegenstands gemäß IPC: *H02P 6/18* (2016.01); *H02P 6/182* (2016.01); *H02P 6/08* (2016.01); *H02P 21/00* (2016.01); *H02P 25/028* (2016.01); *H02P 25/08* (2016.01); *H02P 25/10* (2006.01); *H02K 3/28* (2006.01); *H02K 1/24* (2006.01)	

Klassifikation des Anmeldungsgegenstands gemäß CPC:
H02P 6/181 (2013.01); *H02P 6/182* (2016.02); *H02P 6/183* (2013.01); *H02P 6/085* (2013.01); *H02P 21/0021* (2013.01); *H02P 25/028* (2016.02); *H02P 25/08* (2013.01); *H02P 25/105* (2013.01); *H02K 3/28* (2013.01); *H02K 1/24* (2013.01); *H02P 2203/05* (2013.01)

Recherchierter Prüfstoff (Klassifikation):
H02P, H02K

Konsultierte Online-Datenbank:
EPODOC , WPI

Dieser Recherchenbericht wurde zu Ihrem Arbeitsthema erstellt.

Kategorie*)	Bezeichnung der Veröffentlichung: Ländercode, Veröffentlichungsnummer, Dokumentart (Anmelder), Veröffentlichungsdatum, Textstelle oder Figur soweit erforderlich	Betreffend Anspruch
	DE 112014000512 T5 (AISIN AW CO) 15. Oktober 2015 (15.10.2015) Zusammenfassung; Figur 1	
	US 2016056740 A1 (NONDAHL et al.) 25. Februar 2016 (25.02.2016) Zusammenfassung; Figuren 1-3	
	US 2011175560 A1 (AKIYAMA MASAHIKO) 21. Juli 2011 (21.07.2011) Ansprüche 1-4; Figuren 1-4	
	WO 2005099082 A1 (HONEYWELL INT INC) 20. Oktober 2005 (20.10.2005) Zusammenfassung; Figuren 5a-6b	
	US 6163127 A (PATEL et al.) 19. Dezember 2000 (19.12.2000) Zusammenfassung; Figur 1	
	EP 2023479 A1 (BAUMUELLER NUERNBERG GMBH) 11. Februar 2009 (11.02.2009) Zusammenfassung; Figur 1	
	DE 10301826 A1 (BOSCH GMBH ROBERT) 29. Juli 2004 (29.07.2004) Zusammenfassung; Figuren 1-8	
	WO 2015109150 A1 (RESMED MOTOR TECHNOLOGIES INC) 23. Juli 2015 (23.07.2015) Zusammenfassung; Figuren 1, 2	

Datum der Beendigung der Recherche: 19.06.2017	Seite 1 von 1	Prüfer(in): KOVACS György

*) **Kategorien** der angeführten Dokumente:
X Veröffentlichung **von besonderer Bedeutung**: der Anmeldungs-gegenstand kann allein aufgrund dieser Druckschrift nicht als neu bzw. auf erfinderischer Tätigkeit beruhend betrachtet werden.
Y Veröffentlichung **von Bedeutung**: der Anmeldungsgegenstand kann nicht als auf erfinderischer Tätigkeit beruhend betrachtet werden, wenn die Veröffentlichung mit einer oder mehreren weiteren Veröffentlichungen dieser Kategorie in Verbindung gebracht wird und diese **Verbindung für einen Fachmann naheliegend** ist.

A Veröffentlichung, die den allgemeinen **Stand der Technik** definiert.
P Dokument, das von **Bedeutung** ist (Kategorien **X** oder **Y**), jedoch **nach dem Prioritätstag** der Anmeldung veröffentlicht wurde.
E Dokument, das **von besonderer Bedeutung** ist (Kategorie **X**), aus dem ein „**älteres Recht**" hervorgehen könnte (früheres Anmeldedatum, jedoch nachveröffentlicht, Schutz ist in Österreich möglich, würde Neuheit in Frage stellen).
& Veröffentlichung, die Mitglied der selben **Patentfamilie** ist.

DVR 0078018

Figure A.1: Patent Search Report issued by the Austrian Patent Office

Another classification symbol in Figure A.1 regarding the machine type is **H02K 1/24**. Referring to the CPC scheme of **H02K**, [77] this means:

- *ELECTRICITY*
  - *GENERATION; CONVERSION OR DISTRIBUTION OF ELECTRIC POWER*
    - * *DYNAMO-ELECTRIC MACHINES*
      - ▷ *Details of the magnetic circuit*
        - · *Rotor cores with salient poles {; Variable reluctance motors}*

For a complete translation of the CPC symbols given in Figure A.1 the reader is referred to the schemes of **H02P** [76] and **H02K** [77]. The numerals in brackets refer to the version of the cited scheme. More detailed information on the content of these classes is given by the definitions of **H02P** [78] and **H02K** [79].

A.1.2 Cited Patents

All the patents reported in Figure A.1 are included within the thesis's bibliography using their granted variant (if any):[1] [80], [81], [82], [73], [83], [84], [85], [86].

In [84], work of this institute is cited as prior art: [74]. The document [73] covers transition methods in details. Some of the strategies used in Section 5.4 are also mentioned there. In [85] the PWM mode is switched between sine-commute and block-commute depending on the system's state.

All patents can be found and downloaded at https://worldwide.espacenet.com/ free of charge.

A.2 Implementation and Application of Flux-Weakening LUTs

The c.w. and c.c.w parts of $\widetilde{t}_{max}(\omega)$ and $\widetilde{t}_{min}(\omega)$ from Figure 4.11 have been implemented into four Lookup-Tables (LUTs) in the DSC. These LUTs have to be loaded into RAM at startup-time for optimal performance during runtime. The ω axis is split into two arrays `wwp`, `wwm` representing positive and negative values starting at $\pm\widetilde{\omega}_a^{cw} = \pm0.6$ and ending[2] at $\pm\widetilde{\omega}_{LUT}^{max} = \pm1.0$. As stated in Section 4.7.2 the resolution of these ω grids is specified by the preceding experiment to be $\varepsilon_{FW} = 0.025$.

During operation the speed controller checks if the system speed is within flux weakening range given by $\widetilde{\omega}_a^{cw}$. If true a bisection search algorithm is performed as illustrated in Figure A.2 to find the appropriate interval fulfilling

$$\mathtt{wwp}\left[j^*\right] \leq \omega^{obs} < \mathtt{wwp}\left[j^* + 1\right] \tag{A.1}$$

in case for positive speeds. The resulting indexes of Equation (A.1) are used in the two corresponding previously identified LUTs. Positive and negative limitations for $t_e^r\left(\omega^{obs}\right)$ are found based on a piecewise linear interpolation between values at $[j^*]$ and $[j^* + 1]$. These values are then applied as output limits for the implemented PI-Controller, see Figure 4.8[3] and Figure 4.5.

---

[1]The given sequence of patents printed here is the same as printed in Figure A.1.

[2]this limit expanded to $\pm\widetilde{\omega}_{LUT}^{max} = 1.4$ in Section 4.7.5

[3]The transient/stationary block will be explained at the end of Section 4.7.3 and can be considered as a through connection in this context
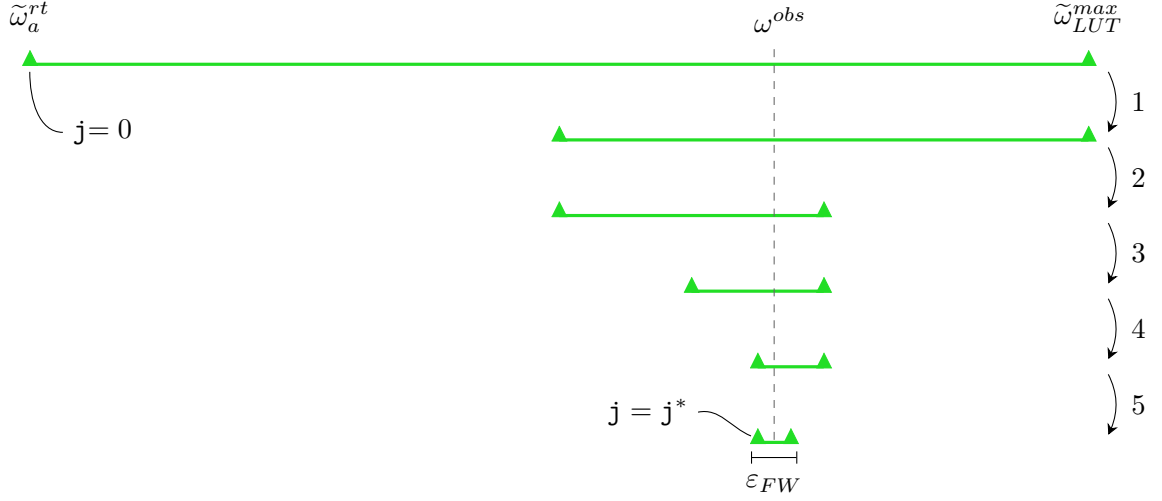
Figure A.2: Bisection search algorithm illustration for FW-subsystem (expanded range of $\widetilde{\omega}_{LUT}^{max} = 1.4$ depicted)

A few remarks on performance and resource requirements:
With parameters stated above the six LUTs range E_{FW} and number of elements for each LUT n_{LUT} results in

$$E_{FW} = \widetilde{\omega}_{LUT}^{max} - \widetilde{\omega}_a^{rt} = 0.4 \tag{A.2}$$

$$n_{LUT} = \frac{E_{FW}}{\varepsilon_{FW}} = 16 . \tag{A.3}$$

Bisection search will then always terminate quickly in

$$s_{bi} = \log_2 n_{LUT} = 4 \tag{A.4}$$

steps if carried out ab initio each SLOW Task. This can be further enhanced by picking the *last* found interval of the preceding SLOW Task as a starting point for the consecutive search. Before commencing the next search it is first checked, if the actual ω^{obs} is still within that interval (this will very likely be the case). In the final firmware of this thesis the maximum provided LUT range has been expanded to $\widetilde{\omega}_{LUT}^{max} = 1.4$. This was done based on an extrapolation of the available identification data. The amount of data is doubled viz. $E_{FW}^{exp} = 0.8$; $n_{LUT}^{exp} = 32$ but the maximum search step count is only increased by one $s_{bi}^{exp} = 5$, emphasizing the capabilities of this algorithm.

Saving the six LUT's data in `long` type consumes $16(32) \cdot 6 \cdot 4 = 384(768)$ `Bytes` that have to be reserved from RAM at runtime. For the TI-28335 an amount of 768 `Bytes` is slightly above 1% of the device's available RAM. This can be seen as substantial figure when taking into account that the final firmware version has a RAM usage of 61.65% and a sweep of the experiment over θ^r would require $16(32) \cdot 4 \cdot 4 = 256(512)$ `Bytes` more for each investigated value of θ^r.

All this is heavily dependent on the choice of ε_{FW} and its used value of 0.025 is proposed/-suggested as sufficient and is probably increasable without a loss of performance. Furthermore

it is recommended to use `int`[4] instead of `long` as LUT identification data type when adopting FW-Control. No performance loss due to lower resolution of these quantities is to be expected, but the memory requirement can be reduced by a factor of two.

Memory availability is also an important topic when performing identification tasks (Section 4.6) and statistical measurements of angular errors (Section 5.2.4).

Sensorless LUTs

The c.w. and c.c.w parts of $\bar{t}_{max}^{sl}(\omega)$ and $\bar{t}_{min}^{sl}(\omega)$ from Figure 5.22 and $i_d|_{min}(\omega)$ from Figure 5.21 have been implemented into six LUTs. Two additional LUTs for positive and negative shaft speeds were also deployed. The resolution of all these LUTs was set to $\varepsilon_{FW} = 0.025$ as before for values above/below the characteristic acceleration velocities given in Table 5.3. For all other (lower) speeds the resolution was increased to 0.05 to save RAM memory. In sensorless operation all LUTs needed to be loaded to RAM at runtime to ensure swift execution within T_{fast}. Search and evaluation is carried out by means of bisection as described above. The LUTs range is set to ± 1, as Section 5.6 reported this as maximum safe-to-operate velocity in sensorless configuration.

The same trade-offs and considerations as described above apply. If a different target than $|\gamma_\Delta| \leq 7.5\,°_{\mathrm{elec}}$ is formulated, the experiments described in Section 5.6.2 need to be repeated and six additional LUTs will be generated at least (when speed LUTs are retained).

---

[4]in the format 4Q12

B Schematics & Drawings

The following documents complete the description of the SynRM drive system.

B.1 Schematics

This section contains some schematic details of the voltage source inverter[1] that was used in this thesis. It was described and referenced in Chapter 2, Chapter 3 and Chapter 4. The inverter was designed prior to this thesis at TU Wien and built by the company *High Tech Drives*. Adjustments were made to the eQEP interface as discussed in Section 2.6. **The inverter is used in the 90 Volt / 30 Ampere configuration.**

---

[1]designation: "HTD_Umrichter_DSP_28335_V5"
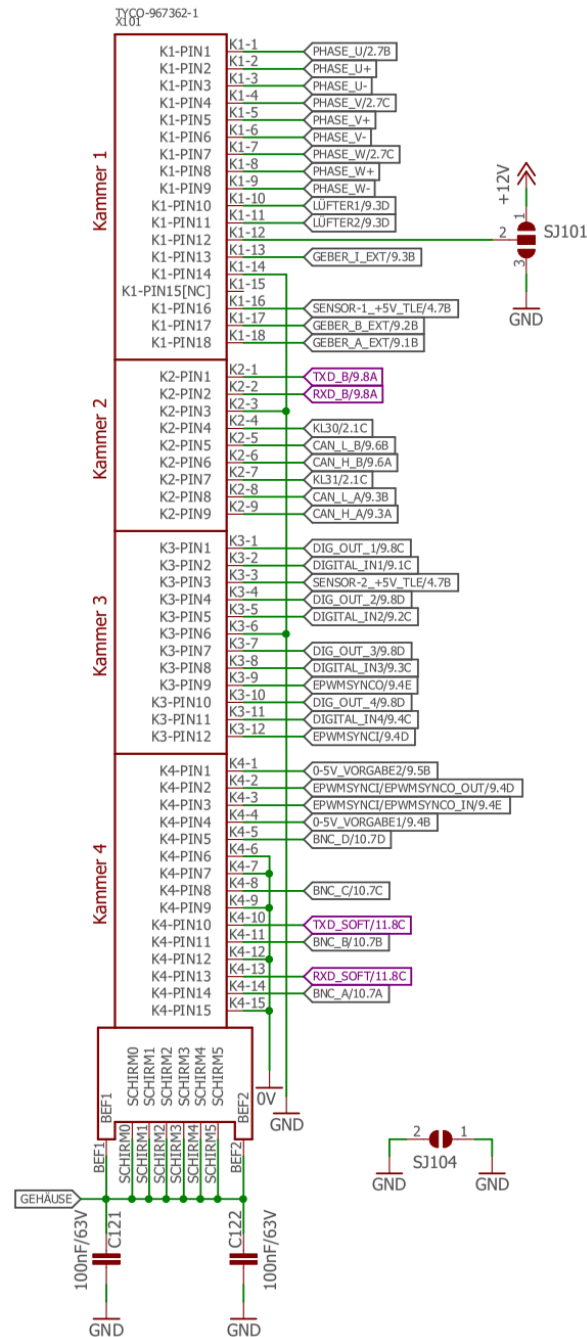
Figure B.1: Schematic Detail 1/5: Front Connector
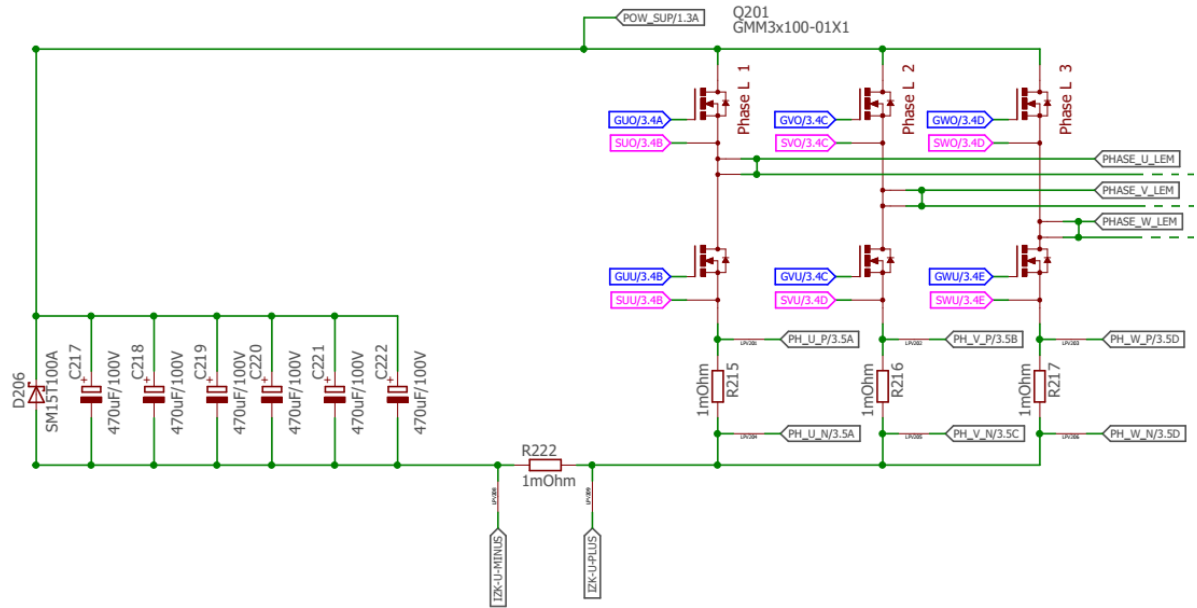
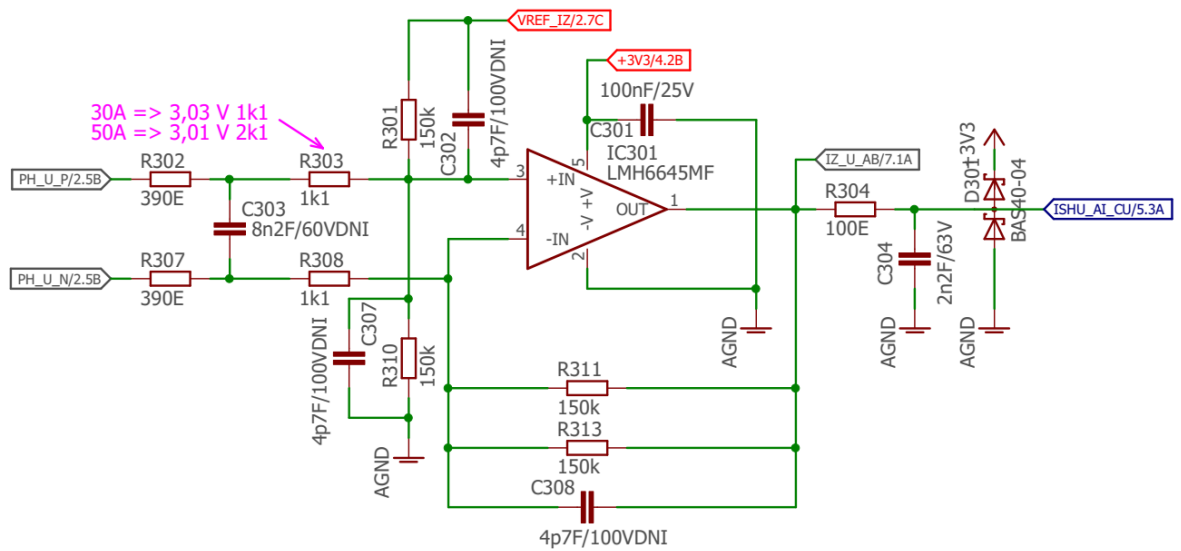Figure B.2: Schematic Detail 2/5: DC-Link, power stage and measurement shunts

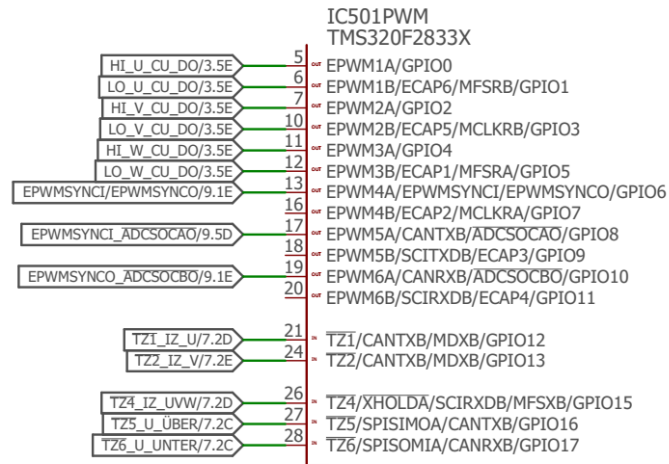Figure B.3: Schematic Detail 3/5: Analog interface for Phase U current measurement

IC501PWM
TMS320F2833X

HI_U_CU_DO/3.5E	5 — EPWM1A/GPIO0
LO_U_CU_DO/3.5E	6 — EPWM1B/ECAP6/MFSRB/GPIO1
HI_V_CU_DO/3.5E	7 — EPWM2A/GPIO2
LO_V_CU_DO/3.5E	10 — EPWM2B/ECAP5/MCLKRB/GPIO3
HI_W_CU_DO/3.5E	11 — EPWM3A/GPIO4
LO_W_CU_DO/3.5E	12 — EPWM3B/ECAP1/MFSRA/GPIO5
EPWMSYNCI/EPWMSYNCO/9.1E	13 — EPWM4A/EPWMSYNCI/EPWMSYNCO/GPIO6
	16 — EPWM4B/ECAP2/MCLKRA/GPIO7
EPWMSYNCI_ADCSOCAO/9.5D	17 — EPWM5A/CANTXB/ADCSOCAO/GPIO8
	18 — EPWM5B/SCITXDB/ECAP3/GPIO9
EPWMSYNCO_ADCSOCBO/9.1E	19 — EPWM6A/CANRXB/ADCSOCBO/GPIO10
	20 — EPWM6B/SCIRXDB/ECAP4/GPIO11
TZ1_IZ_U/7.2D	21 — TZ1/CANTXB/MDXB/GPIO12
TZ2_IZ_V/7.2E	24 — TZ2/CANTXB/MDXB/GPIO13
TZ4_IZ_UVW/7.2D	26 — TZ4/XHOLDA/SCIRXDB/MFSXB/GPIO15
TZ5_U_ÜBER/7.2C	27 — TZ5/SPISIMOA/CANTXB/GPIO16
TZ6_U_UNTER/7.2C	28 — TZ6/SPISOMIA/CANRXB/GPIO17

Figure B.4: Schematic Detail 4/5: PWM and Tripzone Pins at 28335
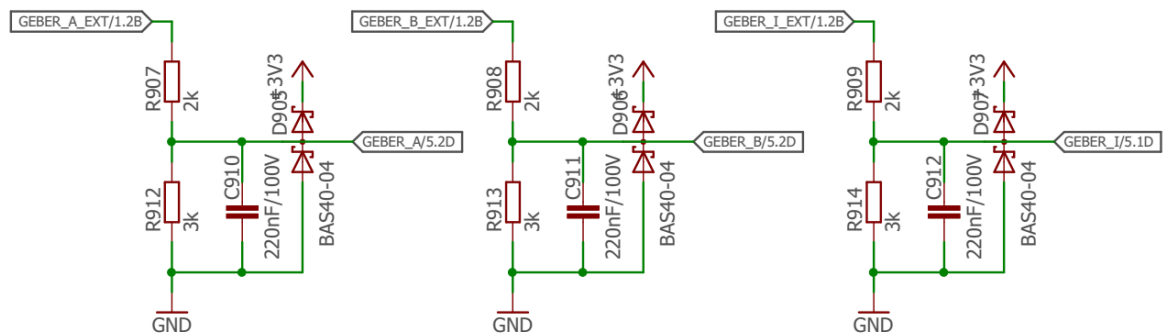
Figure B.5: Schematic Detail 5/5: Encoder eQEP analog interface

B.2 Drawings

This section contains drawings of the parts that were designed constructed during this thesis to complete the experimental breadboard set-up, described in Section 2.1. Machine stator, winding/connection scheme and machine rotor were designed and constructed in the scope of [1]. All other parts of the set-up such as shaft, motor housing, mounting block, ect. were designed and constructed in the context of [9]. One of the first tasks of this thesis was the assembly of all parts.
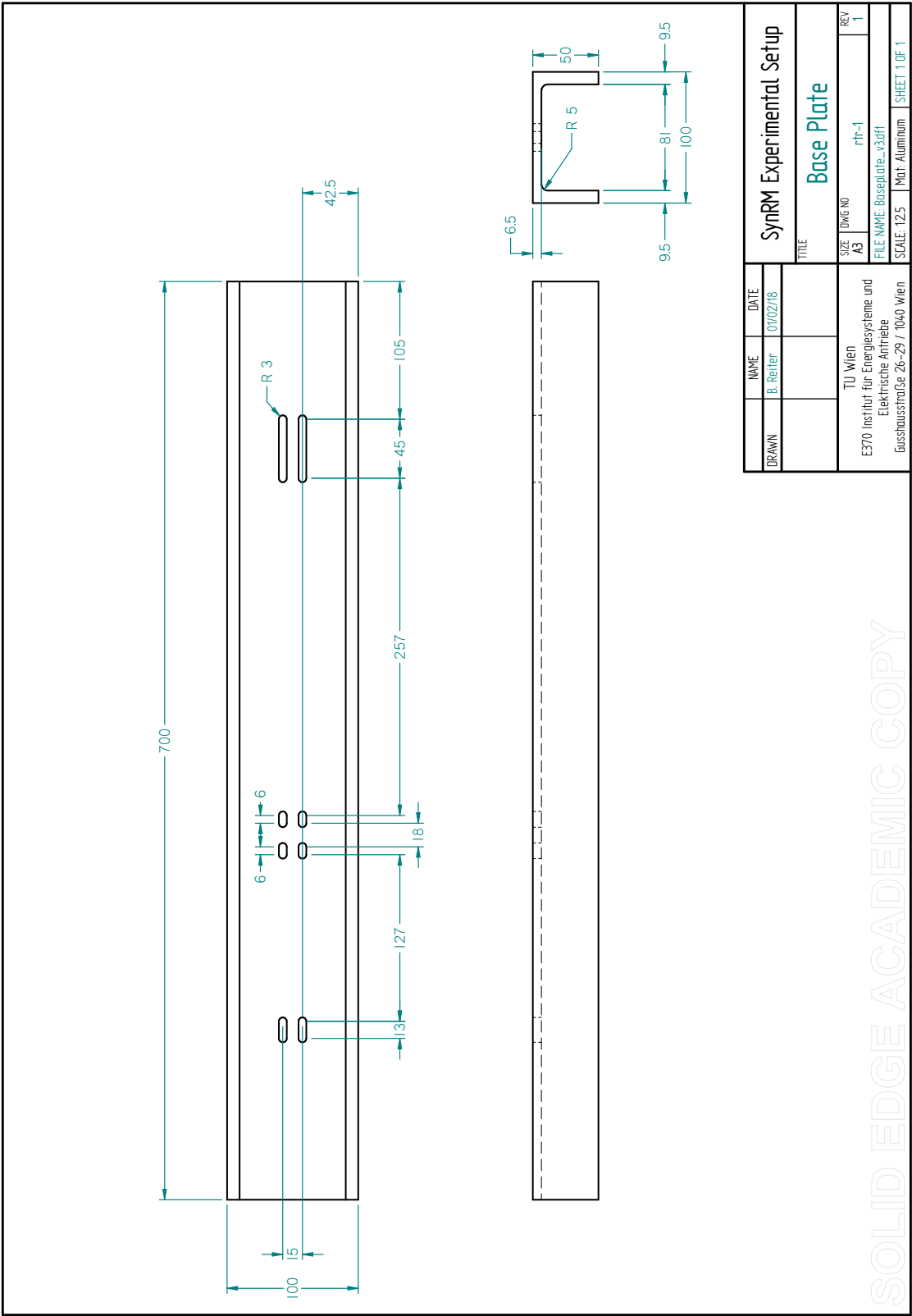
Figure B.6: Base plate drawing
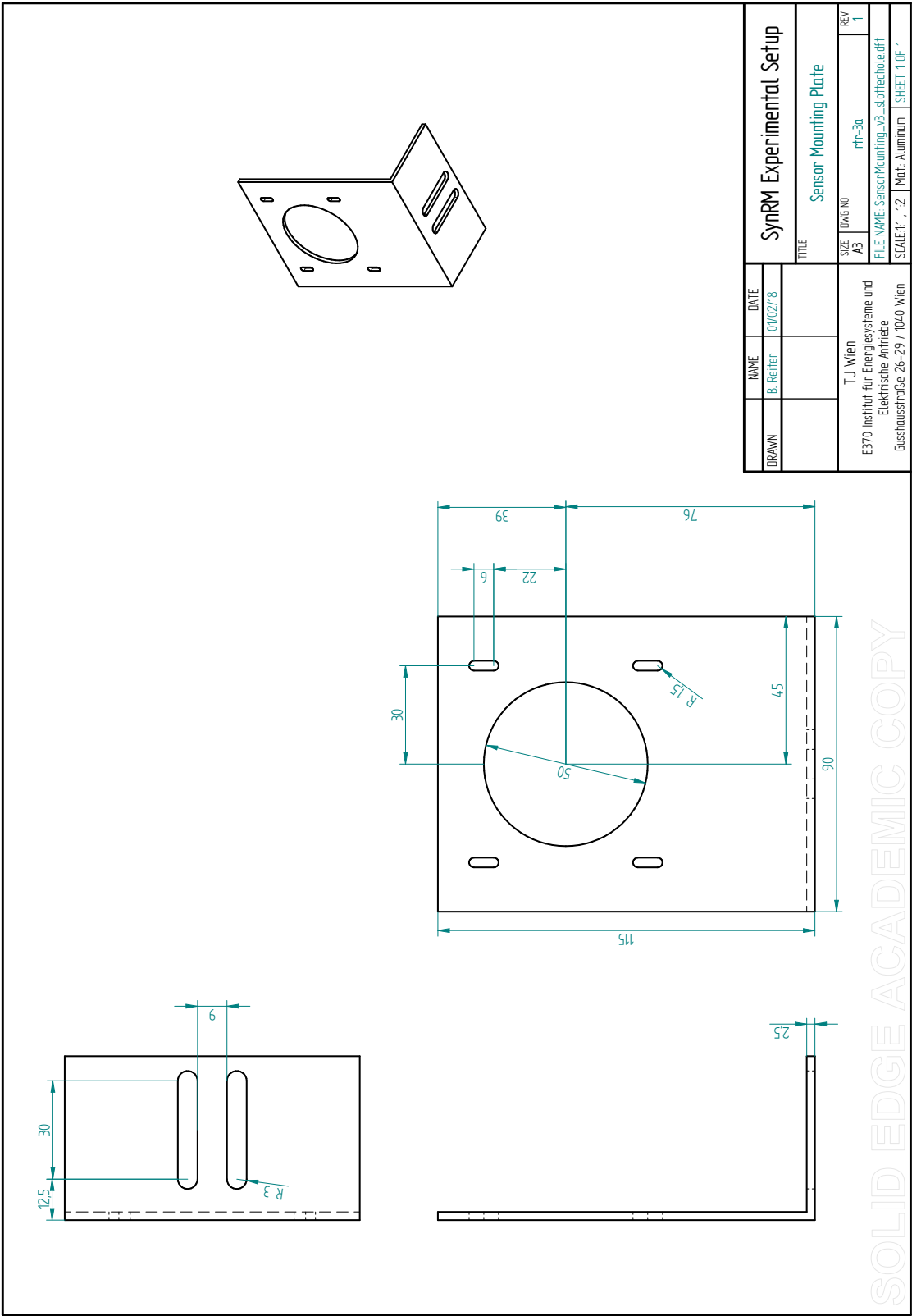
Figure B.7: Sensor mounting plate drawing
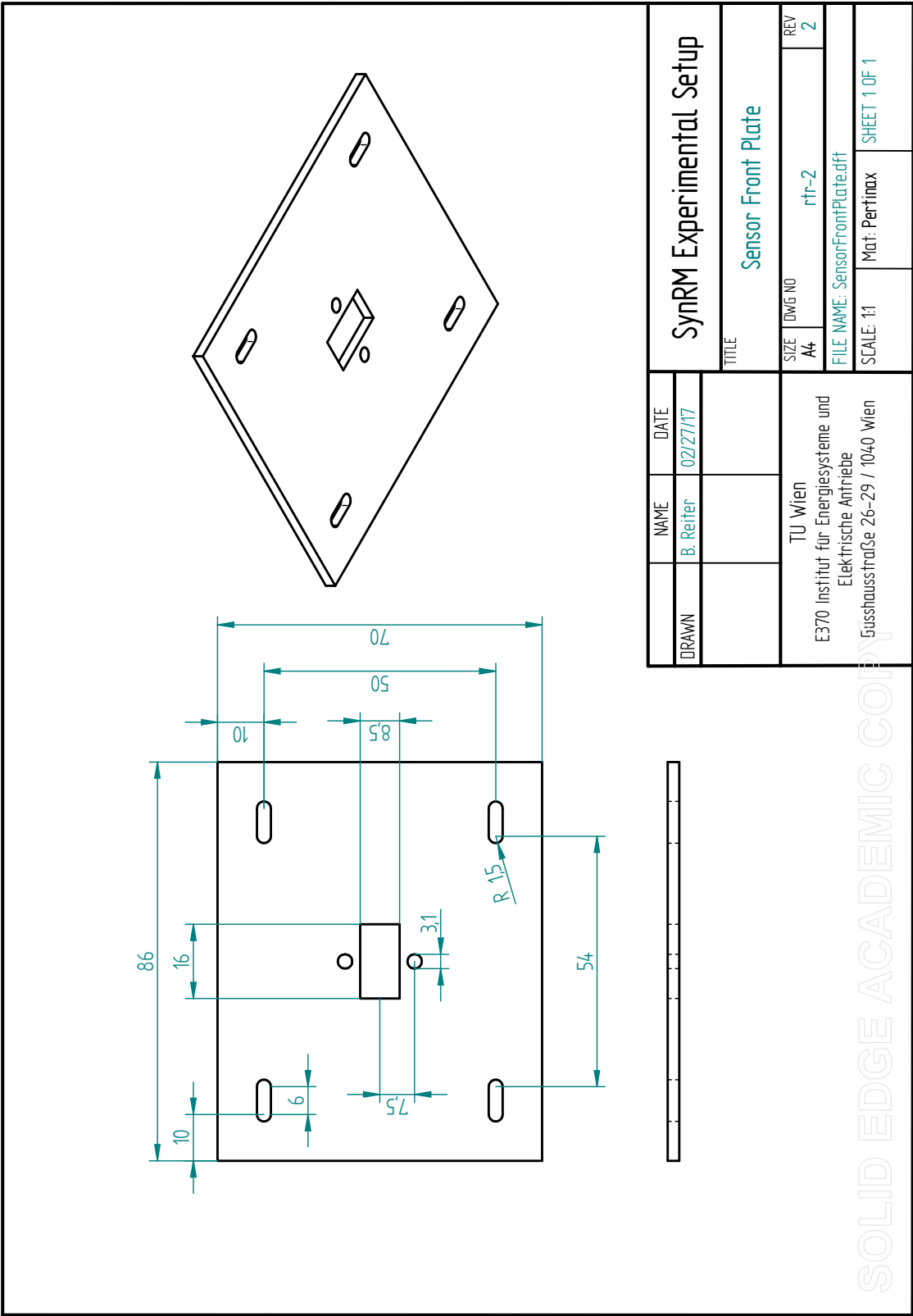
Figure B.8: Sensor front plate drawing

Bibliography

[1] R. Spießberger, "Berechnung einer Synchron-Reluktanzmaschine für einen magnetgelagerten Antrieb," Vienna University of Technology, Tech. Rep., 2015.

[2] J. Höllwerth, "Drehstromantrieb für einen Magnetlager-Demonstrator," Master's thesis, Vienna University of Technology, 2012.

[3] P. Ebermann, "Aufbau und Regelung eines Demonstrators mit sensorlosen aktiven Magnetlagern und einer Synchron-Reluktanzmaschine," Master's thesis, Vienna University of Technology, 2015.

[4] M. Wagner, "Aufbau und Inbetriebnahme eines Umrichters für ein sensorloses Magnetlager," Master's thesis, Vienna University of Technology, 2016.

[5] A. Hauer, "Aufbau und Inbetriebnahme eines Mehrfachstromrichters für einen sensorlosen Magnetlagerantrieb," Master's thesis, Vienna University of Technology, 2017.

[6] M. Hofer, "Design and Sensorless Position Control of a Permanent Magnet Biased Radial Active Magnetic Bearing," PhD thesis, Vienna University of Technology, 2013.

[7] D. Wimmer, "Optimierung eines sensorlosen Magnetlagers mittels variabler Raumzeigermodulation," Master's thesis, Vienna University of Technology, 2017.

[8] G. Pellegrino, T. M. Jahns, N. Bianchi, W. L. Soong, and F. Cupertino, *The Rediscovery of Synchronous Reluctance and Ferrite Permanent Magnet Motors*, 1st Edition. Springer, 2016, ISBN: 978-3-319-32200-1.

[9] M. P. et. al., "Final Report on Electric Machines and Drives - Advanced Studies," Vienna University of Technology, Tech. Rep., 2015.

[10] *Rotex Spielfreie Servokupplungen ROTEX GS, Technische Beschreibung*, 2017.

[11] S. A. T. William H. Press, *Numerical Recipes in C: The Art of Scientific Computing*, 2nd Edition. Cambridge University Press, 1992, William T. Vetterling, Brian P. Flannery, ISBN: 0-521-43108-5.

[12] R. Klima and S. Selberherr, *Programmieren in C*, Dritte Auflage. Springer Vienna, 2010, ISBN: 978-3-7091-0392-0.

[13] D. M. Alter, "IQ Math on the Texas Istruments TMS320C28x DSP," Texas Instruments Inc., Tech. Rep., 2009.

[14] S. Skogestad and I. Postlethwaite, *Multivariable Feedback Control: Analysis and Design, 2nd Edition*, 2nd, reprinted 2007. John Wiley & Sons, 2005, ISBN: 978-0470011676.

[15] M. Schrödl, *Drehstromantriebe mit Mikrorechnern*, Lecture Notes, University of Technology Vienna, 2000.

[16] A. V. Rik De Doncker Duco W.J. Pulle, *Advanced Electrical Drives*, 1st edition, R. D. Lorenz, Ed., ser. power systems. Springer, 2011, ISBN: 978-94-007-0179-3.

[17] H. Ertl, *Leistungselektronik und Stromrichtertechnik*, Lecture Notes, University of Technology Vienna, 2012.

[18] A. Prechtl, *Vorlesungen über Elektrodynamik*, Lecture Notes, University of Technology Vienna, 2005.

[19] J. D. Jackson, *Classical Electrodynamics*. Wiley, 1998, ISBN: 978-0-47130-932-1.

[20] A. Prechtl, *Vorlesungen über die Grundlagen der Elektrotechnik*, 2. Auflage. Springer Wien New York, 2008, vol. Band 2, ISBN: 978-3-211-72455-2.

[21] M. Schrödl, *Maschinen und Antriebe*, Lecture Notes, University of Technology Vienna, 2013.

[22] P. K. Kovács and I. Rácz, *Transiente Vorgänge in Wechselstrommaschinen*. Akadémiai Kiadó, 1959.

[23] P. K. Kovács, *Transient Phenomena in Electrical Machines*, B. Balkay, Ed. Á Akadémiai Kiadó, Budapest, 1984, ISBN: 963-05-2949-1.

[24] H. Sequenz, *Die Wicklungen elektrischer Maschinen*. Springer-Verlag Wien, 1950, vol. Erster Band: Wechselstrom-Ankerwicklungen, ISBN: 978-3-7091-3230-2.

[25] K. V. Bernd Ponick Germar Müller, *Berechnung elektrischer Maschinen*, 6. Auflage. Wiley-VCH Verlag GmbH & Co. KGaA, 2007, ISBN: 978-3527405251.

[26] G. A. Reider, *Photonik*, 2. Auflage. Springer Wien-New York, 2005, ISBN: 3-211-21901-3.

[27] E. Clarke, *Circuit Analysis of AC Power Systems*. J. Wiley & sons, New York, 1943, vol. Volume 1.

[28] R. H. Park, "Two Reaction Theory of Synchronous Machines generalized Method of Analysis-Part i.," *AIEE Transactions*, vol. 48, 1929, p716-p727.

[29] M. Schrödl, *Elektrische Antriebe*, Lecture Notes, University of Technology Vienna, 2013.

[30] A. Fratta, G. Troglia, A. Vagati, and F. Villata, "Evaluation of Torque Ripple in High Performance Synchronous Reluctance Machines," *IEEE Industry Application Society Annual Meeting*, vol. 1, pp. 163–170, Oct. 1993.

[31] A. K. Wolfgang Kemmetmüller David Faustner, "Modelling of a Permanent Magnet Synchronous Machine With Internal Magnets Using Magnetic Equivalent Circuits," *IEEE Transactions on Magnetics*, vol. 50, no. 6, Jun. 2014.

[32] A. S. Tobias Glück Wolfgang Kemmetmüller, *Fortgeschrittene Methoden der Modellbildung*, Lecture Notes, University of Technology Vienna, 2015.

[33] J. Stepina, "Raumzeiger als Grundlage der Theorie der elektrischen Maschinen," *etz-A*, vol. 88, no. 23, p584–588, 1967.

[34] T. J. E. M. Wen L. Soong David A. Staton, "Design of a New Axially-Laminated Interior Permanent Magnet Motor," *IEEE Transactions on Industry Applications*, vol. 31, no. 2, Mar. 1995.

[35] R. E. Doherty and C. A. Nickle, "Synchronous machines i-an extensio of blondel's two-reaction theory," *Transactions of the AIEE*, vol. 45, pp. 912–942, 1926.

[36] A. E. Blondel, *Synchronous Motors and Converters: Theory and Methods of Calculation and Testing*. McGraw- Hill Book Company, New York, 1913.

[37] J. K. Kostko, "Polyphase reaction synchronous motors," *Journal of the American Institute of Electrical Engineers*, vol. 42, no. 11, pp. 1162–1168, 1923.

[38] M. B. Slimane Tahi Rachid Ibtiouen, "Design Optimization Of Two Synchronous Reluctance Machine Structures With Maximized Torque And Power Factor," *Progress in Electromagnetics Research B*, vol. 35, pp. 369–387, 2011.

[39] R. I. Slimane Tahi, "Finite Element Calculation of the dq-Axes Inductances and Torque of Synchronous Reluctance Motor," *International Conference on Electrical Sciences and Technologies in Maghreb*, 2014.

[40] A. Kugi, *Regelungssysteme 2*, Lecture Notes, University of Technology Vienna, 2014.

[41] J. O. R. Petar Kokotović Hassan K. Khalil, *Singular Pertubation Methods in Control: Analysis and Design*. SIAM, Philadelphia, 1999.

[42] *Reference Guide, TMS320x2833x Analog-to-Digital Converter (ADC) Module*, SPRU812A, Texas Instruments, 2007.

[43] TI, *C2000 Delfino Workshop*, T. T. Organization, Ed. Texas Instruments, 2010.

[44] *As5040 Datasheet , Austria Microsystems, Revision 2.10*, 2015.

[45] *AN5000 Rotary Magnetic Position Sensors, Magnet Selection Guide, Austria Microsystems, Revision 1.04*, Sep. 2016.

[46] *Reference Guide, TMS320x2833x Enhanced Quadrature Encoder Pulse (eQEP) Module*, SPRUG05A, Texas Instruments, 2008.

[47] *Data Manual, TMS320F2833x Digital Signal Controller*, SPRS439M, Texas Instruments, 2012.

[48] *Reference Guide, TMS320x2833x Enhanced Pulse Width Modulation (ePWM) Module*, SPRUG04A, Texas Instruments, 2009.

[49] *Reference Guide, TMS320x2833x System Control and Interrupts*, SPRUFB0D, Texas Instruments, 2007.

[50] *C28x IQmath Library v1.6.0*, Texas Instruments, Aug. 2011.

[51] D. Schröder, *Elektrische Antriebe - Regelung von Antriebssystemen*. Springer Vieweg, 2015, vol. 4. Auflage, ISBN: 978-3-642-30095-0.

[52] *Datasheet: GMM 3x100-01X1 Three phase full Bridge with Trench MOSFETs*, IXYS, 2011.

[53] A. Kugi, *Optimierung*, Lecture Notes, University of Technology Vienna, 2015.

[54] ——, *Automatisierung Vorlesung*, Lecture Notes, University of Technology Vienna, 2011.

[55] P. Hippe, *Windup in Control: Its Effects and Their Prevention*, ser. Advances in Industrial Control. Springer London, 2006, ISBN: 978-1-84628-323-9.

[56] R. J. McEliece, *Signals, systems and transforms*, Lecture Notes, California Institue of Technology (Caltech), Feb. 2002.

[57] A. L. S. Barbosa, G. A. Júnior, and P. R. Barros, "Symmetrical Optimum Based PI Control Redesign," *Anais do XX Congresso Brasileiro de Automática*, pp. 1143–1149, Mar. 2014.

[58] M. Schrödl and M. Hofer, *Aufbau hochdynamischer Drehstromantriebe*, Laboratory Exercise Lecture Notes, University of Technology Vienna, 2015.
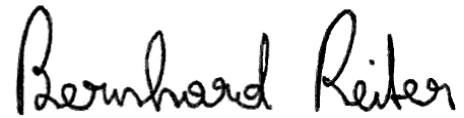
[59] T. Matsuo and T. A. Lipo, "Field Oriented Control of Synchronous Reluctance Machines, Research Report," Wisconsin Electric Machines and Power Electronics Consortium (WEMPEC), Tech. Rep., 1993.

[60] *Digital Motor Control Software Library: F2833x Drivers*, Texas Instruments C2000 Systems and Applications, 2012.

[61] G. Merzinger and T. Wirth, *Repetitorium der Höheren Mathemtaik*. Binomi Verlag, 2006.

[62] R. J. S. S D Calverley G W Jewell, "Aerodynamic losses in switched reluctance machines," *IEE Proceedings Electrical Power Applications*, vol. 147, no. 6, pp. 443–448, 2000.

[63] M. Schrödl, *Sensorless Control of A.C. Machines*, Tenure Thesis, TU Vienna, 1992.

[64] E. Robeischl, "Optimierung der sensorlosen Regelung von permanentmagneterregten Synchronmaschinen und Anwendung in einem kosteneffizienten Positionierantrieb," PhD thesis, Technische Universität Wien, 2003.

[65] U.-H. Rieder, "Optimierung der sensorlosen Regelung von permanentmagneterregten Aussenläufer-Synchronmaschinen," PhD thesis, Technische Universität Wien, 2005.

[66] M. Izaak, "Optimierung des überganges zwischen INFORM- und EMK- basierter sensorloser Regelung von permanentmagneterregten Synchronmaschinen," PhD thesis, Technische Universität Wien, 2009.

[67] A. Eilenberger, "Permanent Magnet Synchronous Machines With Tooth Coils For Sensorless Control Including Overload Range," PhD thesis, Technische Universität Wien, 2010.

[68] G. Kalteis, "Sensorloser Betrieb von permanentmagneterregten Synchronmaschinen mit Sinus- und Blockkommutierung bis Stillstand," PhD thesis, Technische Universität Wien, 2012.

[69] ——, "Verfahren und Schaltungsanordnung zur näherungsweisen Einstellung eines Spannungsraumzeigers; Method and circuit arrangement for approximate adjustment of a voltage space vector," German, European pat. EP 1722470 B1, Nov. 2006.

[70] N. Bianchi, S. Bolognani, J.-H. Jang, and S.-K. Sul, "Comparison of PM Motor Structures and Sensorless Control Techniques for Zero-Speed Rotor Position Detection," *IEEE Transactions on Power Electronics*, vol. 22, no. 6, pp. 2466–2475, Nov. 2007.

[71] J. G. Haitham Abu-Rub Atif Iqbal, *High Performance Control of AC Drives with Matlab/ Simulink Models*. Wiley, 2012, ISBN: 9780470978290.

[72] W. Kemmetmüller, *Regelungssysteme 1*, Lecture Notes, University of Technology Vienna, 2015.

[73] "Adaptive Position Sensing Method and Apparatus for Synchronous Motor Generator System," pat. WO 2005099082 A1, Christian E. Anghel, Nicolae Morcov, Rocco Divito, Oct. 2005.

[74] M. Schrödl and E. Robeischl, "Geregelte Antriebe," *Elektrotechnik und Informationstechnik (e&i , AT)*, 2000.

[75] T. Nenning, "Comparison of position evaluation methods based on current slopes in a self-sensing magnetic-bearing system," PhD thesis, Technische Universität Wien, 2015.

[76] *Cooperative Patent Classification Scheme: H02P*, 2018.

[77] *Cooperative Patent Classification Scheme: H02K*, 2018.

[78] *Cooperative Patent Classification Definition: H02P*, 2018.

[79] *Cooperative Patent Classification Definition: H02K*, 2018.

[80] "Vorrichtung zur Steuerung einer rotierenden elektrischen Maschine," German, German pat. DE 112014000512 T5, Shimada, Arinori, Anjo-shi, Aichi, Saha, Subrata, Anjo-shi, Aichi, Okubo, Tatsuya, Anjo-shi, Aichi, Oct. 2015.

[81] "Transition Scheme for Poistion Sensorless Control of AC Motor Drives," U.S. Patent US 20160056740 A1, Thomas Nondahl, Jingbo Liu, Peter Schmidt, Semyon Royak, Jingya Dai, Ehsan Al-Nabi, Feb. 2016.

[82] "Motor Magnetic-Pole-Position Estimating Apparatus," U.S. Patent US 20110175560 A1, Masahiko Akiyama, Jul. 2011.

[83] "System and Method for Controlling a Position Sensorless Permanent Magnet Motor," U.S. Patent US 6163127 A, Nitinkumar Ratilal Patel, Thomas P. O' Meara, Dec. 2000.

[84] "System zur nahtlosen Geschwindigkeits- und/oder Lageermittlung einschließlich Stillstand bei einem Permanentmagnet-Läufer einer elektrischen Maschine," German, European pat. EP 2023479 A1, Fritz Rainer Goetz, Viktor Barinberg, Feb. 2009.

[85] "Regelsystem mit einer einfachen Hardware-Einheit zur Regelung einer elektrischen Maschine wahlweise im PWM-oder Blockbetrieb," German, German pat. DE 10301826 A1, Martin Eisenhardt, Alexander Seufert, Klaus Rechberger, Jul. 2004.

[86] "Switched Reluctance Motor," pat. WO 2015109150 A1, Aleksandr S. Nagorny, Siavash Sadeghi, David James Fleming, Jul. 2015.

Eidesstattliche Erklärung

Hiermit erkläre ich, dass die vorliegende Arbeit gemäß dem Code of Conduct – Regeln zur Sicherung guter wissenschaftlicher Praxis (in der aktuellen Fassung des jeweiligen Mitteilungsblattes der TU Wien), insbesondere ohne unzulässige Hilfe Dritter und ohne Benutzung anderer als der angegebenen Hilfsmittel, angefertigt wurde. Die aus anderen Quellen direkt oder indirekt übernommenen Daten und Konzepte sind unter Angabe der Quelle gekennzeichnet. Die Arbeit wurde bisher weder im In– noch im Ausland in gleicher oder in ähnlicher Form in anderen Prüfungsverfahren vorgelegt.

Wien, 18 Jan 2018

Bernhard Reiter, BSc.